

# Monitoring Transient Repolarization Segment Morphology Deviations in Mouse ECG

by

Matthew Blake Oefinger

Submitted to the Department of Electrical Engineering and Computer  
Science

in partial fulfillment of the requirements for the degree of  
Doctor of Philosophy in Computer Science and Engineering

at the

MASSACHUSETTS INSTITUTE OF TECHNOLOGY

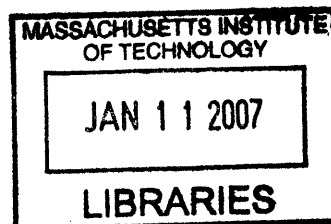
[september 2006]  
July 2006

© Massachusetts Institute of Technology 2006. All rights reserved.

Author .....  
Department of Electrical Engineering and Computer Science  
July 25, 2006

Certified by .....  
Roger G. Mark  
Distinguished Professor of Health Sciences Technology  
Professor of Electrical Engineering and Computer Science  
Thesis Supervisor

Accepted by .....  
Arthur C. Smith  
Chairman, Department Committee on Graduate Students



BARKER





# Monitoring Transient Repolarization Segment Morphology Deviations in Mouse ECG

by

Matthew Blake Oefinger

Submitted to the Department of Electrical Engineering and Computer Science  
on July 25, 2006, in partial fulfillment of the  
requirements for the degree of  
Doctor of Philosophy in Computer Science and Engineering

## **Abstract**

This thesis details the design, implementation and validation of a system that facilitates partial automation for detection of anomalous repolarization segment morphologies in the ECG of mice. The technology consists of hardware for signal conditioning of the electrocardiogram (ECG); software for the collection, archiving and real-time & retrospective Internet visualization of data; and an algorithm for morphology analysis of the repolarization segment in murine ECG. The system was validated using genetically engineered mouse subjects with elevated VLDL, analagous to LDL or “bad cholesterol” in humans, and elevated but modified HDL, or “good cholesterol.” These subjects, so-called “double-knockout” or dKO mice, exhibit repolarization segment morphologies that are manifestations of severe cardiovascular pathophysiology. This thesis describes the technology in detail and its application to elucidating long-term trends in repolarization morphology deviations in dKO mice. The paper concludes with future work that will utilize the technology and potential clinical applications.

Thesis Supervisor: Roger G. Mark

Title: Distinguished Professor of Health Sciences Technology

Professor of Electrical Engineering and Computer Science



# Acknowledgments

In the summer of 2001 I stood outside MIT's Killian Court with my wife, Amy, looking at the majestic dome of building 10. We had left several hours early from our honeymoon destination in Jackson, New Hampshire to witness this culture of academic excellence of which I had long wanted to be a part. Evidently my poker face isn't so good, because Amy patted me on the back and said: "Your face says it all. You'll always wonder what might have been if you don't apply." So began my journey toward entering MIT for graduate studies, a once-smoldering dream that had become a blaze during the last years of my undergraduate work at Southern Methodist University.

Graduate life at MIT proved to be at once exhilarating and extremely humbling. Each year of study brought its own personal and academic challenges greater than the last, and on ever-shifting ground there were some whose support helped pave a gratifying and enjoyable path to fulfillment of a graduate education. It is these people whom I would like to acknowledge with sincere gratitude in this section.

During my first year at MIT, I learned of Professor Roger Mark's Laboratory for Computational Physiology (LCP). Shortly after meeting Professor Mark and learning of his exciting realm of research, I joined the LCP. At the time I couldn't have known that the LCP provided much more than an exciting research environment; I quickly learned that the lab was comprised of personable and supportive people who genuinely enjoyed their work and each other. Professor Mark takes an interest in each student's development and manages to provide a rare combination of exceptional guidance with ample freedom to explore new ideas. A student's sentiment toward graduate school often hinges on his perception of his advisor. I will, in large part, remember my time at MIT fondly because of Professor Mark's calm and pleasant approach, his exceptional talent for bringing intuition to bear on any challenge, and his guidance in matters related to matters both personal and academic. It has been a true privilege working in Professor Mark's lab. On a note of technical acknowledgement I would like to thank Professor Mark for his keen insight that helped pull chapter 2 into a coherent description of the murine repolarization period. His suggestion that I consider

exploiting the large data set of ischemic mice to look at repolarization times - which are impossible to determine from healthy mouse ECG - provided me with an exciting “aha!” moment. The power of his suggestion became more impressed upon me as I wrote chapter 2, as it provides strong motivation for timepoints used in subsequent analyses that would have otherwise been chosen somewhat arbitrarily.

Professor Monty Krieger provided a truly unique and fascinating academic challenge, unwavering enthusiasm for the project, and substantial funding to implement the monitoring system that was the focus of my thesis. I am very grateful for his faith in me and the latitude he permitted the LCP as we explored technologies that I hope will assist his research for many years to come. Without the help of Professor Franc Jager, this project simply wouldn’t have taken shape or come to a meaningful end. His extensive experience in ST segment analysis provided the foundational insight for use of Chebyshev polynomials as a pattern-recognition tool for repolarization segments in mice, which is the crux of my thesis work. Professor Lou Braida showed a great interest in my research from his first exposure to it as a panel member for my Research Qualifying Examination. He remained a valuable member of the thesis committee and was an advocate of focused work and tangible milestones that would keep the project on schedule. I first met Dr. Julie Greenberg, who would later become a member of my thesis committee, as a student in her course on biomedical signal processing. Her course remains my favorite at MIT for its application-oriented, or “hands-on” approach to designing algorithms for interpretation of biomedical signals.

The technical challenges addressed by this work did not begin at “ground zero.” Rather, they relied on a precedent of information and tools first developed by George Moody and Professor Roger Mark. Their invention of Physionet as an open-source repository for physiological data, algorithms and tutorials provided the foundation for the work addressed in this thesis. Dr. Wei Zong’s *wqrs* algorithm for automated QRS detection, which he provided as a contribution to Physionet, was an immensely helpful tool that provided beat and J-point detection, both of which are used extensively as fiducial points in this thesis. George Moody’s extensive WFDB libraries and unparalleled documentation provided an exceptional

framework with which to approach a new system design. Professor Steve Burns provided very helpful advice regarding hardware designs. He quickly and authoritatively answered questions I had during the design and debugging process. Professor Burns is a walking encyclopedia of hardware knowledge without whom I would have wasted many hours re-inventing the wheel.

A doctoral program has the potential to be lonely; after all, the premise of doctoral work is individual research. My time at MIT was anything but lonely thanks to the extremely bright, clever, charismatic and often downright comical labmates at the LCP that have become true friends. Among the friends I would like to thank (simply for being great friends) are Gari Clifford, Katie Dunn, Isaac Henry, George Moody, Rama Mukkamala, Ken Pierce, Mohammed Saeed, James Sun, Mauro Villarroel and Wei Zong. One member of the LCP who has become a particularly great friend and colleague, Thomas Heldt, provided countless hours of challenging banter and even more hours of laughter. Though we'll always remain friends, I'll certainly miss the immediacy of his great mind and wit. On a note more germane to my thesis work, I would like to thank Thomas for acting as a virtual advisor by providing a sounding board and excellent advice on assembling my sometimes loosely-organized thoughts into coherent presentations.

Finally, I want to thank those "behind the scenes," namely my family, who provided unrelenting support during the lengthy graduate education process. My parents-in-law, Jim and Susan, have always been incredibly helpful and caring individuals. Their support came in countless forms with selfless care and constant enthusiasm. I want to thank my brother and best friend, Jon, for providing a steady voice of reason during, and in the wake of, our father's early death. Some of my favorite memories of graduate school include late-night, long-distance phone calls with him during which he would invariably ask the right questions and offer anecdotal humor to offset otherwise serious discussions.

If space permitted I would devote a full chapter to my wife, Amy. It was she who encouraged me to follow my dream of coming to MIT, and it was she who remained supportive, patient and cheerful for a husband whose obsession with research and learning kept him

locked away in his study at best or unseen for several consecutive days at worst. She kept me sane and happy, and in response to my tendency to lose track of time and forget meals, she became a certified professional chef. Amy went beyond vicariously living every challenge of mine; she treated each challenge as her own and offered a balance of listening and advising that helped me to formulate my school, career and family goals. On October 16, 2004, Amy delivered our daughter, Olivia, into the world. Olivia's simple utterances of "da-da" provide an amazingly fresh perspective each morning and night. Olivia is proof that big inspiration can come in small packages.

# Contents

<b>1</b>	<b>Introduction</b>	<b>23</b>
1.1	Animal testing in cardiovascular medicine . . . . .	24
1.2	The double-knockout genotype . . . . .	26
1.3	Of mice and machines . . . . .	29
1.3.1	Thesis foundations and experimental setup . . . . .	29
1.3.2	Thesis outline . . . . .	32
1.3.3	Scope of work . . . . .	33
<b>2</b>	<b>Background: murine cardiac electrophysiology</b>	<b>35</b>
2.1	The depolarization period . . . . .	36
2.2	The repolarization period . . . . .	38
2.2.1	An introduction to the Liu study . . . . .	39
2.3	Selection of time points for repolarization segment measurement . . . . .	46
2.3.1	Repolarization segment: start point determination . . . . .	46
2.3.2	Repolarization segment: end point determination . . . . .	48
2.4	Arrhythmias . . . . .	56
2.4.1	Premature ventricular contractions . . . . .	57
2.4.2	Ventricular tachycardia . . . . .	58
2.4.3	Heart block . . . . .	59
2.4.4	Bradycardia . . . . .	59
2.5	Summary . . . . .	60

<b>3</b>	<b>ECG instrumentation design and analog-to-digital conversion</b>	<b>61</b>
3.1	Signal conditioning hardware . . . . .	62
3.1.1	Single-channel architecture . . . . .	63
3.1.2	Common-mode noise reduction: active grounding circuit . . . . .	66
3.1.3	Increasing input impedance: CMOS buffer stage . . . . .	67
3.1.4	Pre-amplification . . . . .	67
3.1.5	High-pass filtering . . . . .	70
3.1.6	Secondary amplification . . . . .	72
3.1.7	Low-pass filtering and oversampling . . . . .	72
<b>4</b>	<b>Software for data collection and trend visualization via the Internet</b>	<b>75</b>
4.1	Server user interface software . . . . .	75
4.2	Server data acquisition software . . . . .	80
4.2.1	WFDB formatting, server self-diagnostics and email notification . . . . .	80
4.2.2	Server multicast network software . . . . .	81
4.2.3	Server security . . . . .	82
4.3	Client remote real-time monitoring software . . . . .	82
4.4	Client retrospective interactive data mining software . . . . .	83
4.4.1	Record search and load . . . . .	83
4.4.2	Interactive data mining . . . . .	84
4.4.3	Virtual streaming . . . . .	87
4.4.4	Annotating data . . . . .	88
<b>5</b>	<b>The Chebyshev transform</b>	<b>91</b>
5.1	Established approaches in human ECG analysis . . . . .	91
5.1.1	Time domain: the ST deviation function . . . . .	92
5.1.2	The Karhunen-Loeve (K-L) transform . . . . .	93
5.2	A new approach: the Chebyshev transform . . . . .	96
5.3	Sturm-Liouville origins . . . . .	97



5.3.1	Chebyshev decomposition . . . . .	100
5.3.2	The Chebyshev advantage . . . . .	100
5.4	Summary . . . . .	101
<b>6</b>	<b>Automated analysis of repolarization segment morphology</b>	<b>103</b>
6.0.1	Pre-processing . . . . .	103
6.0.2	Applying the transform . . . . .	110
6.1	Post-processing . . . . .	111
6.1.1	Typical repolarization segment morphology of healthy mice . . . . .	111
6.1.2	Multidimensional visualization as a morphology indicator . . . . .	112
6.1.3	Euclidean distance as a morphology anomaly indicator . . . . .	112
6.2	A simple morphology deviation alarm . . . . .	113
6.2.1	Axis shifts . . . . .	114
6.2.2	Signal quality index . . . . .	119
6.3	Summary . . . . .	120
<b>7</b>	<b>Grid computing for high-throughput data processing</b>	<b>121</b>
7.1	Motivation for parallel computing . . . . .	121
7.2	Grid computing defined . . . . .	121
7.3	Methods of parallelizing processing . . . . .	122
7.4	Comparison of grid and cluster performance . . . . .	123
7.5	Grid computing software architecture . . . . .	125
7.5.1	CGI - the Common Gateway Interface . . . . .	125
7.5.2	Load balancing: asynchronous, interrupt-driven job dispatch . . . . .	126
7.5.3	Self-monitoring . . . . .	127
7.5.4	Summary . . . . .	128
<b>8</b>	<b>ECG Trends in dKO mice</b>	<b>129</b>
8.1	Case study A . . . . .	132
8.2	Case study B . . . . .	136

8.3	Case study C . . . . .	146
8.4	Summary . . . . .	157
<b>9</b>	<b>Conclusions and future work</b>	<b>159</b>
9.1	Conclusions . . . . .	159
9.2	Future work . . . . .	161
9.2.1	Murine database episode annotation . . . . .	161
9.2.2	Drug development: toxicity and efficacy screening . . . . .	161
9.3	Potential clinical applications . . . . .	162
<b>A</b>	<b>Repolarization segment onset and offset times</b>	<b>165</b>
<b>B</b>	<b>Trend plots for all mouse subjects</b>	<b>173</b>
<b>C</b>	<b>Hermes user's guide</b>	<b>245</b>
C.1	Intended Audience . . . . .	245
C.2	Getting started . . . . .	246
C.3	Viewing a Record . . . . .	246
C.3.1	Database . . . . .	247
C.3.2	Heart rate . . . . .	247
C.3.3	Signal quality index . . . . .	252
C.3.4	Repolarization segment . . . . .	253
C.4	Annotating data . . . . .	254
<b>D</b>	<b>Hermes as a web portal to Physionet</b>	<b>255</b>
D.1	Physionet background . . . . .	255
D.2	The virtual lab . . . . .	256
D.3	Read-only vizualization of gold-standard databases . . . . .	256
<b>E</b>	<b>Chebyshev Decomposition Examples</b>	<b>259</b>

# List of Figures

1-1	Angiogram, histology and ejection fraction of dKO mice . . . . .	27
1-2	Sample pathophysiologic ECG segments from dKO mice . . . . .	28
1-3	dKO mortality curve . . . . .	29
1-4	tripolar electrodes for ECG recording . . . . .	30
1-5	Commutator swivel permitting subject free range of motion . . . . .	31
2-1	Segmentation of mouse ECG into ventricular depolarization and repolarization periods . . . . .	35
2-2	Simplified diagram of the conduction system . . . . .	37
2-3	The relatively long PR interval of mouse ECG . . . . .	38
2-4	Murine ECG with characteristic absent P wave . . . . .	38
2-5	The Liu study: simultaneous AP and ECG recording . . . . .	41
2-6	Human cellular action potential (AP) and ECG . . . . .	42
2-7	The Liu study: inducing a T wave in murine ECG with transmural temperature differences . . . . .	43
2-8	The Liu study: inducing a T wave in murine ECG with pinacidil on the endocardial surface . . . . .	44
2-9	The human T wave explained: AP activity leading to a T wave . . . . .	45
2-10	The absence of a murine T wave explained . . . . .	47
2-11	Repolarization period start point . . . . .	49
2-12	Action potential morphology during ischemia . . . . .	50
2-13	Example of ST segment elevation in human ECG . . . . .	51

2-14	Example of ST segment depression in human ECG . . . . .	51
2-15	Current of injury model leading to repolarization segment morphology change	52
2-16	Example of elevated repolarization segment in murine ECG . . . . .	53
2-17	Example of depressed repolarization segment in murine ECG . . . . .	53
2-18	Example of depressed repolarization segment in murine ECG . . . . .	54
2-19	Example of elevated repolarization segment in murine ECG . . . . .	54
2-20	Mouse ECG repolarization onset and offset time markers . . . . .	55
2-21	PVC in murine ECG . . . . .	57
2-22	Trigeminy in murine ECG . . . . .	57
2-23	Ventricular tachycardia in murine ECG . . . . .	58
2-24	Ventricular tachycardia spontaneous termination in murine ECG . . . . .	58
2-25	Second-degree heart block in murine ECG . . . . .	59
2-26	Third-degree heart block in murine ECG . . . . .	59
3-1	16-channel mouse ECG signal conditioning hardware photo . . . . .	63
3-2	Simplified diagram of single-channel ECG signal-conditioning hardware . . .	63
3-3	Single-channel ECG signal conditioning hardware schematic (Orcad) . . . . .	64
3-4	Single-channel ECG signal conditioning hardware schematic (PCB123) . . .	65
3-5	Single-channel ECG signal conditioning hardware PCB layout . . . . .	65
3-6	Single-channel ECG signal conditioning hardware PCB photo . . . . .	66
3-7	Active grounding circuit . . . . .	67
3-8	Optical isolation circuit with high-impedance CMOS buffer inputs . . . . .	68
3-9	Example of potential ground fault hazard . . . . .	69
3-10	A ground fault hazard . . . . .	69
3-11	A ground fault hazard averted with optical isolation . . . . .	69
3-12	Bessel filter frequency amplitude characteristics . . . . .	71
3-13	Bessel filter frequency phase characteristics . . . . .	71
3-14	An aliased signal due to undersampling . . . . .	73
3-15	Oversampling as a means of preventing aliasing . . . . .	73

3-16	Digital lowpass filtering and down-sampling . . . . .	73
4-1	Server GUI interface screenshot . . . . .	76
4-2	Server web form for starting data acquisition . . . . .	77
4-3	Server error-checking of form fields . . . . .	77
4-4	Server refusing to accept a redundant record name . . . . .	78
4-5	A screenshot of user adding fields to a mouse record template . . . . .	79
4-6	A warning to the user requesting confirmation before deleting a database field . . . . .	79
4-7	Internet-based data visualization applet: record load panel . . . . .	84
4-8	Internet-based data visualization applet: record navigation panel . . . . .	86
5-1	Example of ST segment elevation in human ECG . . . . .	93
5-2	Example of ST segment depression in human ECG . . . . .	93
5-3	Principal component analysis and the Mahalanobis distance . . . . .	96
5-4	Chebyshev polynomials of the first kind. . . . .	98
5-5	Chebyshev polynomials of the second kind. . . . .	99
6-1	Signal quality index as belief metric - 1 of 3 . . . . .	105
6-2	Signal quality index as belief metric - 2 of 3 . . . . .	105
6-3	Signal quality index as belief metric - 3 of 3 . . . . .	106
6-4	3-d Euclidean vector magnitude (from 3-d Chebyshev feature space) of repolarization segment from wild-type mouse . . . . .	113
6-5	3-d Euclidean vector magnitude (from 3-d Chebyshev feature space) of repolarization segment from dKO mouse . . . . .	113
6-6	User selection of morphology deviation threshold for alarm . . . . .	115
6-7	Axis shift example - before the axis shift . . . . .	116
6-8	Axis shift example - after the axis shift . . . . .	117
6-9	Automated axis shift detection example - before the axis shift . . . . .	118
6-10	Automated axis shift detection example - after the axis shift . . . . .	118
6-11	Automated axis shift detector turned off - after the axis shift . . . . .	119

7-1	Grid vs. cluster performance model . . . . .	124
8-1	Case study A: wild-type mouse - 1 of 3 . . . . .	133
8-2	Case study A: wild-type mouse - 2 of 3 . . . . .	134
8-3	Case study A: wild-type mouse - 3 of 3 . . . . .	135
8-4	Case study B: dKO mouse - 1 of 10 . . . . .	137
8-5	Case study B: wild-type mouse - 2 of 10 . . . . .	138
8-6	Case study B: wild-type mouse - 3 of 10 . . . . .	139
8-7	Case study B: dKO mouse - 4 of 10 . . . . .	140
8-8	Case study B: dKO mouse - 5 of 10 . . . . .	141
8-9	Case study B: dKO mouse - 6 of 10 . . . . .	142
8-10	Case study B: dKO mouse - 7 of 10 . . . . .	143
8-11	Case study B: dKO mouse - 8 of 10 . . . . .	144
8-12	Case study B: dKO mouse - 9 of 10 . . . . .	145
8-13	Case study B: dKO mouse - 10 of 10 . . . . .	145
8-14	Case study C: dKO mouse - 1 of 10 . . . . .	147
8-15	Case study C: dKO mouse - 2 of 10 . . . . .	148
8-16	Case study C: dKO mouse - 3 of 10 . . . . .	149
8-17	Case study C: dKO mouse - 4 of 10 . . . . .	150
8-18	Case study C: dKO mouse - 5 of 10 . . . . .	151
8-19	Case study C: dKO mouse - 6 of 10 . . . . .	152
8-20	Case study C: dKO mouse - 7 of 10 . . . . .	153
8-21	Case study C: dKO mouse - 8 of 10 . . . . .	154
8-22	Case study C: dKO mouse - 9 of 10 . . . . .	155
8-23	Case study C: dKO mouse - 10 of 10 . . . . .	156
A-1	Repolarization onset and offset time examples 1-3 of 18 . . . . .	166
A-2	Repolarization onset and offset time examples 4-6 of 18 . . . . .	167
A-3	Repolarization onset and offset time examples 7-9 of 18 . . . . .	168
A-4	Repolarization onset and offset time examples 10-12 of 18 . . . . .	169

A-5	Repolarization onset and offset time examples 13-15 of 18 . . . . .	170
A-6	Repolarization onset and offset time examples 16-18 of 18 . . . . .	171
B-1	Trend plots for subject 0365121404 . . . . .	175
B-2	Trend plots for subject 0666122303 . . . . .	176
B-3	Trend plots for subject 0800122603 - 1 of 4 . . . . .	177
B-4	Trend plots for subject 0800122603 - 2 of 4 . . . . .	178
B-5	Trend plots for subject 0800122603 - 3 of 4 . . . . .	179
B-6	Trend plots for subject 0800122603 - 4 of 4 . . . . .	180
B-7	Trend plots for subject 0898122703 . . . . .	181
B-8	Trend plots for subject 0902122703 - 1 of 2 . . . . .	182
B-9	Trend plots for subject 0902122703 - 2 of 2 . . . . .	183
B-10	Trend plots for subject 0911123103 - 1 of 2 . . . . .	184
B-11	Trend plots for subject 0911123103 - 2 of 2 . . . . .	185
B-12	Trend plots for subject 0920122903 - 1 of 4 . . . . .	186
B-13	Trend plots for subject 0920122903 - 2 of 4 . . . . .	187
B-14	Trend plots for subject 0920122903 - 3 of 4 . . . . .	188
B-15	Trend plots for subject 0920122903 - 4 of 4 . . . . .	189
B-16	Trend plots for subject 0921122903 - 1 of 3 . . . . .	190
B-17	Trend plots for subject 0921122903 - 2 of 3 . . . . .	191
B-18	Trend plots for subject 0921122903 - 3 of 3 . . . . .	192
B-19	Trend plots for subject 0922122903 - 1 of 2 . . . . .	193
B-20	Trend plots for subject 0922122903 - 2 of 2 . . . . .	194
B-21	Trend plots for subject 1608011604 . . . . .	195
B-22	Trend plots for subject 1808011604 . . . . .	196
B-23	Trend plots for subject 2190020704 . . . . .	197
B-24	Trend plots for subject 2241020104 . . . . .	198
B-25	Trend plots for subject 2334020604 . . . . .	199
B-26	Trend plots for subject 2335020604 . . . . .	200

B-27 Trend plots for subject 2336020604 . . . . .	201
B-28 Trend plots for subject 2338020604 . . . . .	202
B-29 Trend plots for subject 2541020404 . . . . .	203
B-30 Trend plots for subject 2767022103 - 1 of 2 . . . . .	204
B-31 Trend plots for subject 2767022103 - 2 of 2 . . . . .	205
B-32 Trend plots for subject 2786022103 . . . . .	206
B-33 Trend plots for subject 3222031004 . . . . .	207
B-34 Trend plots for subject 3225031004 . . . . .	208
B-35 Trend plots for subject 3231030904 - 1 of 2 . . . . .	209
B-36 Trend plots for subject 3231030904 - 2 of 2 . . . . .	210
B-37 Trend plots for subject 4630040604 . . . . .	211
B-38 Trend plots for subject 4631040604 . . . . .	212
B-39 Trend plots for subject 5462040105 . . . . .	213
B-40 Trend plots for subject 5463040105 - 1 of 3 . . . . .	214
B-41 Trend plots for subject 5463040105 - 2 of 3 . . . . .	215
B-42 Trend plots for subject 5463040105 - 3 of 3 . . . . .	216
B-43 Trend plots for subject 6591081803 - 1 of 2 . . . . .	217
B-44 Trend plots for subject 6591081803 - 2 of 2 . . . . .	218
B-45 Trend plots for subject 6842083003 . . . . .	219
B-46 Trend plots for subject 6846090403 - 1 of 2 . . . . .	220
B-47 Trend plots for subject 6846090403 - 2 of 2 . . . . .	221
B-48 Trend plots for subject 7602091903 . . . . .	222
B-49 Trend plots for subject 8083100303 . . . . .	223
B-50 Trend plots for subject 8086100303 . . . . .	224
B-51 Trend plots for subject 9050040505 . . . . .	225
B-52 Trend plots for subject 9394111603 - 1 of 3 . . . . .	226
B-53 Trend plots for subject 9394111603 - 2 of 3 . . . . .	227
B-54 Trend plots for subject 9394111603 - 3 of 3 . . . . .	228



B-55 Trend plots for subject 9399111603 - 1 of 4 . . . . .	229
B-56 Trend plots for subject 9399111603 - 2 of 4 . . . . .	230
B-57 Trend plots for subject 9399111603 - 3 of 4 . . . . .	231
B-58 Trend plots for subject 9399111603 - 4 of 4 . . . . .	232
B-59 Trend plots for subject 9715112203 - 1 of 2 . . . . .	233
B-60 Trend plots for subject 9715112203 - 2 of 2 . . . . .	234
B-61 Trend plots for subject 9775112103 - 1 of 3 . . . . .	235
B-62 Trend plots for subject 9775112103 - 2 of 3 . . . . .	236
B-63 Trend plots for subject 9775112203 - 3 of 3 . . . . .	237
B-64 Trend plots for subject 9907120503 - 1 of 2 . . . . .	238
B-65 Trend plots for subject 9907120503 - 2 of 2 . . . . .	239
B-66 Trend plots for subject 9908120503 - 1 of 2 . . . . .	240
B-67 Trend plots for subject 9908120503 - 2 of 2 . . . . .	241
B-68 Trend plots for subject 9909120503 - 1 of 2 . . . . .	242
B-69 Trend plots for subject 9909120503 - 2 of 2 . . . . .	243
C-1 Hermes user guide: heart rate . . . . .	247
C-2 Hermes user guide: temporal navigation . . . . .	249
C-3 Hermes user guide: memory depth . . . . .	250
D-1 Hermes showing MIT-BIH record . . . . .	257
D-2 Hermes showing PTB record . . . . .	258
E-1 Chebyshev decomposition example - 1 of 23 . . . . .	259
E-2 Chebyshev decomposition example - 2 of 23 . . . . .	260
E-3 Chebyshev decomposition example - 3 of 23 . . . . .	260
E-4 Chebyshev decomposition example - 4 of 23 . . . . .	261
E-5 Chebyshev decomposition example - 5 of 23 . . . . .	261
E-6 Chebyshev decomposition example - 6 of 23 . . . . .	262
E-7 Chebyshev decomposition example - 7 of 23 . . . . .	262

E-8 Chebyshev decomposition example - 8 of 23 . . . . .	263
E-9 Chebyshev decomposition example - 9 of 23 . . . . .	263
E-10 Chebyshev decomposition example - 10 of 23 . . . . .	264
E-11 Chebyshev decomposition example - 11 of 23 . . . . .	264
E-12 Chebyshev decomposition example - 12 of 23 . . . . .	265
E-13 Chebyshev decomposition example - 13 of 23 . . . . .	265
E-14 Chebyshev decomposition example - 14 of 23 . . . . .	266
E-15 Chebyshev decomposition example - 15 of 23 . . . . .	266
E-16 Chebyshev decomposition example - 16 of 23 . . . . .	267
E-17 Chebyshev decomposition example - 17 of 23 . . . . .	268
E-18 Chebyshev decomposition example - 18 of 23 . . . . .	269
E-19 Chebyshev decomposition example - 19 of 23 . . . . .	269
E-20 Chebyshev decomposition example - 20 of 23 . . . . .	270
E-21 Chebyshev decomposition example - 21 of 23 . . . . .	270
E-22 Chebyshev decomposition example - 22 of 23 . . . . .	271
E-23 Chebyshev decomposition example - 23 of 23 . . . . .	271

# List of Tables

4.1	WFDB Annotations . . . . .	89
B.1	Mouse database information . . . . .	174

THIS PAGE INTENTIONALLY LEFT BLANK

# Chapter 1

## Introduction

The ubiquity of computers and inexpensive storage in healthcare and research has created an opportunity for the archiving of massive amounts of physiological data. With the ease of collection and archiving comes a consequent data glut and challenge in providing the data - along with semi-automated analyses of the data - to appropriate personnel. This thesis, at its most fundamental level, details the development of a technology responding to the need for robust data collection, interpretation, dissemination and visualization of large physiological data sets. The resulting system implementation is intended to meet seemingly opposed objectives: those of the “front user,” such as the technician, whose main criterion for adoption of a new technology is ease-of-use; and those of the “end user,” such as the clinician or researcher, who require accuracy, robustness and speed from technology that will realize the goal of aiding their data interpretation efforts.

A design challenge beginning with such seemingly opposed needs immediately piques the interest of an engineer because it provides fertile ground for creative solutions. Consider, as an example, that the entire automobile industry is founded on the need to allow very simple, rote movements to control a powerful vehicle. Extreme sophistication is hidden beneath the hood, but the driver, even if he appreciates the results of that sophistication, need not concern himself with its details in order to operate the vehicle. So it goes with the system of concern in this thesis. If it has been designed properly, its “drivers” will find it easy to use

and reliable. As for this thesis document, it necessarily reveals what is “under the hood,” to carry the automobile metaphor further; it provides a description of blueprints for scrutiny by those interested in knowing how the technology works. Equally as important as the question of *how* the system is designed is *why* the system was designed. Providing a coherent answer to the former question is the overarching goal of this document. An answer to the latter is the focus of this chapter.

## 1.1 Animal testing in cardiovascular medicine

The term “animal testing” may evoke images of animal rights activists picketing outside a beauty product facility over unfair living conditions for animals subjected to whimsical and cruel tests. In reality the process of testing animals is monitored very carefully by institutional and governmental regulations to ensure the welfare of subjects, and the tests conducted on these subjects are anything but whimsical. Animals are used in tightly controlled experiments by researchers that are pioneering drug development efforts or otherwise contributing to our basic understanding of disease processes. The power of genetic engineering has been most heralded in stories of cloning, but in reality one of the most powerful and widely exploited facets of genetic engineering comes in the form of a paradigm for disease modeling. By manipulating DNA in animals so that they produce particular proteins or enzymes or *fail to* produce particular proteins or enzymes, researchers can create physiological conditions that often very closely emulate a disease in humans. Such disease analogs do not translate perfectly to human disease, but nonetheless they provide a controlled and relatively inexpensive environment in which to explore disease characteristics and potential therapies.

The disease of interest in this thesis is cardiovascular disease, which has been the number one killer in the United States since 1900 (with the exception of 1918, in which an influenza epidemic claimed more lives). Cardiovascular disease comes in many forms, the most predominant of which is coronary artery disease, or CAD. Characterized by the formation of atherosclerosis, or plaques in blood vessels leading to stenosed, or blocked arteries, CAD

may lead to myocardial infarction (MI), or a “heart attack,” when the coronary artery is sufficiently clogged that it cannot supply oxygenated blood to the myocardium.

Given the high prevalence and incidence of CAD and its associated dire consequences, CAD has remained in the spotlight as a primary research topic of interest for many years. It will undoubtedly remain a high priority until an arsenal of drugs and therapies have rendered it a less lethal force. In a country where money and science are inextricably tied together, the motivation for mitigating the effects of cardiovascular disease is not purely altruistic; therapeutic and preventive agents for CAD have a large market. The Center for Disease Control reported in the early 90s that cardiovascular disease accounted for approximately \$80 billion, or 14%, of medical spending annually<sup>1</sup>. An editorial note provided as an addendum to this study says:

*The findings in this report indicate that the largest source of health-care spending in the U.S. population is cardiovascular disease. This reflects the high prevalence of coronary ischemic heart disease, which is the leading cause of death in the United States [14].*

As members of academia and industry alike search for understanding of diseases and their potential therapies, they nearly invariably turn to an animal model of disease for preliminary testing. The mouse has, to date, been a very successful preclinical species for drug development. As a recent report describes:

*A retrospective evaluation of the knockout phenotypes for the targets of the 100 best-selling drugs indicates that these phenotypes correlate well with known drug efficacy, illuminating a productive path forward for discovering future drug targets. Prospective mining of the druggable genome is being catalysed by large-scale mouse knockout programs combined with phenotypic screens focused on identifying targets that modulate mammalian physiology in a therapeutically relevant*

---

<sup>1</sup>Costs associated with disease reflect more than direct costs associated with patient care. For example, the cost calculation often includes a figure reflecting the patient’s lost time at work. The specific details of the components comprising the cost estimate in this report were not provided

*manner...It is clear that reverse genetics enabled by genome-wide KO technologies defines a path forward for the biopharmaceutical industry to discover the next generation of blockbuster therapeutics based on novel targets from the human genome [15].*

The genotypic model utilized in this thesis work is one in which pathways associated with very low-density lipoprotein, or VLDL, and high-density lipoprotein, or HDL, are modified. Designed by the Krieger Lab at MIT's Department of Biology, this so-called "double-knockout mouse," or dKO mouse, shows interesting characteristics that make it a potentially useful model in understanding mechanisms of cardiovascular disease [3, 5, 2].

## 1.2 The double-knockout genotype

Risk for atherosclerosis is proportional to LDL cholesterol levels in the body, while risk is inversely proportional to HDL cholesterol. Michael Brown, Joseph Goldstein and colleagues established an understanding of receptor-mediated metabolism of LDL beginning in the 1970s [3, 5], while only as recently as 1996 did researchers unveil the existence of an HDL receptor and begin to comprehend fully the associated pathways of HDL metabolism [2, 3].

For decades researchers have sought to breed mouse subjects with atherosclerosis in an attempt to model the human disease. Original mouse models, known as "single-knockout" (KO) mice, were genetically engineered with a homozygous null genotype encoding the segment of DNA that would normally encode apolipoprotein E (apoE). Because apoE is a critical molecule in the metabolism of VLDL<sup>2</sup>, single-knockout mice are characterized by severely elevated VLDL levels. A single-knockout mouse, however, does not typically exhibit many of the defining features of human coronary heart disease (CHD), namely spontaneous myocardial infarction, severe cardiac dysfunction, and premature death [5].

With increased understanding of the biochemistry of HDL and its associated role in physiological systems came emphasis of the joint importance of VLDL and HDL as contrib-

---

<sup>2</sup>VLDL in mice functions analogously to LDL, or 'bad cholesterol,' in humans



utors to CHD. Researchers developed a “double-knockout” (dKO) mouse, engineered to stop DNA encoding apoE *and* SR-BI, a critical molecule for cellular utilization of HDL [5]. The double-knockout mouse exhibits symptoms more nearly modeling CHD in humans, namely lipid-rich coronary artery occlusions, multiple myocardial infarctions, an enlarged heart, reduced ejection fraction (fig. 1-1), ECG abnormalities (fig. 1-2), and premature death (fig. 1-3).

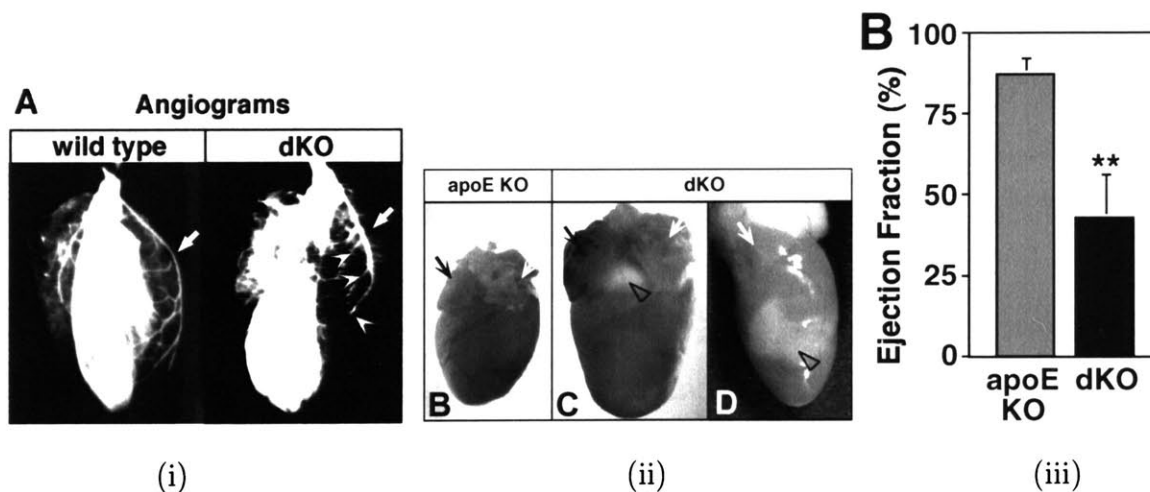
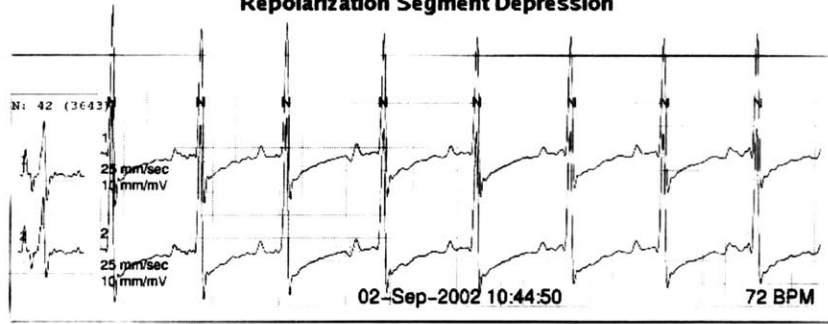


Figure 1-1: (i) Angiogram comparison of wild type (left) vs. apoE/SR-BI dKO (right) mice. The arrows indicate left anterior descending (LAD) coronary artery. The dKO mouse shows multiple severe stenoses in the coronary arteries branching from the LAD.(ii) B and C, Posterior views of perfused hearts from apoE KO (6 weeks old, B) and dKO (5 weeks old, C) mice. D, lateral view of right side of heart from a different 5-week old dKO mouse. Black and white arrows represent left and white atria, respectively; arrowheads, myocardial lesions. Original magnification: 7.5X. (iii) MRI-determined ejection fractions from control apoE KO and dKO mice [5].

Of particular interest in this thesis are details of the dKO ECG, which shows a wealth of arrhythmias and repolarization segment changes analogous to ST segment changes in human ECG [5] (fig. 1-2). These arrhythmias and repolarization segment changes are indicators of underlying cardiovascular pathophysiology; therefore a tool providing an easy mechanism for locating these ECG indicators serves as a useful tool for elucidating the time series of cardiovascular disease in dKO mice. The complete understanding of the mechanisms of underlying disease in the dKO genotype will require a substantial amount of investigation well beyond the scope of this thesis. Nonetheless this future work will use, as its foundation,

Patient: mars\_dko\_11\_1,  
ID:

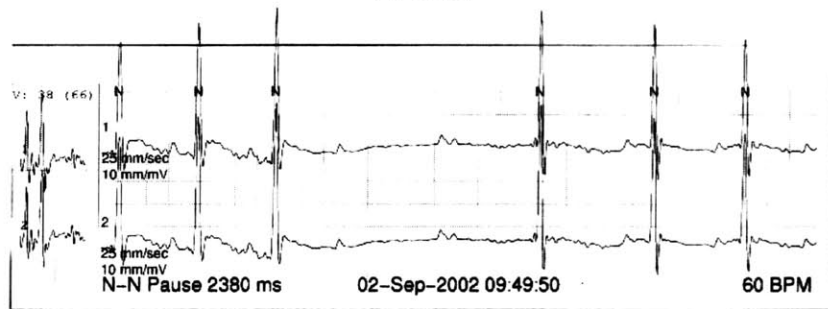
### Repolarization Segment Depression



(i)

Patient: mars\_dko\_11\_1,  
ID:

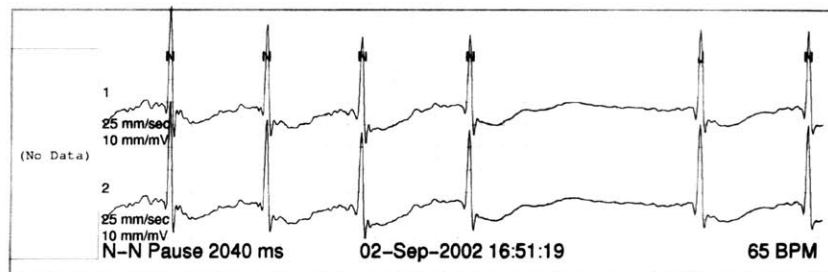
### AV Block



(ii)

Patient: mars\_dko\_11\_1,  
ID:

### JEB



(iii)

Figure 1-2: (i) Repolarization Segment Depression (ii) A/V Block leading to 2 missed beats. Note that the first beat after the two non-conducted beats lacks a P wave, which indicates the beat is junctional in origin (iii) Missed beat. [Above data was scanned by time-expanding mouse data by a factor of 10, then utilizing holter software for automatic arrhythmia detection and annotation.]

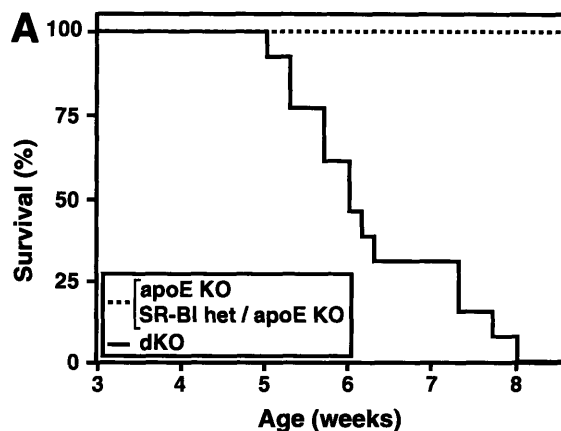


Figure 1-3: Survival (%) as a function of time. The average lifespan of a healthy mouse is approximately 2 years, while 100% of the DKO population has died by 8 weeks of age [5].

the monitoring system described in this paper.

### 1.3 Of mice and machines

ECG data collection in mice requires a different monitoring device from that which may be used on humans. Given that the heart rate of a resting normal mouse is approximately 600 beats per minute, the analog signal conditioning hardware in human monitors is not appropriately suited to mouse ECG. A ten-fold increase in heart rate in mice when compared with humans also translates into a requirement for a ten-fold faster sampling rate in signal digitization. Thus the data storage per unit time, or data throughput, for a mouse ECG monitoring system recording from a single mouse is equivalent to a human monitor recording from ten human subjects simultaneously. Some subtle (and other not-so-subtle) differences in human and mouse ECG waveforms mean that software used in the analysis of human ECG may not be directly applied to the analysis of mouse ECG.

#### 1.3.1 Thesis foundations and experimental setup

Questions concerning disease progression in dKO mice provided the impetus for long-term collection of ECG from subjects. In preparation for data collection, laboratory technicians

in the Krieger Lab implant subjects that are slightly over 30 days of age<sup>3</sup> with subcutaneous tripolar electrodes (figure 1-4) in a procedure lasting approximately 20 minutes. The mice are anesthetized with isoflurane while surgeons create a medial incision approximately one-half inch in length over the cervical vertebrae. Using a blunt dissection technique, surgeons then separate connective tissue to create a tunnel in either direction from the first incision toward the abdomen. After running each of two wires through a tunnel, the surgeon creates an incision approximately one inch in length starting at the sternum and moving toward the abdomen. Upon locating the two electrodes through this incision, the surgeon uses sutures to affix the electrodes to connective tissue covering the ribcage; one electrode is sutured superior and medial to the myocardium, while the other is placed inferior and lateral. After closing the abdominal incision the surgeon finally sutures the remaining electrode to connective tissue beneath the original dorsal incision site, then closes the original incision. The resulting electrode configuration is equivalent to lead 2 with a ground (reference) electrode placed subcutaneously at the back of the neck.



Figure 1-4: Subjects are implanted with tripolar electrodes, with one of the three contacts sutured subcutaneously superior and medial to the myocardium, another inferior and lateral, and the third dorsally. The dorsal contact serves as a ground electrode, while the others create a lead 2 configuration.

---

<sup>3</sup>The subjects must be weaned from the mother, which happens after about 30 days



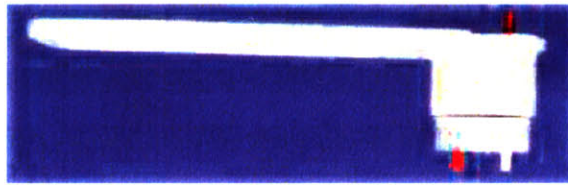


Figure 1-5: One cable (not shown) connects this commutator to the terminal point of the tripolar leads (fig. 1-4). Another cable (not shown) connects this commutator to the input of the analog instrumentation (discussed in chapter 3). The commutator swivels freely and thus permits the subject to move uninhibited and without tangling lead wires.

After surgery the subjects are monitored carefully as they recover from anesthesia. Provided that the subject does not appear from visual inspection to be overly lethargic, the blunt plastic bulkhead of the subject's lead is then connected to a commutator (fig. 1-5), which permits the subject to move freely without tangling wires. A second cable connects the commutator to an analog signal conditioning device.

As upcoming chapters will describe, the analog signal conditioning device and data collection system used in experiments are newly designed as components of this thesis. In the interest of providing appropriate background, we describe here the original data collection system and its limitations as motivators for new system design. The original data collection system used a laptop connected through a serial cable to an external analog signal conditioning and digitization box. The box encoded data in a proprietary digital format, and software on the laptop collected data from the box. Because the data was in a proprietary digital format, we could not assess the transfer function of the analog front end circuitry. Moreover, visualization of the data required a special piece of software - provided by the manufacturer of the system - that converted data into a comma-separated format readable by spreadsheet software. Given the fast sampling frequency required for digitization of mouse ECG, the hard drive of the laptop could hold less than 24 hours of data. Each day a lab technician needed to enter the clean-room mouse facilities, offload a 24-hour file onto a CD, then manually format the data on the CD using the system manufacturer's proprietary decoding software. After formatting the data, a technician could import it into spreadsheet software, chart and print the associated time series data. Due to memory limitations of popular spreadsheet programs, the process of charting and printing a single day of ECG data required almost a

full day of effort on the part of the technician.

The extensive effort required of lab technicians for the seemingly mundane task of data collection provided the primary system design goal: that of automating data collection. However, the system goals become more numerous as we considered the possibilities available through modern programming languages and computer architectures. For example, as researchers we were interested in viewing a real-time data stream, which at the time required physical presence in the mouse (clean room) facilities. We additionally sought automation in *analysis*. That is, we wanted a system that could act similarly to a hospital monitoring technology by providing alarm capabilities rather than just visualization of waveform data.

The project scope for this thesis became an effort toward building a mouse ECG monitoring technology with similar amenities to those provided to clinicians in hospitals. Of specific interest were heart rate and repolarization monitoring, each of which had been shown from manual investigation to be very salient features in dKO mouse data [5]. Interesting ECG features had been identified by researchers in the Krieger Lab bearing the arduous task of reviewing data manually, and the requisite automation tasks for a new system were largely defined by their input. With this input in hand and extensive expertise in signal processing and monitoring technologies provided by the Laboratory for Computational Physiology, we began a collaborative effort toward realizing a monitoring technology that would provide substantial automation and open the possibility of interventional experiments through real-time data visualization and processing<sup>4</sup>.

### 1.3.2 Thesis outline

The unique needs of data collection and analysis of mouse ECG for long-term studies (eg 30-45 days of continuous collection) motivated the system design discussed in this thesis. In order to motivate further the system requirements, Chapter 2 will discuss electrophysiological considerations underlying the unique ECG signal of mice. It will additionally explore

---

<sup>4</sup>The originally-used system required so many days of effort to format and process the data that the subject was invariably dead by the time all data has been aggregated and interpreted, precluding any interventional experimentation

signatures of interest in diagnosing disease states in mice, some of which are quite similar to those found in humans. Chapters 3 and 4 will delve into the details of the data capture and analysis system, providing a discussion of the analog front end for ECG signal conditioning and the software for digitization and data storage (chapter 3); and software comprising an Internet-based tool for visualization and editing of the massive ECG data sets recorded in mouse experiments (chapter 4). Chapter 5 serves as a foundation for chapter 6 by providing the mathematical formulation of Chebyshev polynomials and their utility as a pattern recognition tool for monitoring repolarization period morphology of mouse ECG. Chapter 6 discusses the specific application of Chebyshev polynomials to the dKO mouse repolarization segment for the detection of anomalous morphologies that may signify pathophysiologic events. Chapter 7 describes a parallel computational infrastructure designed to expedite the massive task of processing the large mouse ECG database, and chapter 8 explores long-term heart rate and repolarization segment morphology trends characteristic of the dKO mouse model. Chapter 8 represents the culmination of all previous chapters that explored the foundational tools enabling a long-term ECG trend characterization. The final chapter (chapter 9) discusses the technology's future utilization in interventional experiments that will further explore disease trends in the dKO mouse.

### **1.3.3 Scope of work**

In the interest of stating the scope of work covered in this thesis, it is worth stating up front that a rigorous, quantifiable treatment of a repolarization segment algorithm for mouse ECG is currently not possible. No definitions exist in the realm of mouse ECG for an elevation or depression 'episode.' In human ECG analysis, by contrast, 3 ST-segment episode protocols have been formalized and gold standard databases for algorithm performance have been designed with extensive worldwide collaboration over the course of years [23, 17]. In the absence of formal episode definitions and gold standard databases, we take an approach of designing a repolarization segment morphology metric - and adjustable alarm criteria derived from that metric - as a technology that might facilitate development of episode protocols

and gold standard databases for mouse ECG.



# Chapter 2

## Background: murine cardiac electrophysiology

As a foundation for subsequent discussion we adopt the simplified distinction of ventricular *depolarization segment* and *repolarization segment* from figure 2-1. The apparent dogma of this distinction will fade throughout the chapter as the details of the signal comprising the depolarization and repolarization segments are described.

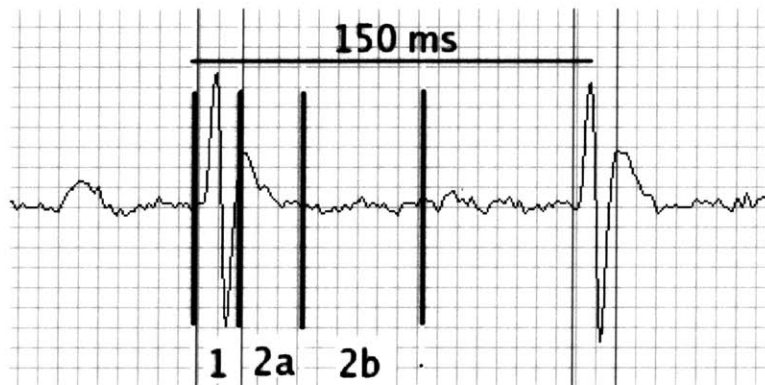


Figure 2-1: Segmentation of mouse ECG into ventricular depolarization (1) and early/late repolarization (2a/2b) periods. The segmentation is intended to depict a general segmentation of the depolarization period as corresponding to the QRS complex and repolarization as beginning approximately at the QRS end - or J point - and ending at about 50% of the RR interval. These time points are approximate and will be formalized in later sections. Note the presence of a positive deflection immediately following the QRS complex. This so-called J wave will be discussed in section 2.2.1 [this ECG is from wild-type subject 5462040105, file 520.hermes]

Section 2.2.1 provides a more appropriate description of the repolarization period in relation to underlying cellular action potential durations. We will see, however, that action potential repolarization time does not manifest on the surface ECG<sup>1</sup> of healthy mice. As Danik et al. concluded in 2002,

*...an accurate measurement of complete repolarization of the murine ventricle cannot be obtained from the surface ECG. [36]*

An ischemic<sup>2</sup> mouse heart, in contrast, may generate an elevated or depressed repolarization segment visible on the ECG that reveals the ventricular repolarization period. We exploit a large data set of ischemic mouse ECGs to arrive at a definition<sup>3</sup> of the time points that will be used in repolarization segment analysis.

## 2.1 The depolarization period

Mice, like humans, have a four-chambered heart consisting of two atria and two ventricles. The mechanical pumping activity of the heart that drives blood flow through the circulatory system is under the control of an electrical conduction system that very closely resembles that of humans [28] (figure 2-2). Electrical activity of the heart begins at the SA node, the heart's natural pacemaker, that generates a sequence of action potentials controlling the rate of the heart.

The action potential spreads from the SA node to the atrial myocardium, the depolarization of which creates the P wave on the ECG recording.<sup>4</sup> After atrial depolarization, the depolarization wave next spreads to the AV node where its conduction velocity slows down dramatically, permitting atrial contraction to complete before ventricular contraction begins.

---

<sup>1</sup>Though the subjects have subcutaneously-implanted electrodes, we still refer to the ECG as 'surface ECG' as distinguished from intracellular recording

<sup>2</sup>Ischemia, or inadequate blood flow, leads to hypoxia, or poor oxygenation; it is the poor oxygenation of the heart that causes damage

<sup>3</sup>The creation of the definition is necessarily based on empirical interpretation of ECG. As is frequently the case in biomedical signal processing, we must apply an appropriate mixture of physiological insight and manual interpretation to arrive at a definition for a model

<sup>4</sup>The mouse P wave is highly sensitive to electrode placement. Consequently even a very slight shift in electrode placement can null an otherwise strong P wave projection onto the measurement lead.

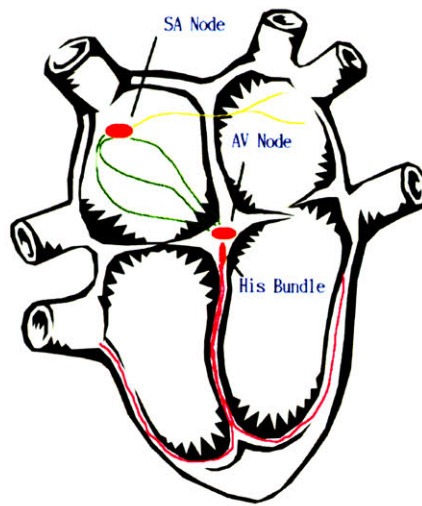


Figure 2-2: Simplified diagram of the heart conduction system: the SA node, “the pacemaker,” is positioned on the posterior wall of the right atrium. SA node action potentials lead to depolarization of the atria. The action potential descends from the SA node through the inter-nodal tract to the AV node, then the Bundle of His and subsequently the bundle branches. The action potential continues to propagate from the bundle branches to Purkinje fibers, which causes depolarization of the ventricular myocardium.

The currents associated with the spread of depolarization through the AVN and ventricular conduction systems are too small to generate visible wavelets on the surface<sup>5</sup> ECG. As a result the period between the end of the P wave and the beginning of the QRS is relatively flat, and is called the isoelectric level.

The action potential next spreads rapidly through the Bundle of His and the ventricular conduction system. Purkinje fibers distribute the action potentials to the inner wall of the ventricles, thus initiating ventricular depolarization and a corresponding QRS complex on the ECG. The measured time period between the P wave onset and the QRS onset is called the PR interval. A comparison of human ECG and mouse ECG shows that mice have a relatively long PR interval (figure 2-3). A prolonged PR interval in *humans* represents a slowed conduction through the AV node, which is a pathophysiologic condition called *first degree heart block*. The relatively prolonged PR interval in mice is not pathological but rather a natural difference between human and mouse physiology.

---

<sup>5</sup>Though electrodes are implanted subcutaneously, we still refer to the ECG as *surface ECG* as contrasted with intracellular recording

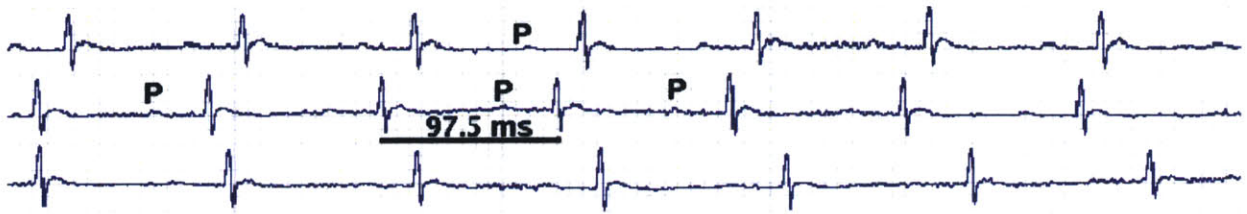


Figure 2-3: The PR interval in mouse ECG is relatively long when compared with that of human ECG. First degree heart block in human ECG is defined as a PR-interval of longer than 0.2s [6]. If we were to assume that all features of the ECG scale linearly by a factor of approximately 10 between mouse and human ECG (human HR is approximately 60 bpm, while mouse HR is approximately 600 bpm), then first degree heart block in mice should be defined as a PR-interval greater than 20 ms. In the above healthy murine ECG, the PR interval is, on average approximately 30 ms (time scale above: 7.5 ms/div). [Record 0921122903, file 0.hermes]

## 2.2 The repolarization period

Whereas the repolarization segment of healthy human ECG typically consists of a characteristic isoelectric segment followed by a T wave, the healthy murine ECG has either a completely isoelectric repolarization segment (as in figure 2-4) or a J wave (short positive deflection) immediately following the QRS complex (as in figures 2-1 and 2-3). Our long-term studies indicate that intra-subject variability is high; that is, one may see a subject with an isoelectric repolarization segment on one day and on another day witness a J wave immediately following the QRS complex.

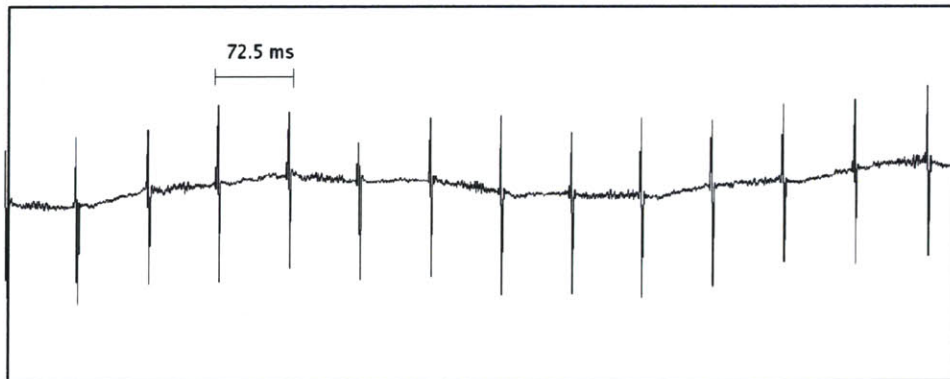


Figure 2-4: Mouse ECG sometimes shows no P wave. The invisibility of a P wave does not indicate a pathology; it may result from transient electrode displacement that attenuates the P wave projection onto the lead vector. Of additional note is the absence of a T wave, a familiar waveform in human ECG that is non-existent in mouse ECG.

The absence of a T wave in mice was first noted nearly a century ago [27] and the

underlying mechanisms distinguishing mouse from human ECG have been a topic of research ever since. An understanding of the murine repolarization period is important, as too vast a difference between the underlying cardiac electrophysiology of mice and humans would arguably render genetically-altered mice useless as preclinical subjects (that is, non-human subjects used as a model from which hypotheses for human physiology are drawn). Several research groups over the years have, in fact, called into question the utility of mouse as a useful model for certain human diseases [29, 30, 31, 32]. One study concludes:

*It is therefore probable that the mouse is less than ideal for studying diseases such as Long-QT or Brugada syndrome that affect the J wave and ST segment [33].*

### **2.2.1 An introduction to the Liu study**

One well-articulated and methodical study (Liu et al. [28]) that provides a reasonable hypothesis regarding the morphology of murine repolarization segments warrants careful review. The study cites lack of robust *in vivo* action potential (AP) measurements as the primary weakness in a full understanding of murine repolarization period. The introduction to the Liu study says:

*Optimal use of a genetically altered murine heart requires an understanding of basic in vivo murine cardiac electrophysiology which is influenced by such factors as the nervous system, circulating humoral factors, metabolism and mechanical stretch. The purpose of this study was to assess the in vivo temporal and spatial distribution of ventricular depolarization and repolarization in the murine heart and to determine if manipulation of transmural action potential durations would result in a discernable repolarization wave or T wave on the mouse ECG [28].*

#### **Does murine ECG have a T wave?**

Of particular relevance to this thesis in the Liu study is its corroboration of the Danik study [36] explaining the presence of a J wave immediately following the QRS complex in mouse

ECG. This wave has been referenced in other literature as a depolarization-repolarization wave [32], a J wave [34], a TRW wave (transient repolarization wave) [35], a b wave [36], and a T wave [37, 38]. The Liu study calls the wave a *J wave* and explains its presence as corresponding to *early* ventricular repolarization (which in turn corresponds to phase 1 of the AP). Figure 2-5 shows a simultaneous AP and ECG recording from the Liu study. Other species' T-wave, by contrast, corresponds to the phase 3 (rapid repolarization) segment of ventricular APs.

Liu et al. conclude that:

*The sequence of activation was endocardial apex to epicardial apex then apex to base while the sequence of repolarization was base to apex and epicardium to endocardium. The onset of phase 0 of the endocardial MAP coincided with the onset of the QRS complex. The peak of phase 0 of the epicardial base MAP correlated with the termination of the QRS complex and the onset of the J wave on the ECG recording*<sup>6</sup>[28].

The Liu study (predated by the comparable Danik study) provides a cornerstone for the design of the repolarization segment morphology monitor described in this thesis. The significance of the study comes from a rigorous investigation into the electrophysiological underpinnings of the presence of a J wave wave immediately following the QRS complex. In the context of this thesis, the most salient result of the Liu study is its revelation of the fact that the J wave is part of early ventricular repolarization. It thus marks the onset of the repolarization segment and is not consistent with the human T wave. The Liu study does not answer the question of where on the ECG (temporally) the repolarization segment *ends*. As future sections will describe, it is impossible to determine the repolarization segment end point from mouse ECG.

---

<sup>6</sup>MAP, or *monophasic action potential*, recordings are obtained with an extracellular pressure electrode



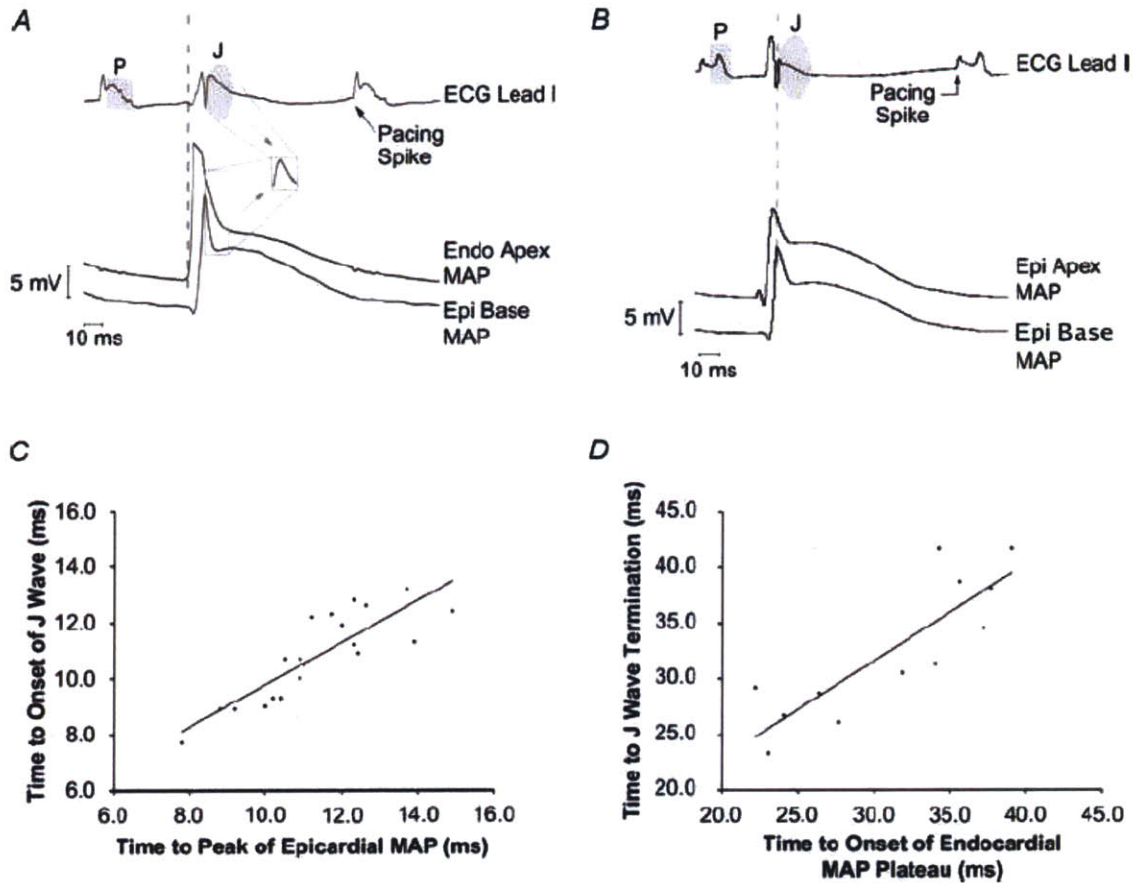


Figure 2-5: Simultaneous ECG and cellular action potential (AP) recordings. A, the onset of the apical endocardial action potential occurs with the onset of the QRS and is earlier than the epicardial AP at the base. Both APs have plateaus. The epicardial AP has a spike and dome appearance and the onset of the plateau occurs earlier in the epicardial AP. B, the epicardial apex activates before the epicardial base. The peak of the upstroke of the epicardial base occurs with the return to baseline of the QRS and the onset of the J wave. C, the correlation between onset of the J wave and the peak of the epicardial AP ( $r^2 = 0.71$ ,  $P = 0.001$ ). D, the correlation between the end of the J wave on the ECG and the onset of the endocardial AP plateau ( $r^2 = 0.72$ ,  $P = 0.001$ ). The subtraction of the endocardial and epicardial AP intervals that correlated with the onset of the J wave (peak of the epicardial AP; C) and the end of the J wave (onset of the endocardial AP plateau; D) resulted in a wave very similar to the J wave of the ECG (inset A). No obvious repolarization wave is seen on the ECG during phase 3 of the repolarization of the APs. During all recordings the atrium was paced at 400 beats per minute (S1S1 interval of 150ms) [28].

## Why doesn't murine ECG have a T wave?

A comparison of murine and human AP morphology reveals a stark contrast in the late repolarization phases. Figure 2-6, a simultaneous AP and ECG recording from a human subject, shows that the T wave corresponds to a rapid late repolarization segment in the AP. Figure 2-5 from a mouse, in contrast, shows no rapid late repolarization segment; the late repolarization phase decays gently. The *early* repolarization segment of the murine AP, however, is quite steep and gives rise to the J wave on the ECG. Both human and murine ECG have waves during rapid repolarization; the wave takes the form of a T wave in human ECG and a J wave in murine ECG.

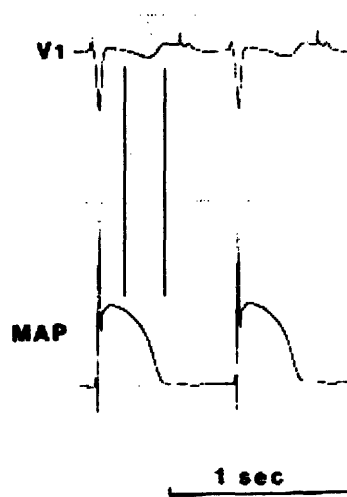


Figure 2-6: A diagram of human cellular action potential and simultaneous ECG recording. The ECG T wave arises from the rapid AP repolarization phase [40].

In the Liu study, AP recordings were acquired simultaneously with ECG recordings. In an attempt to shorten the epicardial action potential duration relative to the endocardial action potential duration, physiological and pharmacological interventions were undertaken. In physiological intervention, the investigators established a transmural temperature difference with a slow drip of physiological saline at 39° C onto the epicardial surface, followed by quick suctioning of the saline to prevent equilibration of the endocardium to the higher temperature. Similarly in the pharmacological intervention, the investigators slowly dripped



then suctioned 37° C 10 $\mu$ mol pinacidil onto the the epicardial surface. By shortening the epicardial AP<sub>90</sub> by 15.6  $\pm$  7.4 ms via warming of the epicardial surface, the investigators generated a positive wave during phase 3 of repolarization similar to T waves seen in larger mammals, including humans (figure 2-7). Similarly by applying 10 $\mu$ mol of pinacidil<sup>7</sup> to the epicardium, the investigators shortened the epicardial AP and generated a positive wave during phase 3 of repolarization (figure 2-8).

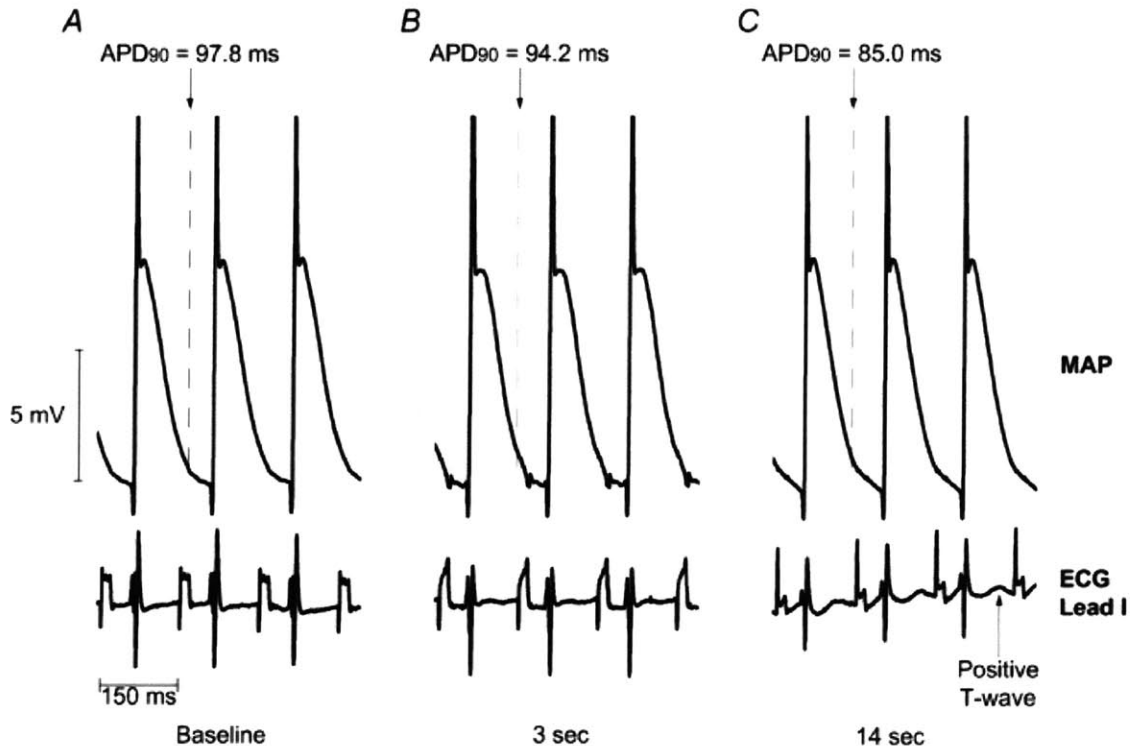


Figure 2-7: Warming of epicardial surface and effects on epicardial APs and murine ECG. Typical epicardial *in vivo* APs during a paced atrial rhythm at an S1S1 interval of 150ms recorded simultaneously with ECG lead I are presented at baseline (A), 3s (B) and 14s (C) during warming of the epicardial surface with physiological saline at 39 degrees C. The warm saline shortened the APD<sub>90</sub> by 12.8 ms and resulted in a positive repolarization wave on the ECG recording during phase 3 of repolarization of the AP [28].

By altering transmural action potential durations between epi- and endocardial APs, Liu et al. generated a T wave on murine surface ECG. In so doing they provided a reasonable hypothesis for the absence of a T wave in murine ECG: the transmural action potential duration difference between epi- and endo-cardial APs is too small to generate a T wave.

<sup>7</sup>a potassium channel opener

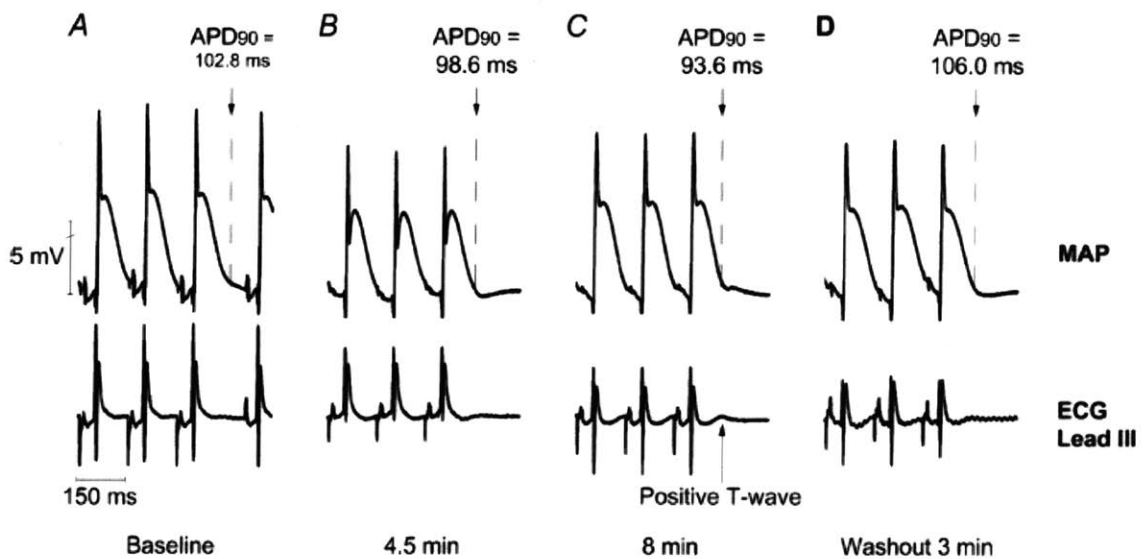


Figure 2-8: Application of pinacidil to epicardial surface and effects on epicardial APs and ECGs. Progressive development of a positive T wave is seen in the ECG during the application of pinacidil. A, baseline recording of atrially-paced ECG and AP before pinacidil (pacing interval of 150 ms). B, at 4.5 min into the pinacidil application there is the suggestion that a positive T wave is developing. C, by 8 min there is a very prominently positive T wave and the  $APD_{90}$  has shortened by 9.2ms. D, by 3 min into the washout period the T wave has almost disappeared [28].

Upcoming sections describing currents of injury explain how differences in AP duration between two regions of tissue can generate a surface ECG deflection. A description of the presence or absence of a T wave follows similar logic. Figure 2-9 diagrams two APs from human tissue, where we arbitrarily designate AP A as endocardial and AP B as epicardial. The epicardial action potentials are shorter in duration than endocardial action potentials. When the APs are overlaid with a slight lag between them (reasonably simulating later epicardial depolarization [28]), they show at times a potential difference (eg during the phase 0 depolarization upstroke and phase 3 rapid repolarization) and at other times no potential difference (eg during the phase 2 plateau). Action potential differences during phase 3 cause current to flow from endocardium to epicardium, and correspond to a T wave deflection in human ECG.

Experimentally, investigators have found that the transmural action potential duration ( $APD_{90}$ ) *difference* between epicardial and endocardial tissue is relatively short in the mouse myocardium when compared with that in other mammals [28]. Of additional note, which

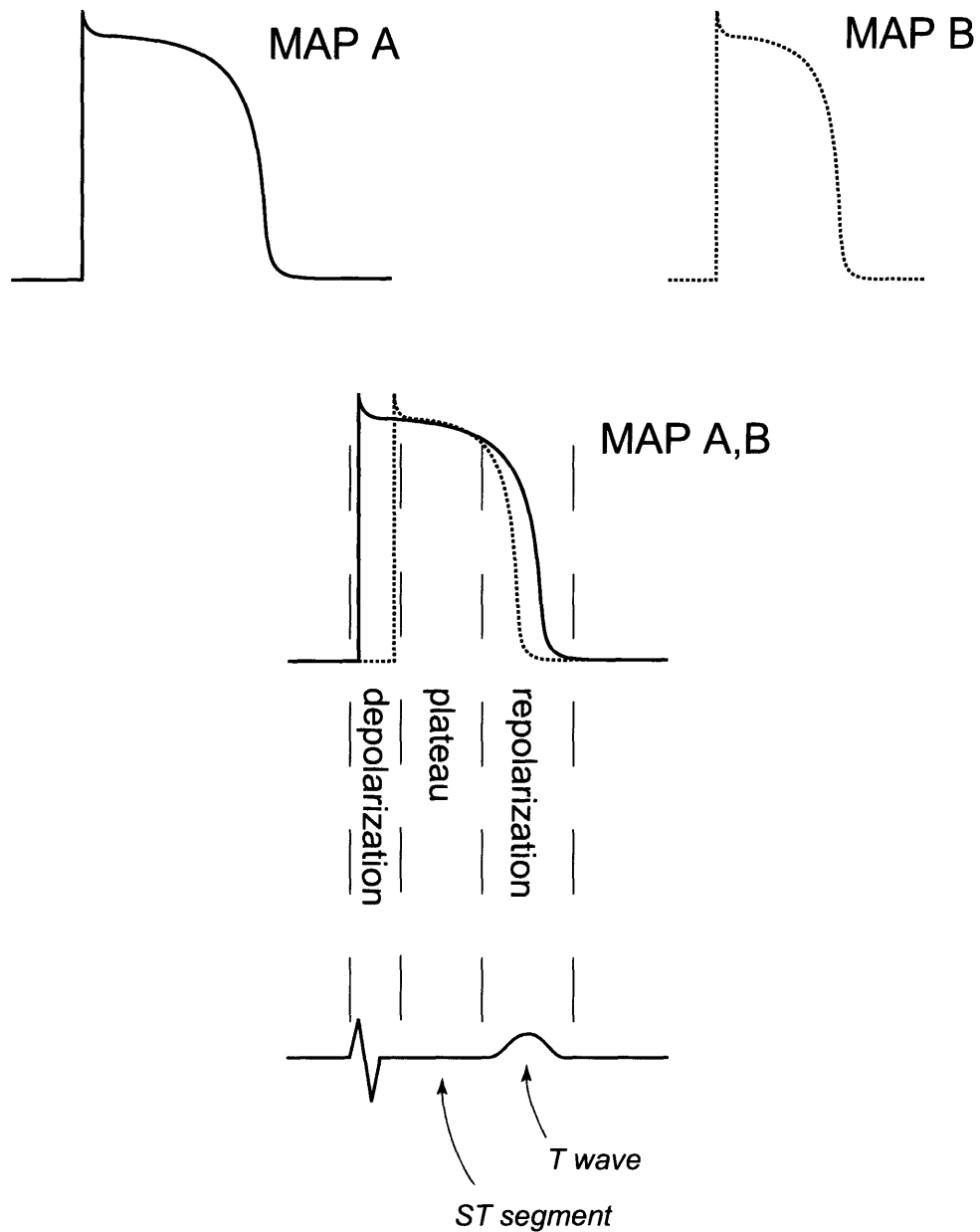


Figure 2-9: A diagram shows two example human intracellular action potentials overlaid with a slight time lag between them, exemplary of epi- end endo-cardial tissue potential differences in a single beat [28]. While in fact the epi and endo APs are slightly different in morphology and have slightly different time durations, the diagram is intended to show a simplified example of the reason that T waves exist in human ECG. AP potential differences during phase 3 correspond to a T wave ECG deflection.

is not specifically highlighted in the Liu study, is the fact that murine AP morphology has a very gentle phase 3 AP decay; that is, it is not steep like its human counterpart. The combination of very similar endo- and epicardial action potential durations with a relatively slowly-changing phase 3 AP leads to a near-zero voltage difference between endo- and epi-APs during phase 3; consequently there is no deflection on the ECG (fig. 2-10).

## 2.3 Selection of time points for repolarization segment measurement

This chapter's introduction provided a very simple, albeit crude, division of the ECG segment into depolarization and repolarization segments based on visual inspection of the waveform (figure 2-1). A better understanding of depolarization and repolarization segmentation should come from an analysis of the underlying cellular electrical activity. As we will see in this section, cellular repolarization times are a function of heart rate and ischemic progression and thus it is difficult to generalize the repolarization segment end point. It is impossible to determine the true repolarization segment offset time from the surface ECG, so we propose a reasonable end point for the measurement of the repolarization period based on sample empirical observations of repolarization segment morphologies in dKO mice during ischemia.

### 2.3.1 Repolarization segment: start point determination

#### QRS detection using *wqrs*

The location of a starting point for the repolarization segment relies heavily on *wqrs* [13], a QRS detector that annotates the onset of the QRS complex and the offset, or the so-called J point. The *wqrs* algorithm was designed for use on human ECG, which does not have a J wave. Given that the QRS complex immediately precedes a J wave, the morphology of which nearly resembles that of a broadened upright S peak, one might reasonably expect that *wqrs* will sometimes incorrectly label the *J wave peak* as the *J point*. Figure 2-11 shows

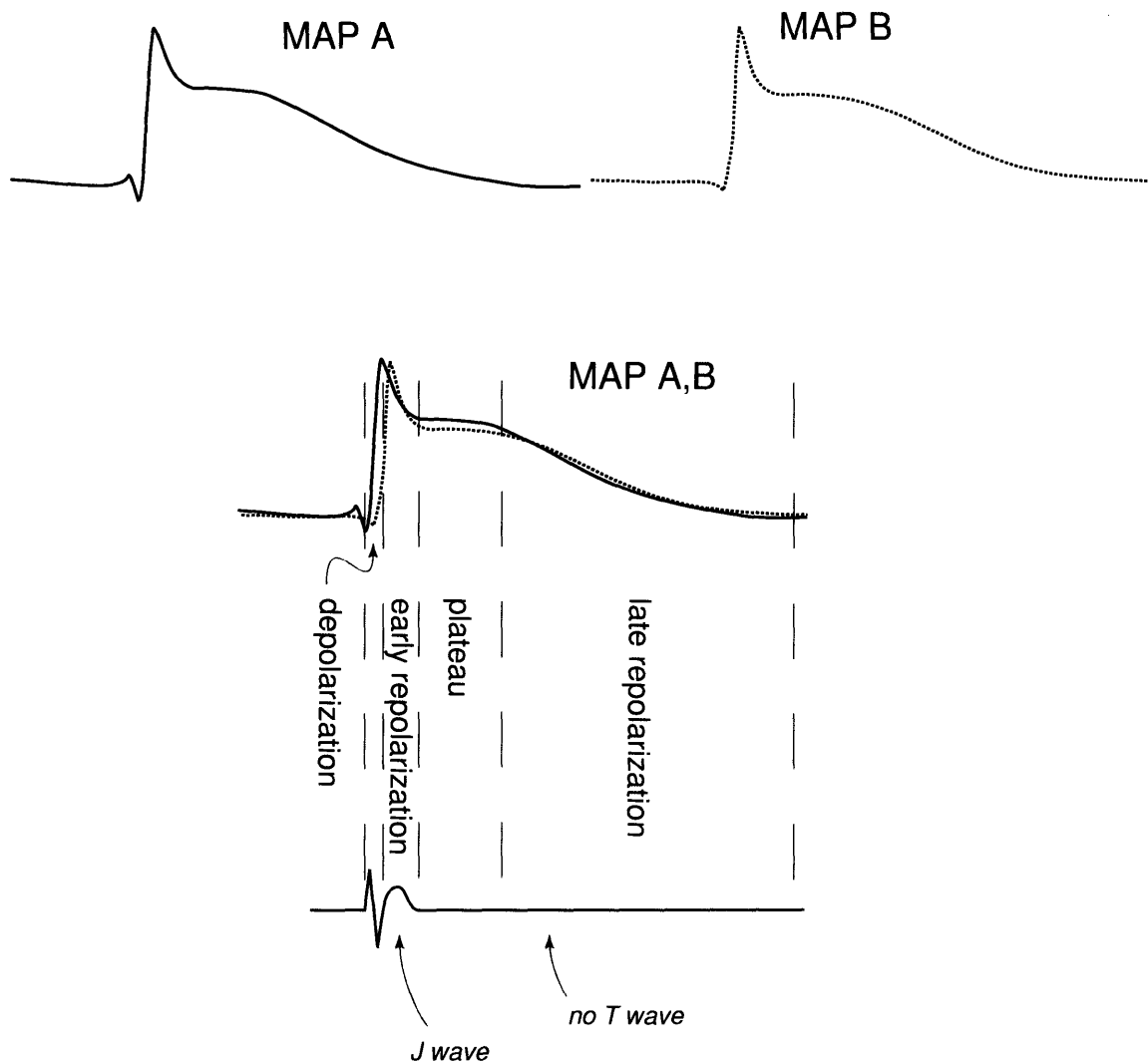


Figure 2-10: A diagram shows two example murine APs overlaid with a slight time lag between them, exemplary of epi- endo-cardial tissue potential differences in a single beat. While in fact the epi and endo APs are slightly different in morphology and have slightly different time durations, the diagram is intended to show a simplified example of the reason that T waves *do not* exist in mouse ECG. The near-zero AP potential difference during phase 3, which has a gradual descent relative to a human AP, generates no significant current flow, and hence no ECG deflection.

an example in which the peak of a sharply-peaked J wave is labeled by *wqrs* as the J point. While the potential inaccuracy of *wqrs*' J point detection is an important observation, we permit the minor time stamp inaccuracy because - as chapter 6 explains - we are interested in characterizing the overall shape of the repolarization segment. Later in this section we define the repolarization segment duration to be approximately 40% of the RR interval, the inclusion or exclusion of the very small segment of data between the J point and the J peak ( 200 us in figure 2-11) is a negligible fraction of the overall segment length.

### **Empirical choice of a repolarization segment start point**

Because the end of the J wave represents the end of phase 1 AP repolarization, we would ideally like to choose the end of the J wave as the repolarization segment start point. Since *wqrs* appropriately locates the J point (in the absence of a sharp J wave) or perhaps the J wave peak (in the presence of a sharp J wave) as the end of the QRS complex, we introduced a small time offset from the *wqrs* J point annotation in order to begin our measurement toward the end of the J wave. After extensive review of data we chose to define the starting point for repolarization segment analysis at 1 ms beyond the *wqrs* J point annotation. This starting point allows appropriate avoidance of the J wave as part of the repolarization segment measurement<sup>8</sup>. Figure 2-11 shows a beat labeled with the repolarization period beginning at 1 ms after the 'J point', which *wqrs* has labeled as occurring at the peak of the J wave.

### **2.3.2 Repolarization segment: end point determination**

In human ECG the T wave end provides a surface ECG indicator of the end of ventricular repolarization; mouse ECG does not have an obvious analog. Consequently one might consider using a statistical approach to characterization of typical repolarization times in mice by using AP recordings. However, such an approach is quite difficult since both heart rate and ischemic progression affect AP repolarization times. The below sections explain the manner in which ischemia and heart rate modulate AP repolarization times.

---

<sup>8</sup>the J wave is representative of phase 1 AP repolarization; the repolarization segment of interest corresponds to phase 2 and phase 3 AP.

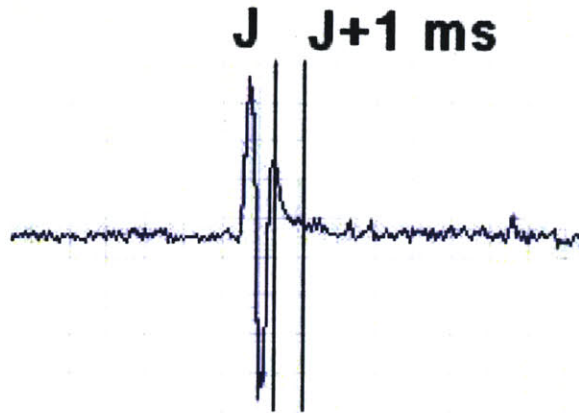


Figure 2-11: The J wave represents early repolarization that is not temporally consistent with the ST period in humans. The repolarization period of interest for morphology measurement begins after the J wave, which is approximately 1 ms after the J point. Note that the *J point* in this example, as detected by *wqrs*, is actually the peak of the *J wave*, which nearly resembles a strong upright S wave. As chapter 6 explains, an algorithm characterizing the entire repolarization segment will be negligibly influenced by this slight inaccuracy. [ 1 ms/div]

## Ischemia and heart rate modulators of action potential duration and resting membrane potential

Saito et. al. [41] showed the relationship between action potential durations and heart rate as well as between heart rate and ischemia. Figure 2-12 shows that cellular action potential duration and resting membrane potential are functions of ischemic progression.

The most germane detail we extract from this study for our goals of establishing time points for ventricular repolarization comes from the simple qualitative recognition that action potential duration and resting membrane potential are not fixed; they depend on heart rate and ischemia [41]. The very feature we seek to measure - namely ischemia as manifested in repolarization segment morphology changes - modulates the ventricular repolarization *period*, the establishment of which is prerequisite for characterizing segment morphology. With this confounding factor we necessarily abandon an attempt at determining repolarization time-point values from literature.

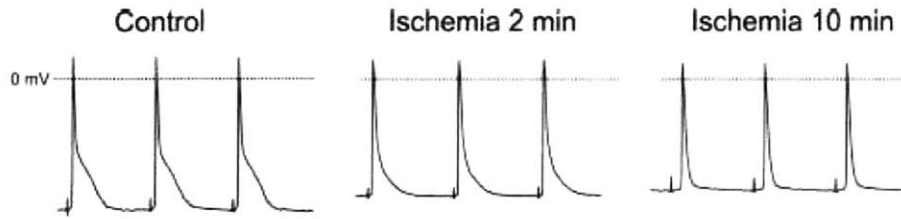


Figure 2-12: Representative recording of action potentials before (left), after 2 (middle) and after 10 (right) minutes of ischemia in wild-type mice. The hearts in this study were mounted on a Langendorff apparatus and coronary perfused at a constant flow (2 ml/min) with Tyrode solution containing (in Mm) 125 NaCl, 4 KCl, 1.8 NaH<sub>2</sub>PO<sub>4</sub>, 0.5 MgCl<sub>2</sub>, 2.7 CaCl<sub>2</sub>, 5.5 glucose, and 25 NaHCO<sub>3</sub> and gassed with 95% O<sub>2</sub> - 5% CO<sub>2</sub>. Coronary flow was completely stopped by closing an electromagnetic valve placed close to the aorta, producing no-flow ischemia of the entire preparation. (no absolute time scale provided). Note that the baseline voltage increases for 2-min ischemia and further increases for 10-min ischemia [41].

### The difficulty of using AP studies to determine repolarization segment measurement end point

Danik et al. recognized the difficulty of discerning repolarization offset times from surface ECG in their seminal paper pre-dating the Liu study by saying:

*...an accurate measurement of complete repolarization of the murine ventricle cannot be obtained from the surface ECG [36].*

Given the impossibility of using surface ECG or AP modeling to determine the endpoint of the repolarization segment, our endpoint definition is necessarily an educated guess. The most educated guess we can make, it turns out, relies on ECG from ischemic dKO mice<sup>9</sup>. The motivation for this approach will be provided in the context of so-called *currents of injury* that generate repolarization segment deviations during ischemia. The duration of repolarization segment deviations in ischemic subjects reveals the length of the repolarization period.

---

<sup>9</sup>While we could attempt to model the relationship between heart rate and the repolarization period from literature values [41], literature does not indicate how we should model the heart rate and repolarization period relationship during extreme bradycardia, such as that seen in dKO mice



## Exploiting ischemia in the dKO mouse to characterize repolarization segment duration

Of particular interest in *human* ECG analysis is the ST segment. The ST segment, which occurs immediately after the QRS complex on a human ECG trace, corresponds to a time at which (in a healthy heart) all the ventricular myocytes are depolarized. Consequently there is no voltage gradient across the ventricular myocardium and the ST segment is at the same voltage as the isoelectric point, which immediately precedes the QRS complex. Deviations from the isoelectric point in the ST segment are indicative of voltage gradients after ventricular depolarization and often reflect an underlying pathophysiologic state, most notably ischemia (inadequate blood flow to the heart) and, in some cases, impending or existing myocardial infarction (death of cardiac tissue resulting from inadequate blood flow - and consequently oxygenation - of the heart). In ST depression the ST segment is below the isoelectric baseline and in ST elevation the ST segment is above the baseline. Examples of human ST elevation and ST depression are shown in Figures 2-13 and 2-14 below.

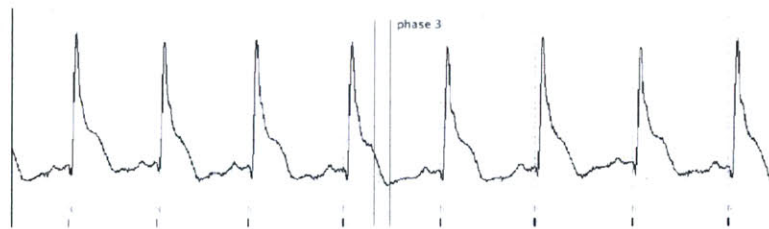


Figure 2-13: ST segment elevation in human ECG. (time scale: 40 ms/div). The waveform comes from a V2 lead configuration. Record e0515 from [13].

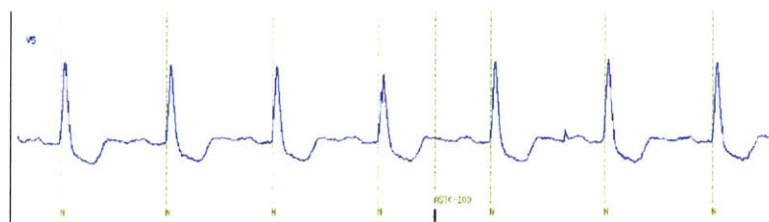


Figure 2-14: ST segment depression in human ECG. (time scale: 40 ms/div). Record e0203 from [13].

ST deviation during myocardial ischemia or injury is thought to be due to the partial depolarization of ischemic myocardial cells during the resting (phase 4) stage. Along the

boundary between normal and depolarized tissue there will therefore be a potential difference, and a current of injury will flow from the ischemic tissue toward normal tissue (see fig. 2-15). The DC injury potential disappears during the plateau phase of the action potential when both normal and ischemic tissues are depolarized. The resultant ECG waveform would appear as in figure 2-15A if amplified by a DC amplifier. However, clinical ECG machines are AC coupled, and therefore the output ECG appears as in Figure 2-15D with an apparent ST elevation.

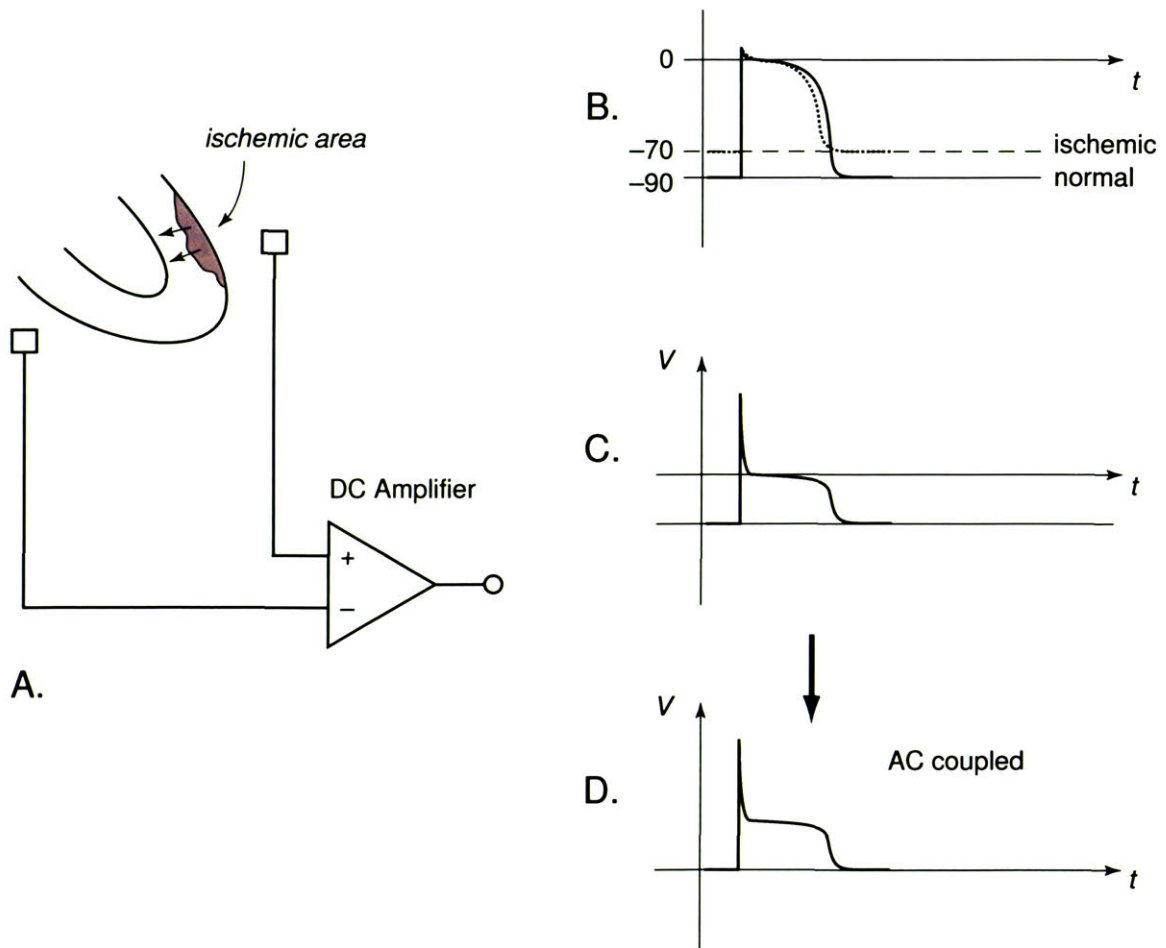


Figure 2-15: Epicardial ischemia and ST-elevation: A. Ischemic epicardial tissue is partially depolarized, resulting in a current of injury running from the depolarized tissue toward the normal tissue. A DC amplifier attached as shown in the figure would record a negative voltage during the resting (phase 4) phase of the action potential; B. During the plateau (phase 2) of the action potential, no potential difference exists between normal and ischemic tissue, and the amplifier output would be zero; C. The ECG complex as recorded with a DC amplifier; D. The ECG complex as recorded with an AC amplifier, showing ST-segment elevation.

The specific waveform details associated with ST segment elevation or depression depend upon the orientation of electrodes as well as the precise location of ischemia or infarction. In diagnostic quality ECG one may even determine the exact location of the coronary artery that is occluded based on which leads show elevation or depression. Since there is no T wave in the murine ECG and the point immediately following the murine QRS complex corresponds to the J wave onset, “ST segment” for mice is a misnomer. However, within the repolarization period of murine ECG we may see, as we would in the ST segment of humans, elevation or depression corresponding to an underlying pathophysiologic condition. Examples of repolarization segment elevation and depression in murine ECG are shown in figures 2-16 and 2-17 below. Another example of mouse repolarization segment elevation from a dKO subject (figure 2-19) more closely resembles an elevation induced in a study by occluding the coronary artery (figure 2-18) [39].

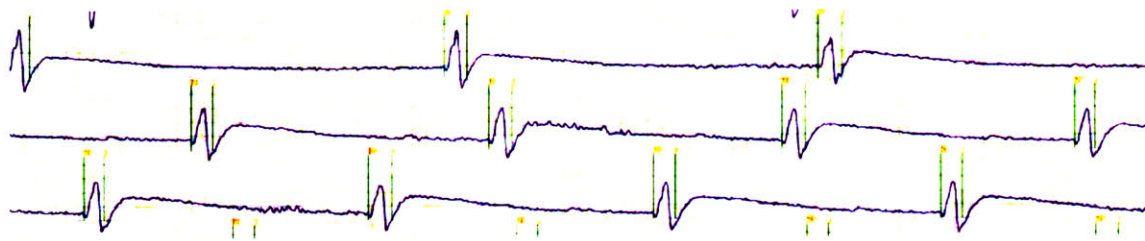


Figure 2-16: Repolarization segment elevation in mouse ECG. (time scale: 7.5 ms/div, heart rate = 300 bpm)

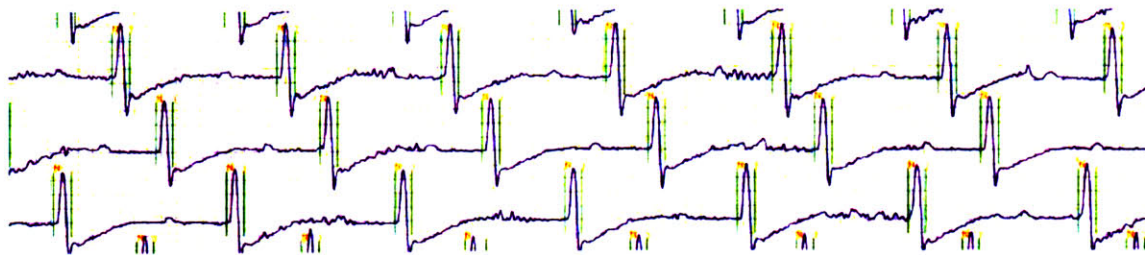


Figure 2-17: Repolarization segment depression in mouse ECG. (time scale: 7.5 ms/div, heart rate = 666 bpm)

Figures 2-17 and 2-19 are exemplary repolarization segment deviations indicative of underlying pathophysiology. Figure 2-17 shows a depression in which slightly less than half of the RR interval is below the isoelectric level. Figure 2-19 shows an elevation in which more

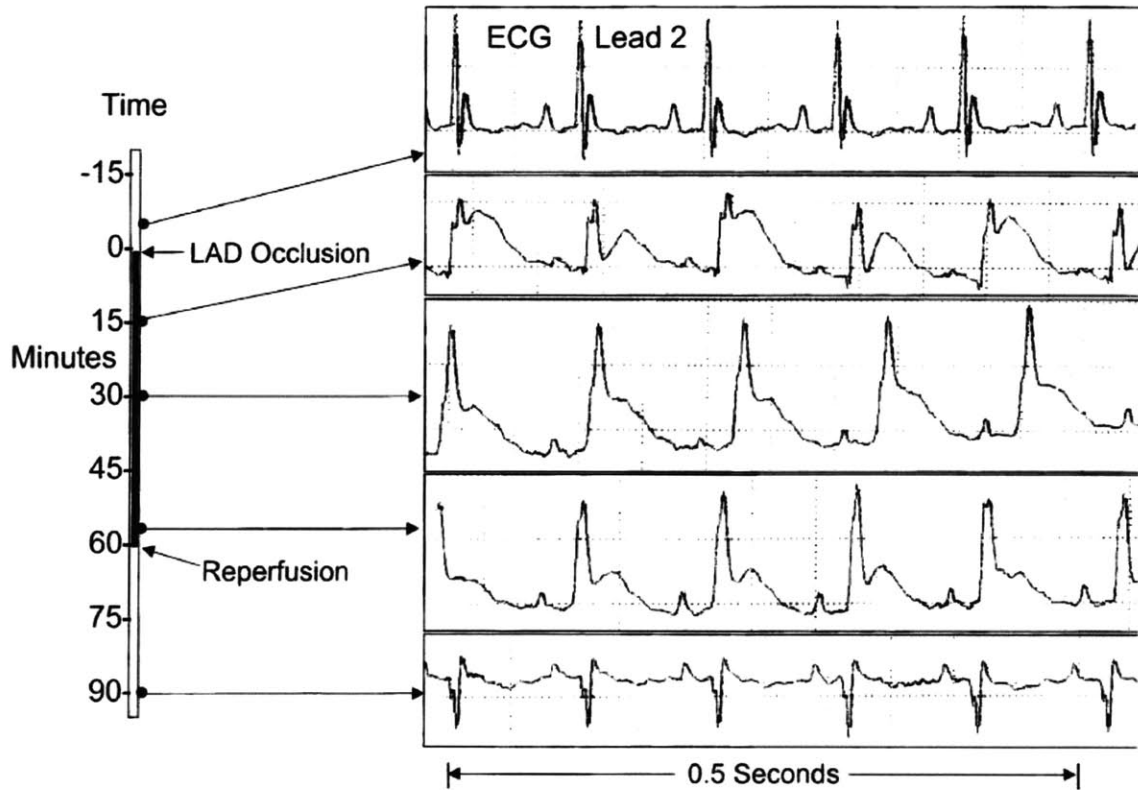


Figure 2-18: Lead 2 ECG signals from a mouse before, during and after occlusion of the left anterior descending (LAD) coronary artery. There is a marked repolarization segment elevation after occlusion. After reperfusion, the shape of the ECG is altered from the control as shown in the bottom panel. Such change is consistent with infarct [39].

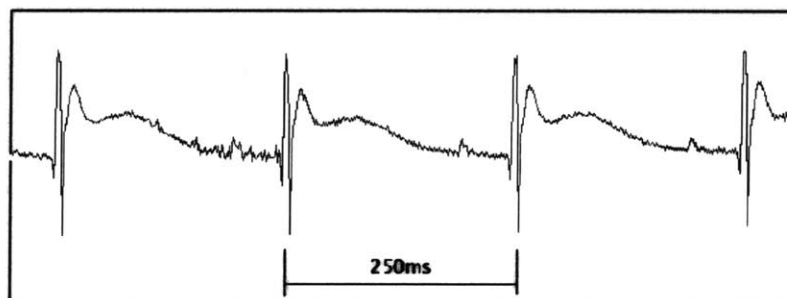


Figure 2-19: This sample elevated repolarization segment in dKO mouse ECG is comparable to that seen in experiments in which the coronary artery is occluded. Note that the first wave following the QRS complex is a J wave and does not itself represent a pathophysiologic condition. Note that the RR interval is 250ms, which corresponds to a profoundly bradycardic rate of 240 bpm.



than half of the RR interval is above the isoelectric level. The current of injury digram (fig. 2-15) implies that the duration of repolarization segment deviations during ischemic episodes reveals repolarization segment duration. In both examples of repolarization segment deviation above (figures 2-17 and 2-16), P waves occur after 50% of the RR interval. We select 40% of the RR interval as a reasonable repolarization offset time point<sup>10</sup>. Clearly utilization of just two examples is insufficient justification for this choice of offset time point. Appendix A shows examples of waveforms and their associated repolarization segment onset and offset measurement time points. The appendix is intended to provide supplemental data with more examples indicating that the chosen repolarization segment onset and offset measurement timepoints - 1 ms after the J point and 40% of the RR interval point, respectively - on average capture a reasonable portion of the repolarization segment morphology. Figure 2-20 summarizes the repolarization period onset and offset points with an example.



Figure 2-20: The repolarization segment onset point is the point 1 ms beyond the J point (which *wqrs* often inaccurately detects as occurring at the J peak, as discussed in a previous section); the offset point is the point 40 percent of the RR interval beyond the onset point. That is, if the RR interval is 10 ms and the J point occurs 0.6 ms after the R peak, then the repolarization segment onset is determined to be 1.6ms after the R peak (1 ms beyond the J point) and the offset is determined to be 5.6ms after the R peak (4.0 ms, or 40 percent of RR interval, after the onset). The calculation is performed on a template comprised of a trailing 64-beat point-by-point average after cubic spline baseline removal, as described in chapter 6.

---

<sup>10</sup>it is not improbable that the repolarization end point will encroach upon the P wave; the mathematics of Chebyshev decomposition, detailed in chapter 5, imply that inclusion of the P wave would have little, if any, effect on the automated algorithm

## 2.4 Arrhythmias

Though the primary objective of this thesis is repolarization segment morphology monitoring, it is certainly worth noting that the dKO mouse exhibits arrhythmias quite similar to those seen in pathological human ECGs. A brief explanation of the origin of arrhythmias follows:

The SA node typically acts as the heart's primary pacemaker, but it can, for various reasons, fail to generate the requisite impulse to stimulate a heartbeat. Under such circumstances, another automatic focus, with a slower inherent pacing rate, compensates as a backup system. There is a distinct hierarchy of dominance, based on a descending inherent pacing rate, dictating which automatic focus will emerge to provide electrical stimulation. Anatomically the dominance descends from the SA node, through the A/V junction and into the ventricles. *Within* a given anatomical region multiple automatic foci vie for dominance since they share similar inherent rates [6].

A lapse in pacemaking from the SA node, or any automatic focus for that matter, may be transient or permanent. In the event that the failure is transient, the inferior automatic focus merely generates one or several escape beats at its inherent pace, after which the original focus resumes pacing. In the event that the failure is permanent, the inferior automatic focus becomes the dominant pacemaker, generating an escape rhythm. In a diseased heart one may find that triggering activity in ectopic sites initiates depolarization, and heterogeneity in refractoriness of myocytes leads to atypical pathways for depolarization. Shortened refractory periods in myocytes perpetuate fibrillation, while if a re-entrant wavelet encounters an area of refractory tissue it may terminate [26]. Re-entrant loops in the ventricles can, in humans, lead to lethal ventricular fibrillation. Sustained ventricular fibrillation in mice and other small animals was deemed impossible according to Garrey's "Critical Mass Hypothesis," published in the early 1900s. Garrey's claim has since been criticized on theoretical grounds and remains contested to this day [18]. Theoretical arguments aside, our empirical findings have not revealed a single dKO mouse with a terminal fibrillation episode.

## 2.4.1 Premature ventricular contractions

An automatic focus at a site other than the SA node may occasionally fire before the SA node, initiating a premature or extra systole. When the automatic focus site is in the ventricles, the resulting QRS complex is distinctly wide because propagation of depolarization among myocytes is slow. We do not monitor blood pressure in the dKO mice. However, were we able to monitor blood pressure in conjunction with ECG we would see that the systole produced by a PVC fails to pump much blood, as sufficient time has not elapsed for ventricular filling. After the PVC, the ventricular myocytes are often still refractory when they receive the next depolarization signal initiated by the SA node. Therefore a longer-than-normal period of electrical silence, called a *compensatory pause*, ensues before normal sinus rhythm resumes. An example of a PVC with a compensatory pause from mouse ECG is shown in Figure 2-21 below. Another interesting phenomenon, characterized by a rhythm of a single PVC followed by two SA beats and called ventricular *trigeminy*, is shown in Figure 2-22.

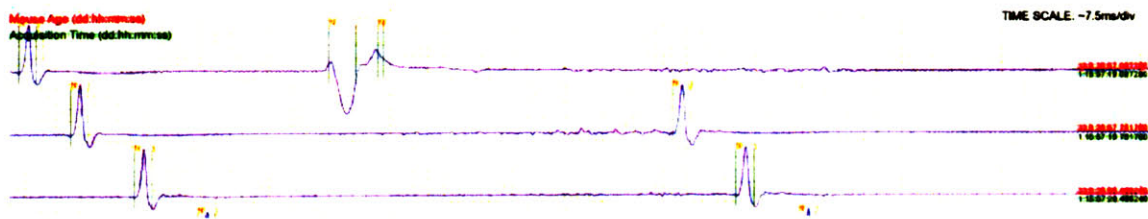


Figure 2-21: A PVC from a dKO mouse. This PVC was found by manually searching through ECG data. The subject is profoundly bradycardic (RR = 360ms, HR = 167 bpm) (time scale: 7.5 ms/div) [screenshot from Hermes applet<sup>11</sup> Record 2190020704 at elapsed time 1:15:57:19, where time is in dd:hh:mm:ss format]

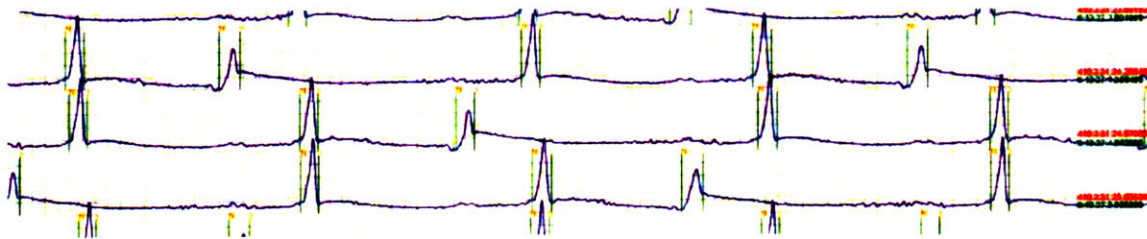


Figure 2-22: Ventricular trigeminy in a dKO mouse, which is characterized by a persistent rhythm of a single PVC followed by two SA beats. This episode of trigeminy was found by manually searching through ECG data. A premature beat (RR = 97.5 ms) is followed by a compensatory pause (RR = 176 ms), after which a sinus beat (RR = 135ms) occurs (time scale: 7.5 ms/div). [Record 2767022103 at elapsed time 6:13:27:04, where time is in dd:hh:mm:ss format]



## 2.4.2 Ventricular tachycardia

Ventricular tachycardia is a tachyarrhythmia with three or more consecutive PVCs. VT is termed non-sustained (in humans) if its duration is less than 30 seconds and sustained if it lasts more than 30 seconds [11]. Ventricular tachycardia does appear in dKO mice, as shown in Figure 2-23 below.

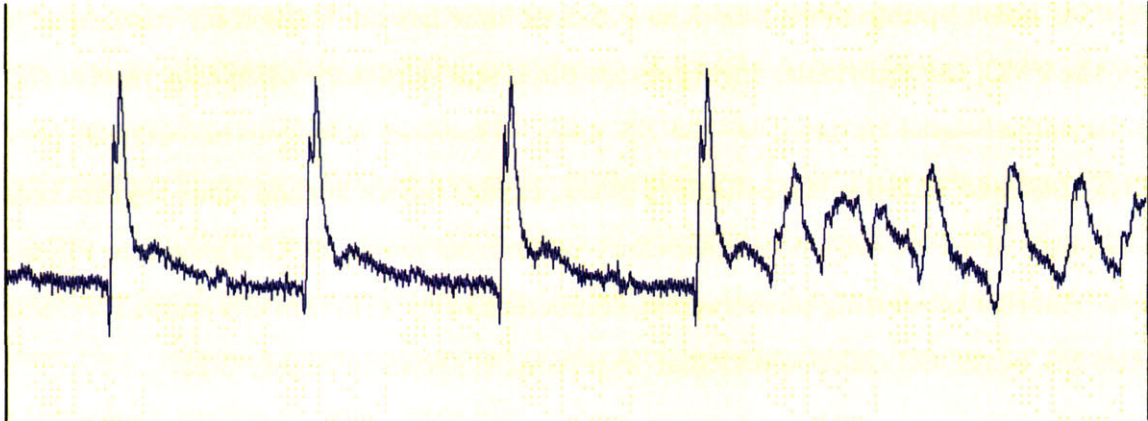


Figure 2-23: Onset of ventricular tachycardia in a dKO mouse. [Screenshot from WAVE[13] viewing dKO record 0911123103, file 1257.hermes at time 19:21]

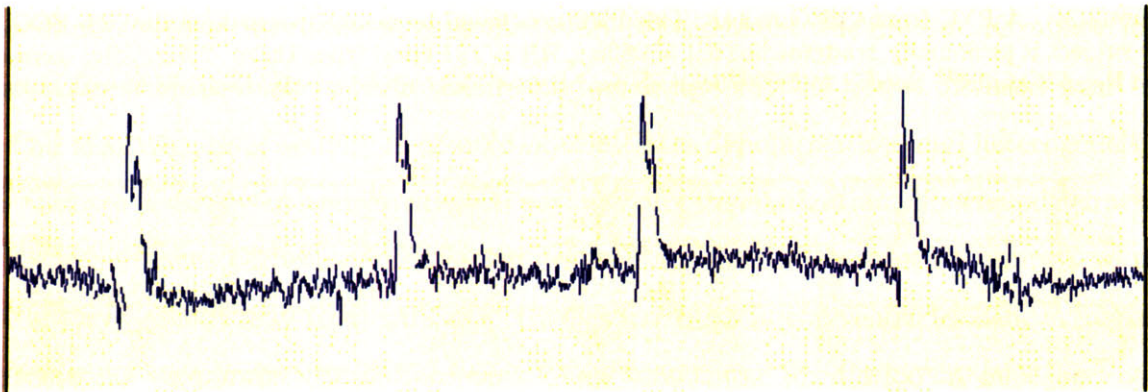


Figure 2-24: Spontaneous termination of ventricular tachycardia in a dKO mouse within approximately 9 seconds of onset (time difference between termination at 21:54 and onset at 19:21 must be divided by 10 to account for factor of 10, which is intentionally introduced to allow QRS detection with human ECG beat detectors). [Screenshot from WAVE[13] viewing dKO record 0911123103, file 1257.hermes at time 21:54]



### 2.4.3 Heart block

The fact that P waves are sometimes altogether undetectable in mouse ECG seems to preclude automated detection of heart block. Nonetheless it is worth noting that there are examples of heart block to be found in dKO ECG data. In 2:1 2nd degree heart block (see Figure 2-25 below), every other P wave conducts through the AV node to generate a ventricular depolarization (QRS complex). An example of 3rd degree heart block, in which the atria and ventricles are paced entirely independently, is shown in Figure 2-26 below.

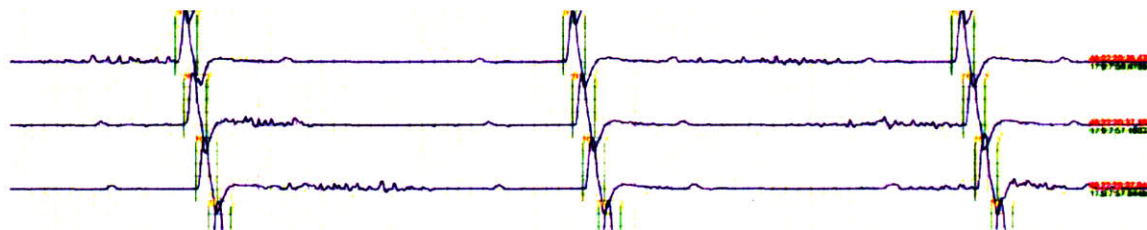


Figure 2-25: An example of 2:1 2nd degree heart block in dKO mouse ECG data. (time scale: 7.5 ms/div) [Record 0920122903 at elapsed time 17:9:7:57, where time is in dd:hh:mm:ss format]

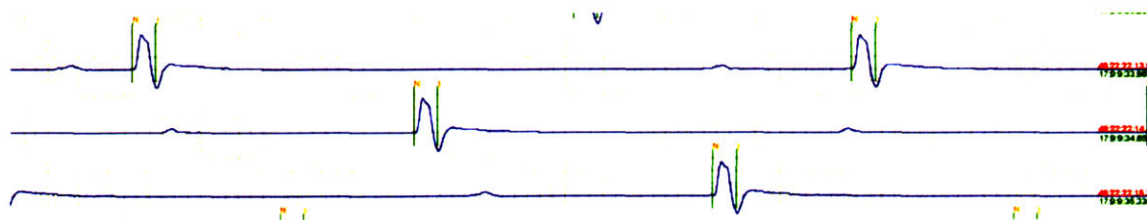


Figure 2-26: An example of 3rd degree (complete) heart block in dKO mouse ECG data. The notched QRS morphology indicates the escape rhythm is likely ventricular in origin, as a junctional escape rhythm would ideally preserve a lead 2 QRS morphology consistent with ventricular depolarization triggered from a superior focus (eg fig. 2-25). The subject also shows profound atrial and ventricular bradycardia (time scale: 7.5 ms/div) [Record 0920122903 at elapsed time 17:9:9:35, where time is in dd:hh:mm:ss format]

### 2.4.4 Bradycardia

The genetically-engineered dKO mouse subjects have frequent episodes of bradycardia, often reaching heart rates as low as 150 or 200 beats per minute. As chapter 8 will describe, dKO mice often suffer a progressive bradycardia over the course of several days or even weeks that culminates in asystole.

## 2.5 Summary

This chapter provides a foundation for cardiac electrophysiology, the aggregate activity of which is measured with ECG. Though the mouse heart is functionally and anatomically quite similar to the human heart, distinct ECG differences between the species warrant the detailed description of correspondence between cellular action potentials (APs) and ECG. Of specific note is the fact that the J wave, often found immediately after the QRS complex in healthy and diseased mice alike, *does not* correspond temporally to phase 3 AP activity (which does correspond to a T-wave in human ECG). With the recognition that dKO mice do exhibit morphological changes comparable to human ST-segment elevation and depression after the J-wave, we provide justification for the measurement of morphology starting 1 ms after the J-point (as determined by *wqrs*) and ending 40% of the RR interval from the onset.

We concede that *wqrs* often inaccurately labels the peak of a J wave as the perceived QRS offset, or J point, likely mistaking the J wave peak as a strong upright S wave<sup>12</sup>. Moreover we recognize the possibility that in the presence of a less prominent J wave, *wqrs* may detect the J point accurately. We accept the possible time stamp errors that arise as an artifact of *emwqrs*' J point detection and argue that they do not lead to significant repolarization segment analysis artifact since the repolarization segment algorithm characterizes a segment with a total duration much longer than the erroneously introduced (or excluded) segment.

While the chapter does show an interesting gallery of arrhythmias present in dKO mice, the focus of this thesis is that of repolarization segment morphology analysis. Subsequent chapters build on the time points for repolarization morphology measurement derived in this chapter to form a statistical representation of normal morphologies (as represented by a variety of wild-type mice) and abnormal morphologies (as seen only in dKO mice).

---

<sup>12</sup>Such inaccuracy should not be deemed a shortcoming of *wqrs*; its authors designed it for use on human ECG, not mouse ECG!

# Chapter 3

## ECG instrumentation design and analog-to-digital conversion

A project on data analysis must necessarily pay close attention to the mechanism by which data is collected. A very common pitfall in data analysis is that of unwittingly assuming that the digitized physiological data on a computer is a perfect representation of the data source, as though the transfer function of the instrumentation were a delta function<sup>1</sup>. Mathematical idealities are extremely useful in understanding theoretical constructs for instrumentation design, but upon implementation one must concede that real components do not behave exactly as their mathematical models would suggest and available components are not available in arbitrary, high-precision values that often result from models. Additionally cost, size, ambient electromagnetic noise and other limitations preclude translation of idealized designs into realizable hardware.

Even if one could build a perfect analog instrument entirely immune to ambient noise, the analog data must still be digitized. Digitization introduces error by discretizing the signal amplitude. A very high-resolution A/D converter can represent the signal extremely well, but invariably discretization of data creates an imperfect representation of its analog counterpart.

---

<sup>1</sup>In the mathematics of signal processing, an impulse response (or transfer function in the Fourier domain) fully represents the characteristics of a linear, time-invariant (LTI) system. A “perfect” impulse response is a so-called Dirac delta, or simply delta. An LTI system with a delta function as its impulse response will perfectly replicate the input as its output with no delay or distortion

Additionally the data must be discretized temporally, since a computer cannot represent the infinite number of data points comprising an analog signal. Temporal discretization is not necessarily a source of error provided that the Nyquist sampling theorem is satisfied<sup>2</sup>.

With the admission that hardware design is a process of tradeoffs, this chapter reviews the design (and associated tradeoffs) of the front-end instrumentation used for analog signal conditioning of the ECG. While several design considerations are specific to mice (such as bandpass frequency settings), many of the design principles apply equally to human-oriented ECG instrumentation.

### 3.1 Signal conditioning hardware

This section outlines the architecture of the 16-channel hardware used for mouse ECG signal conditioning. The final machine, shown in Figure 3-1, is approximately 16" x 9" x 9" in size. It is cooled by two brush-less DC fans (not shown) that emit minimal signal-degrading electromagnetic radiation when compared with their AC counterparts. The lead cables terminating at the input terminals of the analog cards are enclosed in braided metal shielding which is grounded to reduce capacitively-coupled noise. The output of each of the 16 analog signal conditioning cards is wired into a DSP termination card (mostly blocked by the analog cards and therefore barely visible in Figure 3-1). This DSP termination card is connected to a DSP board on the data acquisition RAID server via a ribbon cable, where the conditioned (filtered and amplified) analog signals are digitized and stored.

The signal conditioning cards are built with sockets into which microchips are inserted. Such modularity allows for easy adaptation of the system to other uses. Consider, for example, the case in which the system is to be utilized for human ECG signal conditioning. Simply removing the filters and replacing them with those appropriate for the human ECG spectrum, with no de-soldering and re-soldering of components required, allows for an easy change. The modularity of the hardware has the added advantage that debugging is greatly

---

<sup>2</sup>The Nyquist theorem shows that, for a bandlimited signal with maximum frequency  $F_0$ , sampling at frequency  $F_s > 2F_0$  creates a discretized signal with sufficient information to reconstruct the original analog signal perfectly

simplified. Again due to the socket-connected design of the analog cards, a single part may be swapped without soldering. Such ease of swapping reduced the design time substantially by allowing faulty parts to be identified and replaced efficiently.

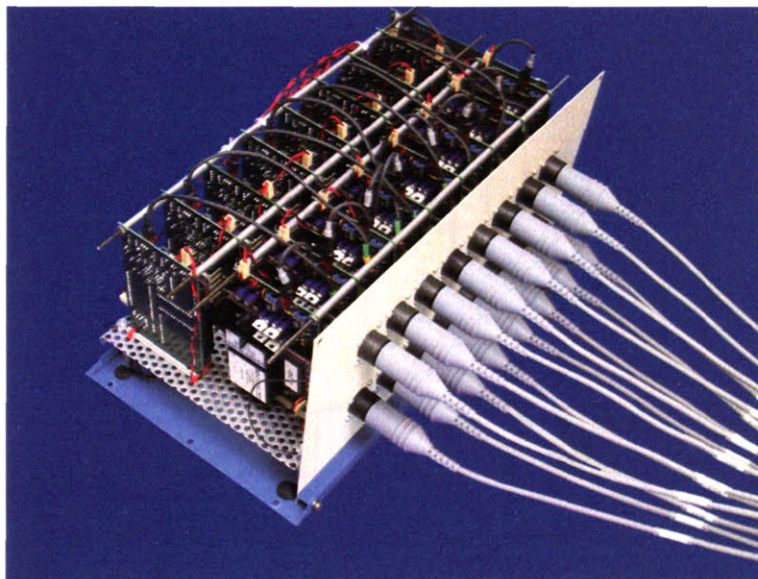


Figure 3-1: 16-channel ECG hardware implementation designed for Krieger Lab murine studies.

### 3.1.1 Single-channel architecture

Figure 3-2 shows the overall ECG instrumentation architecture and figures 3-3, 3-4, 3-5 and 3-6 show schematics, layout and fabrication examples of the hardware. The entire acquisition system consists of 16 such instruments operating in parallel.

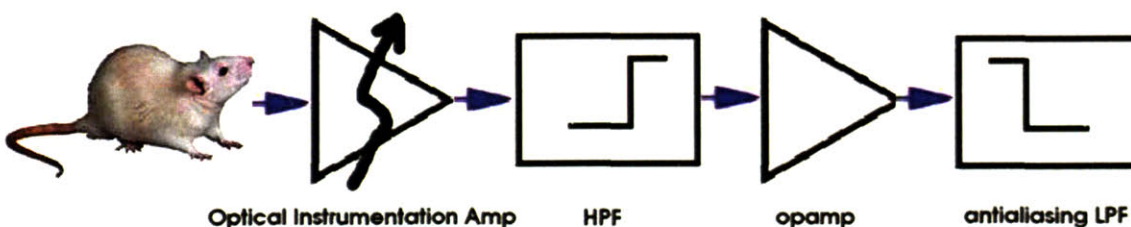


Figure 3-2: Simplified Diagram of Hardware Setup: Mouse ECG signal amplified with optically-isolated instrumentation amp followed by a high-pass filter, second amplification stage, then a low-pass anti-aliasing filter. The signal is finally sampled by a Microstar<sup>©</sup> Laboratories model 4200A A/D card (not shown).

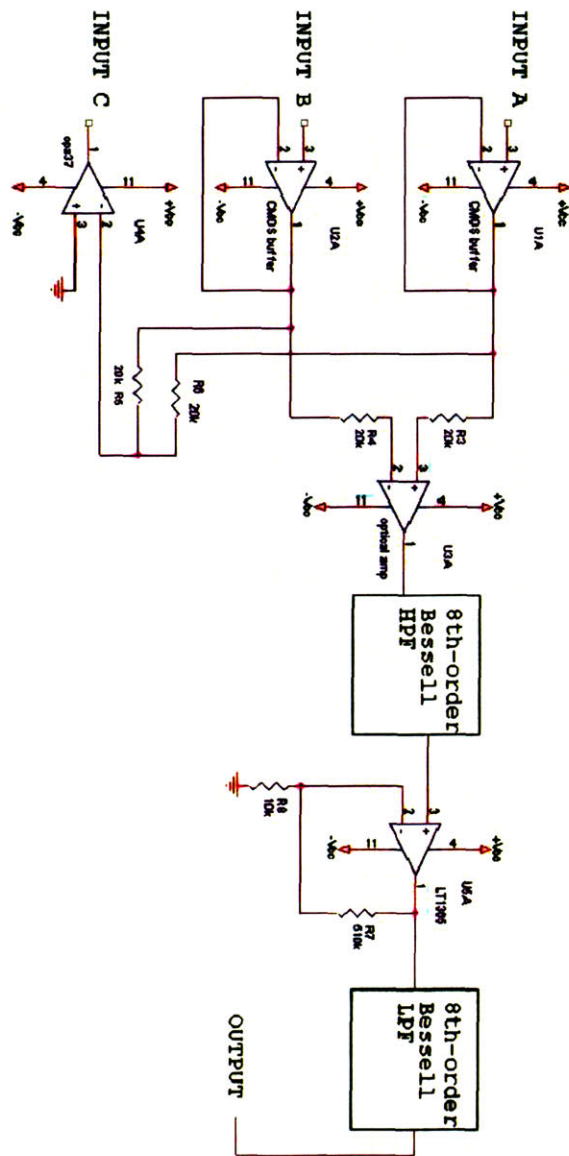


Figure 3-3: Schematics for ECG signal amplification and filtering. Inputs A and B are connected in a lead II configuration across the thorax of the subject, while input C is connected to the back of the subject's neck and is used as a ground electrode.



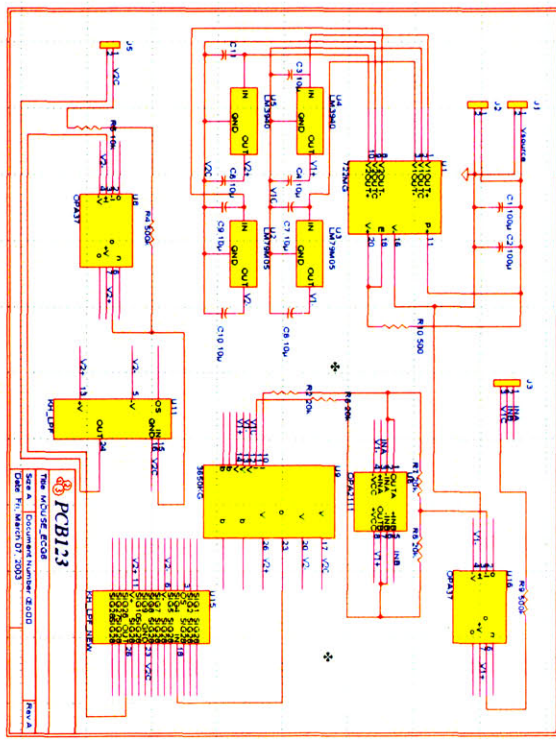


Figure 3-4: This schematic, which comprises a single channel of the ECG instrumentation, was created using PCB123<sup>©</sup> software. As following diagrams show, this schematic is then converted into a PCB (printed circuit board) layout, which includes all necessary hole dimensions and trace connections to allow manufacturers to implement the board.

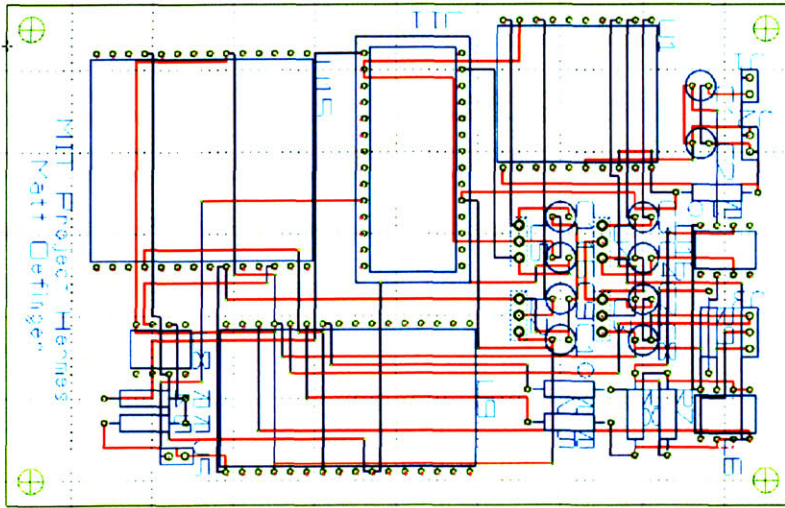


Figure 3-5: The schematic (shown in previous picture) is converted into a PCB (printed circuit board) layout diagram after all microchip dimensions are entered. From this diagram manufacturers can fabricate a printed circuit board to realize the schematic.

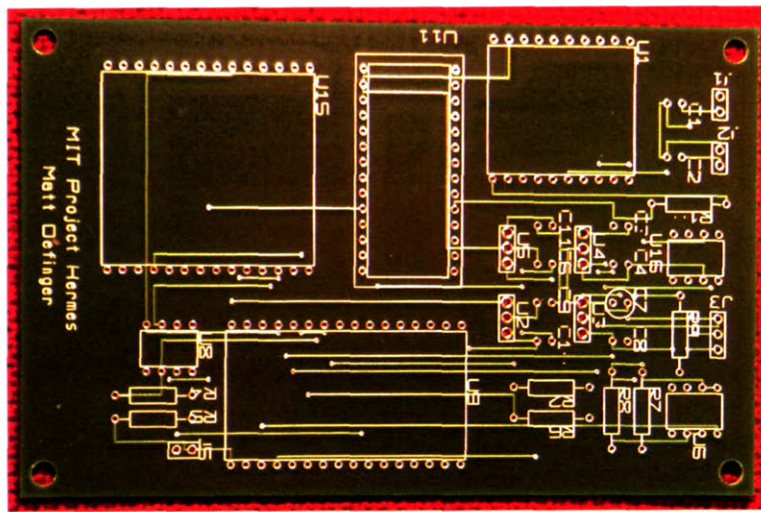


Figure 3-6: Fabricated printed circuit board of single-channel ECG hardware.

### 3.1.2 Common-mode noise reduction: active grounding circuit

Sixty-hertz electromagnetic noise (and to a lesser extent harmonics thereof) is ubiquitous indoors, as electrical systems in buildings utilize AC power delivered at 60 Hz (50 Hz in European countries). Because the spectrum of mouse ECG spans 0-1kHz<sup>3</sup>, using a notch filter to remove 60 Hz noise will invariably remove at least some signal content. An active ground circuit is the preferred means of removing such common-mode noise.

An active grounding circuit, modified from a description by Huhta and Webster [9], is shown in Figure 3-7. The circuit works by taking the average (common mode) of the voltages at the two input terminals of the pre-amplification stage, amplifying and inverting the signal, and feeding that signal back as the ground, or reference voltage, for the circuit. The circuit does not remove differential signal content but mitigates common-mode noise, that is signal that is simultaneously present on both electrodes. With an active grounding circuit included in the architecture, a high-quality signal results.

---

<sup>3</sup>According to one study [8], the frequency range 0-80 Hz contains 45.48 +/- 15.32% of the spectral power, while the range 80-1000 Hz contains 54.52 +/- 15.32% of the spectral power. That is, nearly all the signal power resides in the 0-1000 Hz range, motivating the chosen passband of 0.1 Hz - 1000 Hz.



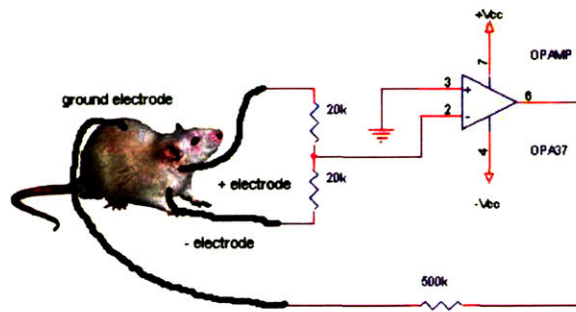


Figure 3-7: Active ground circuit used for common-mode noise reduction. The common-mode signal at the input electrodes is inverted and fed back through a current-limiting resistor (for subject projection). This circuit is particularly useful in reducing prevalent 60 Hz noise, which is capacitively coupled into both signal input wires.

### 3.1.3 Increasing input impedance: CMOS buffer stage

High input impedance is requisite in a biomedical instrumentation design, as the signals of interest (particularly electrophysiological signals) are extremely weak (on the order of several hundred microvolts) and consequently cannot supply substantial current. Inherent in a CMOS circuit is an extremely high input impedance and corresponding power amplification, so a CMOS preamplifier op-amp circuit serves as an ideal decoupling stage between the weak electrophysiological signal and subsequent analog signal processing circuitry. The first stage of signal conditioning in the data acquisition hardware is a pair of CMOS op-amp buffers, one for the positive electrode input and one for the negative electrode. A buffer is an op-amp configured to have unity gain but an extremely high input impedance.

### 3.1.4 Pre-amplification

The first amplifier in Figure 3-2, which represents the pre-amplifier stage of the signal acquisition hardware, is recognized in a single monolithic circuit, the Texas Instruments 3560KG. Figure 3-8 shows the TI 3650KG with CMOS-buffered inputs as described in section 3.1.2.

This circuit provides optical isolation, which ensures that an electrical surge within the instrumentation circuitry cannot electrocute the subject, and conversely a surge at the input terminals will not damage instrumentation circuitry beyond the preamplifier. More danger-

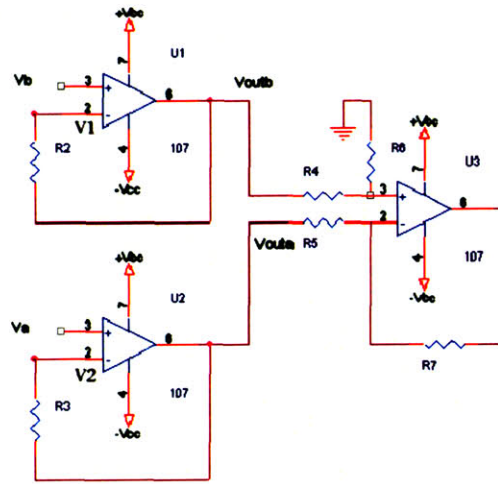


Figure 3-8: The two (CMOS) opamps to the left provide buffering, i.e. extremely high input impedance, that decouples the weak physiological voltage at the electrodes from subsequent circuitry stages. The latter opamp is an optically-isolated pre-amplifier, the TI3650KG.

ous is the threat of 60-Hz leakage current through the subject, minimal amounts of which (less than 100uA [10]) can induce lethal ventricular fibrillation in catheterized human subjects. (The strongest source of such currents originates from capacitive coupling through the power supply to the grounded instrumentation chassis.) Because the mice of interest in this study have surgically-implanted electrodes, they, just as catheterized human subjects, are vulnerable to fibrillation at low levels of leakage current.

Figure 3-9 shows that as long as the chassis that houses the ECG hardware is properly grounded, the minimal resistance of the metal case to ground will lead most of the current to sink to ground through this pathway. In figure 3-10, however, when the chassis is no longer grounded, leakage current only has a pathway to ground through the mouse, which could cause fibrillation if current levels are sufficiently high. As illustrated in figure 3-11, the optical isolator prevents a chassis/ground disconnect from routing leakage current through the subject. The optical isolation amplifier provides a high dielectric interruption in series between the lead wires and instrumentation, protecting the subject from acting as a pathway for leakage current to ground.

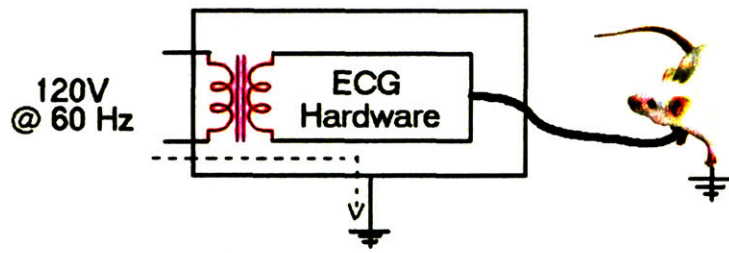


Figure 3-9: When the instrumentation chassis is properly grounded, capacitively-coupled leakage current originating from the transformer follows the pathway as shown by the dotted line. In this example the subject is safe solely because of proper grounding of the chassis.

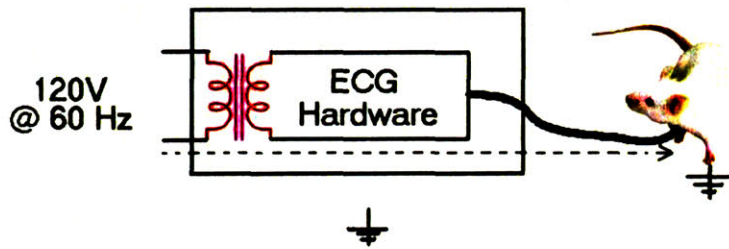


Figure 3-10: In this example the chassis is no longer grounded, and the only pathway for leakage current is through the subject. Sufficiently high levels of leakage current through the subject can cause lethal ventricular fibrillation.

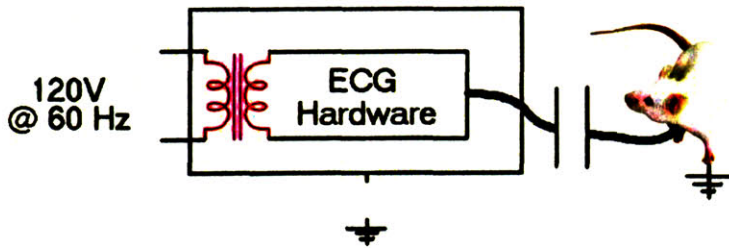


Figure 3-11: In this example the chassis ground is disconnected but there is no pathway for leakage current through the subject due to the extremely high-dielectric interruption, such as that provided by optical isolation. In this case the subject is safe in spite of improper grounding of the chassis.

The gain of the TI 3650KG preamplification stage is determined by the equation  $10^6/(R4+R5)$ , where  $R4$  and  $R5$  are as shown in figure 3-8. The preamplifier gain should be sufficiently large to boost the signal-to-noise ratio (SNR) yet sufficiently small to prevent opamp saturation, or “railing” of the output. Opamp saturation, while not necessarily harmful to instrumentation circuitry, represents an undesirable nonlinear region in the transfer function of the circuit.

The physiological voltages produced by the mouse heart are on the order of 100uV, and the dynamic range of the preamplifier is  $\pm 12V$ . Accounting for different half-cell potentials in the electrodes that could produce a differential DC voltage as high as 100mV, original estimates indicated a gain of 50 was appropriate for the preamplification stage. With this gain, however, the circuit frequently saturated. The saturation resulted from baseline drift (extremely low frequency changes in the signal offset) that was larger than anticipated. With a gain of 25 the circuit provided adequate SNR and, upon reaching steady-state, never appeared to saturate.

### 3.1.5 High-pass filtering

The output signal from the instrumentation amplifier is input to an 8th-order Bessel high-pass filter with a cutoff frequency of 0.1 Hz. This filter serves to remove the DC offset due to half-cell potential differences in the electrodes as well as other low-frequency signal noise (i.e. baseline drift). The choice of a Bessel transfer function is motivated by the fact that it has optimal phase response. That is, it has the desirable property of near-constant group delay, or equivalently negligible phase distortion. In contrast with audio circuits with phase distortion, for example, for which human ear can compensate, the human eye cannot easily compensate for phase distortion on a visual ECG tracing. While one could compensate with a knowledge of the analog circuit’s (frequency-domain) transfer function  $H(\omega)$  and a digital equalizer having transfer function  $H^{-1}(\omega)$ , the overall system architecture is simplified by optimizing the instrument for minimal phase distortion at the analog stage by use of a Bessel filter. The optimality in phase response comes at the price of decreased rolloff steepness in



the transition band relative to other transfer functions (such as Butterworth and Chebyshev).

Figures 3-12 and 3-13 show Bessel high-pass filter amplitude and phase characteristics contrasted with those of other filter implementations of the same order and cutoff frequency.

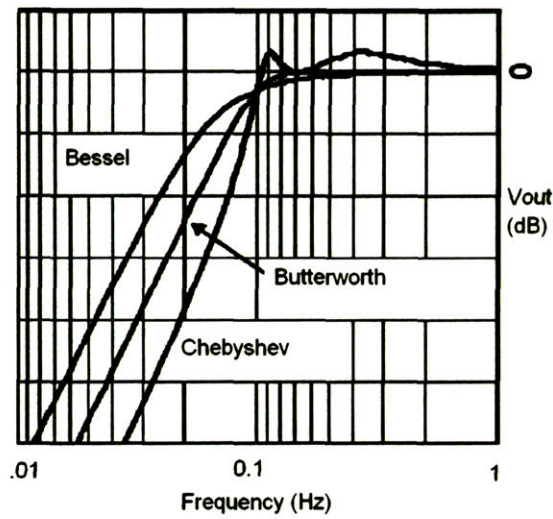


Figure 3-12: The Bessel filter shows a slower rolloff than its counterparts, which is a slightly undesirable characteristic that is compensated for by oversampling in the A/D conversion stage.

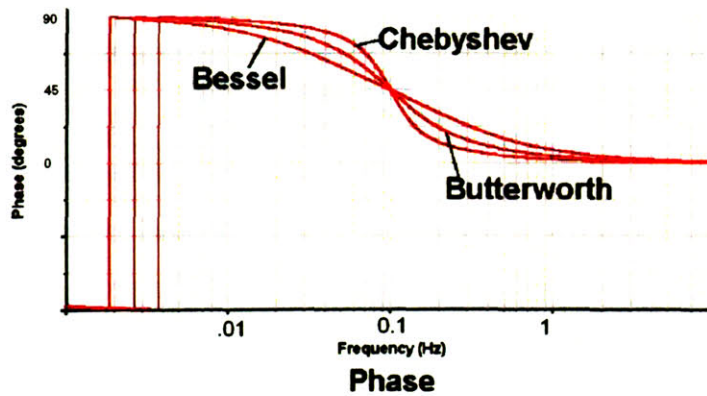


Figure 3-13: The Bessel filter has a highly linear phase response, or equivalently a near-constant group delay, which means that the filter delays all frequencies by the same amount. This linearity in phase means the filter has little to no phase distortion, a requisite feature for high-fidelity signal acquisition.

### 3.1.6 Secondary amplification

After passing through the high-pass filter, the signal is again amplified, this time by a gain of 52. The second amplification stage further boosts the signal voltage to a range appropriate for sampling with an A/D converter with a dynamic range of  $\pm 10\text{v}$ . The amplification circuit is a simple feedback op-amp network utilizing the familiar gain equation  $1 + R_f/R_{in}$ , where in this system  $R_f = 510\text{k}$  and  $R_{in} = 10\text{k}$ , to provide the gain factor of 52. The signal entering this amplification stage, in contrast with that entering the pre-amplification stage, is not offset due to half-cell potential differences and baseline drift because of the preceding high-pass filter stage. As such this amplification stage can comfortably amplify the signal by the rather sizable factor of 52 without saturating the amplifiers.

### 3.1.7 Low-pass filtering and oversampling

Because the mouse ECG spectrum occupies 0-1kHz [8], the Nyquist sampling criterion mandates that, with an *ideal* low-pass filter with passband 0-1kHz one should sample the signal at a minimum of 2kHz to avoid aliasing. Since a circuit filter implementation is never ideal, one must enforce a relationship between the filter type, the filter's cutoff frequency, and the A/D sampling rate that produces an acceptably small amount of aliasing. The filter transfer function for the low-pass filter, as for the high-pass filter, was chosen to have a Bessel transfer characteristic to minimize phase distortion. This optimization for phase response comes at the expense of a slow rolloff in the transition region.

Oversampling is a technique often employed in systems using an anti-aliasing filter with relatively slow rolloff. Though a derivation is not provided here, it can be shown that sampling of an analog signal produces spectral copies of the analog spectrum at multiples of the sampling frequency, denoted  $F_s$ , in the discrete-time frequency domain [7]. Consider the example in which a signal is filtered in the analog domain with a non-ideal lowpass filter of cutoff 1kHz then sampled at 2kHz. The result is an aliased signal, which is manifested in overlapping spectral regions in figure 3-15. One might consider building a higher-order analog filter to reduce the transition band, which would prove costly and time-consuming,

to mitigate the effects of aliasing. Alternatively, one could sample the signal at a faster rate, thereby spreading the spectral copies further apart, as figure 3-14 illustrates.

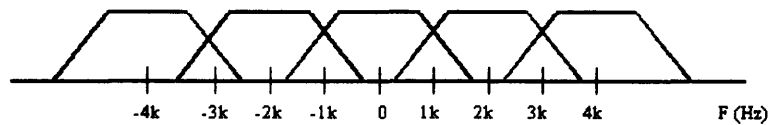


Figure 3-14: A signal band-limited to 1.75kHz (due to slow rolloff of 1kHz cutoff Bessel anti-aliasing analog filter) sampled at 2kHz has spectral copies at multiples of 2kHz and suffers aliasing (overlapping regions).

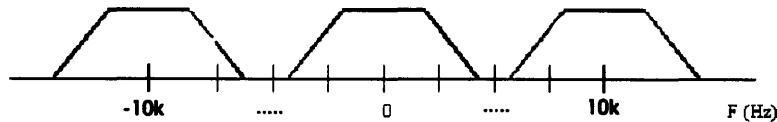


Figure 3-15: The same signal, band-limited to 1.75kHz (due to slow rolloff of 1kHz cutoff Bessel anti-aliasing analog filter) sampled at 10kHz (5x oversampling) has spectral copies repeating at multiples of 10kHz and does not suffer aliasing.

By then employing a high-order digital filter, which is cheap and relatively simple to implement, to low-pass filter the digitized signal, then decimating the signal to reduce the number of time-domain samples required to store the signal, one achieves the same effects as with a high-order anti-aliasing analog filter without the hardware complexity.

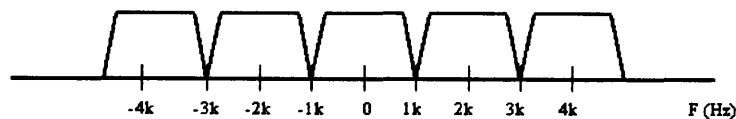


Figure 3-16: After applying a high-order digital low-pass filter then decimating by a factor of 5, the spectra are spaced by multiples of 2kHz but with no aliasing. This combination of digital low-pass filtering and decimation (downsampling) prevents the need for an expensive analog anti-aliasing filter.

Such a technique, known as oversampling, is often employed in data-sampling systems to minimize the complexity and cost of analog circuitry and harness the power of fast digital processing power. In the case of this system a high-order anti-aliasing filter is in place, but

since it is optimized for minimal phase distortion its rolloff is similar to that of a lower-order filter. Thus this system employs 5-times oversampling, meaning that the signal is sampled at 5 times the Nyquist rate of 2kHz. After being sampled at this high rate the signal is then digitally lowpass-filtered with a 256-tap symmetric FIR filter<sup>4</sup> then decimated by a factor of 5 to give an effective sampling rate of 2kHz. The initial use of oversampling minimizes aliasing, and subsequent downsampling (after digital low-pass filtering) provides the minimum allowable lossless data storage requirement without resorting to compression. Figure 3-16 shows the spectral content of a signal after it has been oversampled (5x), digitally lowpass-filtered, then decimated by a factor of 5. The spectral copies do not overlap, indicating that no aliasing has occurred. However, the spectra are closely spaced, indicating that the signal is not oversampled and therefore no disk storage is wasted when the data is archived.

---

<sup>4</sup>Symmetric FIR filters have perfectly linear phase. Since phase linearity was an optimization constraint on the analog front-end design, it is important to ensure that linearity is preserved in subsequent stages of the signal conditioning pipeline.



# Chapter 4

## Software for data collection and trend visualization via the Internet

The server data acquisition software for this system runs on a RedHat Linux 8.0 RAID server and was written in ANSI C, using a custom-written code interfacing with libraries provided by Microstar<sup>©</sup> Laboratories. Utilizing a data acquisition card made by Microstar<sup>©</sup> Laboratories, the server acquires 1 lead of ECG data on 16 mice simultaneously, sampling each channel at a rate of 2kHz<sup>1</sup>. The software simultaneously streams the data to disk and to a network device, permitting real-time network monitoring of the ECG (section 4.2.3). The streaming nature of the design, combined with the fact that the software runs on a high-capacity RAID server, allows full automation of data collection for the duration of a mouse's lifespan. The user simply attaches the requisite leads to the mouse electrodes and starts acquisition via an intuitive graphical user interface (section 4).

### 4.1 Server user interface software

Most details of the data acquisition software described above are irrelevant to one who simply wishes to begin collecting ECG data from a mouse. Therefore an intuitive graphical user

---

<sup>1</sup>The signal is initially be oversampled at 10kHz, then digitally lowpass-filtered and down-sampled by a factor of 5 to an effective sampling rate of 2kHz

interface, written in HTML, SSI (Server Side Includes<sup>2</sup>), JavaScript, and CGI/Perl, allows the operator (most likely a biology lab technician) to view the system's status as well as to start and stop data acquisition on each of the 16 channels independently. A screenshot of one portion of the interface software, that which provides a description of each channel's status, is shown in figure 4-1.

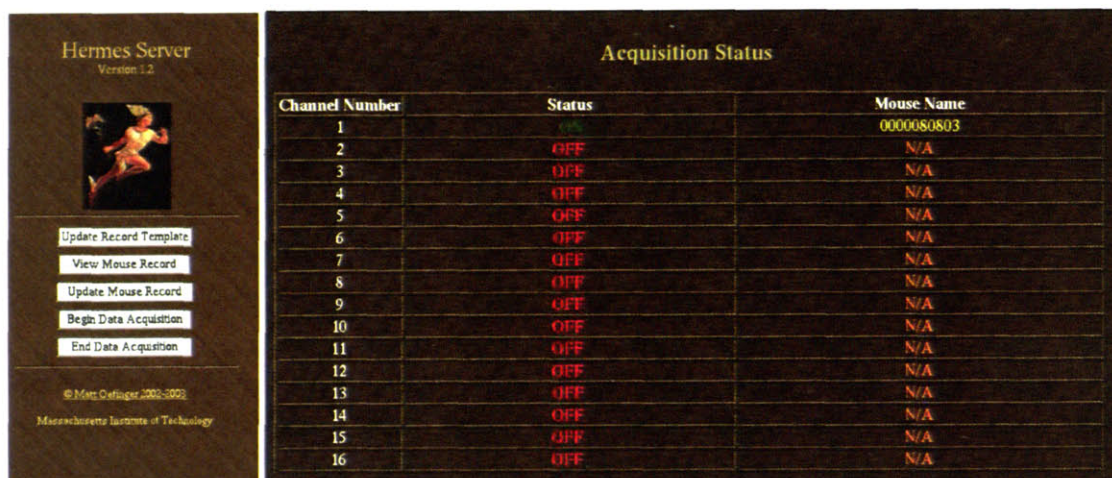


Figure 4-1: Server GUI user interface software showing the status of data collection. Currently only a single channel (channel 1) is collecting data. The mouse name is derived from the concatenation of its four-digit eartag ID (0000) and birth date (08/08/03).

In an effort to enforce good record-keeping, the software requires the operator to enter relevant information about the mouse prior to starting acquisition. The default mouse record template requires that, at a bare minimum, the operator provide a mouse's eartag ID, birth date, and hardware channel to which the mouse is connected before starting acquisition, as it is the unique combination of these fields that ensures a unique record name for each mouse. After the user has entered this information, acquisition is fully automated until the mouse dies and/or the user chooses to end data collection. Figure 4-2 shows the default record template that a user must fill out prior to beginning data acquisition.

Failure to enter reasonable data for one or more of these fields leads to an error message that forces the user to comply, as is shown in figure 4-3. This form-checking functionality is provided by a JavaScript routine.

---

<sup>2</sup>SSI is provided by the Apache web server as a mechanism for inclusion of HTML data generated by an executable on the server. On this system SSI is used to provide dynamic rendering of HTML data

The screenshot shows a web form titled "New Mouse Record". At the top, there are four input fields labeled "Ear tag ID", "Birth Month", "Birth Day", and "Birth Year", each containing a single digit. Below these is a dropdown menu titled "Select Channel For Acquisition" with options from "Channel 2" to "Channel 15". At the bottom are "Submit" and "Cancel" buttons.

Figure 4-2: The server operator, presumably a biology lab technician for this system, must fill out a record before data acquisition will begin. This process enforces good record-keeping and, since the record information is stored in a back-end SQL database, will allow for simple web-based search and retrieval of records.

This screenshot is identical to Figure 4-2, but with a JavaScript error dialog box overlaid in the center. The dialog box has a title bar that reads "127.0.0.1:80 - [JavaScript Application]" and contains the message "The birth month must be between 01 and 12" with an "OK" button.

Figure 4-3: The server operator entered an invalid month (13), and is therefore required to correct the error.



When the JavaScript routine has verified that all form entries are reasonable, it then submits the form to a back-end CGI script for processing. If the mouse record is unique then data acquisition begins, while if the record already exists in the SQL database the user is warned accordingly, as shown in figure 4-4.

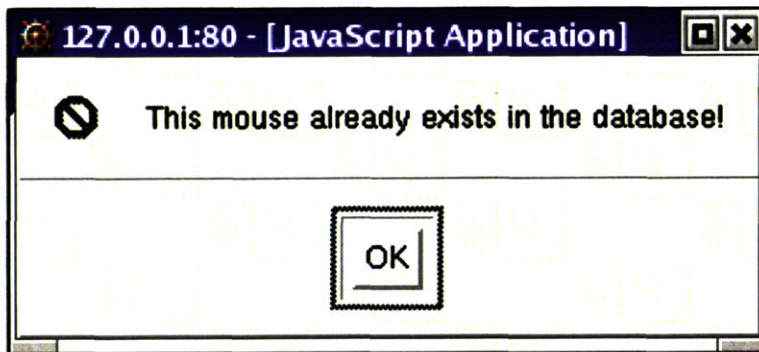


Figure 4-4: The user has attempted to enter a record into the database that already exists. Data acquisition is not started until the user corrects the mistake.

While the software should enforce proper formatting of required record fields, it should also allow a certain degree of flexibility so that additional fields may be entered into the record template to identify and differentiate mice in various studies. If the existing record template fields are inadequate, presumably because the lab has introduced a new option (i.e. drug regimen), then the user may add new template fields. Any new fields introduced are saved to the record template and become requisite entries for each subsequent acquisition. Figure 4-5 shows the software as a new field is being added. A JavaScript routine ensures that entries only contain alphanumeric characters, lest the database contain corrupt field entries.

Just as a user should be able to add data fields, so should he or she be able to remove them. Deletion of a field from the record template warrants a blatant warning that indicates to the user that the action is permanent and a request for an administrator password<sup>3</sup>, as

---

<sup>2</sup>The Apache web server, a product of the Apache Software Foundation, is the most widely-used web server in the world. In addition to serving standard static HTTP content to clients, it can provide dynamic content via its Server Side Include feature. An SSI statement embedded in an HTML document forces the Apache server to run a designated script that determines dynamically the HTTP content to be provided to the client. In the system outlined in this paper, SSI functionality is vital, as much of the web content is dynamic. The screenshot in figure 4-1, for example, provides a readout of the current channel status by using SSI.

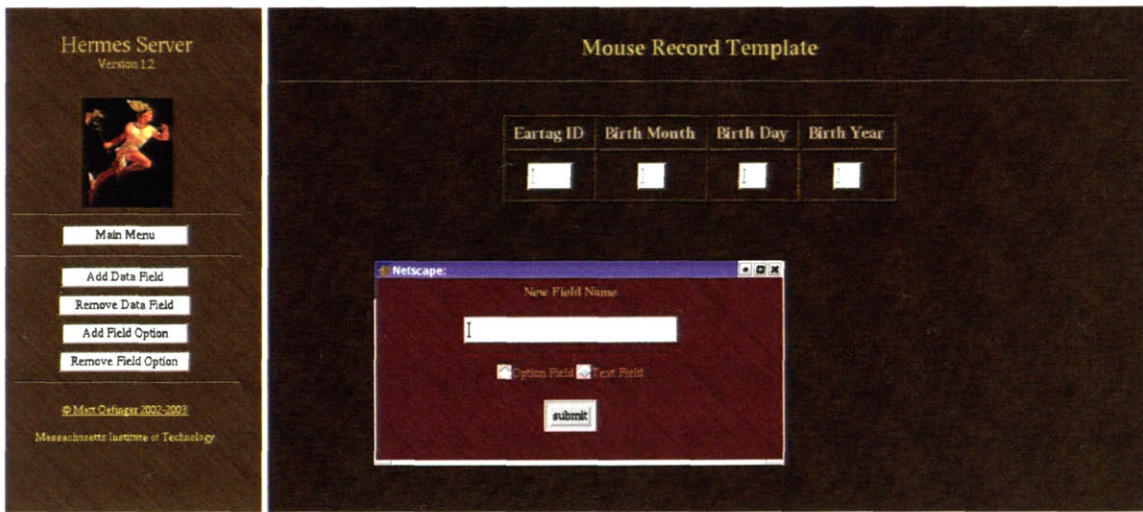


Figure 4-5: In this screenshot the user is adding a field entry to the default mouse record template. Note that the field can be of type “text” or of type “option.” If the field is of type “text,” then the user can freely type alphanumeric characters (enforced by a JavaScript routine) when creating the mouse record. If the field is of type “option,” then the user will select one of several pre-defined mutually exclusive options from which to select in the mouse record. Defining the options themselves for a given field is done in a manner similar to that of adding a field.

figure 4-6 shows. Deletion of a field is reversible within a fixed window of time. The system uses a 5-day rotating backup scheme, permitting restoration of a database before five days have elapsed.



Figure 4-6: The user is attempting to delete a database field, which not only affects the record template but also removes this corresponding field from the back-end SQL database. Such a drastic action should be verified! The user is required to enter an administrator password to proceed.

When the lab technician begins acquisition by filling out and submitting a record form for the subject, the information is stored in a back-end SQL database. This database contains a history of every subject entered into the system, any template entries that were in existence

at the time acquisition began, a timestamp of when data acquisition began and ended, and the hardware channel on which the data was acquired.

## 4.2 Server data acquisition software

Prior to beginning data acquisition, the Microstar<sup>©</sup> driver and associated control software must be downloaded to the A/D card and system daemons controlling data streaming to disk and the network must be initialized. The Microstar<sup>©</sup> control software, written in C, and system daemons controlling data flow to disk and the network, written in Perl, are all started with a simple click of an icon.

### 4.2.1 WFDB formatting, server self-diagnostics and email notification

Because the user interface software employs a fairly complex interaction among many lengthy HTML, SSI (Server-Side Includes), JavaScript, and CGI/Perl files, every action is carefully verified to ensure that it does not produce unexpected results. Any error generated by a script will produce an email with specifics of the problem so that the webmaster can immediately re-activate the server and troubleshoot the bug that led to the error.

The server disk-streaming software operates on the premise that the ECG data being gathered is extremely important and researchers must, in the unfortunate event of data corruption disk errors, learn of the problem immediately. Thus approximately 10 minutes of data are gathered on each channel and are saved to a file before a new file for the data stream is opened for the next 10-minute segment. Software daemons continually monitor the streaming process to ensure that the operating system (Linux) does not report an input-output (I/O) error at any point. In the unlikely event of an I/O error, the software's error-

---

<sup>3</sup>The administrator password referred to here is *not* the Linux operating system administrator password but rather a password associated with the administrator of the software. Therefore technicians and researchers utilizing the software are not necessarily empowered to perform administrative tasks on the computer itself.

checking mechanism detects the error and sends an email to the system's webmaster with specific details about the type and time of the error as well as which script generated the error. In the event that there is such an error the system will stop collecting data, but since the files are broken into 10-minute data segments all previously saved files are unaffected by the error.

The Laboratory for Computational Physiology (LCP) has, over the years, developed extensive software tools for the analysis of ECG data. These analysis tools require that the ECG data be stored in a specific format, namely WFDB format (see <http://www.physionet.org>), and that a WFDB-specific header file be associated with each file. So that this software system produces data that is amenable to analysis with WFDB tools, all files are converted in real-time into WFDB format, and an associated header file is created by the disk-streaming daemon at the end of each 10-minute cycle.

## **4.2.2 Server multicast network software**

A Perl network daemon runs on the server to stream the WFDB-formatted data to a network interface, allowing remote computers (on the MIT network) to monitor the ECG in real time. The server has a static multicast IP address, the first assigned to a non-system-administrator at MIT, that allows the server to broadcast data to multiple clients simultaneously.

Multicasting is not a new concept, but it is relatively new and certainly less utilized in the realm of computer networking when compared with the unicast architecture. A simple analogy clearly distinguishes multicast from unicast networking: multicast is to radio as unicast is to telephone. A unicast network, as its name implies, connects a single computer to another computer. Such is the nature of TCP, arguably the best-known internet protocol, which is a connection-oriented transport protocol for establishing network communication between only two machines. Multicast connections, on the contrary, allow a server to stream data from a given IP address, and any clients that wish to listen to the broadcast IP packets may do so. Typically multicast software relies on a protocol known as UDP rather than on TCP, as UDP does not perform handshaking nor allow the client any flow control (7). That



is, the server simply streams the UDP data, and if the client cannot process the data as fast as the server sends it, or if the client detects that packets were lost in transit, the client has no recourse.

The choice of a multicast architecture is more than an exercise in obscure network programming; rather, the choice of multicast over unicast enables a highly scalable architecture. A unicast server would generate network traffic in direct proportionality to the number of clients requesting data. A multicast server generates a constant amount of network traffic, irrespective of the quantity of clients.

### **4.2.3 Server security**

Because the software that controls data acquisition is HTML-based and the server is online, the software must enforce a simple security check that prevents malicious or unwitting users from tampering with the lab acquisition processes from a remote computer. A CGI script verifies that the IP address generating data acquisition begin and end operations is that of the server itself, meaning that only users physically accessing the data acquisition server in the mouse facilities may control data acquisition.

Another layer of security is included for archived data. The data should be accessible to off-site collaborators under controlled circumstances. Using Apache Web Server's secure HTML access control feature, the software requires a username and password for access to mouse records and data.

## **4.3 Client remote real-time monitoring software**

The server continuously streams (via multicast) real-time one-lead ECG data for each mouse to its network interface. Client software monitors this streaming data and provides real-time plots of the ECG. For the same reason that the server multicast software employs Perl, so does the client software: Perl provides extensive and well-tested socket programming modules. The graphical user interface (GUI) aspect of the software employs Perl/Tk, a



specialized Perl module for incorporating graphics into a Perl script. The client software displays a layered ECG strip that may show ECG data from either a static WFDB-formatted file or from one of the available 16 network data streams.

## 4.4 Client retrospective interactive data mining software

A data analyst or clinician is primarily interested in visualization and annotation of data sets. A data analyst will have a different user experience from a technician because an analyst may work remotely from any computer via the Internet. Consequently the clinician will not have a sense that a system is tied to a specific laboratory (as a lab technician will). In fact the data archiving software is intended to integrate disparate data sources and sites seamlessly.

The data analyst interacts with data on the Internet via a Java applet. The intention of the applet is to provide a point-and-click environment in which the user may perform interactive data mining. The user must first access the appropriate web page associated with the server. (Such a web page should be placed in a secure directory to prevent all Internet users from viewing data.) Depending upon the security precautions necessary, a system administrator may wish to ensure that the data channel is encrypted via SHTTP or an alternative means. When the user has logged into the appropriate web page, he/she will see the Java applet.

### 4.4.1 Record search and load

The *Search* tab of the applet allows the user to peruse records. Using the up/down arrow or a single mouse click to highlight a record triggers a CGI request to the server for the SQL database information associated with the record, which is displayed in the panel to the right of the record selection column. Upon finding the record of interest the user must click the *Load Record* button in order to trigger a CGI request that begins loading appropriate data

from the server to the applet.

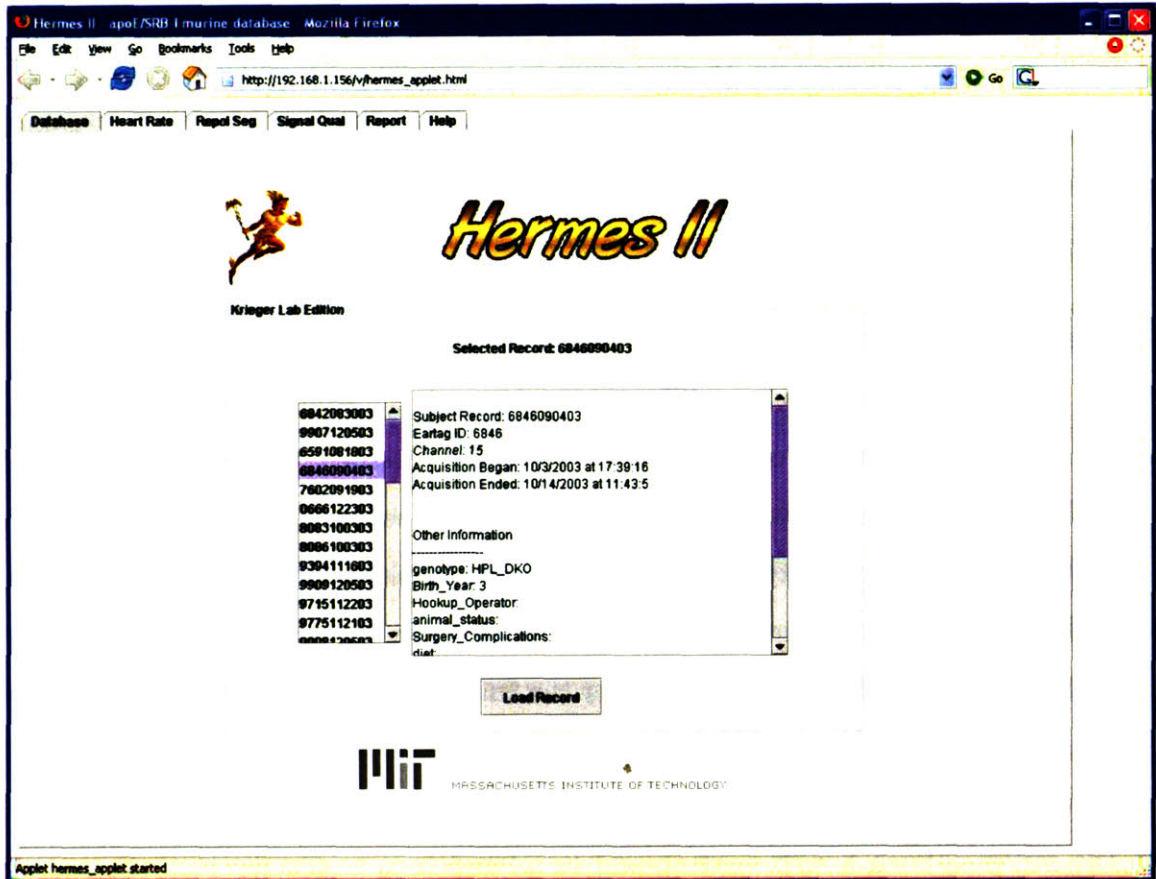


Figure 4-7: The applet panel shows the available records in the database. The user selects a record and clicks the *Load Record* button to pull buffered data from the server.

#### 4.4.2 Interactive data mining

The applet operates on an interactive data mining paradigm. The idea is to provide the user with very powerful trend information and - with a point-and-click approach - permit the user to hone in on details of interest. Interactive data mining can take two forms: temporal or statistical. These two methodologies are described in the below sections.

## Temporal navigation

The screenshot in figure 4-8 shows the applet immediately after a record has been loaded. Note that the tab labeled *Heart Rate* is highlighted. The top-left panel shows a long heart rate time-series. The x-axis is labeled with the day number (number of days elapsed recording time<sup>4</sup>) and the light/dark cycles for the laboratory are shaded (known a priori because the lab uses controlled light settings). Each pixel in the top-left plot corresponds to ten minutes of averaged heart rate data. The middle panel shows a 20Hz tachogram (instantaneous heart rate plot) comprising the point in time of the active pixel in the top-left panel (denoted by a vertical bar). Upon loading a record the left-most pixel in both the middle and top time-series panels are active, as indicated by the vertical bars at these points. Clicking at a time point of interest on the top-left plot loads the appropriate instantaneous heart rate time series into the middle panel. The lower panel loads with the raw ECG waveform corresponding to the active time. Clicking on the middle panel time series advances the lower panel waveform to the corresponding point in time.

The browse buttons in the lower left of the applet window permit the user to move forward and backward through the data. There are four browse buttons: the top two permit left and right navigation by one full screen: that is, the right-most time point in the bottom panel becomes the left-most point on the screen for a click on the right button, and conversely for the left button. The bottom two browse buttons permit left and right navigation by one half screen: that is, the middle time point in the bottom panel becomes the left-most point on the screen for a click on the right button, and conversely for the left button.

The zoom buttons in the middle-bottom portion of the applet permit x- and y-axis zoom in and out.

## Statistical navigation

The top-right window of the heart rate panel shows an RR-interval histogram for each heartbeat in the ten minutes comprising the active time point (as denoted by the vertical

---

<sup>4</sup>a user-configurable option permits change of the x-axis to mouse age rather than elapsed recording time

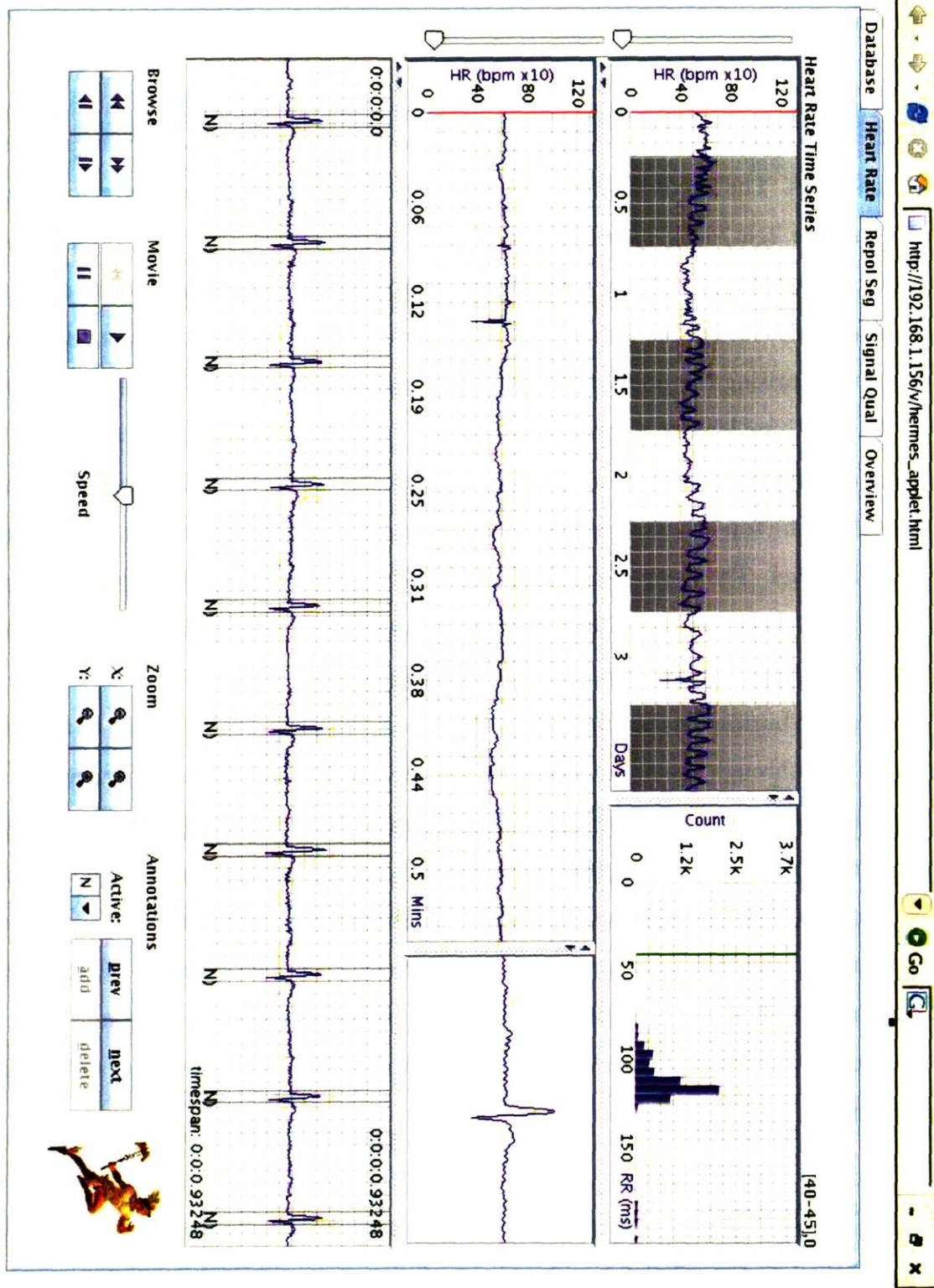


Figure 4-8: The applet screenshot shows a sample mouse record for interactive data mining. The top-most panel represents a long-term heart rate trend plot, where each pixel represents 10 minutes of averaged heart rate data, with light and dark cycles shaded. The middle plot represents the instantaneous heart rate signal comprising the selected point in the top plot (as evidenced by the vertical bar in the top plot). The lower panel displays the ECG waveform at the point in time corresponding to the selected offset in the middle panel (as evidenced by the vertical bar in the middle plot). The upper-right panel shows an RR-histogram that allows the user to select one or more bins of interest to view and annotate outliers with ease.

line in the top-left window of figure 4-8).

Right-clicking<sup>5</sup> within this window brings up a popup menu option allowing the user to set a scan range. Upon selecting the *set scan range* option, the user's movement in the panel will be traced with a magenta vertical bar. Left-clicking once will set one boundary of the scan range. As the user moves the mouse with one scan range set, the area above the selected scan range will turn red. Left-clicking again sets the scan range per the highlighted red region.

Once the scan range has been set, a user may navigate the selected beats represented by the highlighted bins in the histogram by clicking on the *next* and *previous* buttons in the *Annotations* bounding box at the lower-right corner of the applet. The scan moves from the lowest highlighted bin in the histogram to the highest, so that *next* means move to the next beat within this bin or to the next highest bin in the scan region if there are no more beats in this bin. The *previous* button works conversely.

In order to restore normal functionality to the browse buttons and other features of the applet, the user must right click within the histogram window and select *Cancel Scan*. Upon cancellation of the scan the red highlighted region in the histogram will disappear.

### 4.4.3 Virtual streaming

The *Movie* bounding box in the lower-left of the applet permits a user to begin viewing a virtual data stream. The *play* button, at the top-right of the *Movie* bounding box, begins the stream and either the *pause* or *stop* buttons (lower left and lower right, respectively) stop the stream. The speed of the stream is controlled by the speed sidebar immediately to the right of the buttons.

Because the virtual stream is actually performing sequential server accesses as though the user were clicking the browser button in rapid succession, the exact speed at which the data renders depends upon network conditions (just as the speed with which Google loads

---

<sup>5</sup>MAC computers may not have a mouse with left and right buttons. While the software can be modified with ease to accommodate MAC users without multi-button mice, we have not yet established MAC users' preferred method for emulating left and right clicks.

into your browser depends upon network conditions).

#### 4.4.4 Annotating data

The point of interactive data mining is not just viewing data of interest but, when necessary, annotating it as well. For example, the QRS detector that preprocessed the ECG data may have falsely detected some high frequency noise as QRS complexes. Alternatively it may be that the QRS detector is not in error at all; perhaps it accurately detected premature contractions. One does not know until he/she views the underlying data after selecting the appropriate time point (in time series navigation) or histogram bin (in statistical navigation). This methodology is precisely the essence of interactive data mining.

If the user determines the QRS detector was incorrect and the annotations should be deleted, he/she may do so by clicking on the *delete* button in the *Annotations* bounding box (or using  $\langle \text{Alt} - d \rangle$  on the keyboard). By then clicking on the appropriate annotation it will be deleted immediately, not only on the user's screen but also in the server's annotation file.

If the user wishes to add an annotation he/she should select the desired annotation from the drop down list in the *Annotations* bounding box. The annotation meanings, as also used on Physionet's WAVE software (<http://www.physionet.org>), are:

<b>WFDB Annotations</b>			
<i>Symbol</i>	<i>Meaning</i>	<i>Symbol</i>	<i>Meaning</i>
.	(Deleted Annotation)	t	T wave peak
N	Normal Beat	+	Rhythm Change
L	Left bundle branch block beat	u	U wave peak
R	Right bundle branch block beat	?	Beat not classified during learning
a	Aberrated atrial premature beat	!	Ventricular flutter wave
V	Premature ventricular contraction	L	Start of ventricular flutter/fibrillation
F	Fusion of ventricular and normal beat	J	End of ventricular flutter/fibrillation
E	Ventricular escape beat	x	Non-conducted P wave
j	Nodal (junctional) escape beat	f	Fusion of paced and normal beat
/	Paced beat	(	Waveform onset
Q	Unclassifiable beat	)	Waveform end
	Change in signal quality	r	R-on-T premature ventric. contract.
[15]	(Unassigned annotation type)	[42]	(Unassigned annotation type)
—	Isolated QRS-like artifact	[43]	(Unassigned annotation type)
[17]	(Unassigned annotation type)	[44]	(Unassigned annotation type)
s	ST segment change	[45]	(Unassigned annotation type)
T	T wave change	[46]	(Unassigned annotation type)
*	Systole	[47]	(Unassigned annotation type)
D	Diastole	[48]	(Unassigned annotation type)
“	Comment annotation	[49]	(Unassigned annotation type)
=	Measurement annotation	:	(Index mark)
p	P wave peak	i	(Start of analysis)
B	Bundle branch block (unspecified)	ı	(End of analysis)
shift-6	(Non-captured) pacemaker artifact	;	(Reference mark)

Table 4.1: WFDB Annotations

THIS PAGE INTENTIONALLY LEFT BLANK



# Chapter 5

## The Chebyshev transform

Chapter 2 explores the electrophysiology of the murine ECG, drawing specific attention to the repolarization segment. Analogous to the ST segment in human ECG, the repolarization segment morphology in the dKO mouse shows elevation and depression that are likely manifestations of ischemia or injury. Repolarization segment analysis provides the best opportunity for automated assessment of the dKO cardiovascular condition as influenced by hypercholesterolemia (a by-product of the dKO genetic engineering model), and as such it is the crux of this thesis. In this chapter we motivate use of the Chebyshev transform of the repolarization segment as a means of recognizing the general shape of the segment. Professor Franc Jager<sup>1</sup> first suggested the use of Chebyshev polynomials as a pattern recognition tool for repolarization segment morphology analysis.

### 5.1 Established approaches in human ECG analysis

Automated ST segment episode algorithms for human ECG are tested against one of several accepted gold standard databases<sup>2</sup>. Murine ECG has no such precedent by which to quantify algorithm performance. Nonetheless a reasonable starting point for automated assessment of

---

<sup>1</sup>Professor Franc Jager's doctoral thesis [23] is an excellent reference on techniques for ST segment analysis in human ECG. Other publications of his ([20],[25]) also warrant review.

<sup>2</sup>The European Society for Cardiology Database and the Long-Term ST Database are both available on Physionet - [www.physionet.org](http://www.physionet.org)

morphology deviations in mice comes from an investigation of algorithms applied to human ECG.

### 5.1.1 Time domain: the ST deviation function

Time domain ST-segment algorithms provide a very intuitive but quantifiable description of the ST segment. For the sake of simplicity we describe the time domain approach with the assumption that we have an extremely clean signal, devoid of arrhythmia, baseline drift or motion artifact. Clearly these assumptions cannot hold in an algorithm implementation, but for now we focus only on the methodology.

Figures 5-1 and 5-2 show sample human ECG strips with the isoelectric point marked. The isoelectric point, as detailed in chapter 2, represents a time at which the heart is electrically “silent.” Consequently it is the reference point against which an ST voltage deviation should be measured. In the absence of injury currents, the ST segment should also be electrically “silent.”<sup>3</sup> When injury current is present, however, the ST segment is non-isoelectric; the ST segment is above (elevation) or below (depression) the isoelectric voltage. As a simple approximation one might imagine that an ST deviation could be detected by measuring the offset of a specified point in the ST segment relative to the isoelectric voltage value. A time series of such a measurement, in fact, provides the basis for the ST deviation function. An ST deviation function in practice requires either manual annotation of a reference voltage or an adaptive algorithm to correct automatically for deviations that are chronic, but in its simplest form the ST deviation function is the voltage at a fixed point in time from a fiducial point relative to the isoelectric voltage [23].

A time-domain approach proves to be inappropriate in the assessment of dKO repolarization segment deviations. One contributing factor to the failure of time-domain approaches in dKO mice is their extremely high heart rate variability; bradycardic episodes in dKO subjects frequently produce heart rates of 150 beats per minute or slower. Since the repolarization segment duration varies with the RR interval (as discussed in chapter 2), one

---

<sup>3</sup>In the interest of simplicity we attribute an ST deviation to injury currents. In reality axis shifts can cause benign ST segment deviations.

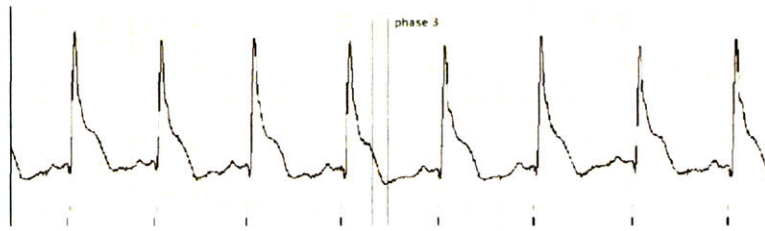


Figure 5-1: ST segment elevation in human ECG. (time scale: 40 ms/div). The isoelectric point and R peak + 80ms points are labeled. The voltage difference between the isoelectric point and R-peak + 80ms represents the ST deviation value.

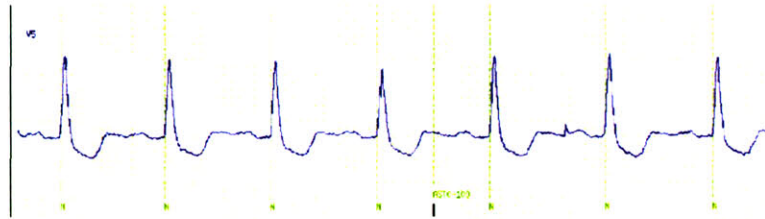


Figure 5-2: ST segment depression in human ECG. (time scale: 40 ms/div). The isoelectric point and R peak + 80ms points are labeled. The voltage difference between the isoelectric point and R-peak + 80ms represents the ST deviation value

cannot choose a fixed time value from a fiducial point as an appropriate point at which to measure deviation. Equally as confounding is the high morphological variability in murine repolarization segment morphologies, examples of which are shown in Appendix A. Even a heart rate-corrected offset for deviation measurement can fail to capture what the human eye would discern as a distinct deviation.

Given the shortcomings in time-domain approaches applied to murine ECG, we consider a more robust measurement that looks at the entire repolarization segment shape. Again in the interest of understanding comparable predicate technologies already used in human ECG, we look at an ST-segment shape categorization algorithm based on statistical analysis of the entire ST segment of human ECG.

### 5.1.2 The Karhunen-Loeve (K-L) transform

The K-L Transform calculates orthogonal basis functions using training data instead of a polynomial determined a priori. The K-L transform has been used successfully in human ECG beat classification and ST-segment detection [23, 24] and therefore represents a logi-

cal technique to apply to mouse ECG. Given a set of time series vectors  $\mathbf{x}_0, \mathbf{x}_1, \dots, \mathbf{x}_n$  each consisting of discrete-time repolarization segment amplitude values, we define the covariance matrix  $\mathbf{C} = E\bar{\mathbf{x}}\bar{\mathbf{x}}'$ , where  $\bar{\mathbf{x}}$  is the mean pattern vector from  $\mathbf{x}_0, \mathbf{x}_1, \dots, \mathbf{x}_n$ . The eigenvectors of the covariance matrix  $\mathbf{C}$  can be shown to form an orthogonal basis set. The corresponding eigenvalues,  $\lambda_n$ , are sorted in descending order and the first 5 [23] are chosen to represent a reasonable approximation of  $\bar{\mathbf{x}}$ <sup>4</sup>. Any given repolarization segment from a new repolarization time series vector  $\mathbf{y}$  can be projected onto the eigenvectors determined from the training set mean pattern vector. A reasonable reconstruction of  $\mathbf{y}$  presumably then comes from a linear combination of the eigenvectors, each weighted according to its projection (dot product) from  $\mathbf{y}$ .

The motivation for use of the K-L transform is feature reduction. The rank-order of a given eigenvalue determines the corresponding eigenvalue's relative contribution to the mean vector information content, and it is for this reason that the eigenvectors from the highest-valued eigenvalues are preserved and lower-valued eigenvectors discarded as an approximation to the mean vector (in the case of training data, as in  $\bar{\mathbf{x}}$  above) or the input vector (in the case of new input data, as in  $\mathbf{y}$  above).

### **Classification using the K-L transform: distance metrics**

If we are interested in identification of abnormal morphology, then we allow  $\mathbf{x}$  to represent a window of  $n$  averaged repolarization segments, creating a K-L eigenspace based on typical samples for the most recent window of time from eigenvectors of the covariance matrix of  $\mathbf{x}$ . Using a sliding window approach that dynamically updates the K-L eigenvectors and corresponding eigenvalues, and calculating the K-L coefficients for each *individual* repolarization segment 'on-the-fly,' we can compare the K-L composition of the individual segment to that of the most recent  $n$  averaged beats' composite segment to determine whether the beat is substantially different from previous ones [24]. As a metric for quantifying *how dif-*

---

<sup>4</sup>Determination of the number of K-L coefficients to use in classifying a beat is intuitively similar to the logic used in determining how many Fourier coefficients to use in a spectral approximation of a signal, following an argument along Parseval's Theorem

ferent a beat is from the average beat we may use a Euclidean distance measure between the instantaneous beat and average beat vectors in  $n$ -space, where  $n$  is the dimensionality of the eigenspace. More specifically, the average beat vector in  $n$ -space takes the form of a centroid, a point mass placed at the  $n$ -dimensional mean. If the average beat is comprised of eigenvectors with mean values  $x_0, x_1, \dots, x_n$  then the Euclidean distance metric quantifying the difference between a beat with eigenvalues  $y_0, y_1, \dots, y_n$  is calculated as  $\sqrt{(x_0 - y_0)^2 + (x_1 - y_1)^2 + \dots + (x_n - y_n)^2}$ .

Consideration of the Euclidean distance metric reveals a potential weakness. Consider, for example, the 2-d centroid at  $[x_0, x_1]$ . If  $x_0$  comes from a distribution with standard deviation  $\sigma = 1$ , while  $x_1$  comes from a distribution with standard deviation  $5\sigma = 5$ , a point at  $[y_0, y_1] = [x_0 + 5, x_1 + 5]$  will treat a distance of 5 in one dimension with equal weight as a distance of 5 in the other. Such a treatment would fail to account for the fact that the vector differs by one standard deviation in one dimension but by five standard deviations in the other. A simple modification of Euclidean distance might normalize each dimension's distance by that dimension's standard deviation, creating a modified distance metric of  $\sqrt{\left(\frac{x_0 - y_0}{\sigma_0}\right)^2 + \left(\frac{x_1 - y_1}{\sigma_1}\right)^2 + \dots + \left(\frac{x_n - y_n}{\sigma_n}\right)^2}$ .

A yet more robust approach in assessing the distance of a vector from a centroid could account for correlations among dimensions in the joint distributions generating the centroid. Consider the scatter plot in figure 5-3, for example, a case in which  $x$  and  $y$  are positively correlated. Consider now two points:  $A = [0.5, 1.5]$  and  $B = [1.5, 1.5]$ . From the centroid at  $[1, 1]$ , the Euclidean distance of each point is  $\sqrt{0.5}$ . However, since  $x$  and  $y$  are correlated positively with a correlation coefficient of approximately 1, the point  $[0.5, 1.5]$  seems 'further' from the centroid.

If we derive a parametric statistical model, i.e. a 2-d Gaussian distribution, of  $x$  and  $y$  from the scatter plot, it becomes clear that  $[0.5, 1.5]$  represents a lower probability event than does  $[1.5, 1.5]$ . The *Mahalanobis distance*, determined from principal component analysis (PCA) of the data, appropriately accounts for this phenomenon by generating eigenvectors along axes of maximum variance. In figure 5-3 a linear regression line  $z$  (the primary

*principal component*), and its orthogonal (secondary principal component) vector are shown. The Mahalanobis distance from a centroid accounts for the standard deviations of different dimensions as well as correlations among dimensions, effectively calculating distance relative to PCA-derived eigenvectors that are scaled based on variance. The Mahalanobis distance metric is useful for data with correlation and differences in standard deviations among components. The Euclidean distance metric is equal to the Euclidean distance (within a scale factor) only if there is neither correlation among components nor a difference in standard deviations.

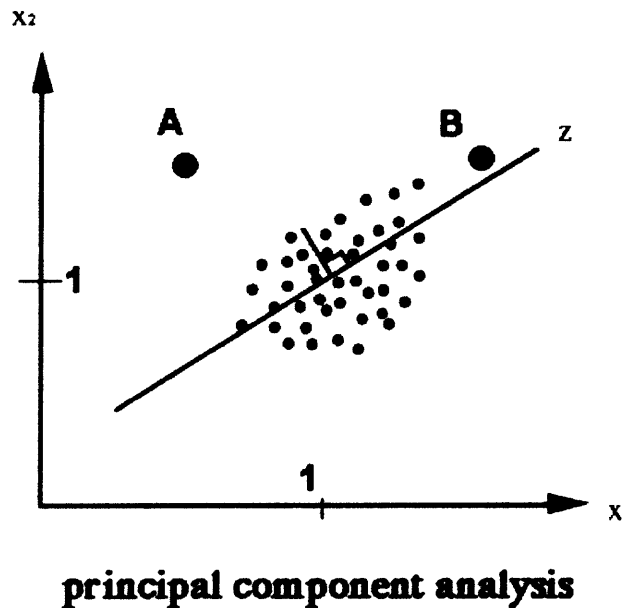


Figure 5-3: The principal components of the 2-d data set are determined along axes of maximum variance. In the 2-d case, the primary principal component is the linear regression line and the secondary principal component is a vector perpendicular to the primary component. The Mahalanobis distance metric, uses as a basis set principal component vectors that are scaled based on variance in the dimensions and correlation among dimensions.

## 5.2 A new approach: the Chebyshev transform

Insight from Professor Franc Jager leads us to investigate an alternative to the K-L transform. The ST segment in humans, and the repolarization segment in mice, seem almost entirely described by an offset, a slope, and a curvature. The naked eye interprets these characteristics

quite well, and a means of quantifying these parameters seems an appropriate method of automating the task of morphology recognition. Three Chebyshev polynomials are described independently by offset (Chebyshev polynomial 0), slope (Chebyshev polynomial 1), and curvature (Chebyshev polynomial 2). A linear combination of these polynomials can very nearly emulate ST segment (or murine repolarization segment) morphology. Moving from a time series segment to its constituent Chebyshev coefficients, or Chebyshev decomposition, is possible through equation 5.10.

### 5.3 Sturm-Liouville origins

A field of mathematics called Sturm-Liouville theory reveals a generalized Fourier analysis that permits time-domain eigenfunctions  $\phi_n(t)$  to form a “complete set,” meaning that any piecewise smooth function  $f(x)$  can be represented by a generalized Fourier series of the eigenfunctions [12]:

$$f(x) = \sum_{n=1}^{\infty} a_n \phi_n(x) \quad (5.1)$$

The eigenfunctions of any regular Sturm-Liouville eigenvalue problem will always be orthogonal, and the orthogonality relationship is defined by the equation:

$$\int_a^b \phi_n(t) \phi_m(t) \sigma(t) dt = 0, n \neq m \quad (5.2)$$

Here  $\sigma(t)$  is the possibly variable coefficient that multiplies the eigenvalue  $\lambda$  in the differential equation defining the eigenvalue problem. In the case of Fourier sine series, the defining differential equation is

$$\phi''(t) + \lambda \phi = 0 \quad (5.3)$$

A comparison with the form of the general Sturm-Liouville orthogonality relation of Equation 5.2 shows that  $\sigma(t) = 1$  and the familiar resulting orthogonality condition for

Fourier sine series results:

$$\int_0^L \sin\left(\frac{n\pi t}{L}\right) \sin\left(\frac{m\pi t}{L}\right) dt = 0, n \neq m \quad (5.4)$$

In the Sturm-Liouville boundary value problem there is a special case called Chebyshev's differential equation that leads to *two sets* of basis eigenfunctions,  $n$  such that we speak of Chebyshev polynomials of "the first kind" and "second kind" [21]. Chebyshev polynomials of the first kind are defined as

$$T_n(t) = \frac{n}{2} \sum_{k=0}^{n/2} (-1)^k \frac{(n-k-1)!}{k!(n-2k)!} (2t)^{n-2k} \quad (5.5)$$

Chebyshev polynomials  $T_n(t)$ ,  $n=0,1,2,3,\dots$ , form a complete orthogonal set on the interval  $-1 \leq t \leq 1$  with respect to the weighting function  $\frac{1}{\sqrt{1-t^2}}$ . That is,  $\sigma(t) = \frac{1}{\sqrt{1-t^2}}$  in Equation 5.2 for Chebyshev polynomials of the first kind. Figure 5-4 shows Chebyshev polynomials of the first kind.

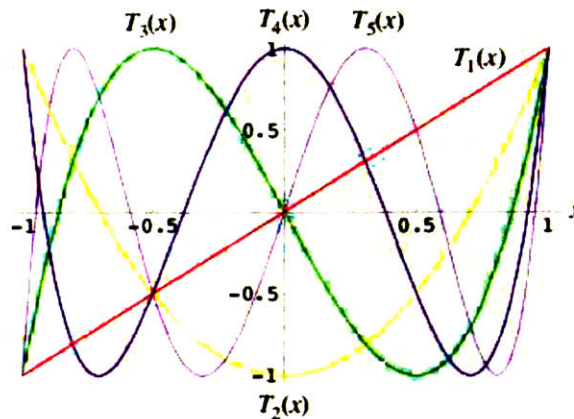


Figure 5-4: Chebyshev polynomials of the first kind.

Chebyshev polynomials of the second kind are defined as

$$U_n(t) = \sum_{k=0}^{n/2} (-1)^k \frac{(n-k)!}{k!(n-2k)!} (2t)^{n-2k} \quad (5.6)$$

Chebyshev polynomials  $U_n(t)$ ,  $n=0,1,2,3,\dots$ , form a complete orthogonal set on the interval



$-1 \leq t \leq 1$  with respect to the same weighting function as used in Chebyshev polynomials of the first kind:  $\frac{1}{\sqrt{(1-t^2)}}$ . Figure 5-5 shows Chebyshev polynomials of the second kind.

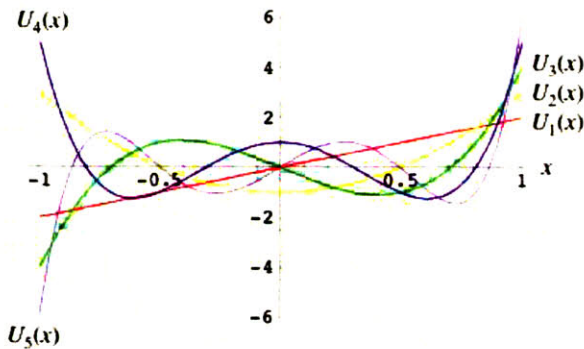


Figure 5-5: Chebyshev polynomials of the second kind.

The Chebyshev transform of interest in this thesis uses Chebyshev polynomials of the first kind, as they more adequately capture the elements of offset, slope, and curvature that comprise most of the energy in a repolarization segment signal. In theory one can sum an infinite number of weighted Chebyshev polynomials to create an arbitrary time series, as equation 5.7 shows.

$$f(x) = \sum_{k=0}^{\infty} c_k T_k(x) \quad (5.7)$$

The choice of Chebyshev polynomials, however, ensures that we nearly match the repolarization segment morphology by summing only three polynomials.

$$f(x) \approx \sum_{k=0}^3 c_k T_k(x) \quad (5.8)$$

The use of the first several polynomials in approximating the underlying waveform is directly analogous to the feature reduction by selecting eigenvectors from the highest rank-ordered eigenvalues in K-L analysis. In the case of Chebyshev analysis, however, the polynomials are selected without training data and without a rank-order procedure; no rank order is needed, as visual inspection makes it clear that offset, slope and curvature - the first three coefficients - carry the majority of signal information for a repolarization segment.

### 5.3.1 Chebyshev decomposition

In section 5.2 we noted that one may sum an infinite number of weighted Chebyshev polynomials to create an arbitrary finite-duration time series, but that most of the signal energy of the repolarization segment could be found in the first three Chebyshev coefficients. We now turn to the question of how the weighting coefficients are determined. That is, given time series  $x(t)$ , how do we determine  $c_j$ ,  $j = 0, 1, 2$  for equation 5.8?

Given the Chebyshev polynomials have a range of  $[-1,1]$ , we must first map the range of the arbitrary finite-duration time series,  $[x_0, x_1]$  to  $[-1,1]$ . For all  $x_0 \leq x \leq x_1$ , the appropriate mapping results from a change-of-variable equation

$$\chi = \frac{x - \frac{1}{2}(x_0 + x_1)}{\frac{1}{2}(x_1 - x_0)} \quad (5.9)$$

With the range of  $x$ , where  $x_0 \leq x \leq x_1$  now mapped to  $\chi$ , where  $-1 \leq \chi \leq 1$ , we compute  $c_j$  ( $j = 1, 2, 3$ ) as

$$c_j = \frac{2}{N} \sum_{k=1}^N f(\chi_k) T_j(\chi_k) \quad (5.10)$$

where  $N = 3$  for  $j = 1, 2, 3$ ;  $T_j(\chi)$  is the  $j^{\text{th}}$  Chebyshev polynomial of the first kind (equation 5.3); and  $x_k = \cos(\frac{\pi(k-\frac{1}{2})}{N})$ .

### 5.3.2 The Chebyshev advantage

Use of Chebyshev polynomials as an orthogonal polynomial set, rather than eigenvectors derived from characteristic ECG training data, is more than a mathematically interesting exercise. By using an orthogonal feature space determined *a priori*, we avoid altogether the need for building a training set upon which repolarization feature detection is based. The use of Chebyshev polynomials instead of K-L derived eigenvectors casts the overall repolarization feature detection problem as an unsupervised algorithm<sup>5</sup>. As the next chapter will discuss,

---

<sup>5</sup>In the field of machine learning, *supervised* and *unsupervised* have a specific meaning. Unsupervised algorithms have no feature or classification foundation based on knowledge derived from sample data, while supervised algorithms fit a model description between input and output based on use of training data

use of Euclidean distance from the origin in Chebyshev space maintains avoidance of training data - and in so doing maintains an unsupervised approach - while providing a very useful metric by which to recognize repolarization segment morphology changes.

## 5.4 Summary

Chapter 2 examines the electrophysiological differences leading to differences between human and mouse ECG signatures. In spite of the inter-species differences, the existence of a repolarization segment elevation or depression in mouse ECG, as in humans, is a useful indicator of ischemia. This chapter examines techniques used in assessment of human ST-segment, concluding that a time-domain deviation measurement is less robust than a full segment analysis. Insight into the K-L transform, using a supervised feature space from stochastically-derived vectors, gives rise to a simpler approach: the Chebyshev transform. Chebyshev polynomials are known from Sturm-Liouville theory to be orthogonal. The first three Chebyshev polynomials of the first kind, quantifying offset, slope and curvature, quantify the most important shape features of the repolarization segment.

In the following chapter we explore in greater detail exactly how Chebyshev decomposition fits into a larger algorithm structure that performs pre-processing to remove noise and post-processing to quantify anomalous repolarization segment morphologies. Though the post-processing procedure provides a quantitative output, no performance metrics can be calculated since the database is not annotated<sup>6</sup>.

---

<sup>6</sup>Algorithm performance requires a gold standard database that has been annotated by humans; the algorithm's performance in detecting and/or classifying events is then compared against that of the expert annotators

THIS PAGE INTENTIONALLY LEFT BLANK

# Chapter 6

## Automated analysis of repolarization segment morphology

Repolarization segment analysis provides the best opportunity for automated assessment of the dKO cardiovascular condition, and as such it is the crux of this thesis. In this chapter we build upon last chapter's description of Chebyshev decomposition, integrating the Chebyshev transform into a larger signal processing algorithm that performs pre- and post-processing of the ECG waveform.

### 6.0.1 Pre-processing

ECG waveforms invariably contain noise. Sources of noise include motion artifact, which can result from subject locomotion, breathing, feeding and scratching. Motion artifact creates high-frequency noise, often with such high amplitude that noise spikes are falsely detected as QRS complexes by beat detection software; or low-frequency baseline drift, for which the human eye and mind can easily account in assessing repolarization morphology but automated algorithms cannot. Additional sources of noise include power mains noise<sup>1</sup> and, to a lesser extent, spurious or ambient electromagnetic noise. Pre-processing of the waveform seeks to remove these various noises to the extent possible.

---

<sup>1</sup>Mains noise is 60 Hz in the US, 50 Hz in most European countries

## Consensus annotation and the signal quality index (SQI)

QRS detection in mouse ECG is quite similar to that in human ECG; inter-species QRS morphology, much more so than inter-species repolarization segment morphology, is quite similar. However, one may not glibly apply a human QRS detection algorithm to mouse ECG since the resting mouse heart rate of 600 beats per minute far exceeds even a tachyarrhythmic human heart rate. Given the fact that morphologies are similar but time scales are different by approximately an order of magnitude, we simply adjust the sampling frequency parameter of mouse ECG files by an order of magnitude so that a rate of 600 beats per minute maps to 60 beats per minute. We then apply *wqrs*<sup>2</sup> to create an annotation output file including QRS onset and j-point timestamps.

While *wqrs* performs well in the absence of noise, it generates a substantial number of false positive detections in the presence of high-frequency noise. Mice move and scratch extremely quickly, generating frequent bursts of high-frequency noise. To mitigate false positive detections we perform *consensus annotation* using *wqrs* and a second, less sensitive QRS detector<sup>3</sup>. The consensus annotation algorithm works as follows: if both QRS detectors detect a beat at a given point in time, the beat is recorded in the output annotation file; if one detector detects a beat that the other does not, the beat is not recorded in the annotation file. The resulting beat detector has a sensitivity less than or equal to the less sensitive of *wqrs* and the EP Ltd. algorithm.

One could argue that the consensus annotation process is unnecessarily complex given that the EP Ltd. software is far less sensitive than *wqrs*; the output annotator very nearly resembles that produced by the EP Ltd. beat detector. Were we only interested in the output annotation file, we could indeed simply dispense with *wqrs* as a beat detector and use EP Ltd. instead to achieve comparable performance to the consensus algorithm. However, the existence of two different perspectives provided by *wqrs* and the EP Ltd. beat detector provides an important piece of information about the signal. When both detectors consistently detect beats at the same points in time, the signal is presumably relatively noise

---

<sup>2</sup>a QRS detector designed by Dr. Wei Zong - available on Physionet ([www.physionet.org](http://www.physionet.org))

<sup>3</sup>Designed by Pat Hamilton and freely available from EP Limited - [www.eplimited.com](http://www.eplimited.com)

free. The extent to which the beat detectors disagree reflects the extent of noise in the ECG. With this realization in mind, we use consensus annotation not just as a means of robust beat detection; we also use it to derive a metric describing the degree of noise. The signal quality index, or SQI, is a sliding-window ratio of consensus beats to total beats (consensus and non-consensus). The index can range between 0 and 1 in an increment that depends on the window size. We use a window size of 10, which means the SQI can take on values of 0 to 1 in 0.1 value increments. The resulting SQI annotation file is an unevenly-sampled time series that is ultimately linearly interpolated to create an evenly-sampled SQI time series. Appendix B shows the signal quality index time series for each record in the mouse database.

The signal quality index provides a 'faith' metric to a database annotator. That is, if a repolarization morphology metric indicates that the repolarization segment is drastically elevated, a low signal quality metric at the same time point likely indicates the morphology metric is processing noisy data and producing unreliable results. Consider, for example, figures 6-1 and 6-2 below.

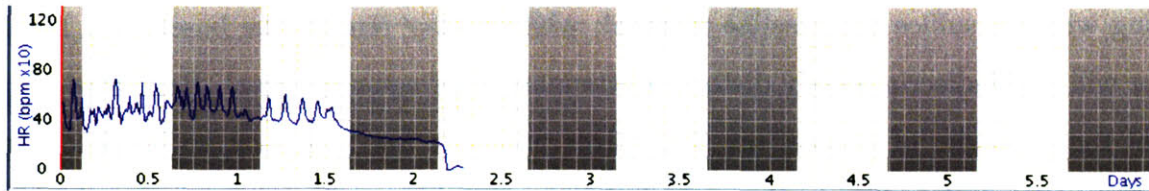


Figure 6-1: Repolarization morphology metric time series. A deviation from the baseline is intended to reflect an underlying abnormal morphology. Toward the end of recording - shortly after the onset of the third light cycle (unshaded region) - a dramatic dip in the repolarization metric indicates a possible change in morphology. [Record 7602091903]

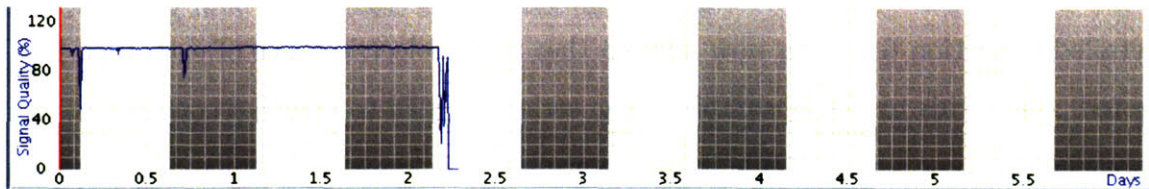


Figure 6-2: The signal quality at the same point in time (approximately 2.2 days of recording) indicates that interpretation of repolarization segment morphology from the repolarization morphology metric time series is likely to be unreliable.



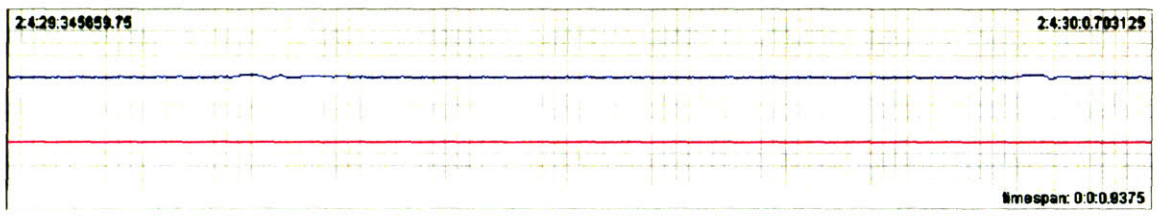


Figure 6-3: Inspection of the waveform confirms that the signal quality is extremely poor (in this case the subject is apparently dead).

## Baseline subtraction

Baseline drift is a low-frequency noise that presents little or no challenge to a human interpreting ECG. However, baseline drift can be a source of substantial error to a repolarization segment algorithm. Contrast, for example, two QRS complexes with an RR interval of 10ms resting on a line of zero slope with the same QRS complexes (also with 10ms RR interval) resting on a line of unit slope. A repolarization segment algorithm must reference the segment's elevation with respect to a *single* isoelectric value, which is trivially understood on the zero-slope line but less-easily understood on the sloped line. Frequency-domain filtering will not suffice for baseline removal; while it may remove the baseline, a high-pass filter will also indiscriminately distort or attenuate low-frequency signal. Repolarization segment morphologies of interest are themselves primarily low-frequency, so baseline removal via frequency-domain filtering is particularly unacceptable as a pre-processing method before repolarization segment analysis.

A frequently-used method for removing low frequency drift is baseline subtraction via a cubic spline. In this process, an unevenly-sampled time series is created where each sample is the isoelectric value of a beat. The process for detecting the isoelectric value of a beat is detailed in section 6.0.1; for now assume that the isoelectric value of each beat has been detected. From this unevenly sampled time series we wish to create a continuous, smooth, evenly sampled time series. While linear interpolation achieves continuity, a piecewise-linear function is not smooth in the first derivative or continuous in the second derivative between and across “knot points,” as represented by isoelectric points for our baseline time series.

A cubic spline interpolation formula starts with the same concepts used in linear inter-

polation. Linear interpolation between  $x_i$  and  $x_{i+1}$  with  $y_i = y(x_i)$ ,  $i = 1, 2, 3, \dots, N$  gives the below formulas [4].

$$y = Ay_i + By_{i+1} \quad (6.1)$$

where

$$A = \frac{x_{i+1} - x}{x_{i+1} - x_i} \quad (6.2)$$

and

$$B = 1 - A = \frac{x - x_i}{x_{i+1} - x_i} \quad (6.3)$$

Adding non-zero second derivative terms to the right-hand side of equation 6.1, where we ensure that these terms add zero at  $x_i$  and  $x_{i+1}$ , leads to a cubic interpolation formula of

$$y = Ay_i + By_{i+1} + Cy_i'' + D_{i+1}'' \quad (6.4)$$

where  $A$  and  $B$  are defined in 6.2 and 6.3 and

$$C = \frac{1}{6}(A^3 - A)(x_{i+1} - x_i)^2 \quad (6.5)$$

$$D = \frac{1}{6}(B^3 - B)(x_{i+1} - x_i)^2 \quad (6.6)$$

The resulting first and second derivatives for 6.4 are

$$\frac{dy}{dx} = \frac{y_{i+1} - y}{x_{i+1} - x} - \frac{3A^2 - 1}{6}(x_{i+1} - x_i)y_i'' + \frac{3B^2 - 1}{6}(x_{i+1} - x_i)y_{i+1}'' \quad (6.7)$$

$$\frac{d^2y}{dx^2} = Ay_i'' + B_{i+1}'' \quad (6.8)$$

If we now require that the first derivative, computed from 6.7, be continuous across the

boundary between two intervals, we arrive at the equation

$$\frac{x_i - x_{i-1}}{6} y''_{i-1} + \frac{x_{i+1} - x_{i-1}}{3} y''_i + \frac{x_{i+1} - x_i}{6} y''_{i+1} = \frac{y_{i+1} - y_i}{x_{i+1} - x_j} - \frac{y_j - y_{j-1}}{x_j - x_{j-1}} \quad (6.9)$$

These are N-2 linear equations in the N unknowns  $y''_i$ ,  $i = 1, 2, \dots, N$ . For a unique solution we set  $y''_i$  and  $y''_N$  to zero, which gives the so-called *natural cubic spline* with zero second derivative on its boundaries [4].

Using the isoelectric values obtained per beat, we generate a cubic spline-interpolated signal of the same sampling frequency as the ECG waveform. Computing a point-by-point subtraction creates a baseline-subtracted ECG waveform that is used in subsequent pre-processing steps.

### Beat filtering

Premature beats - and the beat afterward, often following a compensatory pause - represent an instantaneous departure from normal depolarization and repolarization of the heart. Therefore such beats' repolarization segments should not be analyzed. After baseline subtraction of the ECG waveform, a scan checks instantaneous RR interval and instantaneous QRS amplitude compared to a 64-beat trailing average. If a beat's instantaneous RR interval or QRS amplitude differs from the average by 35% or more, it and the following beat are rejected. That is, they are not added to the average beat template<sup>4</sup>, the details of which are discussed in the section 6.0.1 below.

### Beat averaging

All beats that pass the beat filter (6.0.1) are added to a moving-window, first-in, first-out (FIFO) beat template. This template consists of an R-aligned point-by-point average of the most recently accepted 64 beats. The template necessarily undergoes a "ramp-up" period at the beginning of a file; this period occurs as the first 64 beats of the record are processed.

---

<sup>4</sup>Nor is the average heart rate updated to include the RR intervals corresponding to the premature beat and subsequent beat

During the ramp-up period a weighted average of the previous beats and the current beat is calculated to create the new beat average template. That is,

$$\mathbf{avg}_n = \mathbf{beat}_{\text{this}} + \frac{1}{n-1} \mathbf{avg}_{n-1} \quad (6.10)$$

After the template is filled with a 64-deep average, the new average is calculated as the weighted average from removing the oldest beat comprising the average and the inclusion of the newest beat. That is,

$$\mathbf{avg}_n = \frac{\mathbf{beat}_{\text{this}}}{64} - \frac{\mathbf{beat}_{n-64}}{64} + \frac{63}{64} \mathbf{avg}_{n-1} \quad (6.11)$$

### **Violations of stationarity: parallel average beats**

The beat filter (section 6.0.1) for distinguishing which beats will comprise the average beat template (section 6.0.1) assumes a feature stationarity within fixed thresholds. Specifically the filter assumes that a change in QRS amplitude or RR interval greater than 35% is transient. When one or several “beats” (possibly true beats, possibly false positive detections by the QRS detector) are rejected by the filter, the template average beat is not updated.

Consider now the case in which a step change in QRS amplitude occurs. Such a phenomenon occurs fairly frequently in the mouse data, possibly due to an axis shift or a change in contact impedance when the subject scratches an electrode loose. If the step change in amplitude is greater than or equal to 35% of the average amplitude of the template average beat, *all* subsequent beats in the template will be rejected.

To avoid data loss that would otherwise occur from a violation in stationarity, a second average template is updated on a beat-by-beat basis with *no beat filtering pre-processing*. In the event that 5 or more consecutive beats are rejected, the backup template becomes the new active template and the active template is cleared and re-commissioned as the backup template. This process of providing parallel beat average templates, the active one with beat filter pre-processing and the backup without, prevents a step change in waveform morphology from creating a permanent block from the active beat filter.

## Isoelectric point determination

The process of isoelectric point determination is performed twice in pre-processing: first to determine beat-by-beat points to build a spline for baseline subtraction (section 6.0.1), and secondly on the average beat template (section 6.0.1) to determine a reference voltage for repolarization segment analysis (section 6.0.1). Whether the beat is a single beat or an average beat template, the process of isoelectric point determination is the same.

A sequential scan is performed in which the voltage range in a sliding window is calculated for each 1.5 ms interval between the QRS onset and 8 ms preceding the QRS onset. For the first data point of the scan, the range is determined within the time window of 1.5 ms - beginning 1.5 ms before the QRS onset and ending at the QRS onset. The window is consecutively moved backward in single-sample increments until the window onset precedes or equals  $QRS_{onset} - 8ms$ . The midpoint of the window position at which the minimum voltage range occurs, the so-called maximally flat region, is marked as the time stamp of the isoelectric value; the isoelectric value is calculated as the mean voltage within the 1.5 ms window.

### 6.0.2 Applying the transform

With the isoelectric value determined as in section 6.0.1, we perform a Chebyshev decomposition to determine Chebyshev coefficients  $c_k$ ,  $k=0,1,2$  on the repolarization segment of the average beat template. In chapter 2 we defined the repolarization period as beginning at 1 ms after the J-point (as determined by the *wqrs* beat detector, which as indicated in chapter 2 will frequently incorrectly - but with no bad side effect - inaccurately label the *J peak* as the *J point*) and ending at an offset of 40% of the RR interval<sup>5</sup> from the start point. The average beat template is a representative composite of recent beats but it is not the original waveform on which QRS onset and J-point timestamps were annotated. Consequently the J-point of the average beat template is calculated as the average J-point offset from an easily-located fiducial marker - the R-peak. That is, for each beat accepted by the beat filter

---

<sup>5</sup>with a maximum value of 15 ms imposed

discussed in section 6.0.1, the R-peak to J-point interval and instantaneous RR interval are stored, as are an average R-peak to J-point and RR interval.

Using the average beat template as computed in section 6.0.1, the repolarization segment period for this average beat is computed as the R-peak plus the average R-peak to j-point interval plus another 1 ms; the repolarization segment offset is computed as the R-peak plus 40% of the average RR interval. Finally, a Chebyshev decomposition on the average beat - relative to the isoelectric value as determined in section 6.0.1 - provides coefficients  $c_0$ ,  $c_1$  and  $c_2$  corresponding to the weights of the  $0^{th}$ ,  $1^{st}$  and  $2^{nd}$  Chebyshev polynomials comprising the repolarization segment.

The aggregate output of the Chebyshev transform applied to a 64-beat average is an annotation file including timestamps and  $c_0$ ,  $c_1$  and  $c_2$ , which is an unevenly-sampled 3-dimensional time series of Chebyshev coefficients. Additionally written at each beat time stamp is a QRS integral metric, the motivation for which is described in section 6.2.

## 6.1 Post-processing

Our original motivation for using Chebyshev decomposition of the repolarization segment lay in the fact that the first three polynomials correspond to offset (relative to the isoelectric point), slope and curvature, respectively. ECG signal pre-processing and subsequent Chebyshev decomposition of the repolarization segment provide quantitative data that serves as foundation for *interpretation* of the data. Of specific interest is the question of whether, at a given point in time, the Chebyshev decomposition of the average beat indicates normal or abnormal morphology.

### 6.1.1 Typical repolarization segment morphology of healthy mice

A cursory review of human electrophysiology might lead one to expect that - in the absence of axis shifts and noise - a normal ST segment is not offset relative to the isoelectric point, is flat and has no curvature. In Chebyshev terms, a normal ST segment's 3-dimensional

Chebyshev coefficient vector should be close to  $[0,0,0]$ . As chapter 2 shows, the murine repolarization period has a fairly variable morphology, even in healthy mice. A J wave may be present transiently or permanently in a recording. The beginning time point for measurement however - namely 1 ms after the average J-point - was chosen expressly because it should allow the repolarization segment to exclude a J wave. Therefore the origin in Chebyshev space represents a reasonable point from which to measure a given beat's feature vector.

### **6.1.2 Multidimensional visualization as a morphology indicator**

Chebyshev coefficients 0, 1 and 2 correspond to offset (relative to isoelectric voltage), slope and curvature respectively. One can, therefore, mentally map Chebyshev coefficients to a general shape. Appendix F shows a variety of waveform morphologies with corresponding Chebyshev coefficient scatter plots. Interpretation of repolarization morphology features at a given time from such plots is intuitive for a human interpreter, but scatter plots fail to impart the dimension of time. While one can certainly view any given Chebyshev coefficient value as a time series, a more comprehensive metric - one that includes information from all coefficients - seems a more appropriate tool for interpreting morphology deviations.

### **6.1.3 Euclidean distance as a morphology anomaly indicator**

While a Mahalanobis distance metric would account for variance of the different Chebyshev coefficients as well as correlation among dimensions, the calculation of a Mahalanobis distance represents a supervised approach. The very premise of using Chebyshev basis functions instead of derived functions lay in the simplicity of the unsupervised technique; in keeping with a mantra of simplicity we use a Euclidean distance metric rather than a Mahalanobis distance.

The Euclidean vector magnitude from the origin should represent the repolarization segment morphology deviation from normal. Figures 6-4 and 6-5 show long-term repolarization time series from wild-type and dKO mice, respectively. The wild-type mouse shows a consistent low-amplitude vector magnitude, while the dKO mouse shows drastic fluctuations.



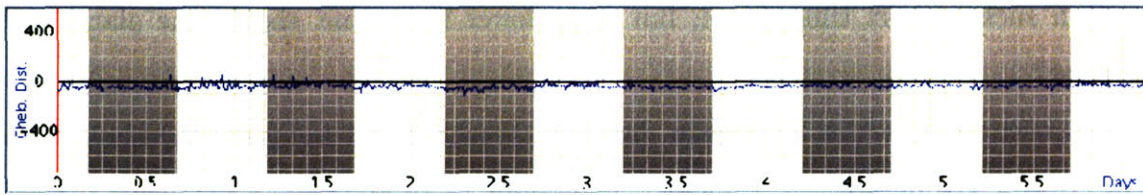


Figure 6-4: 3-d Euclidean vector magnitude (from 3-d Chebyshev feature space) of repolarization segment in wild-type mouse subject 9907120503

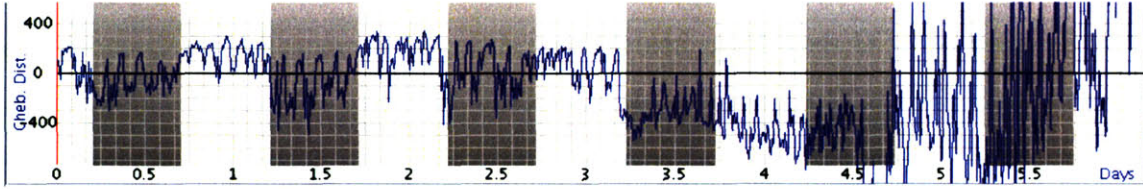


Figure 6-5: 3-d Euclidean vector magnitude (from 3-d Chebyshev feature space) of repolarization segment in dKO mouse subject 2767022103

### Augmenting the Euclidean distance metric: signed distance

Euclidean distance is always a positive value, as it is calculated as the square root of a real, positive number. One might like to see deviations from elevation and depression as positive and negative Euclidean distances, respectively. A sign for the Euclidean distance metric is assigned based simply on the sign of  $c_0$ , the average repolarization segment offset relative to the isoelectric voltage.

## 6.2 A simple morphology deviation alarm

With the Euclidean distance as a measure of morphology deviation from isoelectric, we have a simple value from which we can flag segments of data for further review by an investigator. A natural question, then, is *what threshold delineates normal from abnormal morphology?* Several considerations reveal that a threshold distinction between normal and abnormal morphology provides a reasonable and simple starting point for creating a morphology deviation alarm, but the simplicity comes with inherent limitations. Consider for example, the element of time. Is a momentary breach, say for 2 seconds, of a defined threshold worthy of an alarm? Physiologically we do not expect ischemia to come and

go within such a short time frame, but what lower time limit should the alarm use as a constraint?

The questions of which Euclidean distance threshold and temporal threshold to use as alarm criteria are deceptively difficult. In human ECG analysis, 3 protocols for defining episodes have been defined based on different time-domain ST-deviation function thresholds and temporal thresholds. The design of such protocols requires extensive analysis and expert annotation of ECG data from healthy and diseased subjects. In the absence of formal definitions for mouse ECG that define alarm-worthy episodes, we leave threshold settings to the investigator<sup>6</sup>. Through trial-and-error experimentation to determine an alarm sensitivity level appropriate to his/her research goals, the researcher can learn to tune the alarm individually for different experiments as needed.

Figure 6-6 shows a user selecting elevation and depression thresholds.

Though the morphology deviation thresholds are obviously mandatory parameters in alarm control, in the absence of other information they will be very prone to error. The sources of these errors, as well as user-adjustable controls for mitigating errors from these sources, are discussed in the following sections.

### 6.2.1 Axis shifts

Up to this point we have assumed that all repolarization segment deviations from isoelectric are pathological, but in reality a healthy subject's ECG may show deviations. In human ECG, for example, the ECG of a patient who rolls over in bed may show a transient ST segment change. Such a change in the ST segment is called an axis shift, as the movement of the patient's torso displaces the electrodes relative to the heart's dipole, thereby generating a change in the dipole's projection onto the measurement lead. Looking at only several beats of ECG, one cannot possibly distinguish repolarization segment changes resulting from an axis shift from those resulting from ischemia. However, given proper context, one may reasonably distinguish.

---

<sup>6</sup>The software currently does not allow the time window to be adjusted - any deviation beyond the set threshold is flagged for review

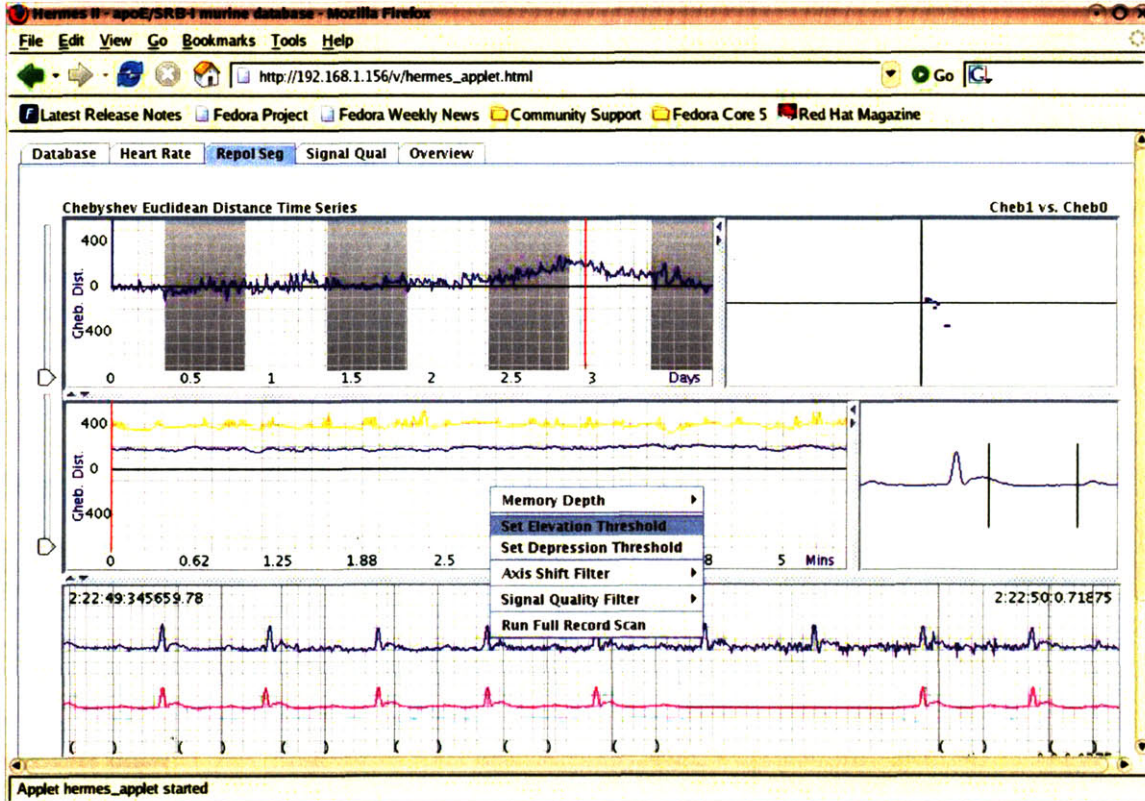


Figure 6-6: User selection of morphology deviation (elevation and depression) thresholds for alarm. A popup menu invoked with a right click on the middle-left panel allows the user to select *Set Elevation Threshold* or *Set Depression Threshold*. Selecting one of these two options creates a magenta horizontal bar on the panel, the location of which is controlled by user mouse movement and the placement of which is set with a left-button click.



Since an axis shift changes the measurement lead relative to the heart dipole, the entire ECG signature is likely to change - not just the repolarization segment. The QRS complex, the most prominent feature of ECG, provides a good indicator of an axis shift. If QRS morphology *and* repolarization segment morphology change together, the cause is quite likely an axis shift resulting from subject movement rather than ischemia. Additionally the onset of an axis shift from subject movement is often much more sudden than that of an ischemia-induced repolarization segment morphology change. Consequently one might use information about the rate of change of morphology as an additional piece of information in distinguishing ischemia from axis shifts. Figures 6-7 and 6-8 show an example of an axis shift. Because the repolarization morphology change occurs so suddenly (less than a minute - between minute 2.5 and 3.5) and a QRS morphology change accompanies the repolarization morphology change, the repolarization segment deviation arises from an axis shift.

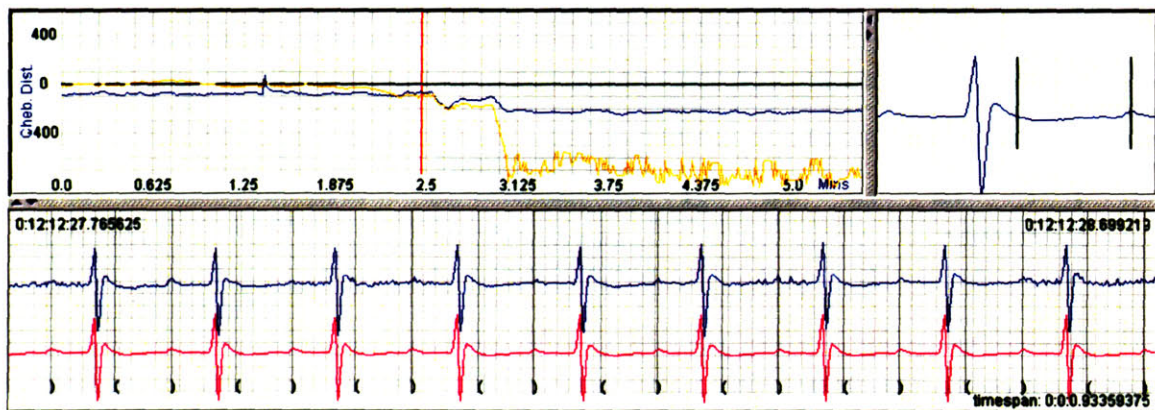


Figure 6-7: The upper-left panel shows the blue repolarization metric time series (signed Euclidean morphology metric, which remains closer to zero after 3.125 minutes than the other signal) and the yellow QRS integral time series (to be discussed in upcoming sections); the upper-right panel shows a 64-beat trailing average beat with repolarization period time markers (vertical bars); the lower panel shows the original ECG waveform time series (upper signal) and the 64-beat trailing average waveform time series. The placement of the vertical bar in the upper-left panel indicates that the waveform data in the other panels corresponds to a point in time before a substantial change in the repolarization metric from approximately -100 at 2.5 minutes to approximately -200 at 3.125 minutes.

While assimilation of a QRS morphology change accompanying a repolarization segment morphology change by visual inspection might be within reach of the human interpreter, an automated process requires less obtuse information. Time series data of the QRS morphology, as shown in figures 6-7 and 6-8, provides an ancillary signal for the alarm that can serve



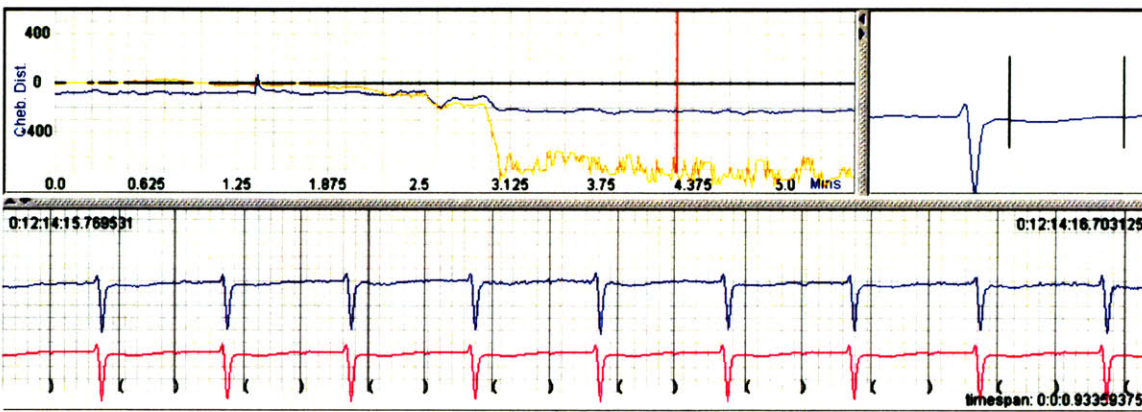


Figure 6-8: The upper-left panel shows the blue repolarization metric time series (signed Euclidean morphology metric, which remains closer to zero after 3.125 minutes than the other signal) and the yellow QRS integral time series (to be discussed in upcoming sections); the upper-right panel shows a 64-beat trailing average beat with repolarization period time markers (vertical bars); the lower panel shows the original ECG waveform time series (upper signal) and the 64-beat trailing average waveform time series. The placement of the vertical bar in the upper-left panel indicates that the waveform data in the other panels corresponds to a point in time after a substantial change in the repolarization metric from approximately -100 at 2.5 minutes to approximately -200 at 3.125 minutes. Inspection of QRS morphology and the rapidity of its change indicate a probable axis shift from subject movement.

to filter out axis shift changes from alarm-worthy ischemic changes. The axis shift alarm filter has three pre-set thresholds allowing the user to select the degree to which the QRS morphology must change in order to be considered an axis shift.

The axis shift algorithm looks 30 seconds to the left and 30 seconds to the right of the time at which the threshold is breached, and if the QRS morphology range during that 1-minute period exceeds a certain value (determined by one of the three user-selectable modes) then the threshold breach is flagged as an axis shift rather than an alarm episode.

Performing axis shift discrimination by tracking QRS morphology is not fail-safe. QRS morphology can change as a result of ischemia and MI. This confounding factor plagues the best of automated human ST-segment algorithms, so it is not one that we can hope to address in the less-structured field of mouse ECG. The admonition one must heed in the use of *any* automated interpretation of mouse ECG features, whether repolarization segment morphology, QRS morphology or beat classification, is well-understood by clinicians working with human ECG: the results of automated data analyses should be reviewed by a human who can determine when an alarm was justified, when it was not, and when an alarm-worthy

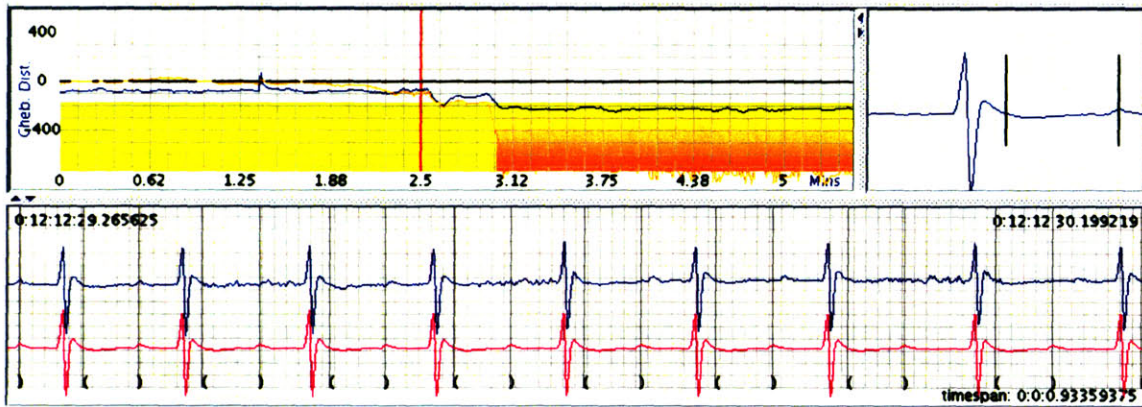


Figure 6-9: Automated axis shift detection example - before the axis shift. The vertical bar in the upper-left panel indicates the current time point of ECG data displayed in the lower panel. The blue line (Euclidean Chebyshev morphology metric) has not yet dropped below the threshold. The slight discolorations below the morphology time series line at points that the repolarization metric drops below the threshold are color codes indicating an axis shift was detected. In the event that the deviations below the line had not been determined to be axis shifts, a very dark discoloration would appear - as in figure 6-11

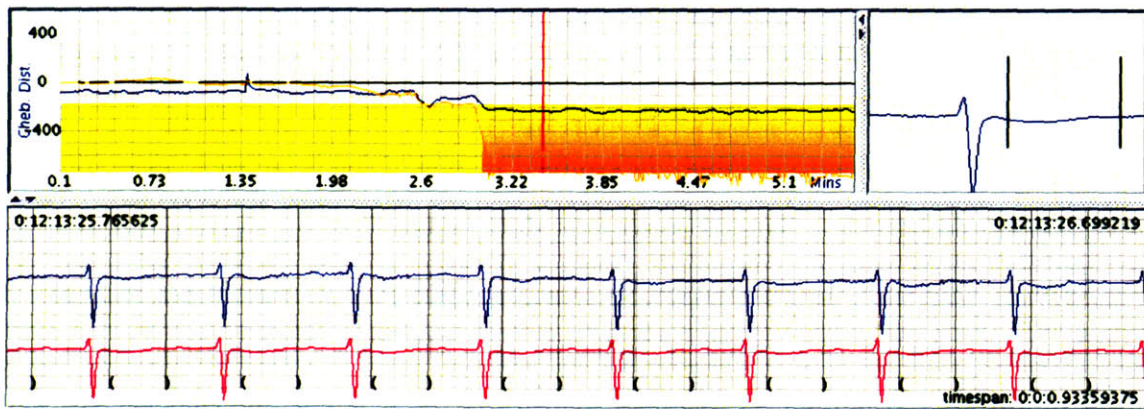


Figure 6-10: Automated axis shift detection example - after the axis shift. The dark time series line (Euclidean Chebyshev morphology metric) has dropped below the user-selected deviation threshold, but the axis shift detector recognizes an accompanying change in QRS morphology (light time series line). Consequently the deviations below the threshold are marked as the result of axis shifts rather than probable ischemia.



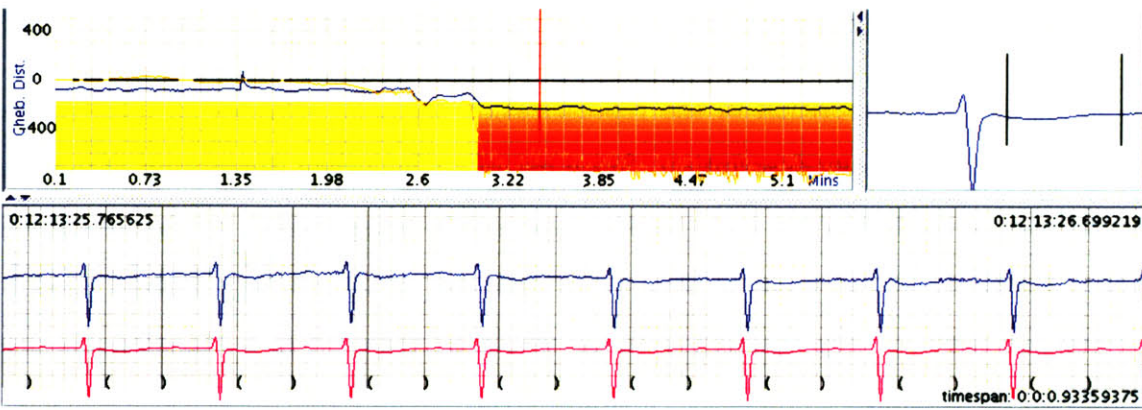


Figure 6-11: The automated axis shift detector has been turned off by the user, so any deviation below the threshold is flagged as an alarm condition (denoted by darker discolorations below the morphology time series line).

episode remained undetected altogether.

## 6.2.2 Signal quality index

As a final consideration in the alarm algorithm's determination of whether to alert a user or not, one must consider the signal quality. Section 6.0.1 shows a pictorial example in which poor signal quality might indicate to the user that a high repolarization segment morphology distance value is not reliable. Since the signal quality index (SQI) is a single-dimensional time series, it too may be used as was the QRS morphology time series to mitigate spurious alarms. Just as for the axis shift filter, the user can select a threshold below which the signal quality may not dip as additional input into the overall alarm. Each of the three pre-configured modes is distinguished by the minimum required during the entirety of a threshold breach. That is, if the threshold remains above or below the user-set morphology deviation threshold for a period of time  $t$ , then the episode is flagged as an alarm if the signal quality remains above the appropriate threshold for all of  $t$ ; otherwise the episode is flagged as noise.



## 6.3 Summary

The Chebyshev decomposition of the repolarization segment provides an intuitive feature reduction and morphology description. Since use of a Chebyshev description of morphology was partially motivated by the fact that the approach is unsupervised, we choose a Euclidean distance metric to obtain a single time series indicator of morphology change. In so doing we avoid the need for any training data, as would be required in a Mahalanobis distance calculation, for example.

Before performing Chebyshev decomposition, however, we perform pre-processing steps including consensus annotation, cubic spline baseline subtraction, noisy beat rejection and beat averaging. Using a 64-beat trailing average beat, we determine the isoelectric point and then perform Chebyshev decomposition on the repolarization segment, which begins 1 ms after the J point and ends at the repolarization period onset<sup>7</sup> + 40% of the RR interval<sup>8</sup>. In addition to Chebyshev coefficients, a signed QRS integral (relative to the isoelectric voltage) is written to the output annotation file for post-processing.

Post-processing can take one of two forms: visual data mining through the point-and-click multi-scale trend plots<sup>9</sup> or automated alarm generation. The alarm sensitivity is user-adjustable with a 3-d Chebyshev Euclidean vector magnitude denoting the threshold for elevation and another for depression. The user can further control alarm sensitivity by selecting from one of three axis shift discriminator options (based on different allowable QRS integral changes ) and similar threshold values in a signal quality index filter.

Pre-processing and generation of trend data for the massive database used in this thesis required extensive computation. In the next chapter we explore a parallel computing infrastructure that helped expedite data analysis and algorithm testing.

---

<sup>7</sup>defined in chapter 2 as the J point + 1 ms

<sup>8</sup>with an imposed upper limit of 15 ms

<sup>9</sup>Discussed in chapter 4

# Chapter 7

## Grid computing for high-throughput data processing

### 7.1 Motivation for parallel computing

Beat detection, consensus annotation, waveform pre-processing and processing of repolarization segment data require substantial computing resources, and the cumulative processing requirements for our massive mouse database appear daunting. If we think of the entire mouse database in "human time" - that is, as being multiplied in duration by ten, as is done for *wqrs* - then we are working with roughly 7.5 years of continuous ECG data. Even a machine employing algorithms working at an order of magnitude faster than real time would require the better part of a year to process the entire database. The problem imposed by the sheer magnitude of our data set has a simple solution: use multiple computers to work simultaneously on the data.

### 7.2 Grid computing defined

To expedite computation on the large mouse database, we designed an Internet-based communication and data processing architecture. This *grid computing* infrastructure bears many

similarities to cluster computing. Both grid and cluster architectures are parallel computing architectures, but grid computing is WAN-based <sup>1</sup> and cluster computing is LAN-based <sup>2</sup>. That is, a cluster computer typically has multiple processors in immediate proximity to one another with a dedicated network, while a grid computing network has its processors distributed in geographically disparate areas. A grid architecture, therefore, permits use of machines in their existing locations with a simple software modification; a cluster, in contrast, is an integrated entity. While in general a cluster provides superior performance over a grid architecture, a grid is an acceptable - often advantageous - alternative. A grid computing network requires no special knowledge of MPI <sup>3</sup> and one may build a grid network with neither capital expenditure on new equipment nor relocation of existing equipment to be used in the grid.

### 7.3 Methods of parallelizing processing

Parallel processing can take different forms. One might divide the database among machines, with each machine having all algorithms pre-loaded, and allow each machine to process an entire record. Alternatively each machine might be responsible for one or more select algorithms, so that a given record is processed by the effort of different machines.

Our parallel processing network uses a variation on the former approach. Rather than pre-populating each machine with a fraction of the database, we distribute data dynamically as needed through a mechanism described in section 7.5.1 . A given record is comprised of multiple files - each representing approximately 10 minutes of data. Since each file simply represents a time-slice of a record, we can send one *file* at a time - rather than an entire record - to a node for processing.

---

<sup>1</sup>Wide Area Network

<sup>2</sup>Local Area Network

<sup>3</sup>Multi-Processor Interface is the industry standard cluster computing API

## 7.4 Comparison of grid and cluster performance

A simple model for understanding the performance of parallel computing architectures relies on several approximations of LAN and WAN bandwidth. Since a cluster typically has a dedicated LAN connection that is completely isolated from other machines on a network, the nodes are capable of communicating at a rate of 1 gigabit per second <sup>4</sup>. While in reality the true data rate is lower since network packets carry overhead information as part of their communication protocol, we approximate the aggregate available data bandwidth as 1 gigabit per second for simplicity.

WAN-based communications, in contrast with LAN, are not necessarily on dedicated connections with blazing speed. The network traffic between nodes may pass through a variety of different network interfaces, some of which may be burdened with excessive loads. The slowest network link in the signal pathway between nodes represents the fastest sustainable bandwidth between nodes. A *very* good bandwidth between WAN nodes is 10 megabits per second, which is two orders of magnitude slower than LAN communications in a cluster. Though in reality WAN nodes rarely sustain such a fast communication rate, we use 10 megabits per second as a liberal estimate of WAN network performance. Figure 7-1 shows a performance comparison of a single node, a grid with 10 megabits/second WAN bandwidth, and a cluster with gigabit/second LAN bandwidth.

Given the fact that a cluster has dedicated bandwidth for communication among its nodes <sup>5</sup>, cluster computing is often the preferred architecture for parallel algorithms requiring frequent communication among different nodes. The algorithms running on the mouse database do not require frequent communication among nodes; each algorithm simply scans through the waveform data and one or more accompanying annotation files to create an output annotation file.

In determining whether a given data processing task is suited to grid computation one must also consider the algorithm computation time relative to the transfer time. Intuitively

---

<sup>4</sup>Gigabit ethernet is now commonly supported on new computers

<sup>5</sup>A node is a single machine, but a single node may have more than one processor.

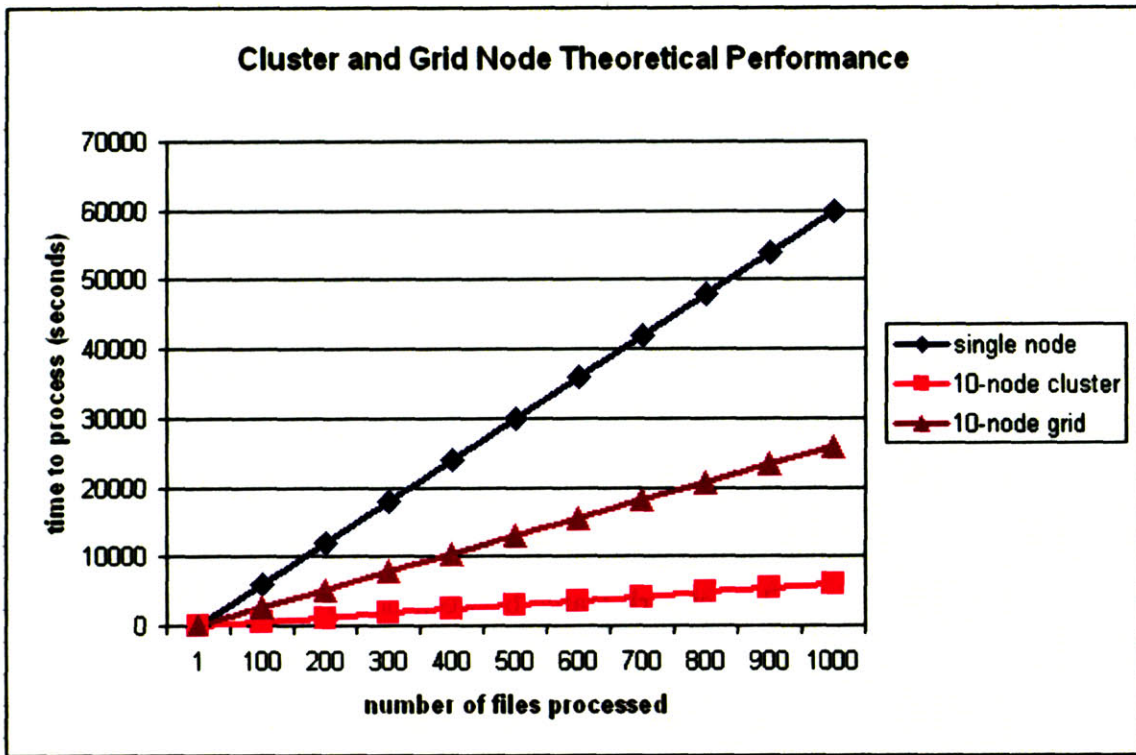


Figure 7-1: Grid vs. cluster performance model. The model is based on the assumption that a cluster has a bandwidth of 1 Gpbs and the grid has a bandwidth of 10 Mbps. Each file is approximately 2.5MB in size, which accurately reflects the size of each file in a mouse record.

we might expect that if the amount of time required to transfer a data segment to a target node for analysis far exceeds the time required to process the data, then a grid approach has not really improved overall computation time. The time spent in transferring the data would offset any benefit we might have otherwise gained by relieving the single node from processing the data. We have not studied in detail the statistics of our architecture to determine exactly how much improvement in computation time we derive by employing a grid network. As a crude empirical approximation, we have found that the average ratio of calculation time to transfer time for a node is approximately 5. Consequently the time required for processing the mouse database on the grid is dramatically reduced relative to the time required performing a sequential scan on a single machine, so use of a grid is well justified. The overall time savings, however, is not as dramatic as that which a cluster with gigabit-per-second network bandwidth can realize.

## 7.5 Grid computing software architecture

With the clear performance enhancements of parallel computation motivating use of a parallel computing system for analysis of our massive database, we now turn to a discussion of the manner in which the grid computing system was built. As with most systems, a grid computing environment can be constructed in many ways. Two architectural considerations, discussed below, permitted optimal use of node resources in calculations and maximum code re-use to minimize deployment time.

### 7.5.1 CGI - the Common Gateway Interface

CGI, or the Common Gateway Interface, is comparable in principle to an API <sup>6</sup>. Using CGI to encode parameters within an HTTP <sup>7</sup> transfer, machines on the network may invoke tasks on other networked machines by simply appending parameter names and values to a URL <sup>8</sup>. Consider, as an example, a machine with a web server that can be accessed on `http://www.myurl.com`. If the web server additionally has a remotely-callable script called *remotescript.cgi* that accepts input parameter names *num1* and *num2* that performs addition of the parameter values associated with these parameter names, then an HTTP request to the URL `http://www.myurl.com/cgi-bin/remotescript.cgi?num1=2&num2=8` <sup>9,10</sup> results in a response of '10.'

The server script, *remotescript.cgi*, can be written in any language that the server can execute; so long as the script parses the input parameters and outputs the appropriate output, the client calling the script will not know the difference. The client is agnostic to the server's implementation in the same way that a routine calling an API is agnostic to

---

<sup>6</sup>Application Programming Interface - an API is an implementation of a function in software with documented input and output specifications. APIs permit a programmer to invoke tasks without re-inventing source code or concerning him/herself with underlying implementation details.

<sup>7</sup>Hypertext Transfer Protocol, the application-layer client/server protocol most notably used for transfer of web content in web browsers

<sup>8</sup>Universal Resource Locator, often simply called a *web address*.

<sup>9</sup>Web servers most often have CGI scripts in a directory called *cgi-bin*

<sup>10</sup>The question mark after the URL indicates the beginning of the parameter list, where each parameter name/value - separated by '=' - is separated by an ampersand symbol (&).



the underlying source code implementation. The server script can be arbitrarily complex in nature. In the case of the ECG analyses performed on the mouse database, the scripts are responsible for extensive calculations on time series data that is loaded from the client prior to the CGI call to the server node that is to run the script <sup>11</sup>. For the purposes of simplification, and in accordance with traditional computer science nomenclature, we call the machine requesting work of a remote node the *master* and the node to which a CGI call is made the *slave*.

### 7.5.2 Load balancing: asynchronous, interrupt-driven job dispatch

The premise of building a custom parallel computing architecture was simultaneous use of resources. However, given that network speed differs from node to node as does processing speed <sup>12</sup>, we cannot assume that an identical job request of two different nodes on the grid will complete in the same time. Since modeling dynamic network bandwidth <sup>13</sup> is intractable, the grid system has no mechanism to dispatch jobs in an optimal fashion dictated entirely by the master node.

In order to avoid the shortcomings of fixed-schedule job dispatching from the master node, we use an interrupt-driven architecture in which communication between the master and each slave node is bi-directional. When a slave node has completed a job, it notifies the master via a simple CGI call, permitting the master to dispatch a new job to that slave <sup>14</sup>.

---

<sup>11</sup>Data files are exchanged across the grid network among Linux-based machines by using password-less *SCP*, a file-copying protocol employing *SSH*. *SCP* is an acronym for *secure copy*; *SSH* is an acronym for *secure shell*. *SSH* communications channels enable encrypted remote login capabilities and *SCP* transfers files between machines using an *SSH*-encrypted channel. Password-less *SCP* allows file transfer to occur, without prompting the connecting machine's user to enter a password for authentication, by using a public key configuration. Password-less *SCP* permits encrypted file transfers within scripts by precluding the need for keyboard input for authentication.

<sup>12</sup>The grid machines vary from very old laptops with little RAM to new, higher-performance machines with fast CPUs and extra RAM.

<sup>13</sup>Network bandwidth varies by time of day, day of the week and season. Additionally, less accessible parameters such as outages on a network causing a re-routing of network traffic, may cause transient bandwidth changes

<sup>14</sup>The IP address of the machine making a CGI request is sent as a non-explicit, immutable parameter - that is, embedded within the CGI call is a read-only environment variable identifying the source of the CGI call.

This asynchronous, interrupt-driven architecture prevents variable network conditions and different node computational efficiencies to dictate the master node's dispatch schedule.

### **The watchdog timer and dynamic load balancing**

Consider the very real possibility in which a slave node is processing a job and is shut down or disconnected from the network. In such a case the master node would await confirmation from the incapacitated slave indefinitely. To avoid such a stalemate, the grid software has a watchdog timer that periodically checks a log file to determine the time at which jobs were dispatched to nodes and the time at which those jobs completed. If a job is outstanding for too long <sup>15</sup> an email is sent to notify the grid operator of the problem. Upon receipt of the notification the user may then determine the nature of the problem.

### **7.5.3 Self-monitoring**

A slave node may encounter an abnormality during its processing. Each slave node is equipped with extensive self-monitoring routines that confirm success of operations. For example, file opening, data writing, and transfer of results back to a data archive server are confirmed. In the event that an error or unexpected condition occurs, the self-monitoring software generates an email with relevant details of the anomaly.

The self-monitoring component has become less used with each new iteration of algorithms used on slave nodes. Processing many thousands of ECG files with various algorithms over time generated alarm notifications providing information for fixing bugs efficiently. The self-monitoring software ultimately led to very robust algorithms that could process the entire database without error.

---

<sup>15</sup>The length of time for even the slowest nodes on the grid to process a single file is approximately 5 minutes; the threshold for the watchdog timer is set at 10 minutes

## 7.5.4 Summary

Parallel computing is an exciting area of computer science with a continuous stream of theoretical publications and problems warranting extreme sophistication. Our problem is amenable to a very simple application of parallel computing, as several identical algorithms need to be processed on thousands of individual files. Since each file is processed independently of all others<sup>16</sup>, parallelization takes the form of pre-populating multiple machines across the Internet with algorithms then sending data files to each node to undergo processing.

Our simple but effective parallel computing system dramatically reduced the time required for analyzing ECG data. Moreover, the parallel architecture with self-monitoring software on each node provided a high-throughput testbed for detecting software bugs. Since multiple files were simultaneously processed on different machines, the self-monitoring software provided a mechanism for rapid convergence toward a robust set of algorithms.

With the electrophysiology of mice (chapter 2) and the Chebyshev decomposition pattern classification technology (chapters 5, 6) as background, we move next to a discussion of the trends provided by performing processing of heart rate and the repolarization segment of all records in the mouse database. As this chapter describes, the trends of interest required extensive computation, the time of which was drastically reduced by a grid computing system.

---

<sup>16</sup>Analyses are not 'carried over' from one file to the next. For example, information used in running averages such as those in consensus annotation and beat template formation are built starting with the first beat of each file. Given that running averages in repolarization segment calculations are 64 beats, the 'ramp-up' period of approximately 1 second - assuming a heart rate of 600 beats per minute - introduces a negligible discontinuity in accumulated trend information across files

# Chapter 8

## ECG Trends in dKO mice

Though chapters 3 through 7 focused exclusively on engineering technologies associated with the acquisition and analysis of murine ECG, chapter 1 framed the origins of this thesis work in the context of a genetically-engineered mouse subject whose disease progression was unknown. The purpose of the system designs permitting collection and analysis of massive mouse ECG data sets was not a task without focus; these systems permit us to learn something about long-term ECG trends in the dKO mouse, examples of which will be explained in this chapter.

This chapter provides examples of repolarization segment morphology changes in mice through the use of case studies, as a summary description of disease progression is well beyond the scope of this thesis, if not altogether impossible. In fact perhaps the most definitive statement we can make about the dKO disease progression is that there is not a 'typical' time course by which all mice abide. As a review of the trends in Appendix B will reveal, there are certainly similarities among some records. Of particular note are episodes of severe bradycardia and high-amplitude ultradian<sup>1</sup> heart rate variability and an end of life characterized by drastic QRS widening and progressive bradycardia. These qualitative descriptions of dKO ECG characteristics are not, in fact, new discoveries enabled by the technology described in this thesis; the Krieger Lab had come to such conclusions with

---

<sup>1</sup>An ultradian rhythm is one that occurs more frequently than a circadian rhythm

manual perusal of massive quantities of data from earlier processes outlined in chapter 1.

An additional point of interest may be observed in the form of apparent correlation during certain time segments between heart rate and the repolarization segment metric (Euclidean distance of 3-d Chebyshev decomposition vector). A review of time series charts in Appendix B reveals several such examples. As one specific example, consider subject 0898122703, in which the heart rate and Euclidean metric plots are nearly mirror images. A fair question arises as to whether the correlation (or inverse correlation) might indicate that the Euclidean metric bears substantial heart rate artifact, perhaps as a result of error in J point detection by *wqrs*<sup>2</sup>. Review of other records indicates that correlation is not necessarily a persistent trend, which is a promising indication that the Euclidean metric is not an artifact of heart rate. Record 0800122603, for example, shows dramatic variation in the Euclidean metric in days preceding the end of life ( 20 days of recording) when the heart rate is relatively stable.

In the interest of providing an exemplary use of the monitoring system detailed in this thesis, we methodically and chronologically explore several records, focusing attention on several examples in which our repolarization segment analysis technology permits insight into ECG trends of a few select subjects.

In the following sections we detail three records to highlight the variability in disease trajectory among dKO mice as well as the utility of the repolarization segment analysis tool detailed extensively in previous chapters. Each figure represents a screenshot from the software detailed in chapter 3. The upper panel shows the long-term Euclidean distance metric with light and dark cycles shaded. Each datum in this time series trend plot represents 10 minutes of averaged data. The middle plot shows a higher-resolution time series of the point selected in the top plot (denoted by the vertical bar). An additional lighter-colored signal also appears in the middle panel; this signal is the signed QRS integral. Both the middle and top plots have horizontal shaded regions corresponding to a user-selected threshold. The lower panel shows the original ECG waveform (top) and a 64-beat trailing

---

<sup>2</sup>Chapter 2 discusses the fact that *wqrs* will often, in the presence of a sharp J wave, label the J point - or end of the QRS complex - as occurring at the peak of the J wave. Apparently *wqrs* detects the J wave as a strong S wave.

average waveform (bottom).

An important point to bear in mind during comparison of the Euclidean morphology metric with the corresponding ECG waveform is that the time series metric can, at times, defy intuition. The 1-d metric aggregates information about offset, slope and curvature, and consequently distills information. Consequently one might expect that an increase or decrease in the morphology metric amplitude to reveal a corresponding change in the apparent repolarization segment *offset* relative to the isoelectric value. While such is often the case, one may also find examples in which the slope or curvature (the other dimensions embedded in the Euclidean metric) seems to change more than the offset. Such examples are a poignant reminder that every simplification - including that created by our need to view a single time-series metric describing a 3-d feature vector - comes with a cost.



## 8.1 Case study A

As a starting point we show a very simple case study that is notable for its absence of repolarization segment morphology deviation. The subject in this case study is a wild-type mouse<sup>3</sup>, and as such one would not expect to find deviation episodes indicative of pathology.

---

<sup>3</sup>Subject 9907120503

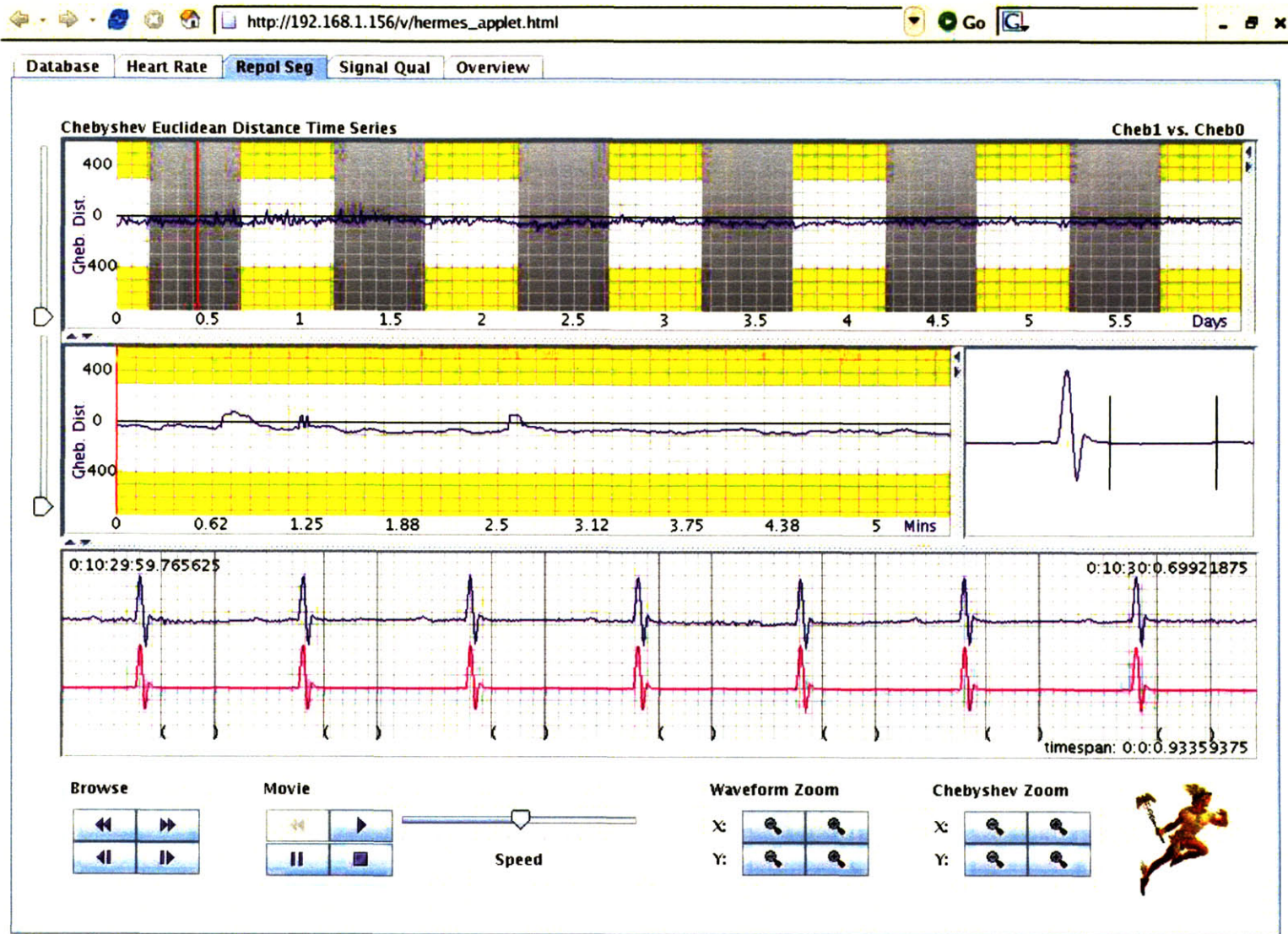


Figure 8-1: After approximately half a day of recording the repolarization segment remains well below the elevation and depression thresholds (shaded) in the long-term (top) time series and the short-term (middle) time series. The middle panel also shows a time series trend representing the QRS integral (above repolarization segment time series).

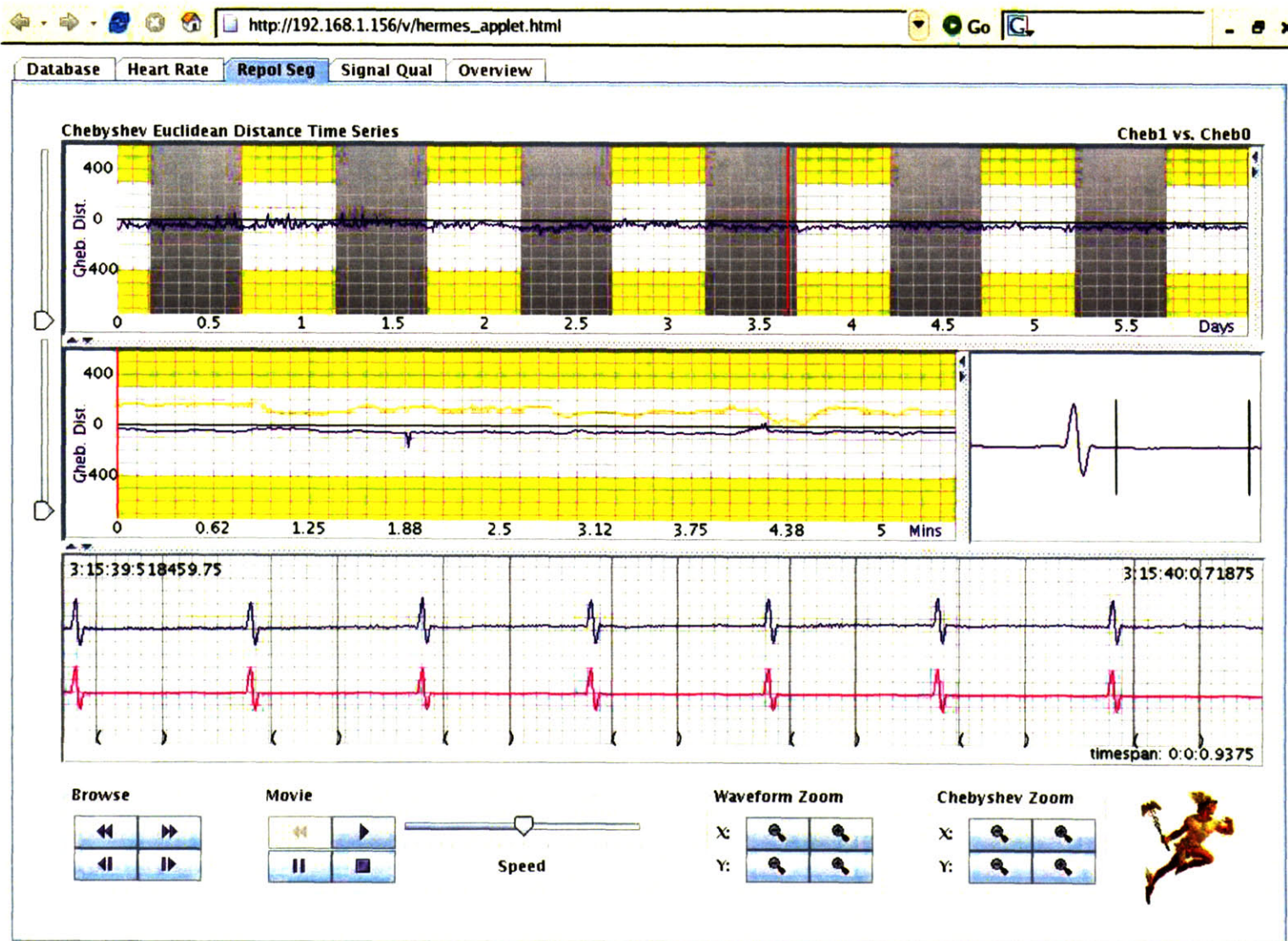


Figure 8-2: After over 3.5 days of recording the repolarization segment remains well below the elevation and depression thresholds (shaded) in the long-term (top) time series and the short-term (middle) time series.



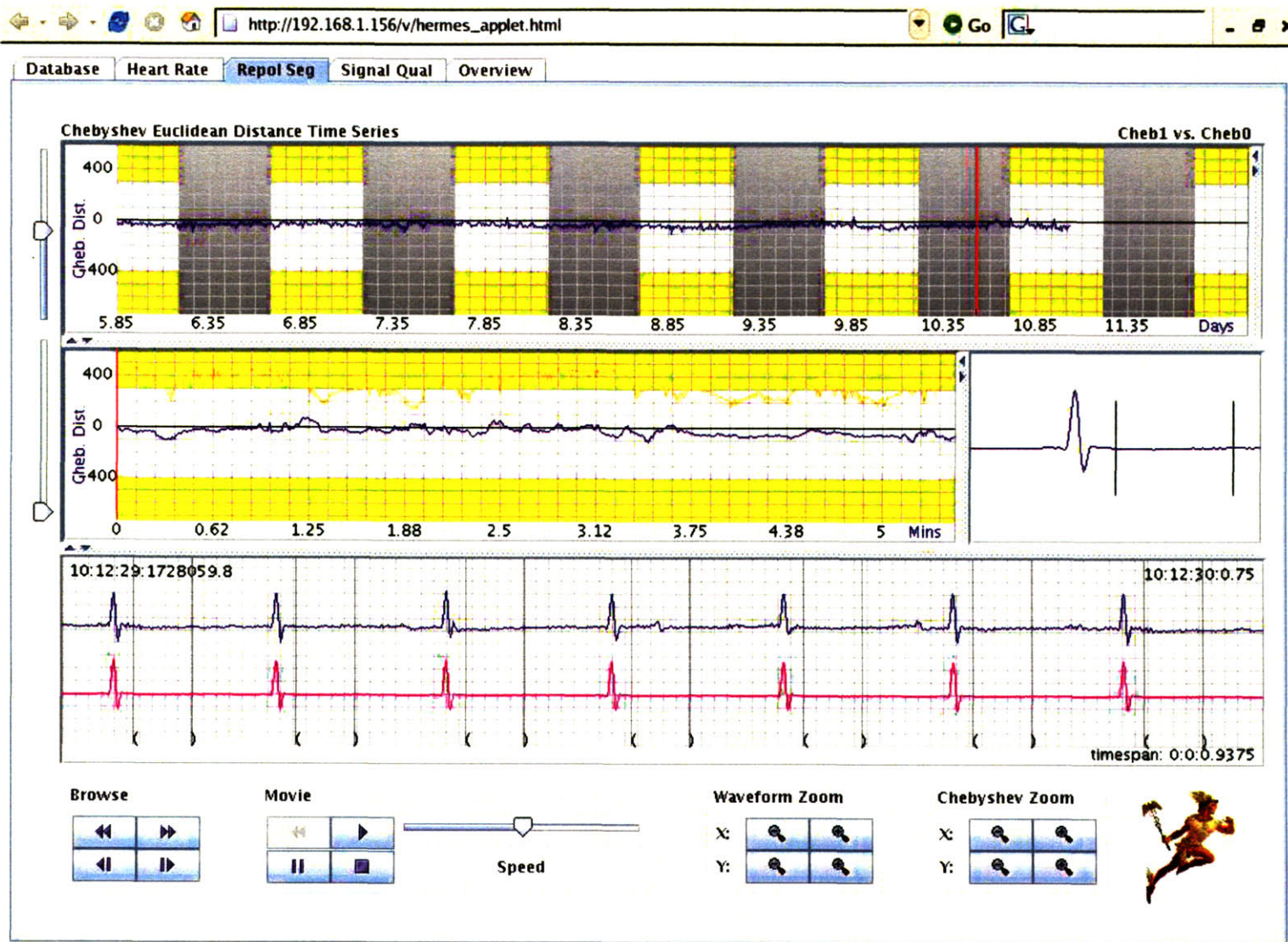


Figure 8-3: After over 10 days of recording the repolarization segment remains well below the elevation and depression thresholds (shaded) in the long-term (top) time series and the short-term (middle) time series.

## 8.2 Case study B

In this case study we review a dKO subject<sup>4</sup> with very little indication of pathology during the first several days of monitoring.

---

<sup>4</sup>Subject 0902122703

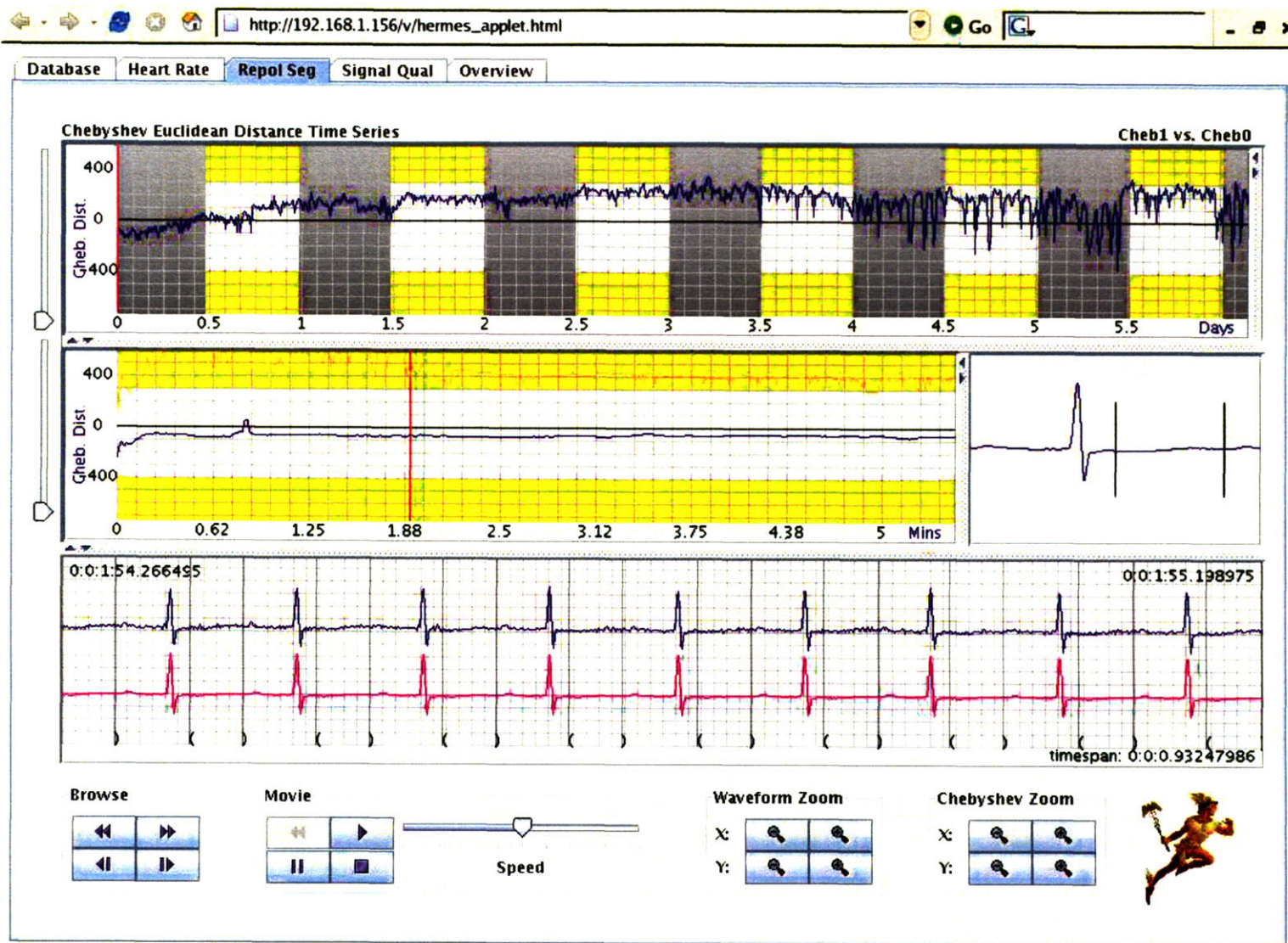


Figure 8-4: At the onset of recording, the subject shows a moderately depressed repolarization segment. The morphology does not, however, come close to the user-set threshold.



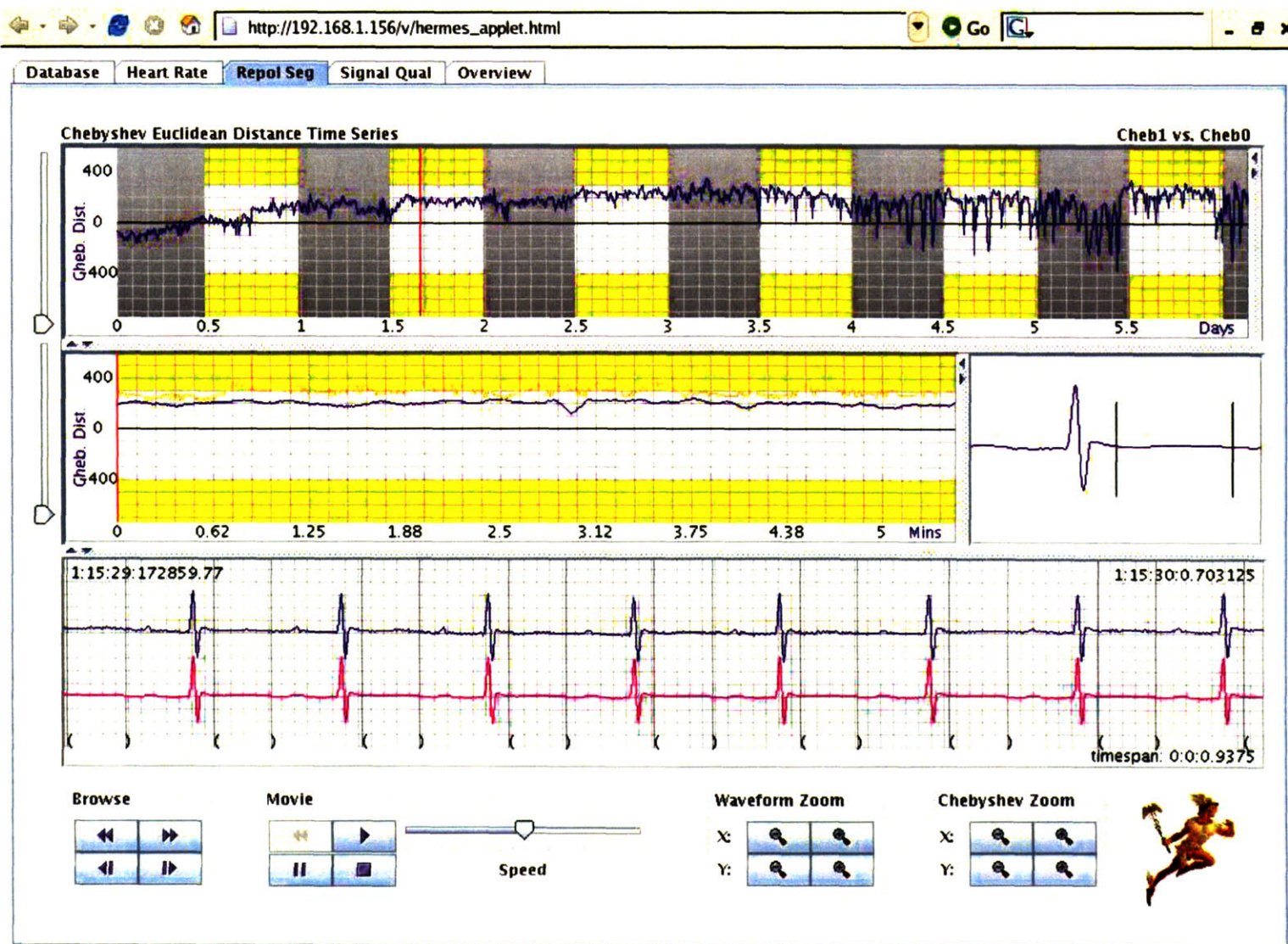


Figure 8-5: After approximately 1.75 days of recording the ECG looks very healthy. P waves are visible and only a hint of a J wave exists.



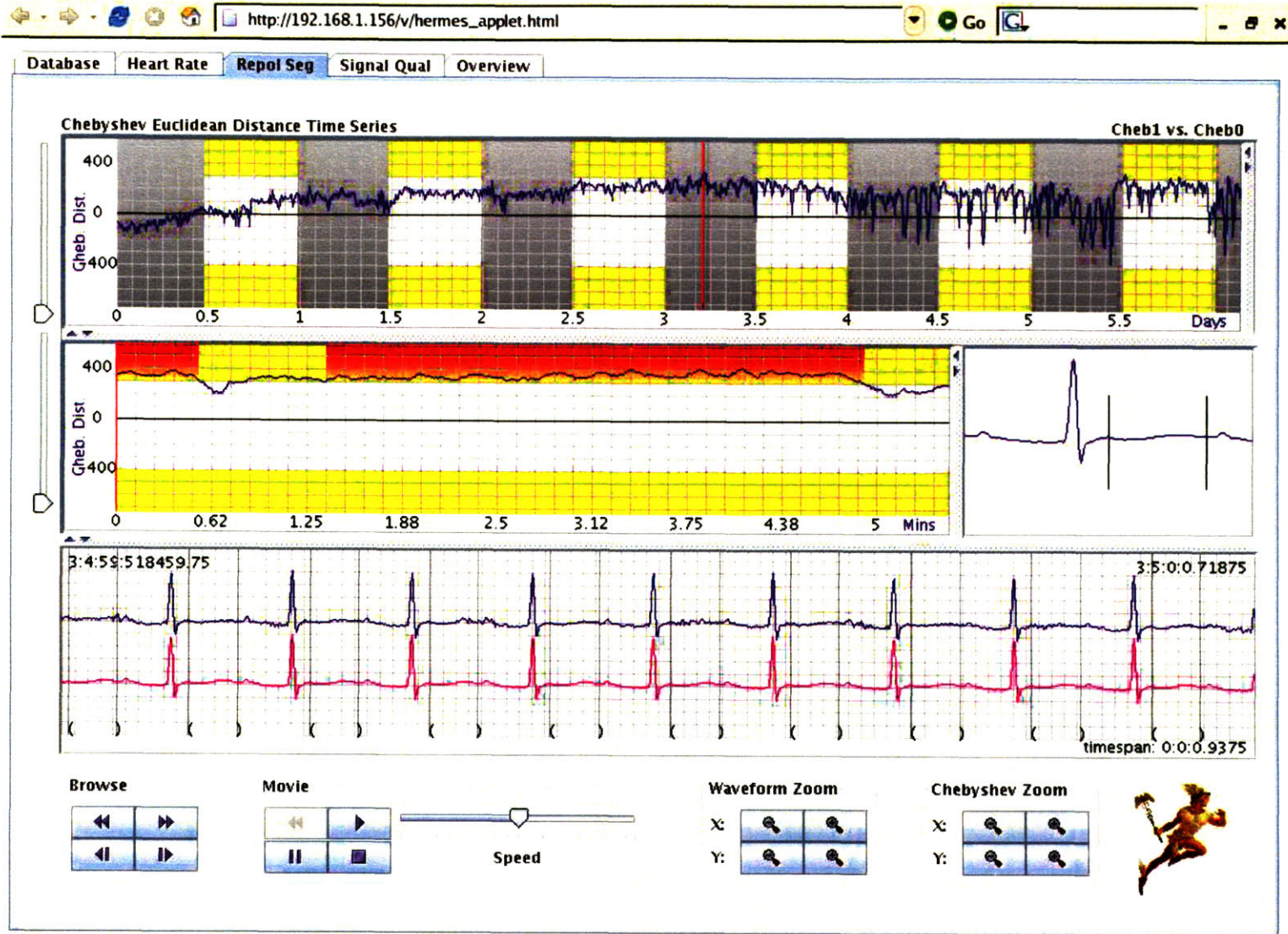


Figure 8-6: Selecting a peak in the repolarization segment metric at approximately 3.25 days into recording reveals a repolarization segment elevation that only barely exceeds the threshold. Up to this point the repolarization segment has changed relatively slowly over time (particularly when compared with activity in the repolarization segment beyond 4 days of recording).



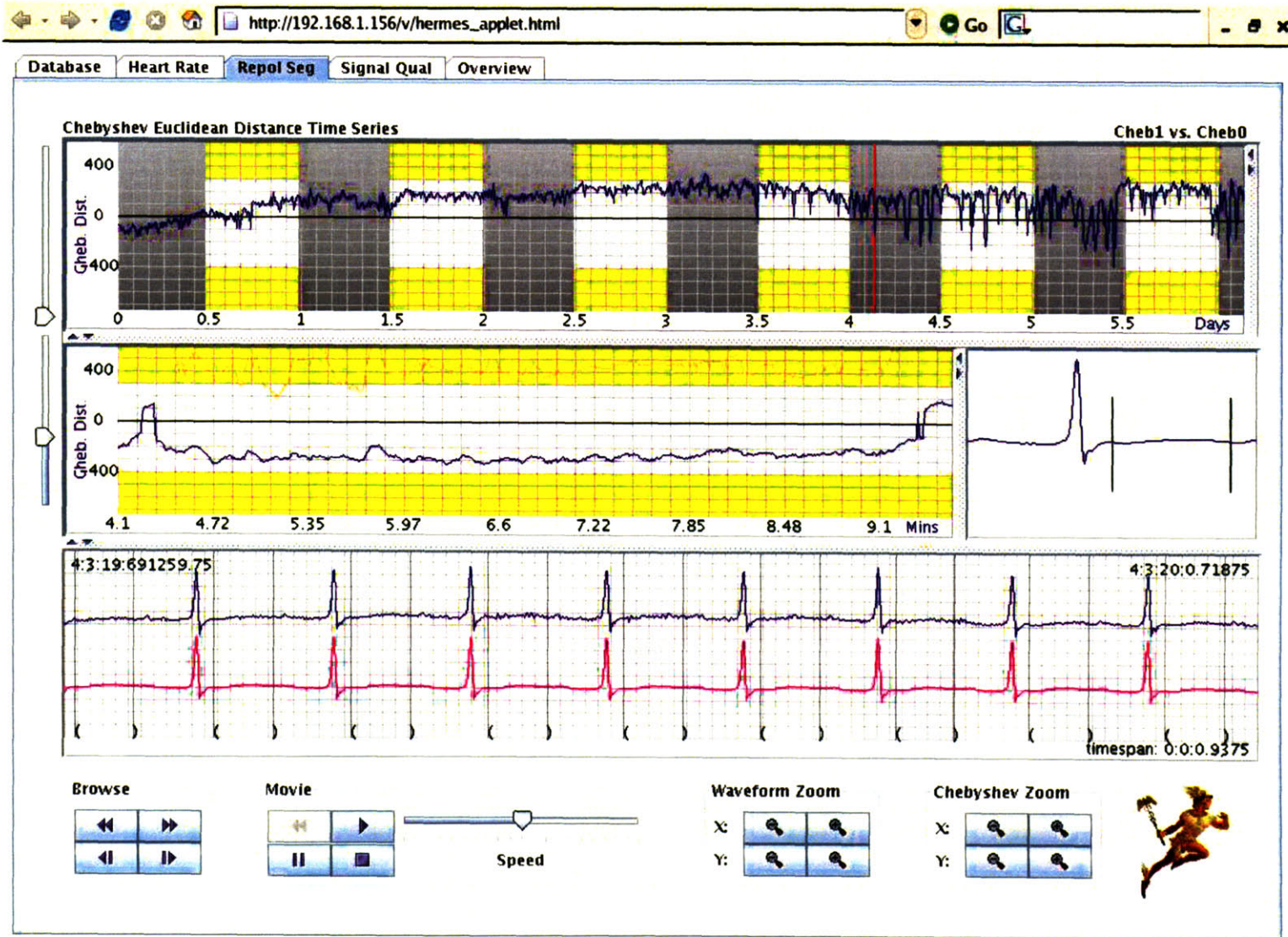


Figure 8-7: After approximately four days of recording, more drastic oscillations in the repolarization metric occur. Selecting a local minimum (denoted by the vertical bar in the top plot) reveals that the repolarization segment is only moderately depressed on average. The middle panel reveals that during the selected ten-minute period the repolarization metric occasionally dips below the threshold (user-selected threshold).



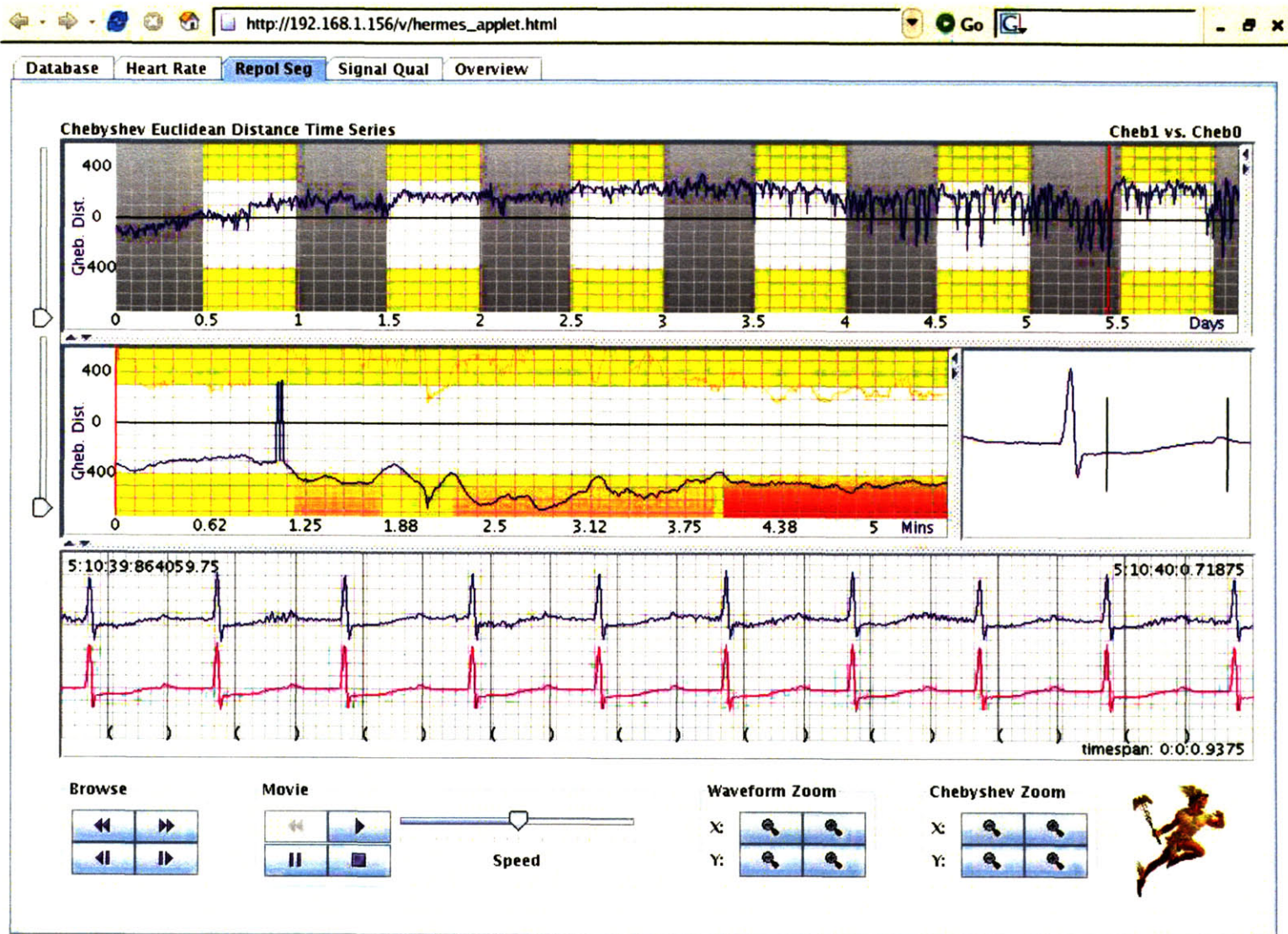


Figure 8-8: At about 5.5 days of recording the average repolarization plot dips below the depression threshold.

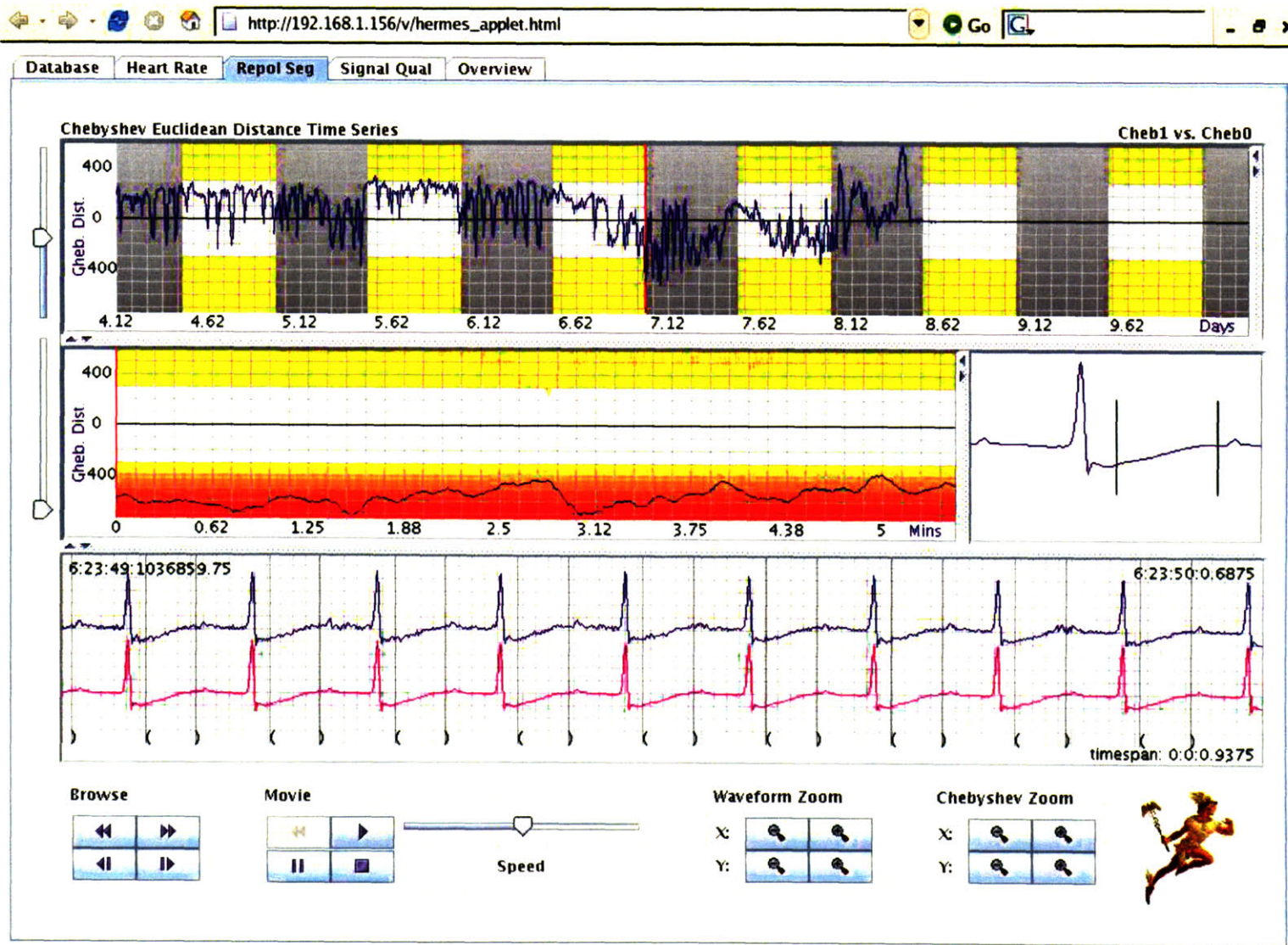


Figure 8-9: The morphology metric dips below the threshold again at approximately 7 days. The morphology at this point very nearly resembles that of the depression occurring at day 5.5 (previous figure).



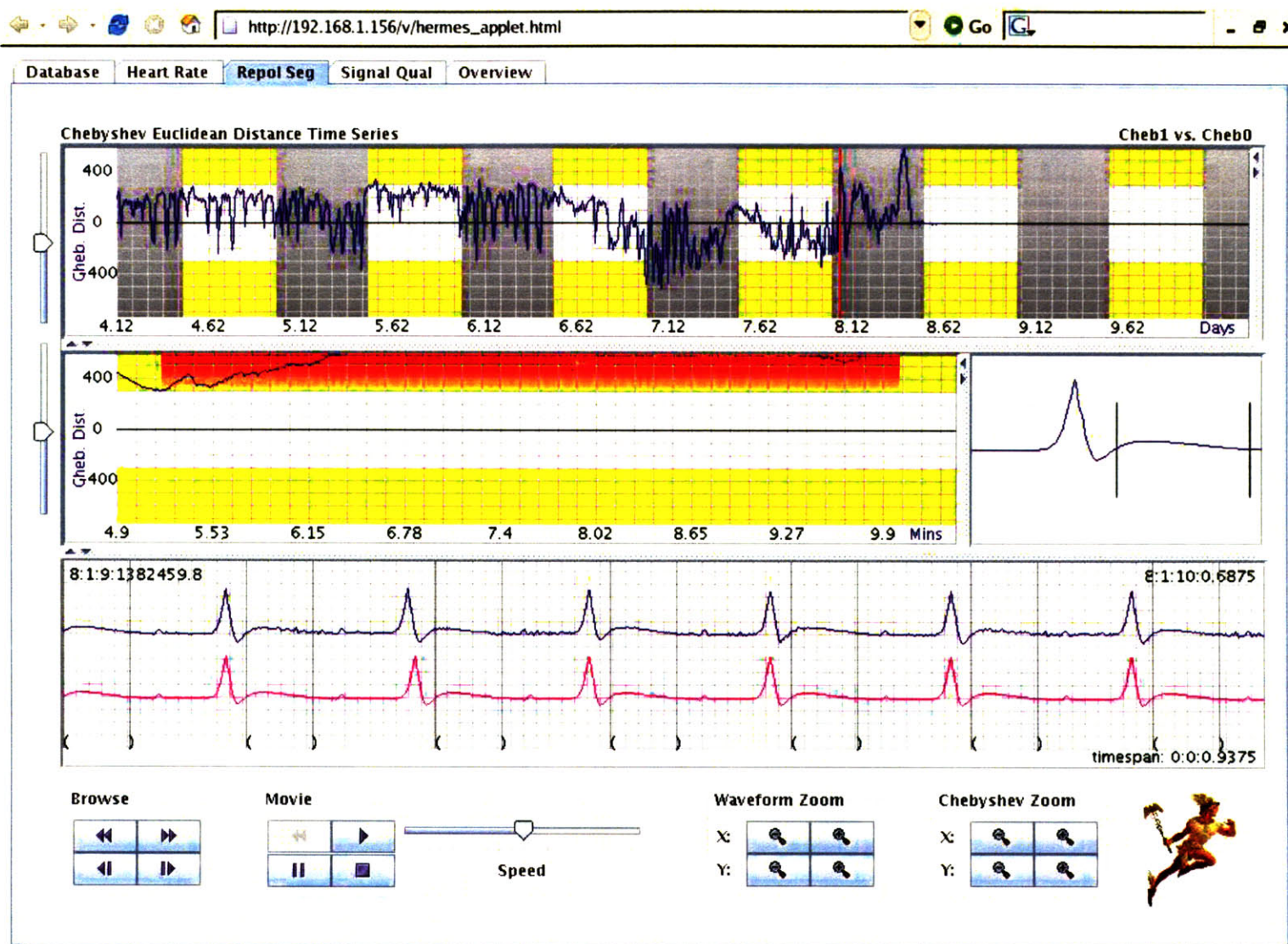


Figure 8-10: After approximately 8 days of recording the repolarization segment rises rapidly above the elevation threshold. The QRS complex is notably different, with a triangular and slightly widened appearance.

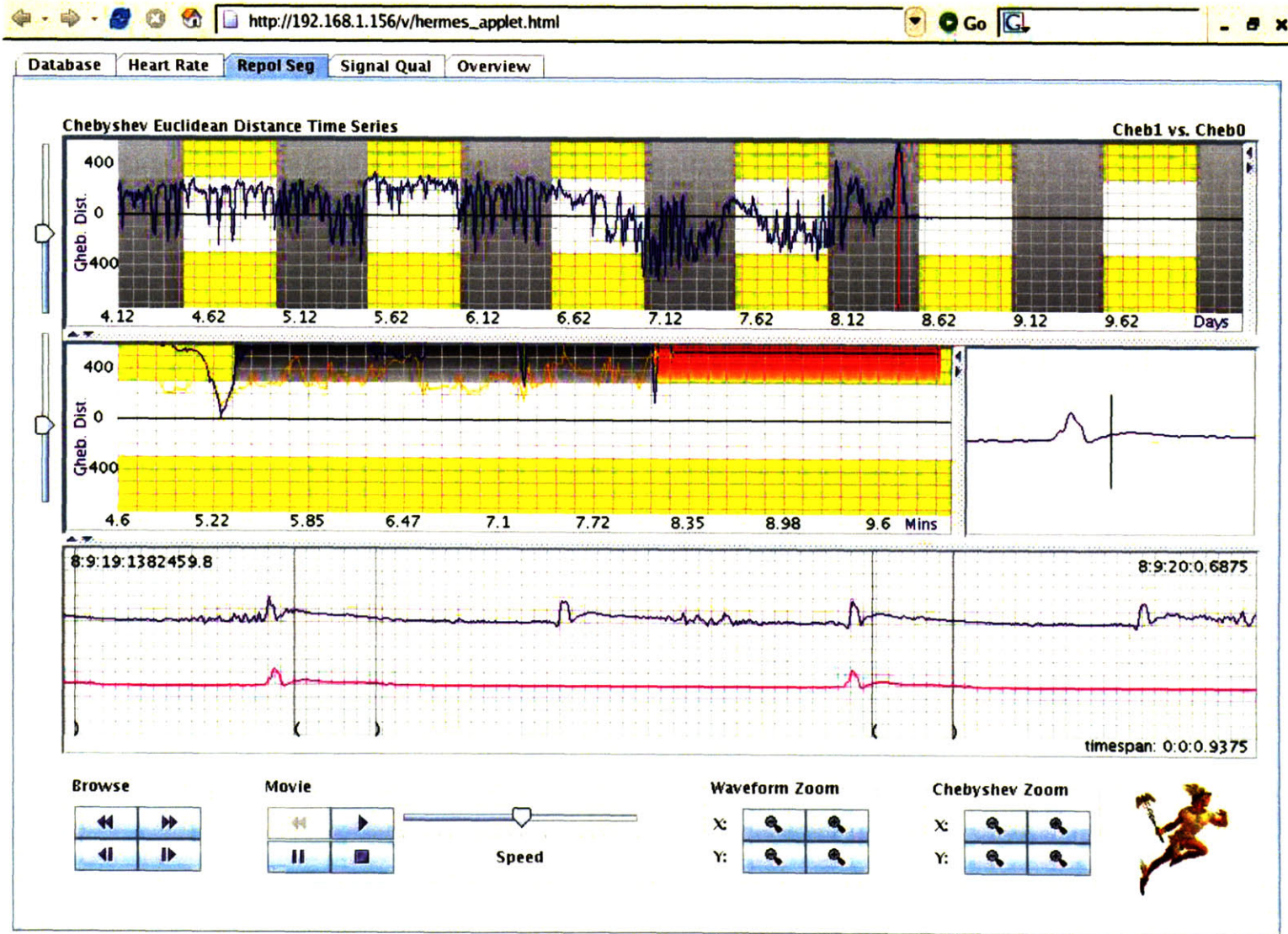


Figure 8-11: Another significant elevation shows on the long-term plot at about 8.5 days of recording. The heart rate is approximately 250 beats/min, severely bradycardic for a mouse. Note that the average waveform is attenuated relative to its original counterpart, most probably due to noise or an unstable fiducial point (namely the R-peak, which is used as the center point for beat averaging).



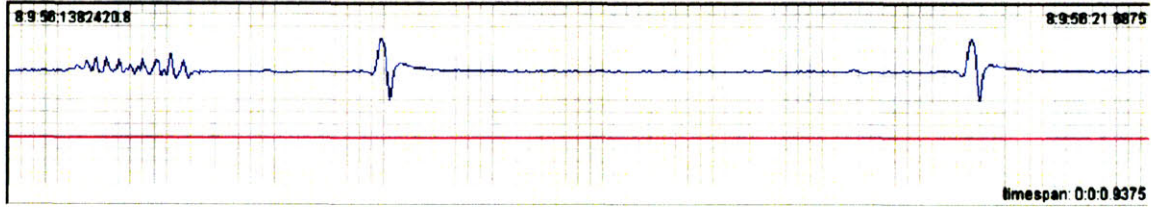


Figure 8-12: Only seconds later (see time stamp, in dd:hh:mm:ss format, in lower panel, upper-left and upper-right corners) the QRS morphology has changed but the animal is still severely bradycardic (approximately 150 beats/minute). Note that the average waveform (lower signal in bottom panel) is flat, indicating that the consensus annotator is having trouble detecting QRS complexes during this severe bradycardia. Such QRS-detector performance degradation during severe bradycardia is common in the mouse subjects, particularly when the QRS complex has widened and is somewhat smooth.

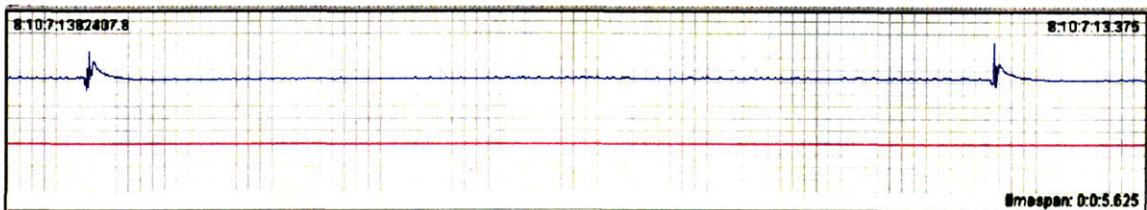


Figure 8-13: NOTE: the timescale on this ECG strip is different from all previous figures in this case study. This ECG strip spans 5.6 seconds, while in previous figures the ECG strip spans less than one second. It is improbable that the subject is alive at this point, though periodic electrical activity occurs. After several more sparse beats the ECG becomes a flat line (not shown).

### 8.3 Case study C

In this case study we review a dKO subject with ECG indications of pathology beginning during the first several days of monitoring. In spite of an oscillation between elevation and depression, the subject survives for nearly a week.



Figure 8-14: At the beginning of recording this subject shows a moderately depressed repolarization segment. The depression is not, however, close to the user-set threshold.



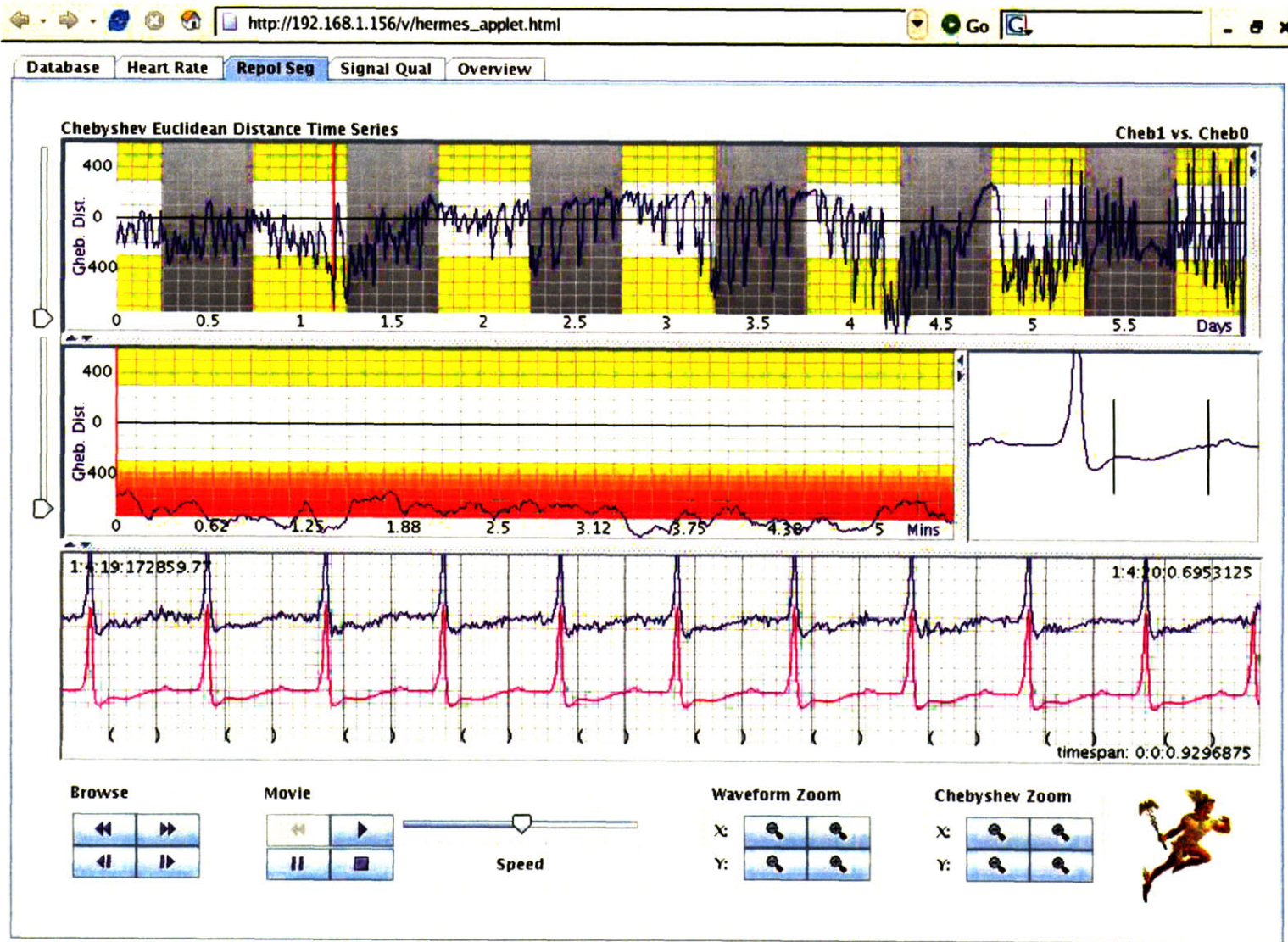


Figure 8-15: A sharp decline in the repolarization segment morphology metric at about 1.25 days drops the metric well below the threshold.



Figure 8-16: After about 2.5 days of recording, evidence of depression is altogether absent.



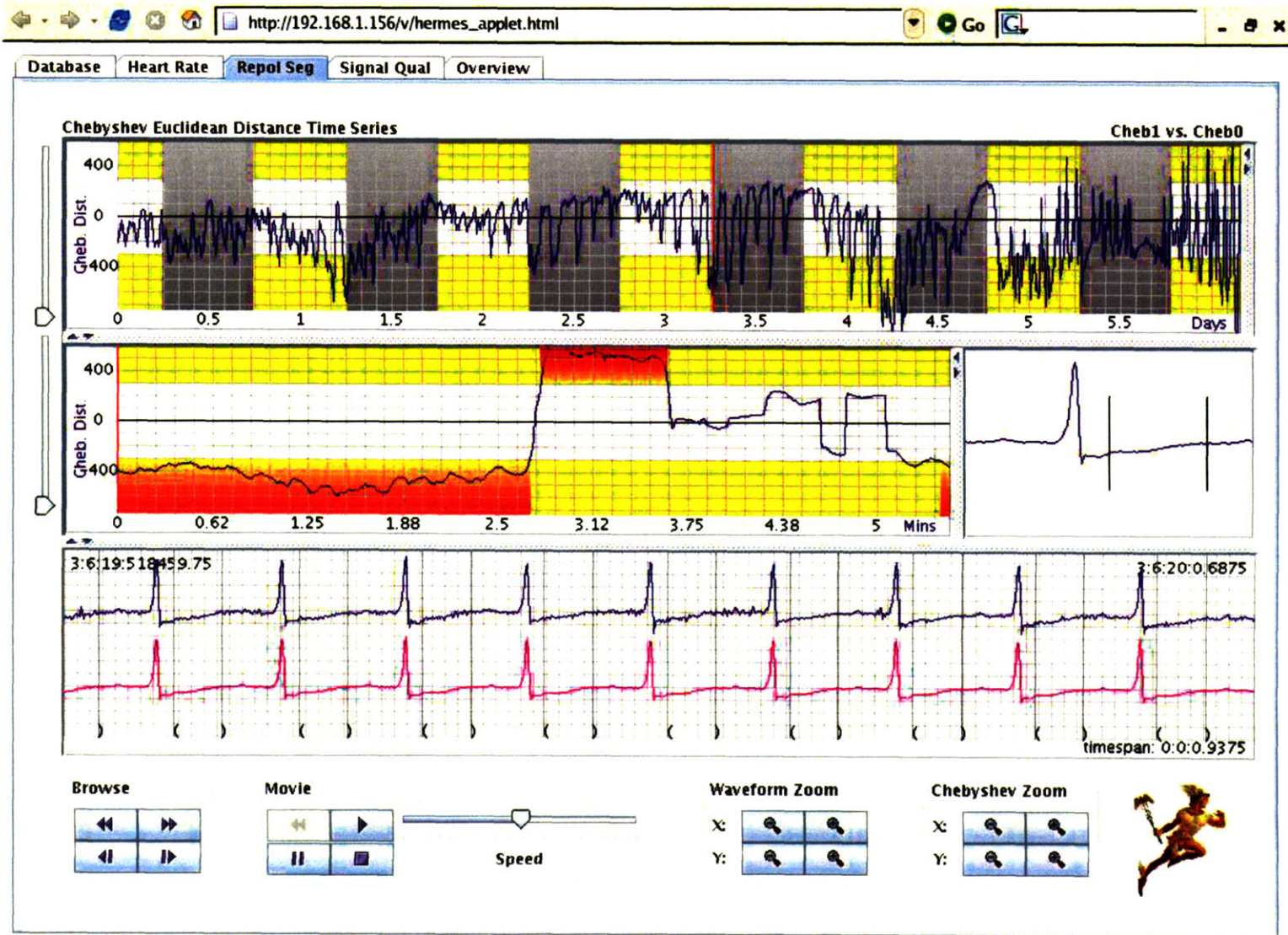


Figure 8-17: The long-term trend plot indicates a severe dip in the repolarization morphology metric at about 3.25 days. The middle panel reveals an extremely drastic and nearly instantaneous swing from depression to elevation. This figure corresponds to a 0.3 minute offset within the middle panel, which is during the depression episode; figure 8-18 shows an offset after the upswing.



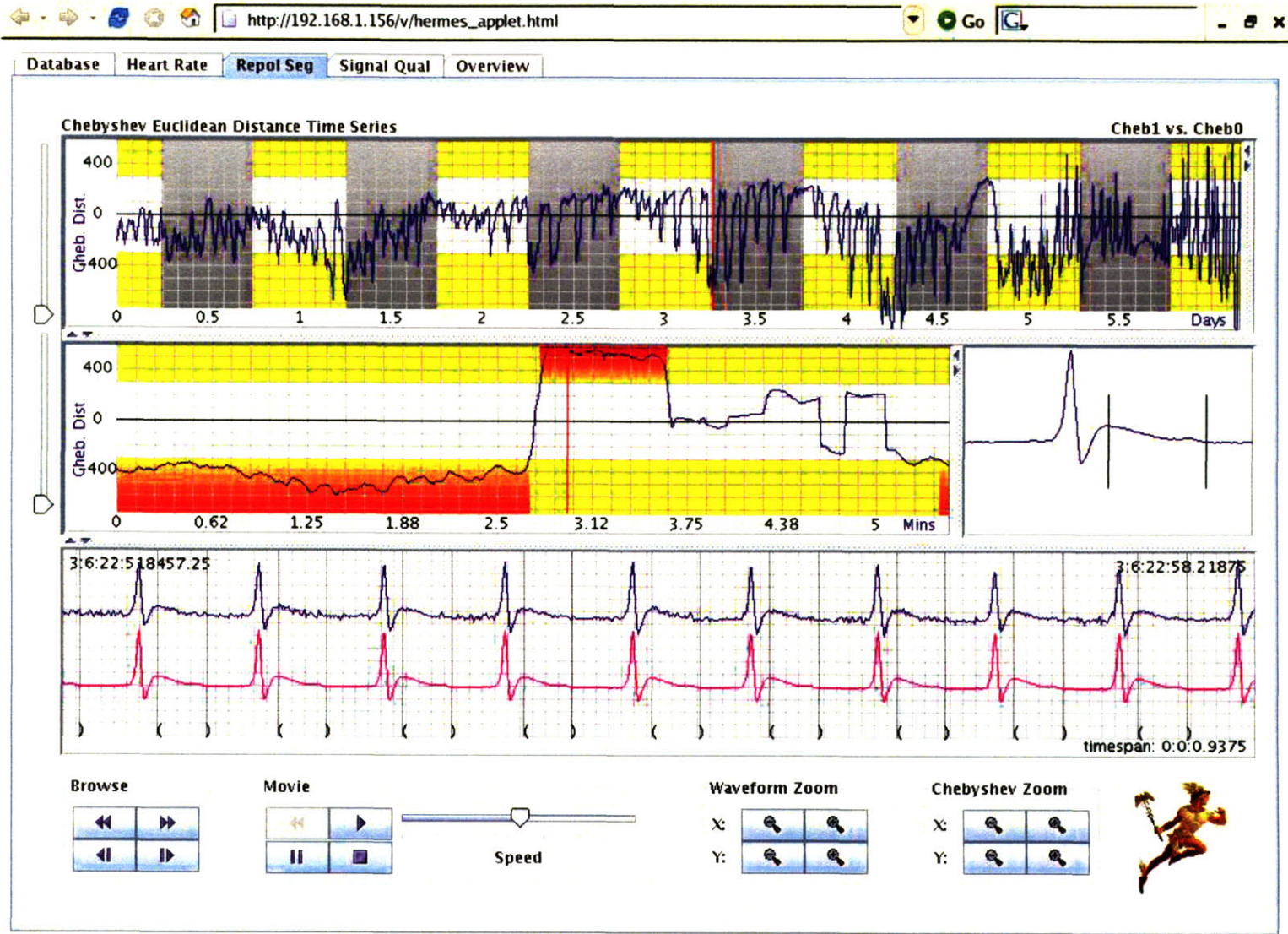


Figure 8-18: Only seconds after a stable depression morphology, the morphology metric swings in the direction of elevation. The QRS morphology does not change substantially, so the sudden change is not consistent with an axis shift.

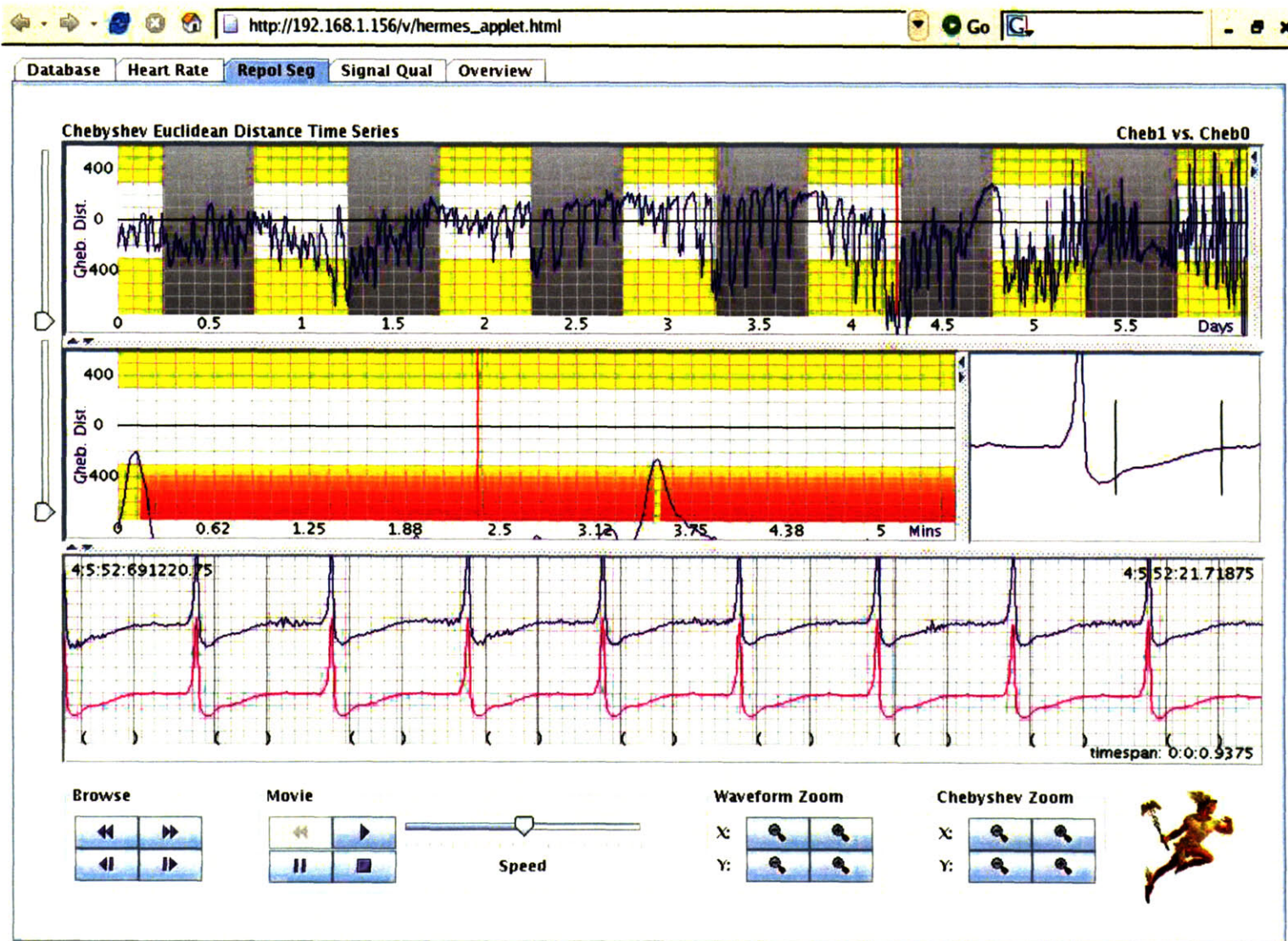


Figure 8-19: At about 4.25 days of recording the long-term trend plot reveals another drastic change consistent with repolarization segment depression.



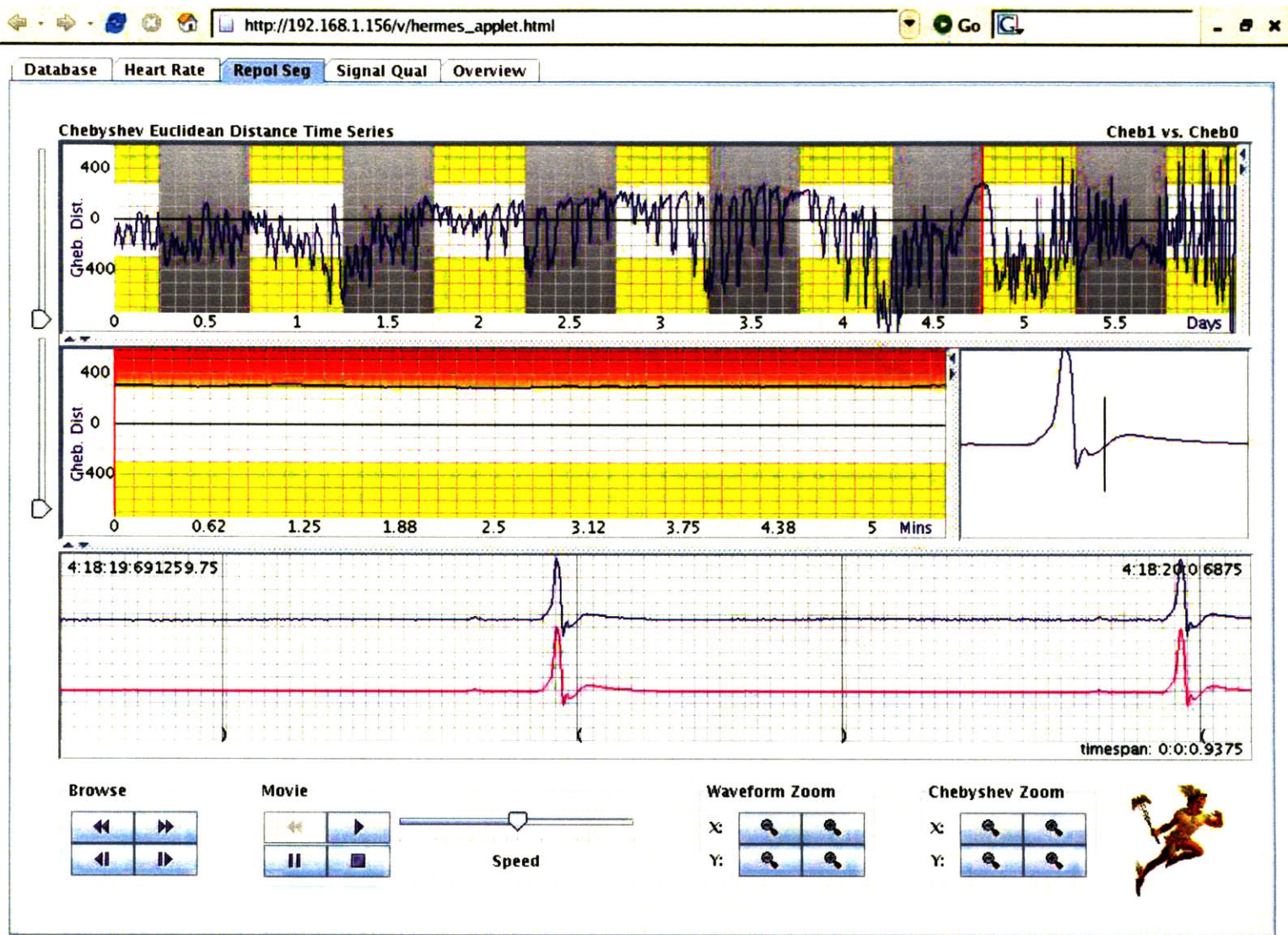


Figure 8-20: After approximately 4.75 days of recording, a drastic but longer-lasting elevation episode occurs.

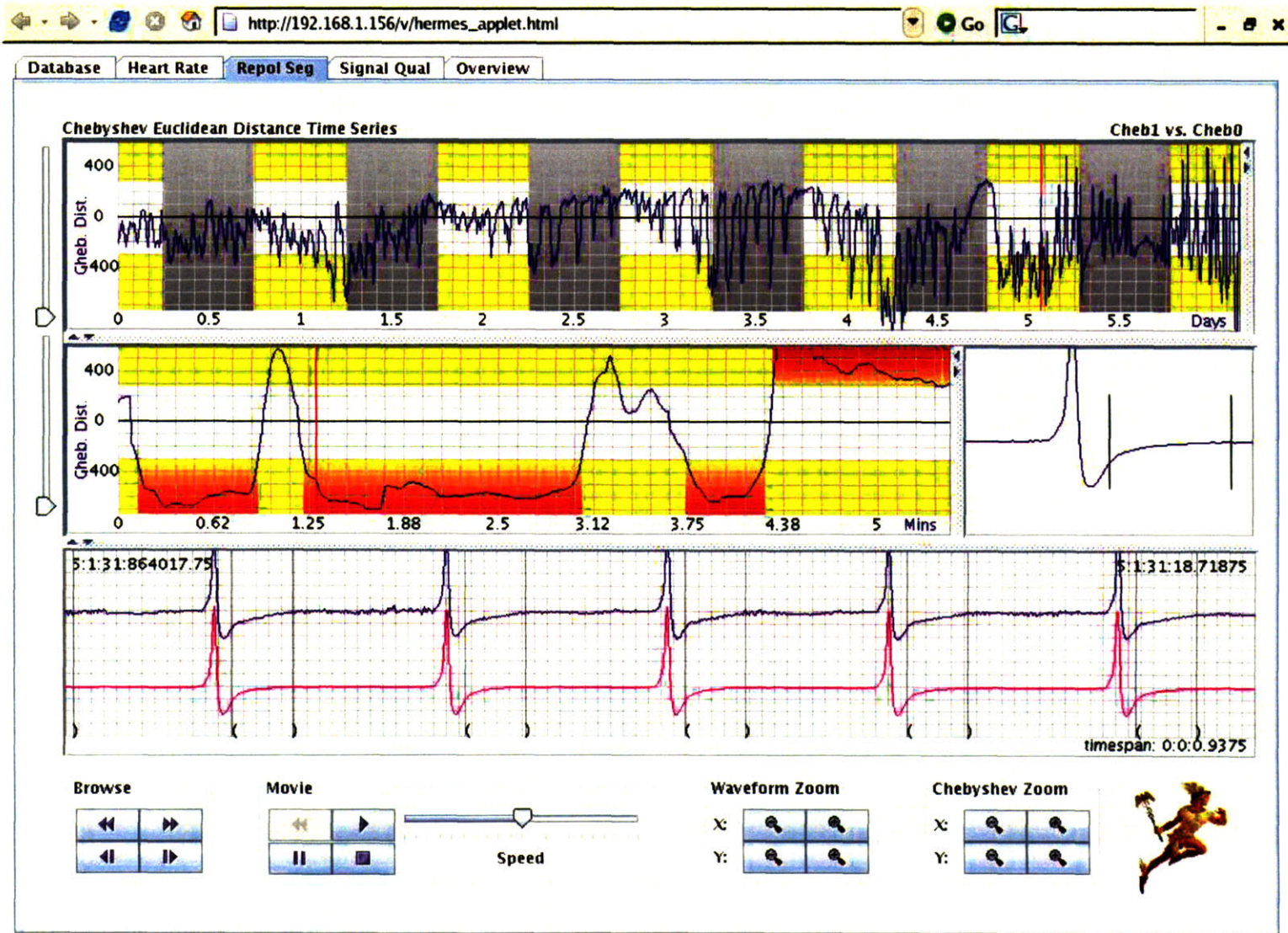


Figure 8-21: After about 5 days the long-term trend plot reveals much more rapid oscillations between elevation and depression. The ECG signature during this depression episode closely resembles that of previous episodes.



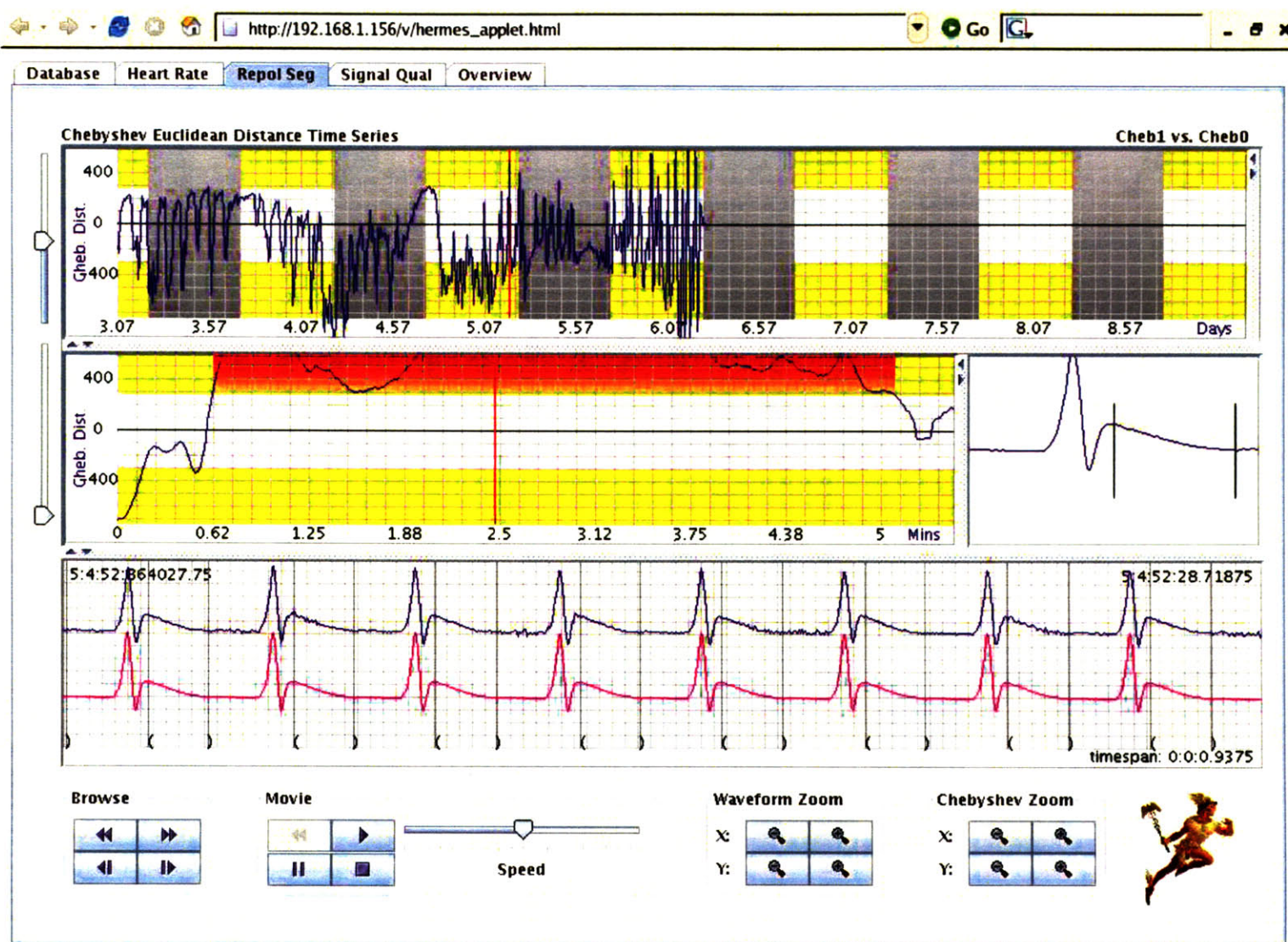


Figure 8-22: This figure shows an elevation episode during a drastic upswing on the long-term trend plot. At times the middle plot shows no time series signal; it is literally off the chart.





Figure 8-23: After a series of oscillations between elevation and depression, the heart rate slows and the QRS broadens after about 6.25 days. As with the previous dKO case study, the QRS detector fails to detect beats when the QRS complex is broad and the heart rate slow. After about a minute of progressive QRS broadening the ECG reveals only barely discernible blips of electrical activity (not shown).

## 8.4 Summary

In this chapter we qualitatively validate the use of the repolarization segment metric - discussed in previous chapters - through several case studies. As a control we review a wild-type mouse in case study A; its morphology reveals no anomalies and at no point comes close to breaching the threshold. The absence of substantial morphology deviation for the wild-type mouse provides a degree of confidence in the repolarization segment algorithm's sensitivity; if the algorithm shows little deviation for a wild-type mouse we may proceed with confidence that it is not overly sensitive.

Case studies B and C on dKO mice reveal slightly different disease progressions. The subject in study B shows little repolarization segment morphology change during the first several days of recording. After several days, however, the trend appears to oscillate between elevation and depression. The subject ultimately experiences profound bradycardia, a drastically widened QRS and terminal asystole. The subject in study C similarly shows drastic swings in morphology between elevation and depression and similar end-of-life characteristics.

Appendix E shows the trend plots for all subjects in the murine database. A brief perusal of the plots reveals that the database reveals a variety of different apparent disease progressions and no obvious predictors of death.

THIS PAGE INTENTIONALLY LEFT BLANK

# Chapter 9

## Conclusions and future work

### 9.1 Conclusions

This ECG monitoring technologies described in this thesis arose from a need to view and analyze ECG trends in dKO mouse subjects. Because of electrophysiological differences between mouse and human ECG, instrumentation for humans is ill-suited for use in mouse subjects. The spectral content of mouse ECG is far different from that of humans, and human ECG instrumentation blocks spectral content beyond several hundred hertz. Given that the spectrum of mouse ECG continues up to 1kHz, human instrumentation would filter out a substantial portion signal energy if used on a mouse. Equally as important a motivator in the design of new instrumentation is the fact that dKO mice die while they are still quite young, weighing less than 12 grams at the time of their inevitable death before eight weeks of age. The instrumentation designed for this monitoring system, therefore, used a filter bandwidth tuned to the mouse ECG spectrum and inputs compatible with the wired implantable electrodes used for ECG collection from very small mice.

The new monitoring system also required careful attention to software design. Custom digital signal processing firmware running on an A/D converter performs 5x oversampling, digital lowpass-filtering with a symmetric FIR filter, and subsequent 5x downsampling. Oversampling ensures that the relatively slow rolloff of the analog Bessel anti-aliasing low-pass

filter does not introduce aliasing upon signal discretization, and use of a symmetric FIR filter prevents phase distortion in the digital domain. Since the motivation for using Bessel-type analog filters lay in their phase linearity, the digital filter design necessarily employs a transfer function that does not ruin the carefully selected linear-phase analog filter.

Application software on the data collection server provides an intuitive and simple interface for lab technicians to begin long-term data acquisition and analysis. Data is stored on a high-capacity server and processes perform “on-the-fly” data analysis. Data analysis includes beat detection, rhythm trend creation, and repolarization segment morphology analysis. Additional software permits remote viewing of ECG signals in real-time via the Internet; similar software allows the user to navigate retrospectively through the vast amount of data comprising a mouse’s lifespan.

A major contribution of this thesis comes in the form of a repolarization segment analysis algorithm. Use of Chebyshev polynomials is a general technique that can be applied to any species’ repolarization or ST segment. The application of Chebyshev decomposition requires species-specific parameters in order to produce meaningful results. For example, repolarization segment time points - which we defined based on examination of ECG from ischemic dKO subjects<sup>1</sup> - depend on electrophysiology particular to a species. Even with reasonable time points, an appropriate *interpretation* of Chebyshev decomposition for repolarization or ST segments will differ across species; one cannot glibly compare a 3-d Euclidean metric between mice and humans to derive any meaningful interpretation. Nonetheless the approach of Chebyshev pattern analysis on the repolarization or ST segment is a very reasonable approach that should be applied to and tested on databases of other species’ ECG.

As is frequently the case in research, this project answered one challenge only to raise a multitude of others. We do not aim to provide an exhaustive list of possible future uses of the monitoring technology discussed in this thesis; we sincerely hope that users will find it useful in projects that its designers had not even anticipated. Nonetheless we provide in this chapter several logical next steps and uses for the monitoring technology described this thesis work.

---

<sup>1</sup>Chapter 2



## 9.2 Future work

### 9.2.1 Murine database episode annotation

A rigorous and mechanistic approach to system validation requires a gold standard by which an automated or semi-automated detection algorithm is judged. In the case of this thesis work, we used Chebyshev decomposition as a means by which to characterize the shape of the repolarization segment. Based on the premise that the late repolarization (post J wave) segment of mice is nearly isoelectric in wild-type mice, we designed a classification and alarming scheme based on deviations of the repolarization segment from an isoelectric line. Though the alarm thresholds were necessarily quantitative, the absence of a gold standard database - created by expert human reviewers - precludes an exposition of alarm performance in the familiar terms of specificity and sensitivity. Utilization of the tool designed in this thesis provides the framework for a collaborative effort toward development of a gold standard murine database. The annotation effort will use the online visualization and annotation capabilities as well as the Chebyshev pre-processing metric to expedite the process of searching for repolarization segment episodes. In ECG algorithm nomenclature, *episode* has a well-defined, quantitative meaning. For example, we might define an elevation episode as beginning when the Chebyshev decomposition is greater than or equal to  $x$  units from the origin for more than  $y$  seconds. With a formalized episode definition in hand, annotators will meticulously review the mouse database and - with the help of the tools designed in this thesis work - create a benchmark database by which algorithms can be tested more formally.

### 9.2.2 Drug development: toxicity and efficacy screening

The process of drug development invariably takes the form of a basic science study; moreover, the process invariably involves animal tests. Cardiovascular drug candidates are tested first for potential toxicity effects, after which they are assessed for efficacy. In efficacy studies, effects of subjects receiving the drug candidate are compared with those of placebo recipients. In the absence of a long-term monitoring tool, cardiovascular effects that are compared take

the form of histology or biochemical information, which may require animal sacrifice. Given that the ECG represents a minimally- or non-invasive means of viewing cardiovascular disease manifestations, a monitoring system such as that designed in this thesis may improve the work flow of cardiovascular drug development in academic or industry settings. Without monitoring ECG of the subjects we are unlikely to know whether the subject is ischemic or has experienced an MI. Determining appropriate *timing* of drug candidate administration relative to disease progression currently requires a large number of subjects and retrospective analyses to correlate drug administration times and disease progression at these times (as determined by histology and biochemical data).

With a monitoring system for animals that more closely resembles that available for humans, researchers can gather and analyze real-time ECG data to enable more finely-tuned studies. For example, researchers can design studies around administration of the drug immediately following the first ST-segment episode<sup>2</sup> or other fixed time-points beyond the first or subsequent episodes in order to determine the efficacy of the drug candidate at different points in cardiovascular disease progression.

### 9.3 Potential clinical applications

Medical diagnoses are increasingly data-driven, and the trend is unlikely to lose momentum. From MRI and CT scan overlays for algorithm-based tumor recognition or surgery planning to fully computer-automated laboratory analyses, data systems are a cornerstone of medical diagnostics. The repolarization segment pattern-recognition technology discussed in chapter 7 has the potential to improve the sensitivity and positive predictivity of automated human ECG analysis. Future studies in collaboration with Franc Jager, who originally suggested the Chebyshev orthogonal decomposition as an appropriate pattern-recognition for repolariza-

---

<sup>2</sup>In human ECG analysis, an ST-segment *episode* has a quantitative meaning. Currently ST-segment episodes for animals are not as well-defined in literature, so *episodes* in animal studies are species-dependent and prone to ad-hoc, per-study definition. Nonetheless researchers can set a pre-defined criterion for ST-segment deviation in the time-domain, or perhaps deviation from an established point in Chebyshev space, as discussed in chapter 7 - for episode definition.

tion segments, will likely explore use of Chebyshev analysis on human ST-segment databases such as the Long-Term ST Database and the European Society for Cardiology Database.

THIS PAGE INTENTIONALLY LEFT BLANK

# Appendix A

## Repolarization segment onset and offset times

Chapter 2 provides a detailed justification of a repolarization period onset beginning 1 ms after the J point and ending at 40% of the RR interval after onset. This appendix provides sample ECGs and repolarization period time markers. The purpose of the appendix is to provide support for the repolarization period time point selections detailed in chapter 2. The time scale of each plot in this appendix is 1 ms/div.



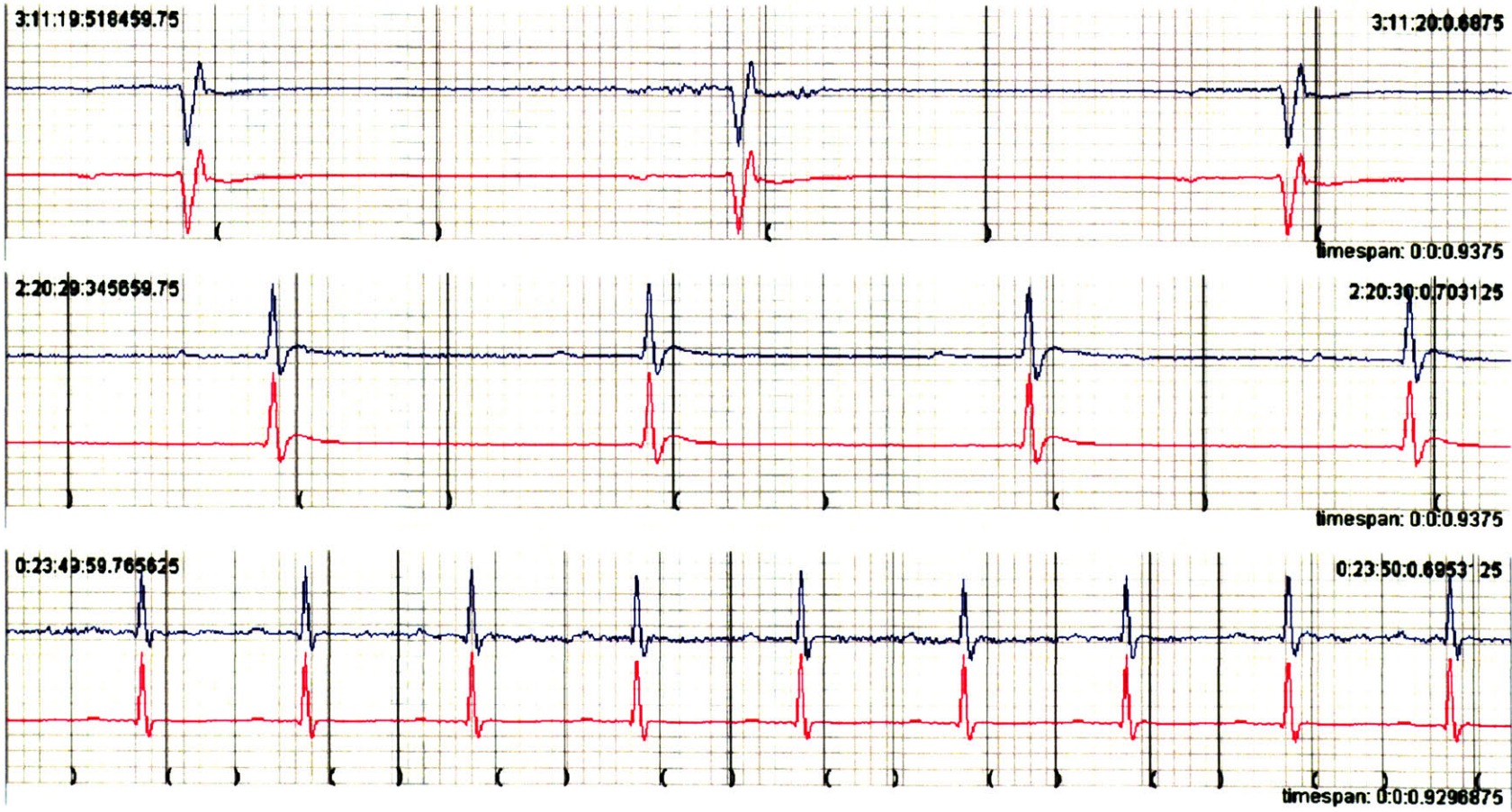


Figure A-1: Repolarization onset and offset time examples 1-3 of 18

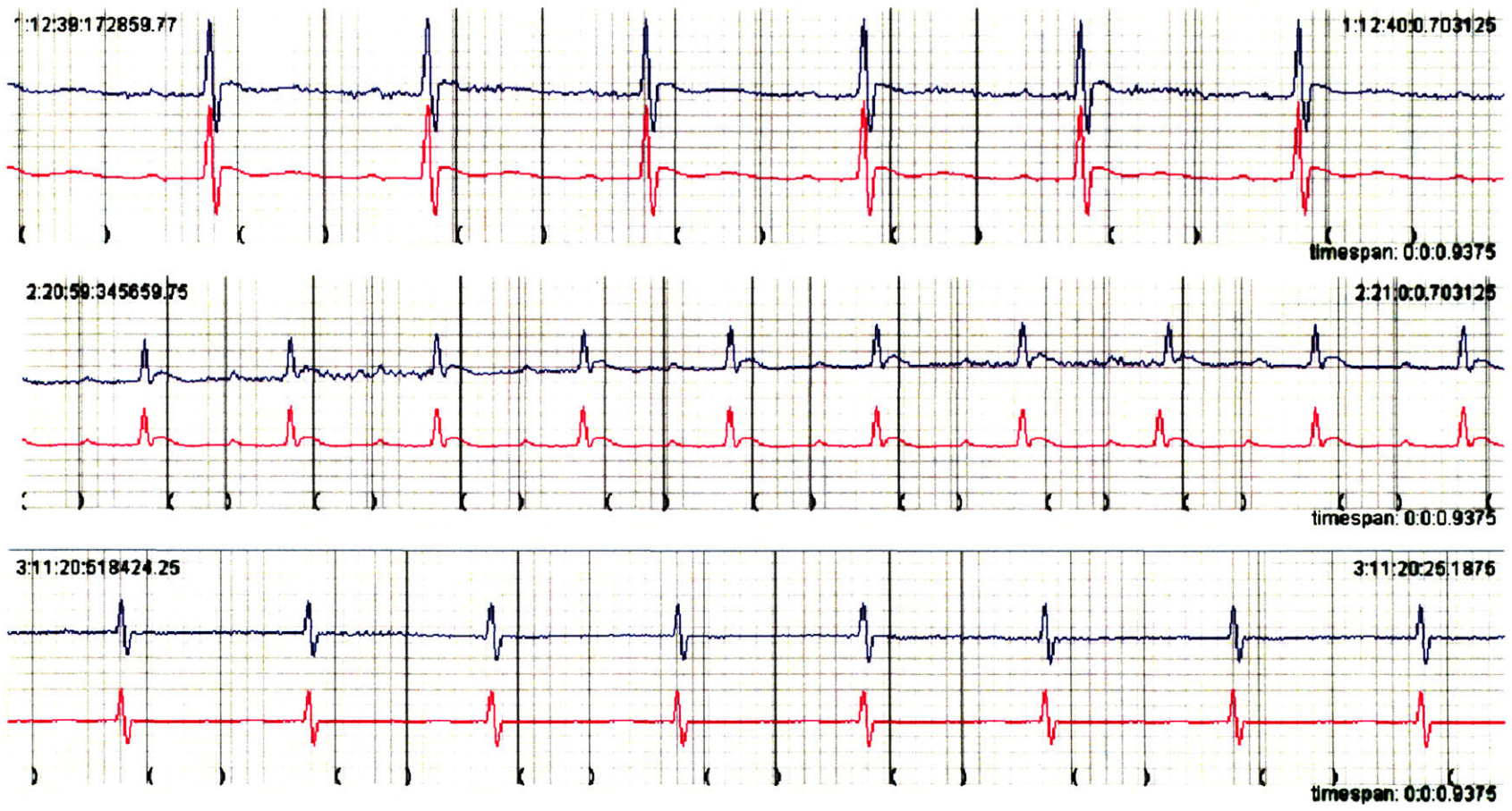


Figure A-2: Repolarization onset and offset time examples 4-6 of 18



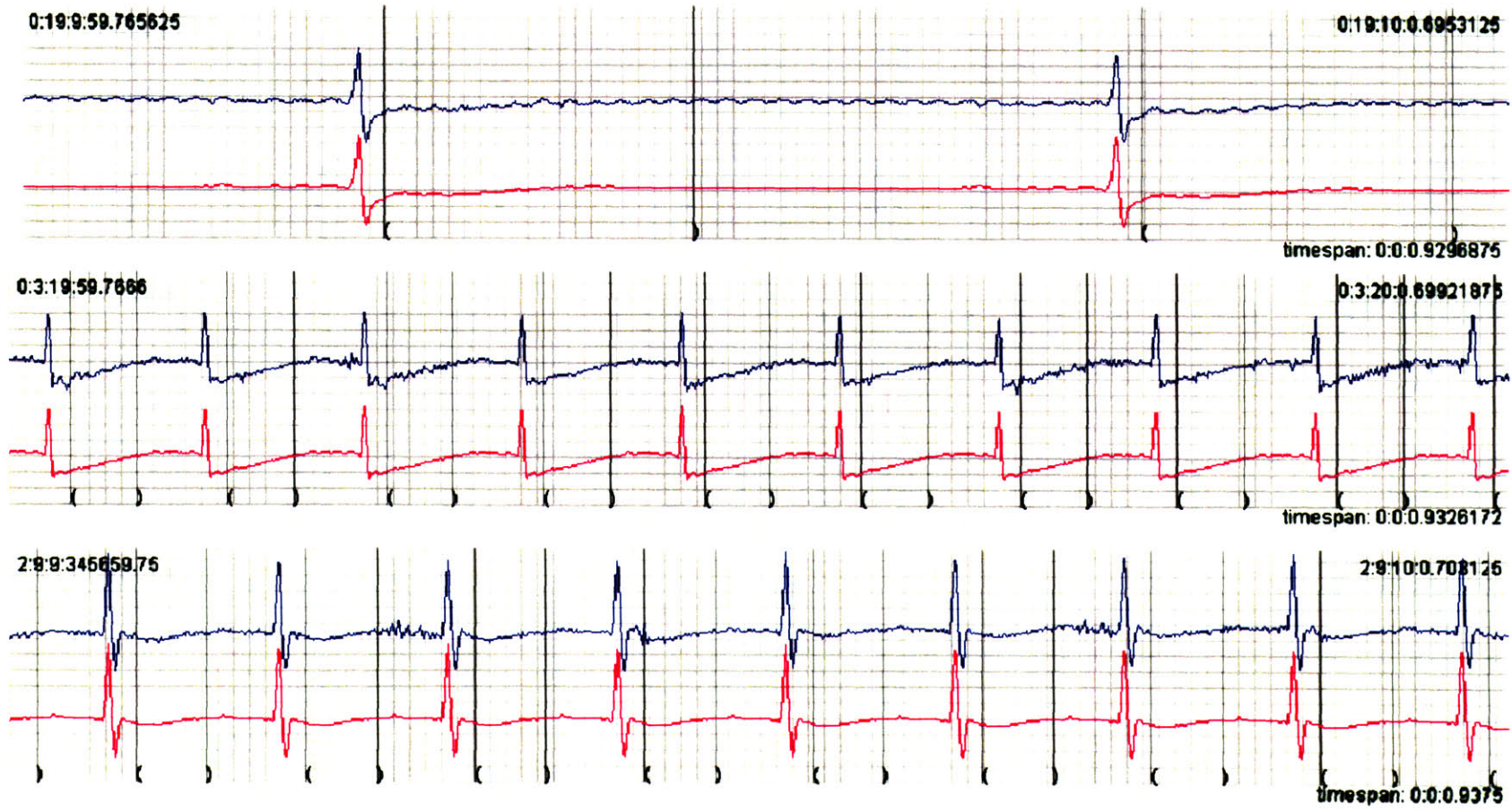
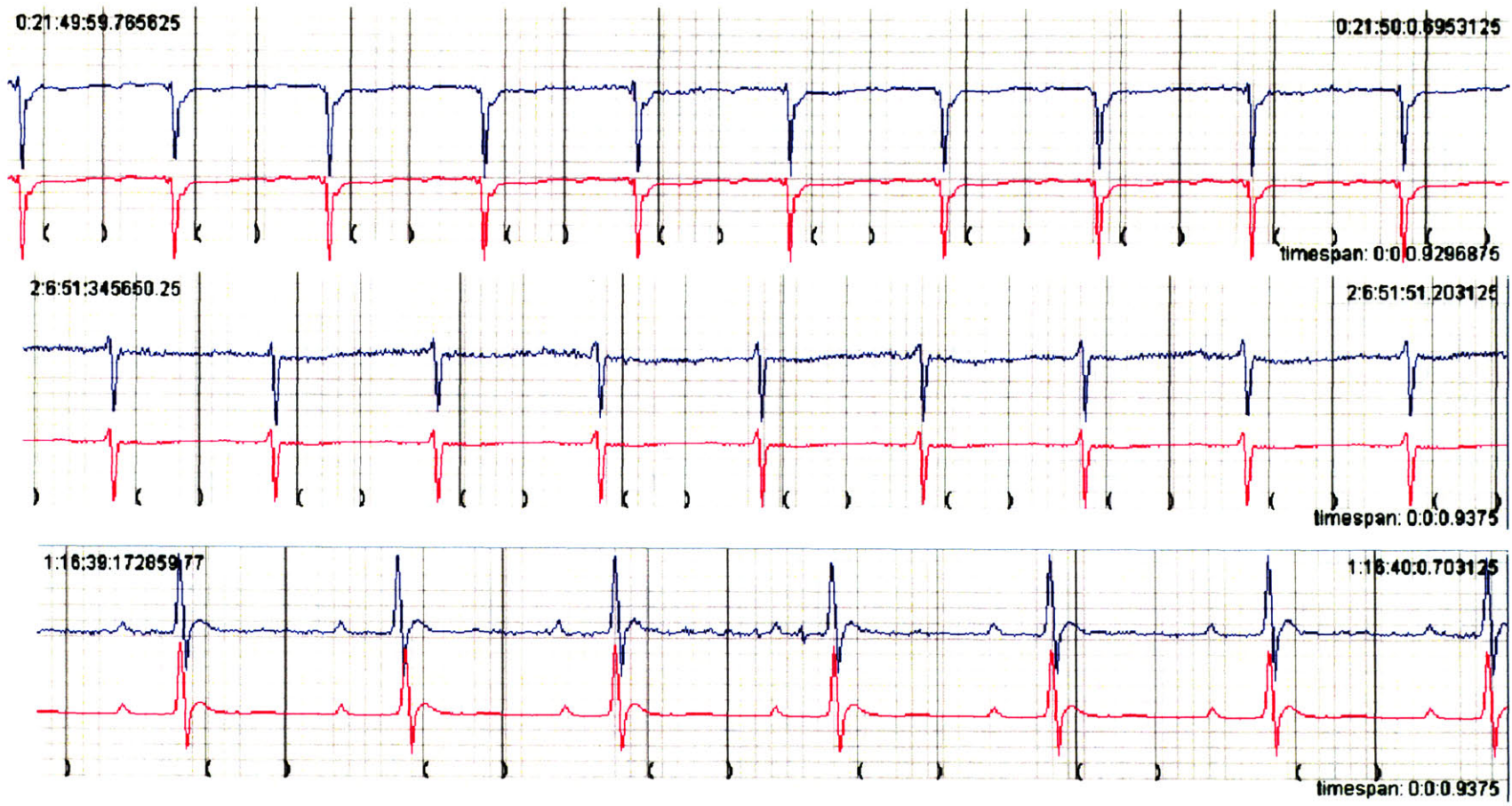
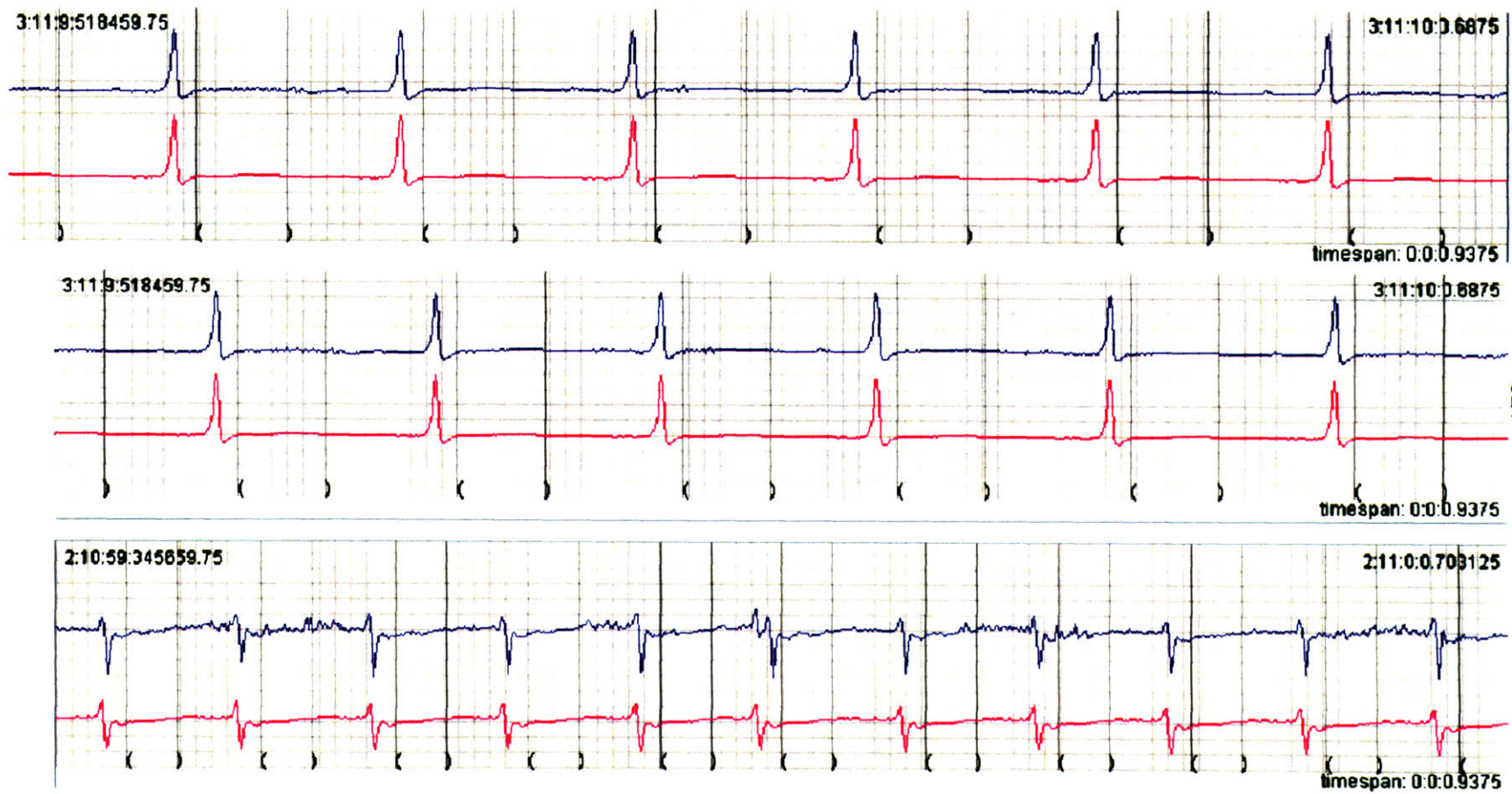


Figure A-3: Repolarization onset <sup>68</sup> and offset time examples 7-9 of 18



169  
Figure A-4: Repolarization onset and offset time examples 10-12 of 18





170

Figure A-5: Repolarization onset and offset time examples 13-15 of 18



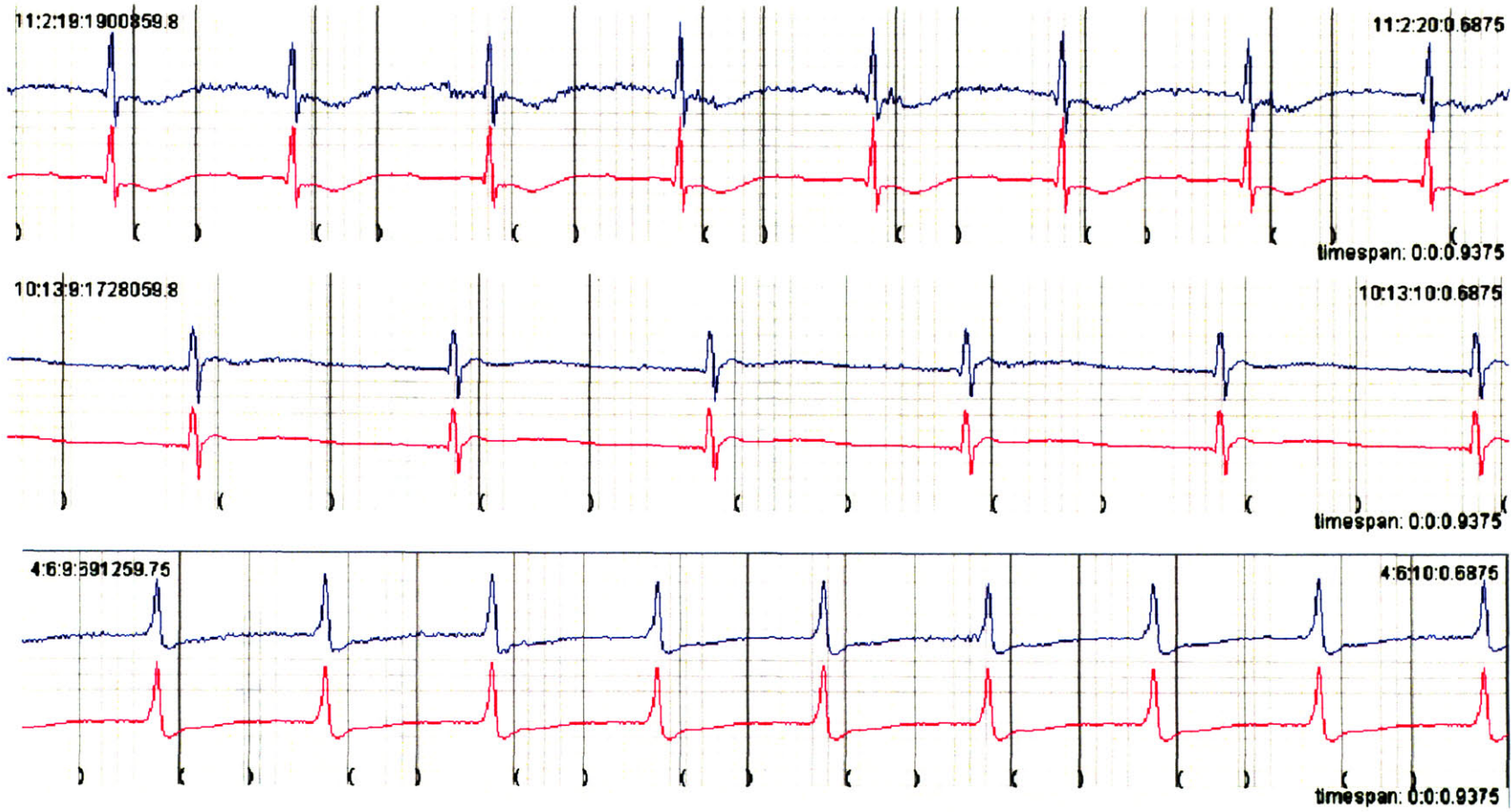


Figure A-6: Repolarization onset and offset time examples 16-18 of 18

THIS PAGE INTENTIONALLY LEFT BLANK

# Appendix B

## Trend plots for all mouse subjects

<b>Krieger Lab Mouse Database (as of July 25, 2006)</b>		
<i>Record ID</i>	<i>Genotype</i>	<i>Age at Recording Onset (days)</i>
0365121403	RAG DKO	37
0666122303	RAG DKO	31
0800122603	HPL TKO	35
0898122703	RAG DKO	33
0902122703	RAG DKO	32
0911123103	RAG DKO	33
0920122903	RAG DKO	31
0921122903	RAG DKO	31
0922122903	RAG DKO	31
1608011604	HPL DKO	35
1808011604	HPL TKO	32
2190020704	HPL DKO	31
2241020104	RAG DKO	30
2334020604	RAG DKO	32
2335020604	RAG DKO	33
2336020604	RAG DKO	33
2338020604	RAG DKO	33
2541020404	RAG DKO	41
2767022103	RAG DKO	38
2786022103	RAG DKO	38
3222031004	RAG DKO	33
3225031004	RAG DKO	33
3231030904	RAG DKO	34
4630040604	RAG DKO	31
4631040604	RAG DKO	31
5462040105	RAG KO WT	125 <sup>1</sup>
5463040105	RAG KO WT	125 <sup>2</sup>
6591081803	HET DKO	43
6842083003	HPL TKO	32
6846090403	HPL DKO	29
7602091903	HYPOE	49
8083100303	HPL TKO	35
8086100303	HPL TKO	61 <sup>3</sup>
9050040505	RAG DKO	32
9394111603	RAG DKO	33
9399111603	RAG DKO	33
9715112203	HET DKO	31
9775112103	HPL TKO	32
9907120503	RAG DKO	34
9908120503	RAG DKO	34
9909120503	RAG DKO	34

Table B.1: This table reflects all records in the Krieger Lab mouse database as of July 25, 2006.

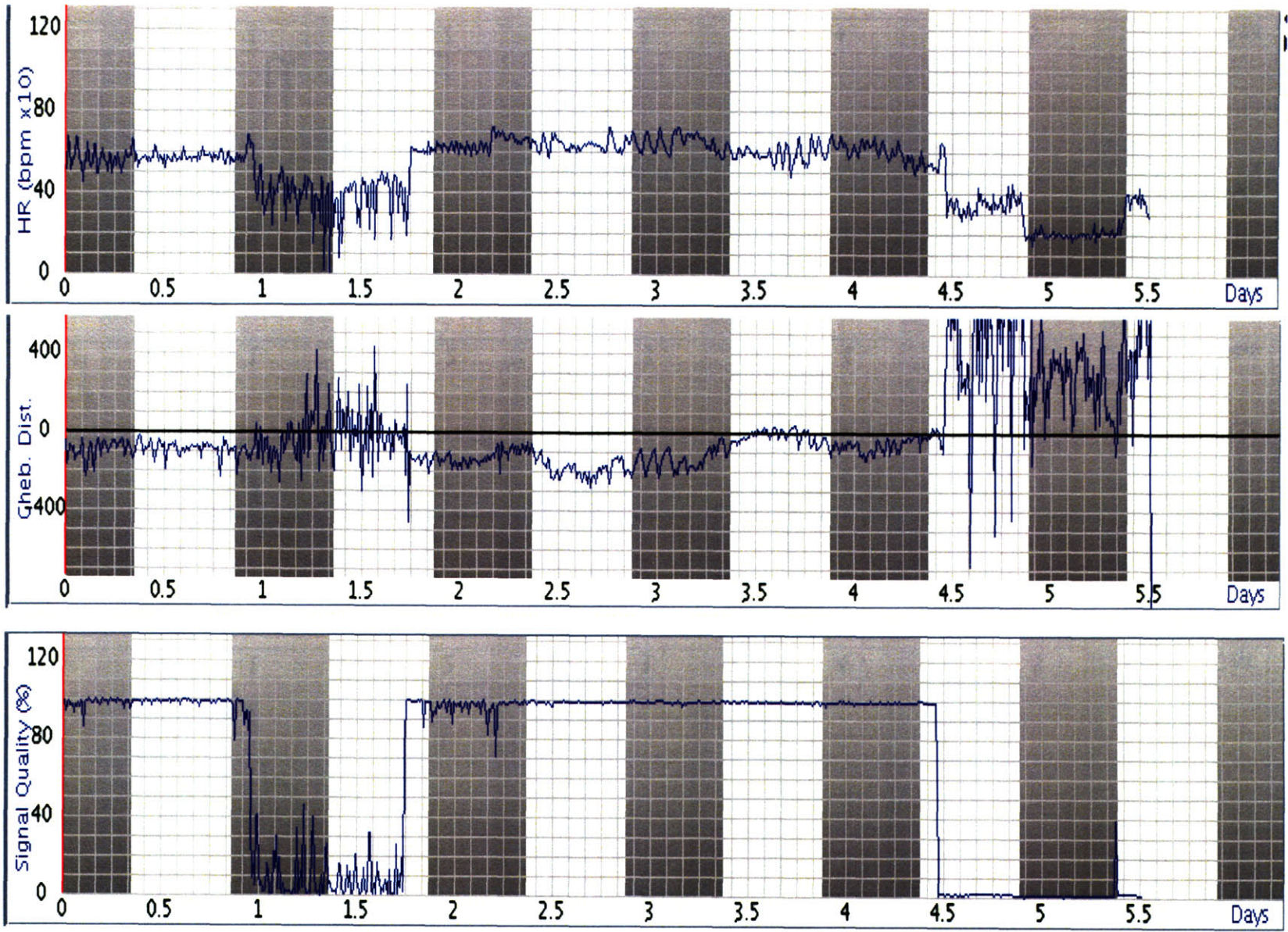


Figure B-1: heart rate, repolarization morphology and signal quality index for subject 0365121403  
175



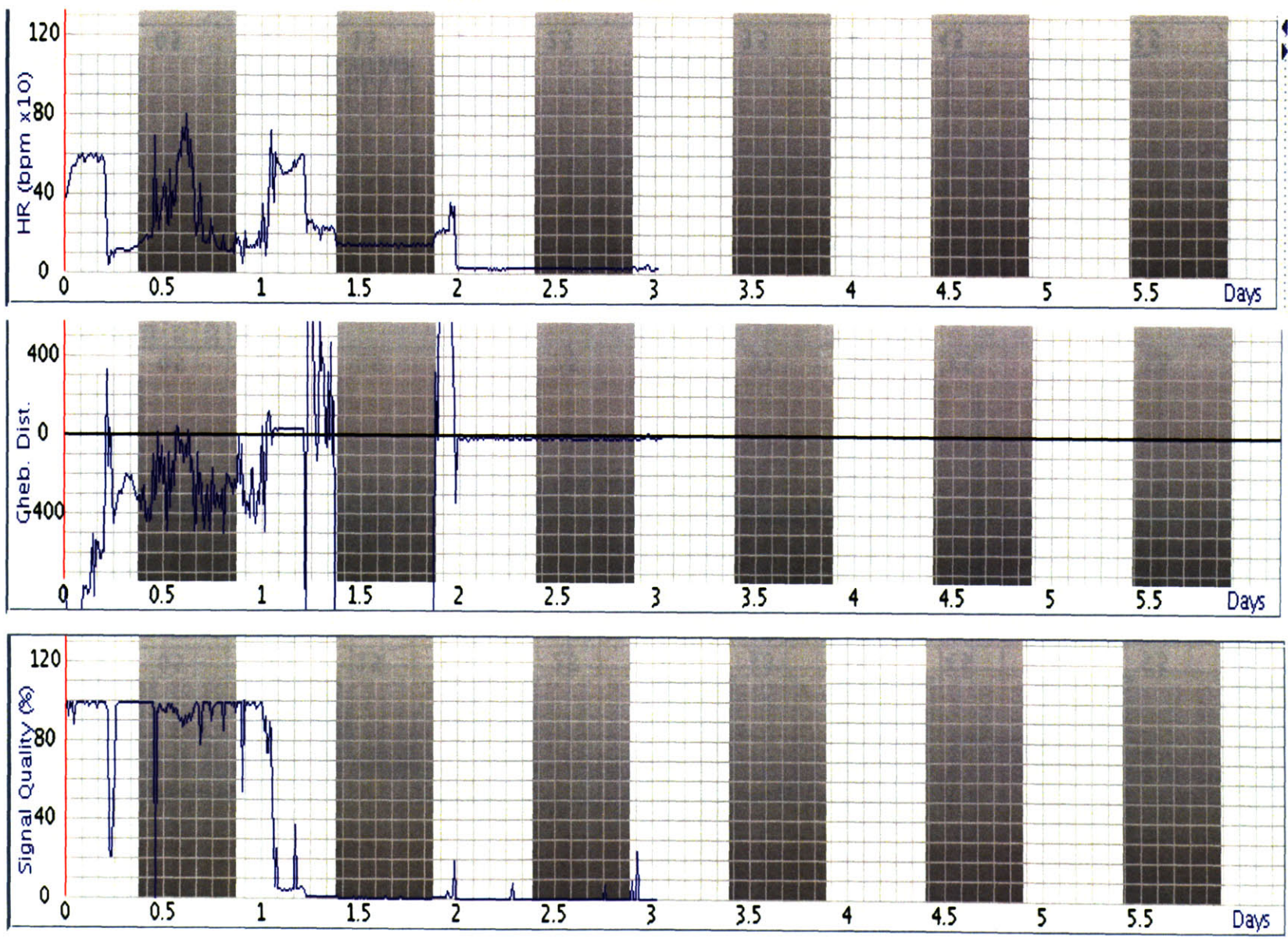


Figure B-2: heart rate, repolarization morphology and signal quality index for subject 0666122303  
176



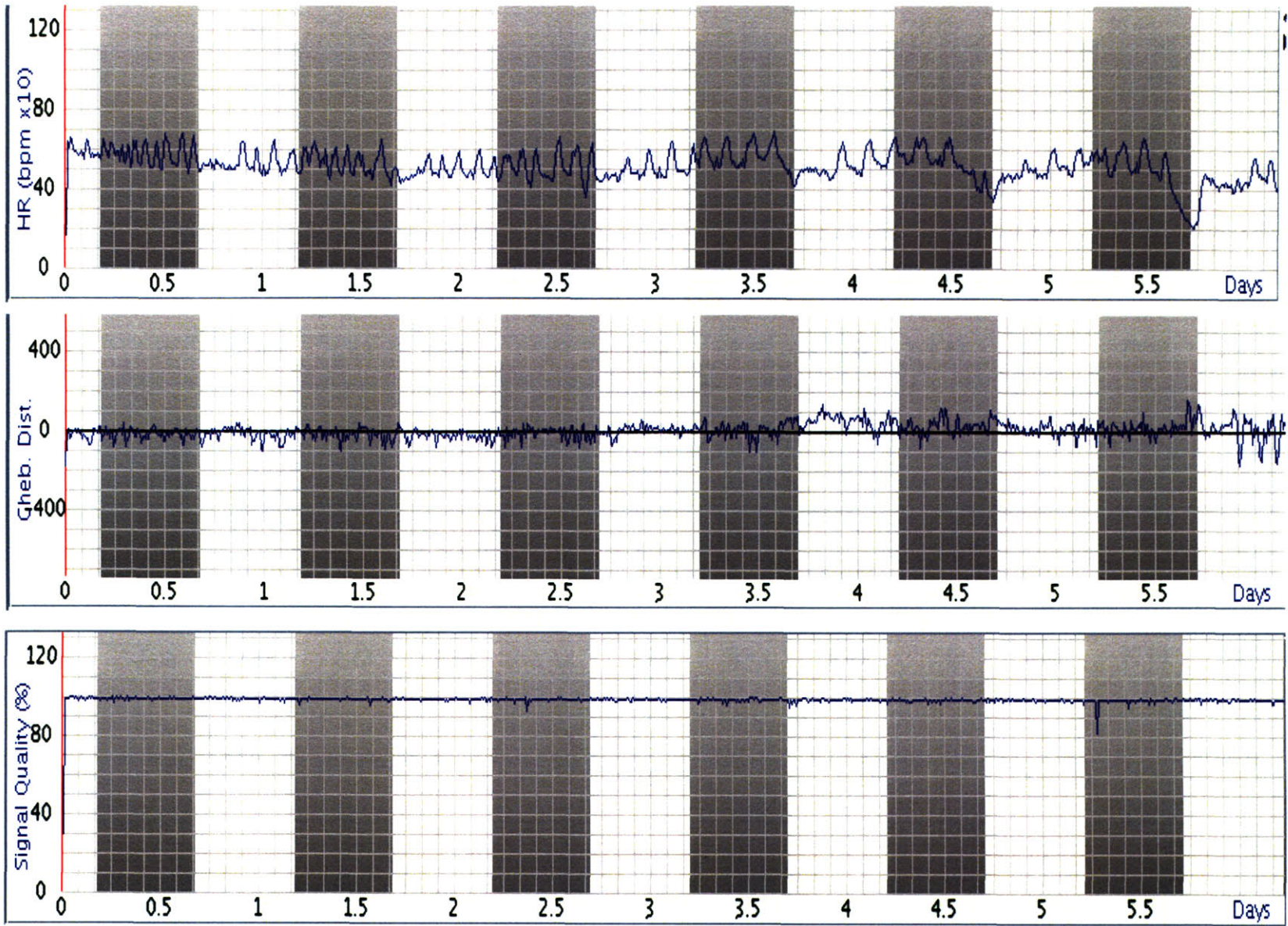


Figure B-3: heart rate, repolarization morphology and signal quality index for subject 0800122603 - 1 of 4



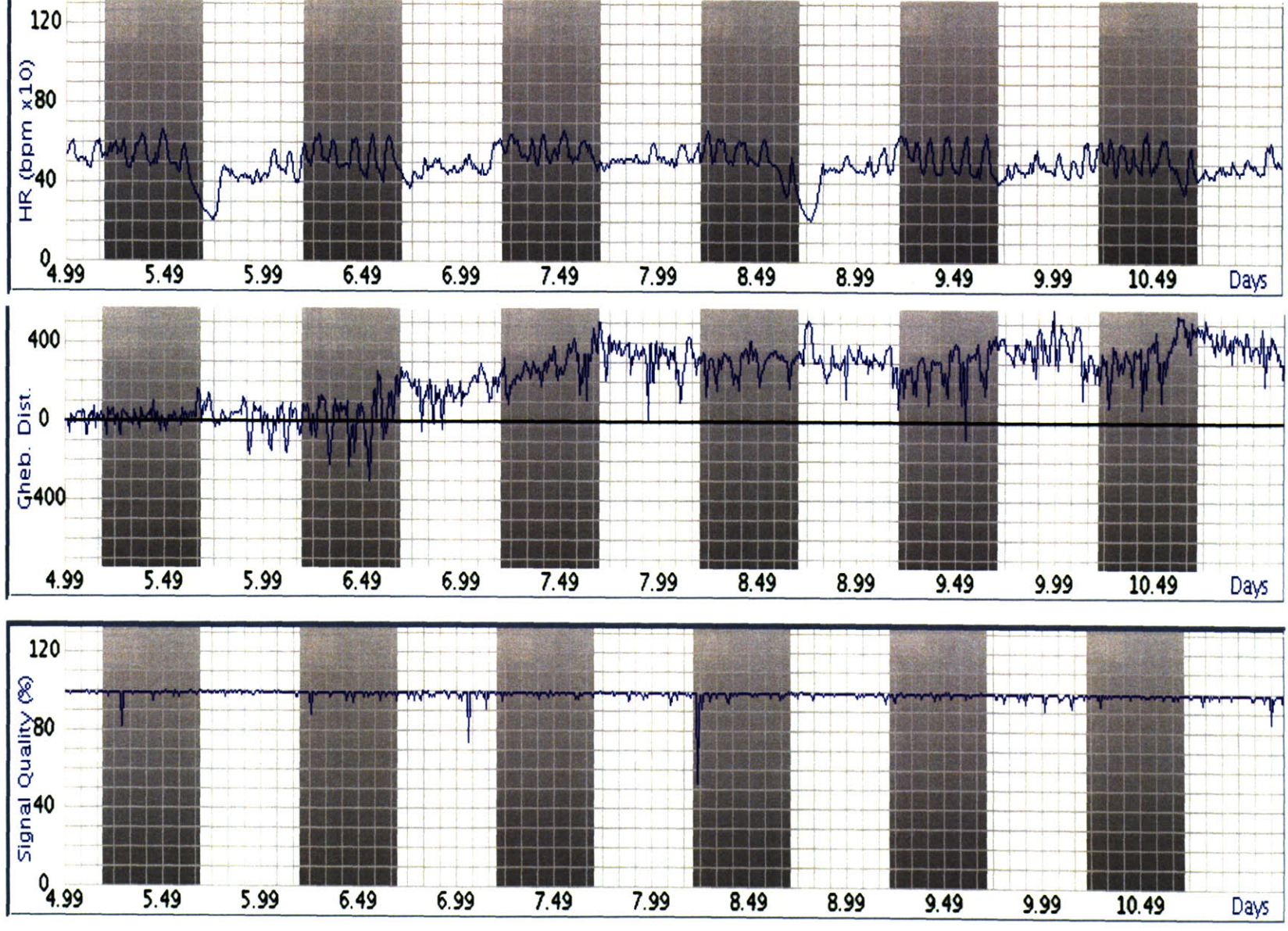


Figure B-4: heart rate, repolarization morphology and signal quality index for subject 0800122603 - 2 of 4  
178



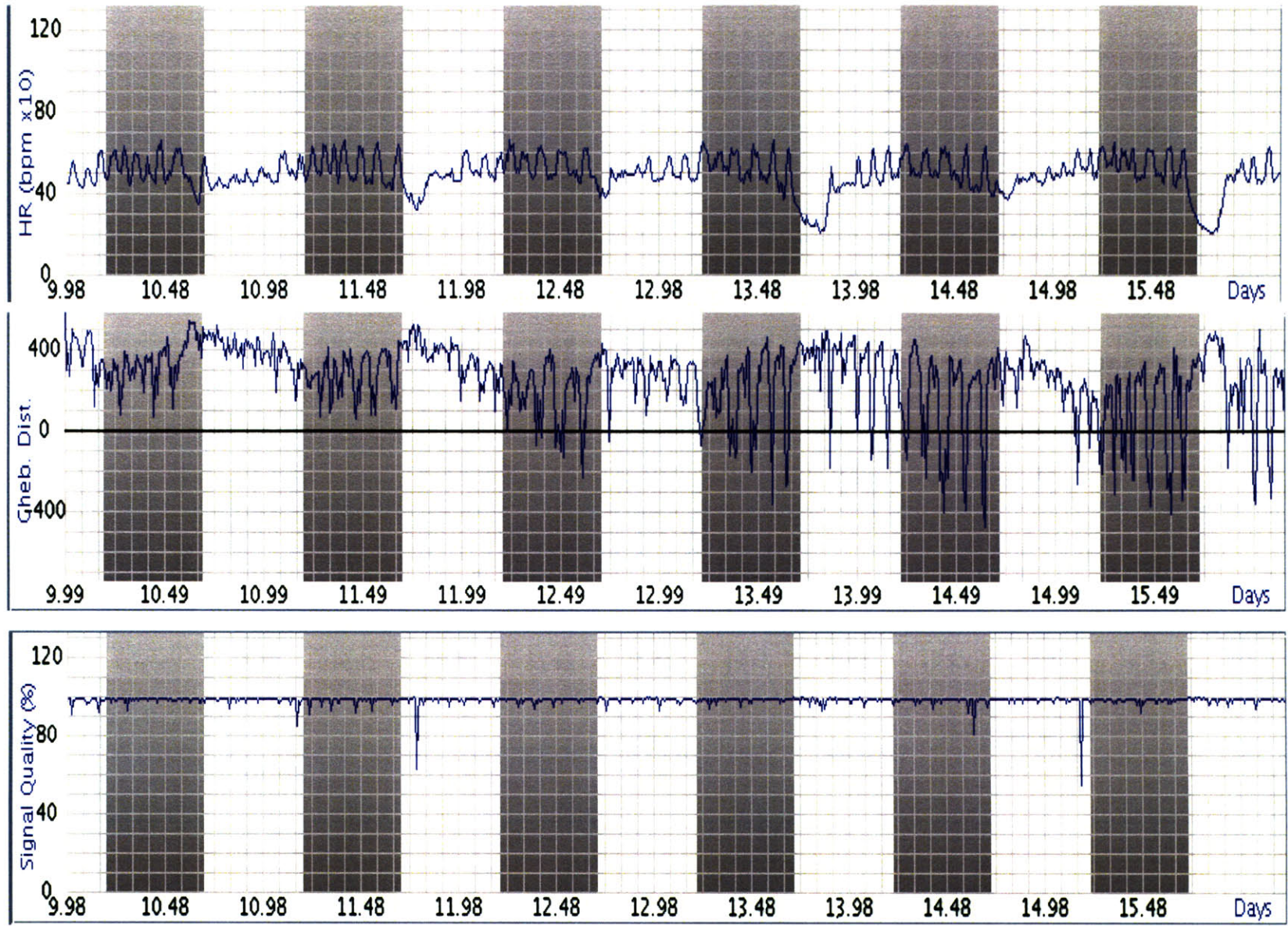


Figure B-5: heart rate, repolarization morphology and signal quality index for subject 0800122603 - 3 of 4  
179



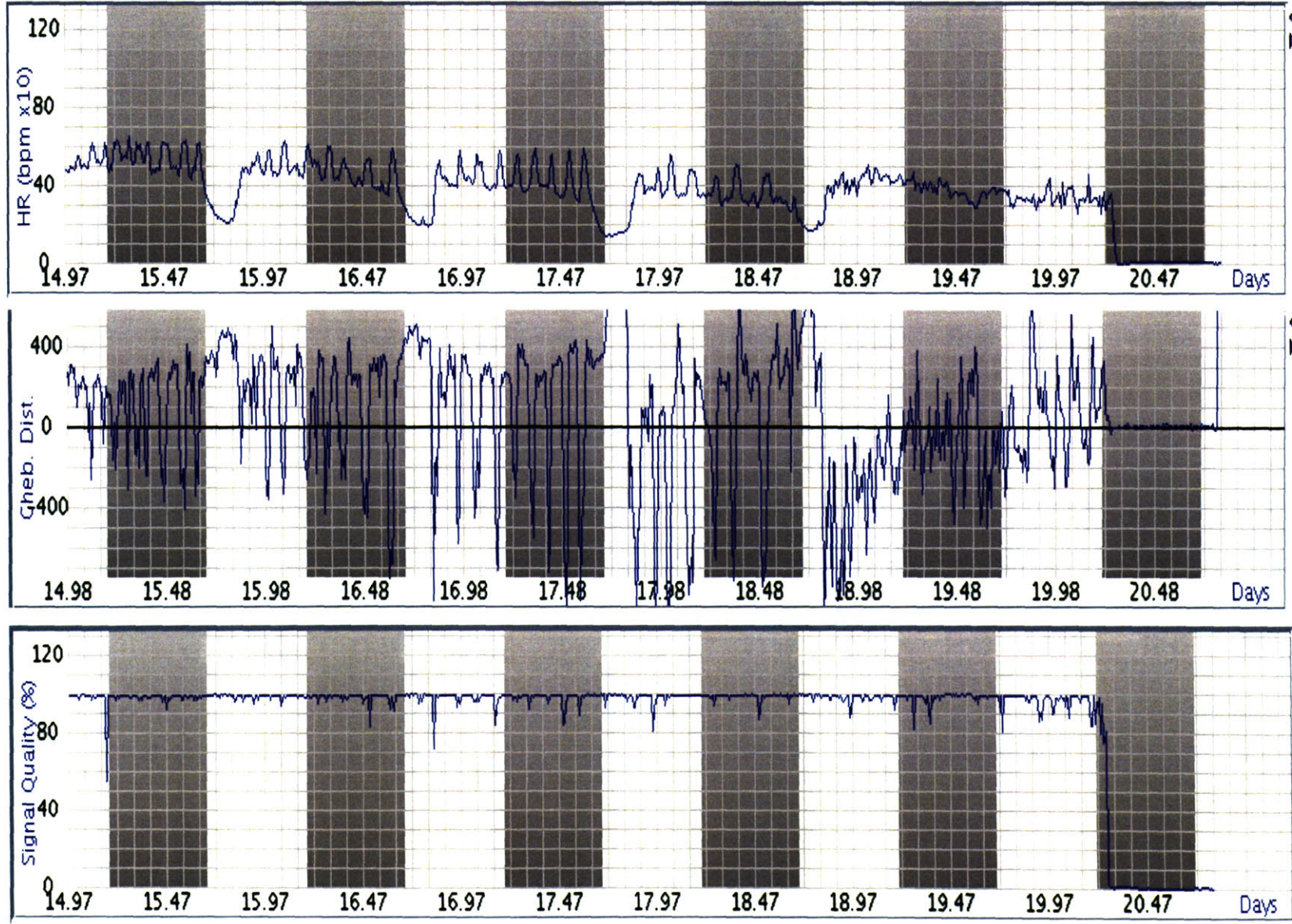


Figure B-6: heart rate, repolarization morphology and signal quality index for subject 0800122603 - 4 of 4  
180



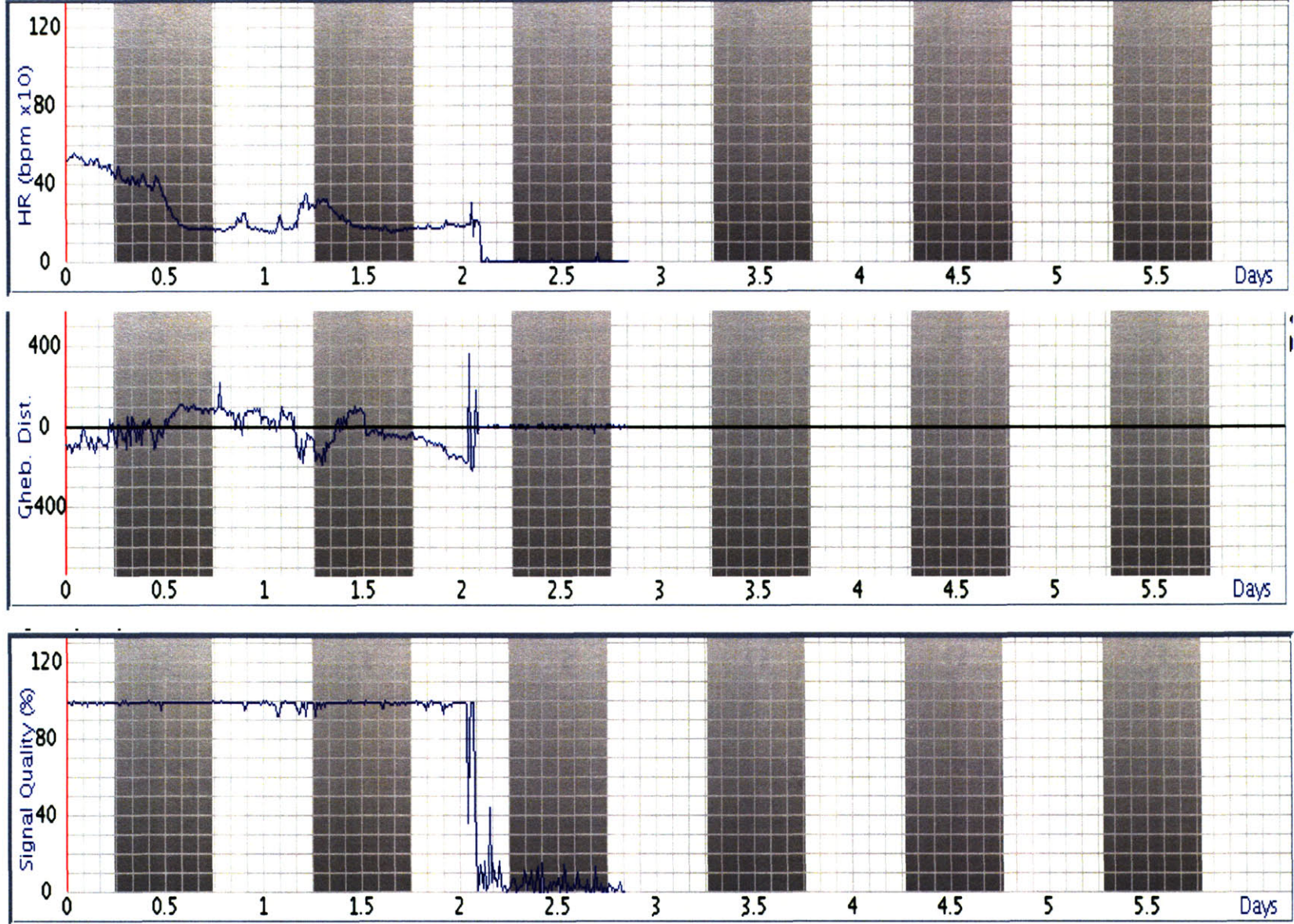


Figure B-7: heart rate, repolarization morphology and signal quality index for subject 0898122703



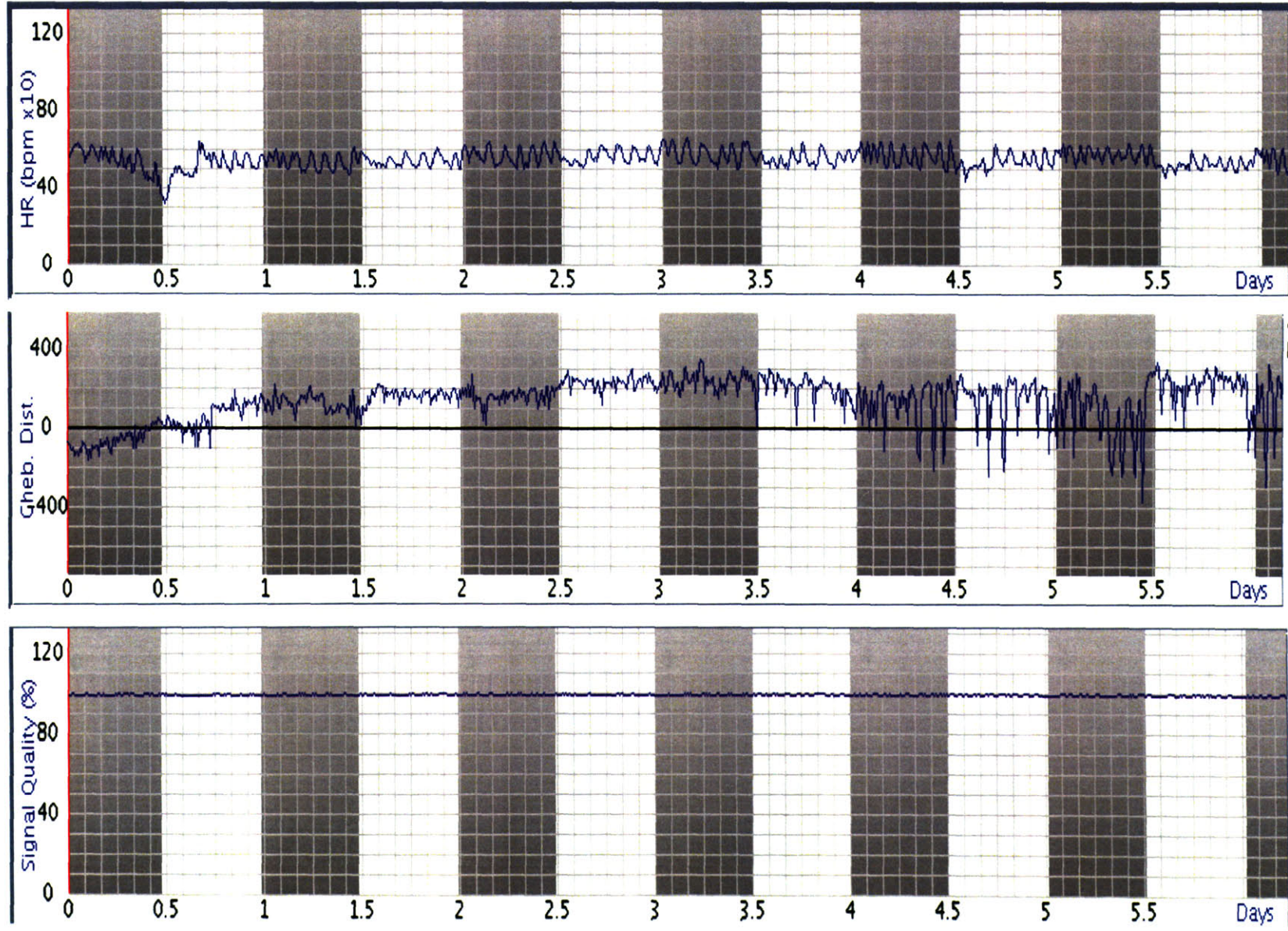


Figure B-8: heart rate, repolarization morphology and signal quality index for subject 0902122703 - 1 of 2  
182



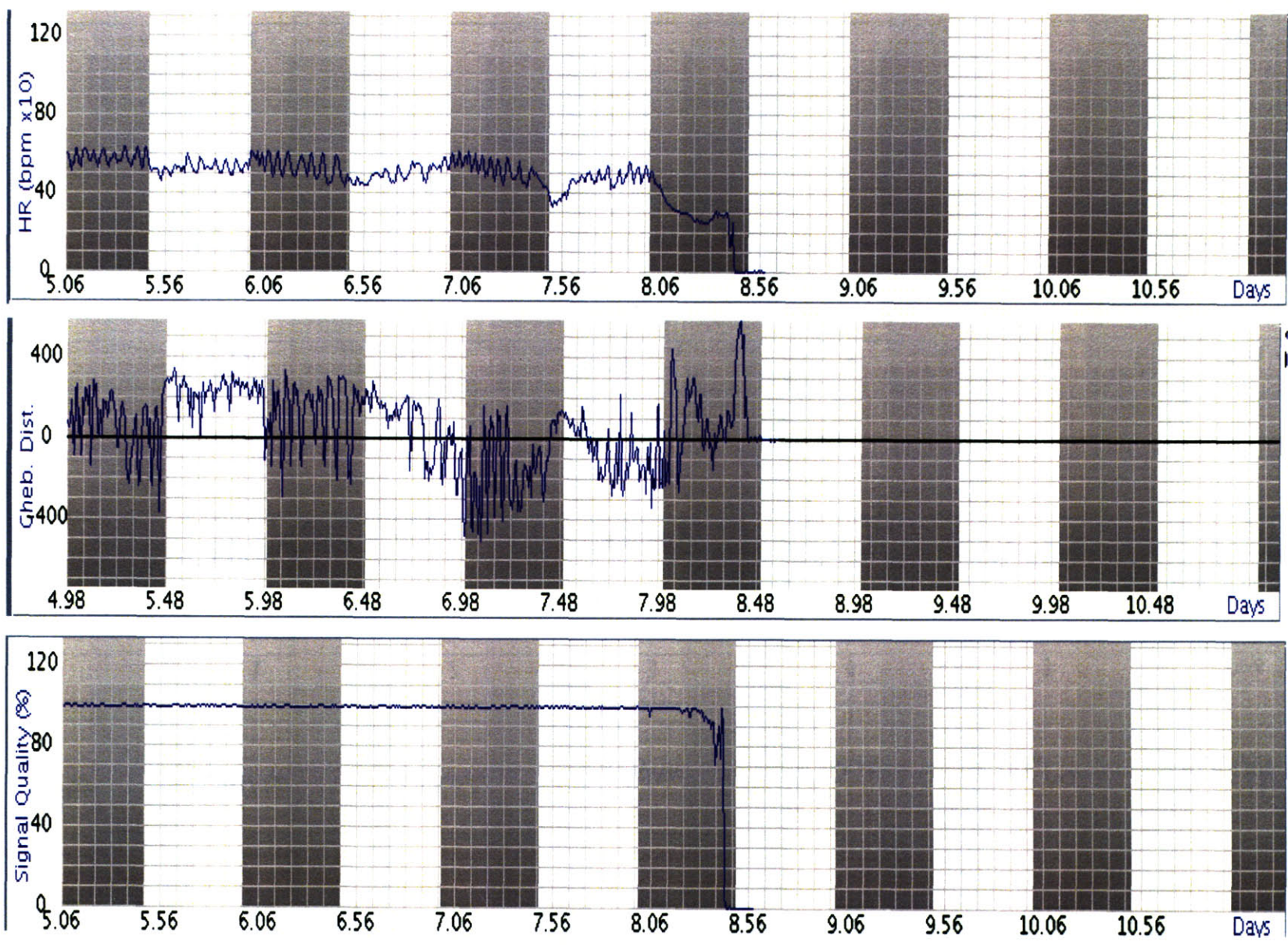


Figure B-9: heart rate, repolarization morphology and signal quality index for subject 0902122703 - 2 of 2



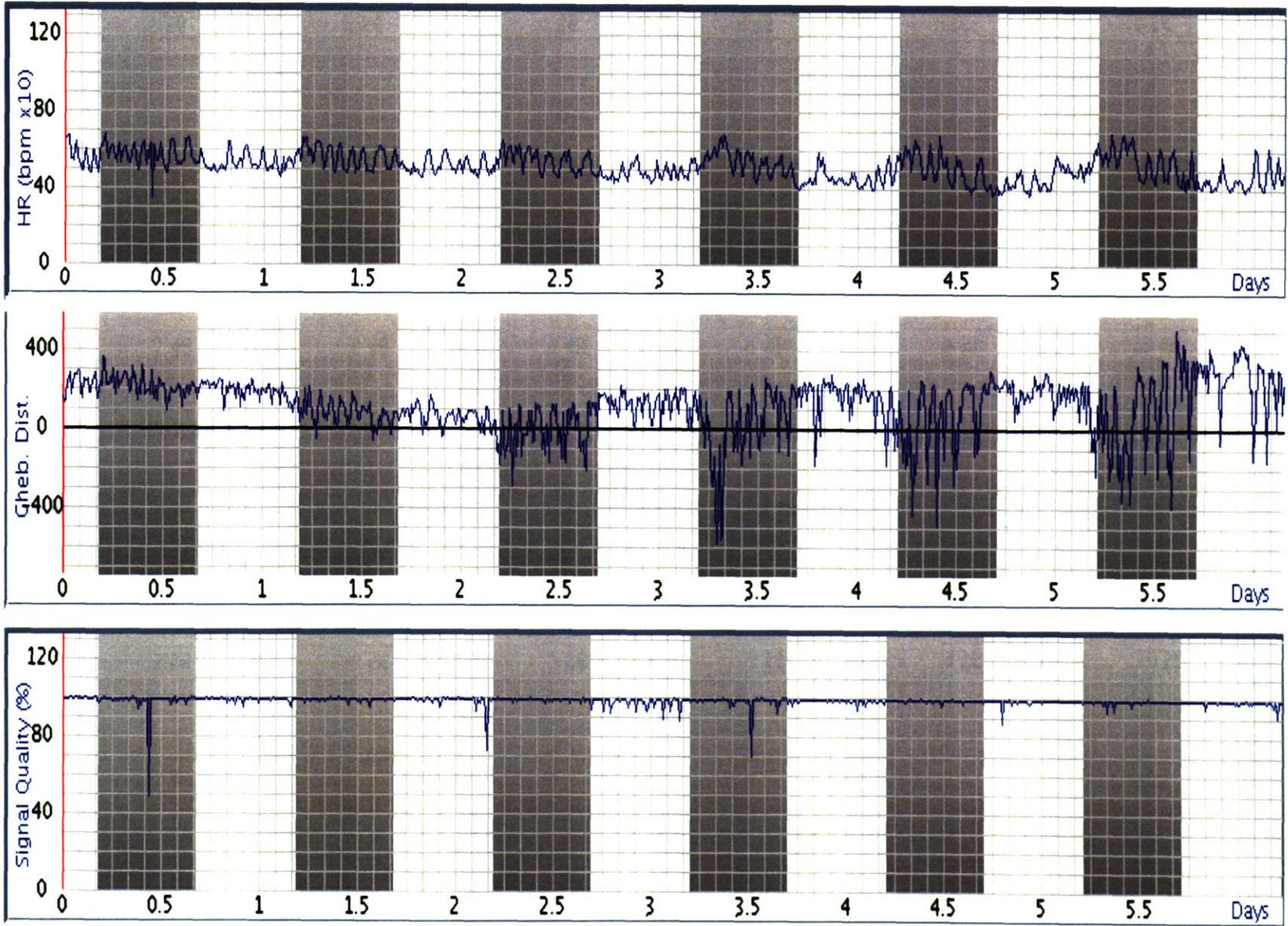


Figure B-10: heart rate, repolarization morphology and signal quality index for subject 0911123103 - 1 of 2  
184



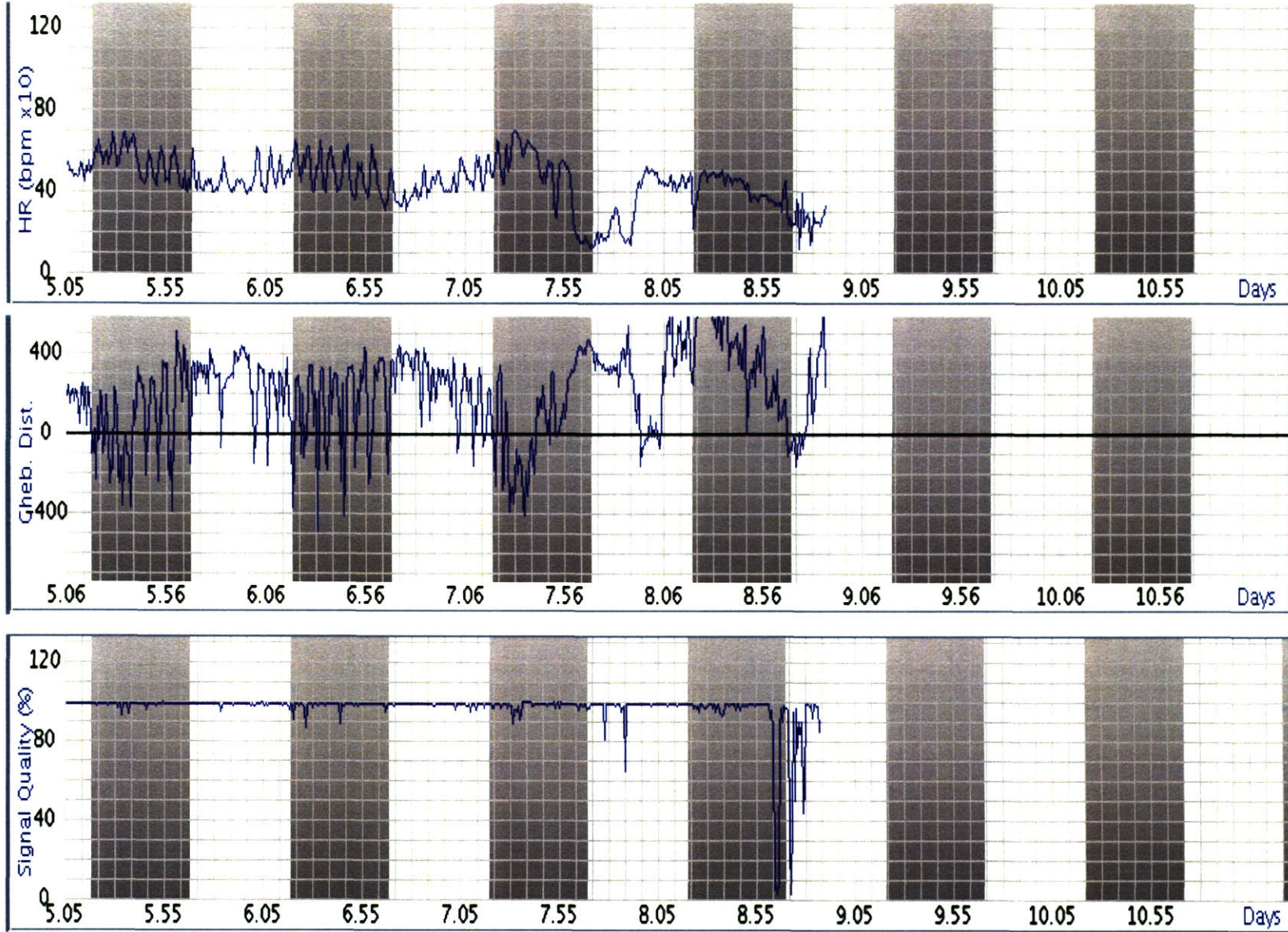


Figure B-11: heart rate, repolarization morphology and signal quality index for subject 0911123103 - 2 of 2



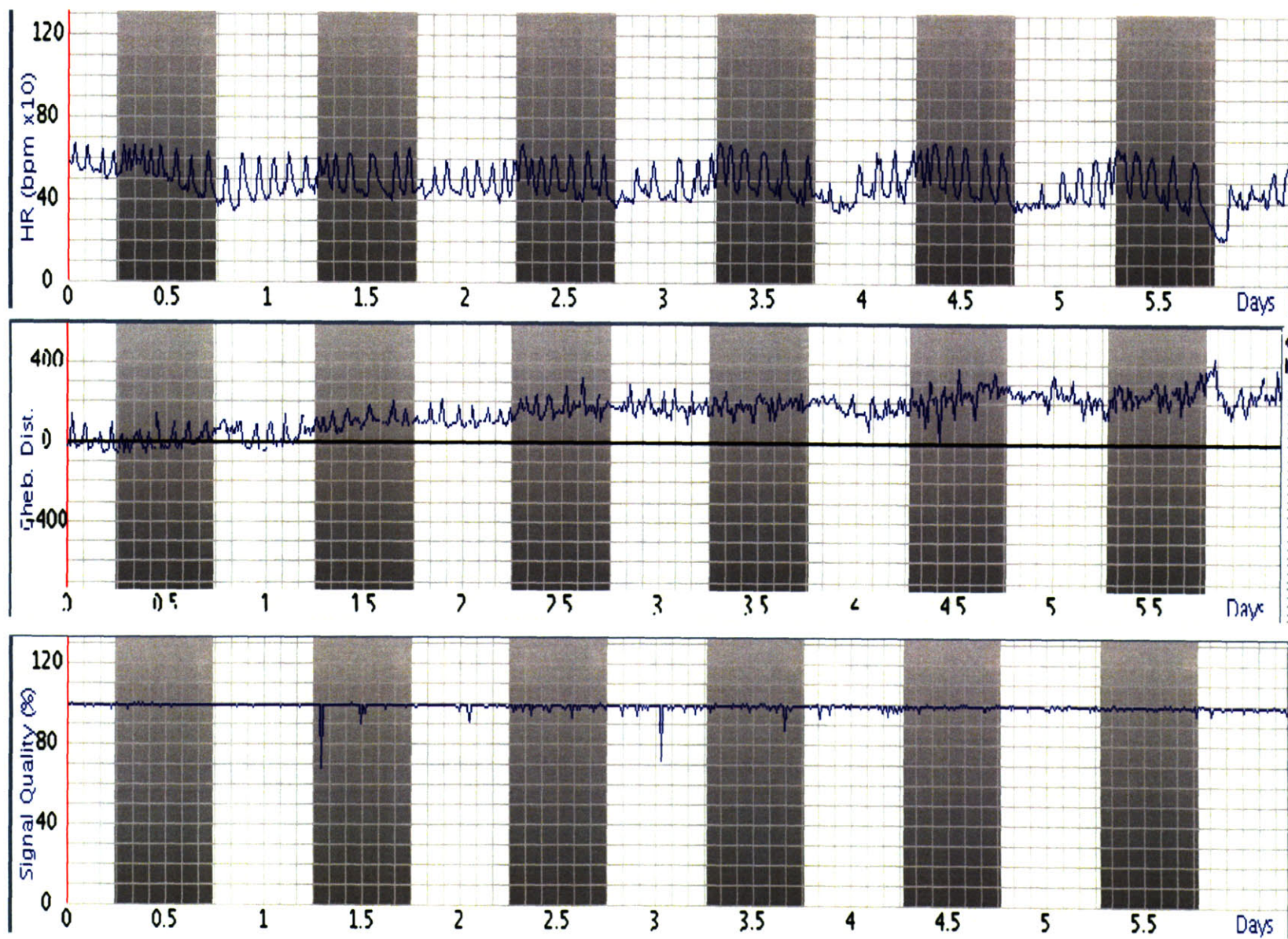


Figure B-12: heart rate, repolarization morphology and signal quality index for subject 0920122903 - 1 of 4  
186



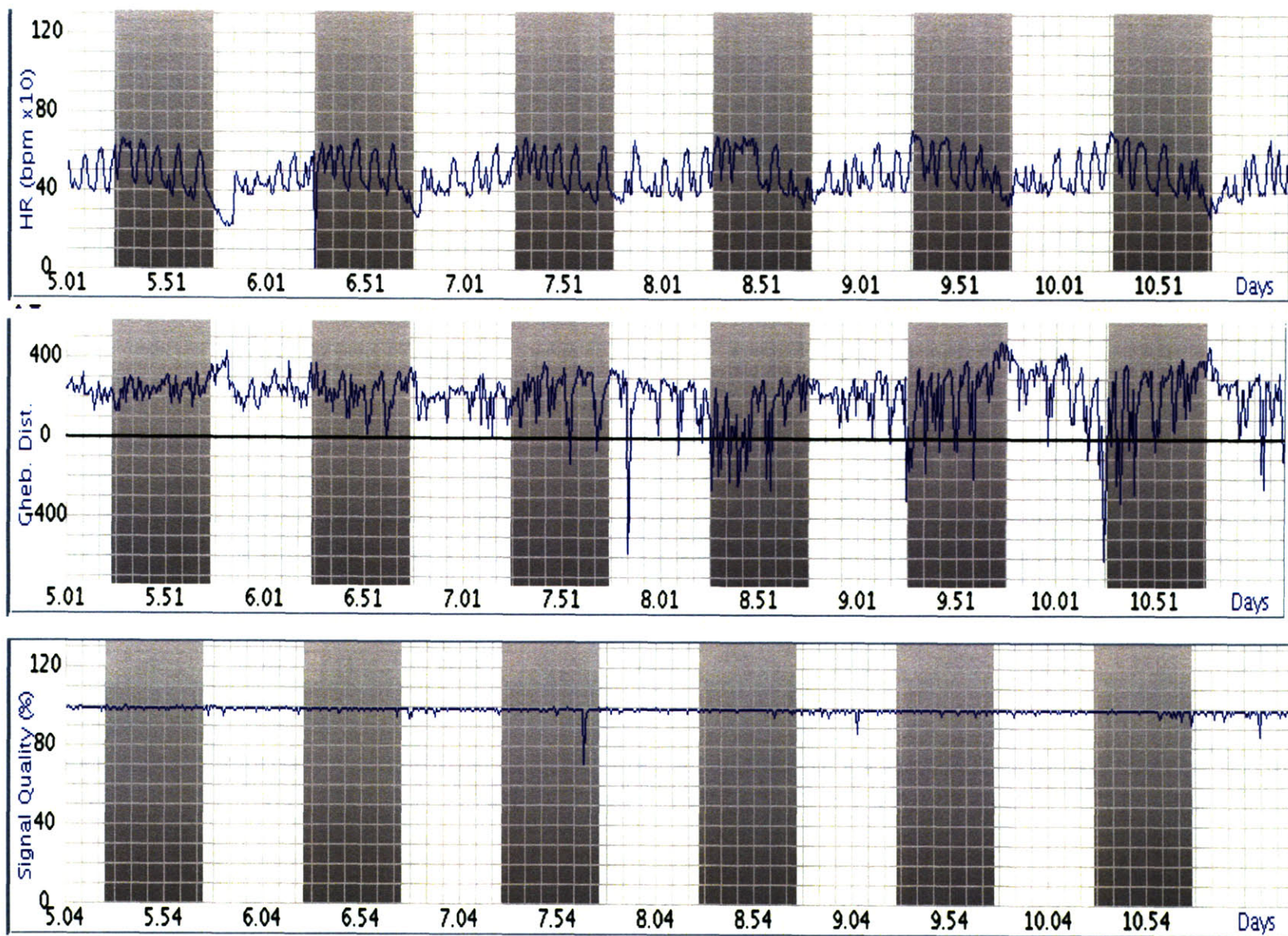


Figure B-13: heart rate, repolarization morphology and signal quality index for subject 0920122003 - 2 of 4  
187



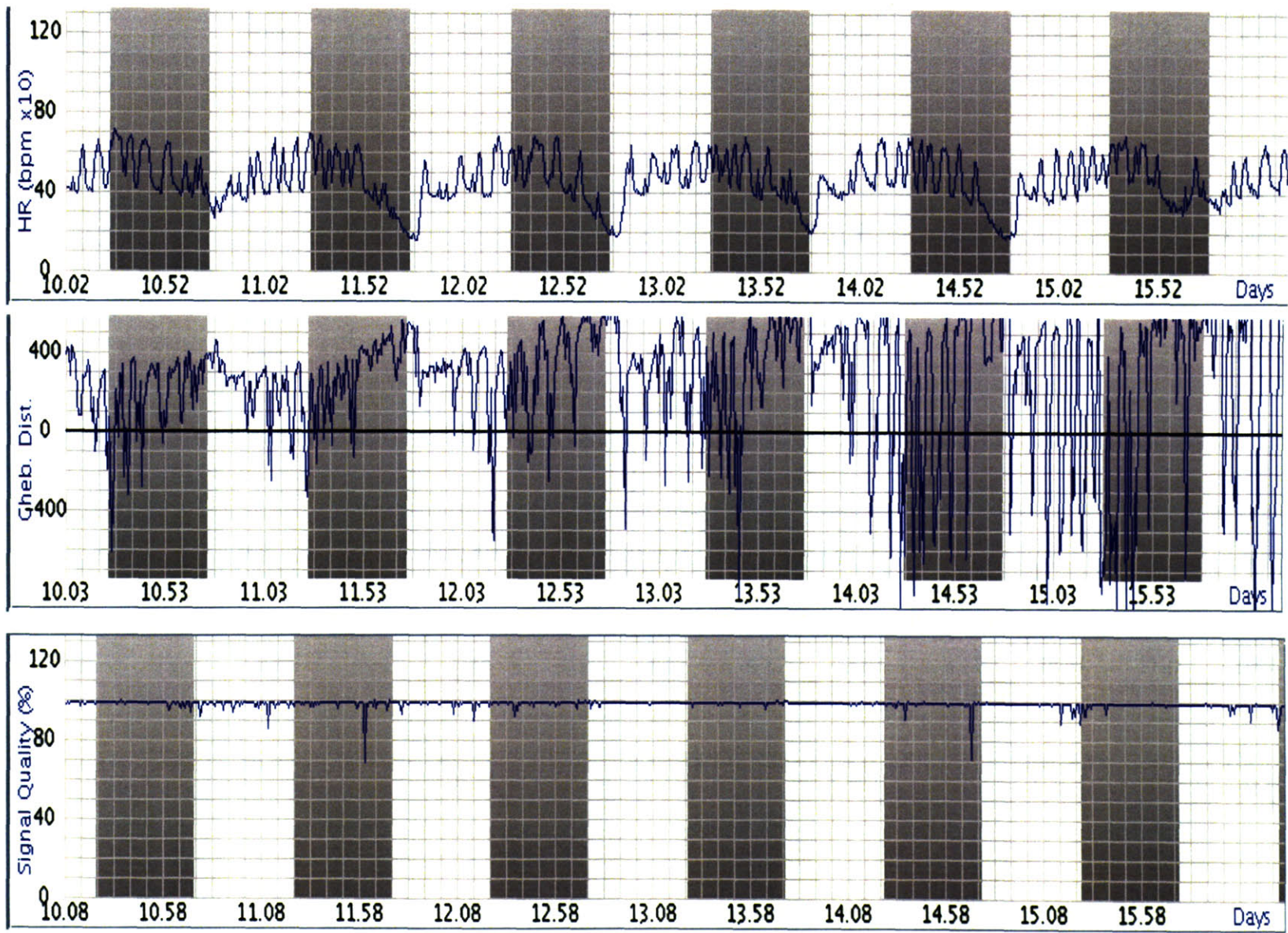


Figure B-14: heart rate, repolarization morphology and signal quality index for subject 0920122903 - 3 of 4



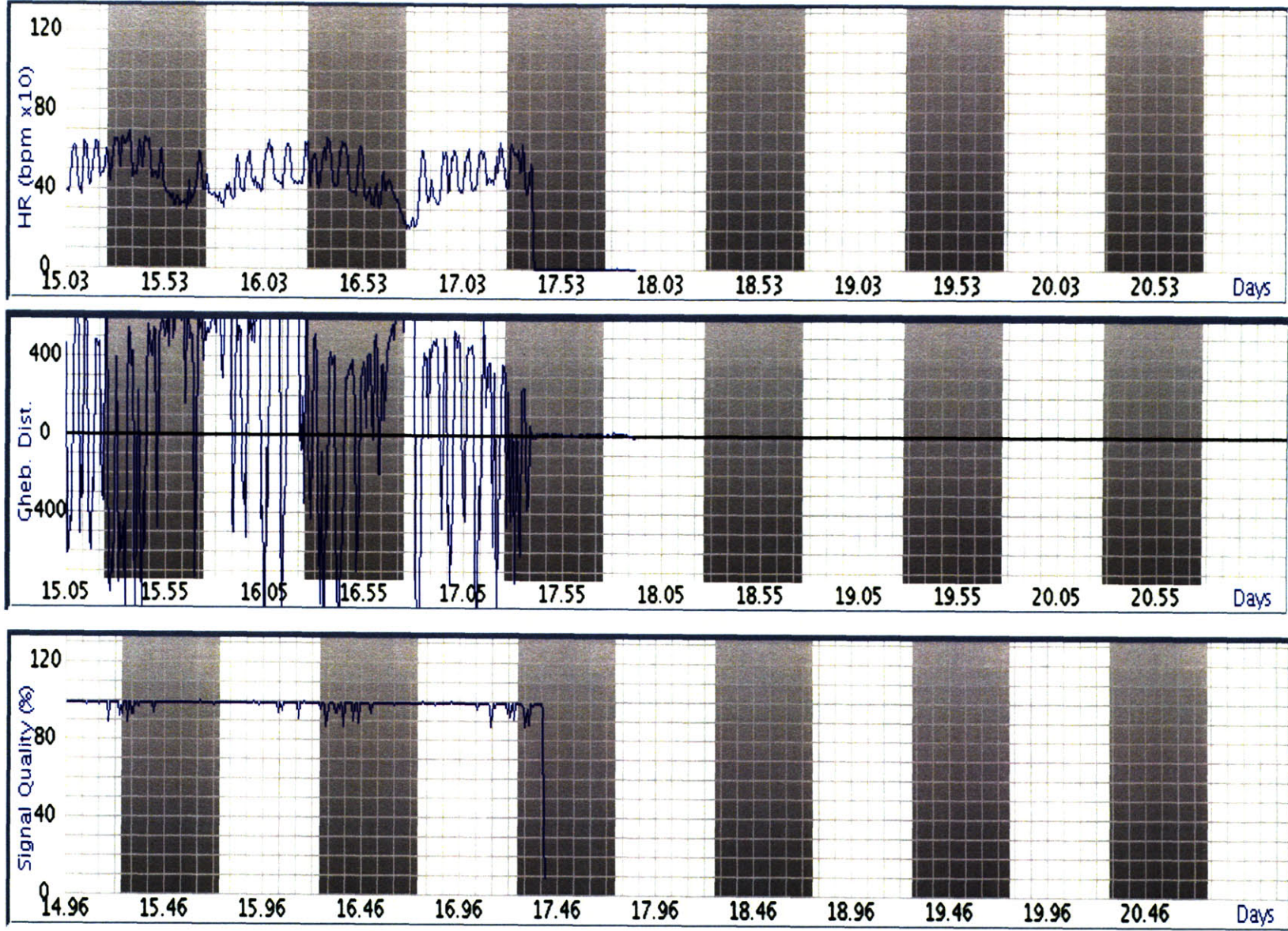


Figure B-15: heart rate, repolarization morphology and signal quality index for subject 0920122903 - 4 of 4  
189



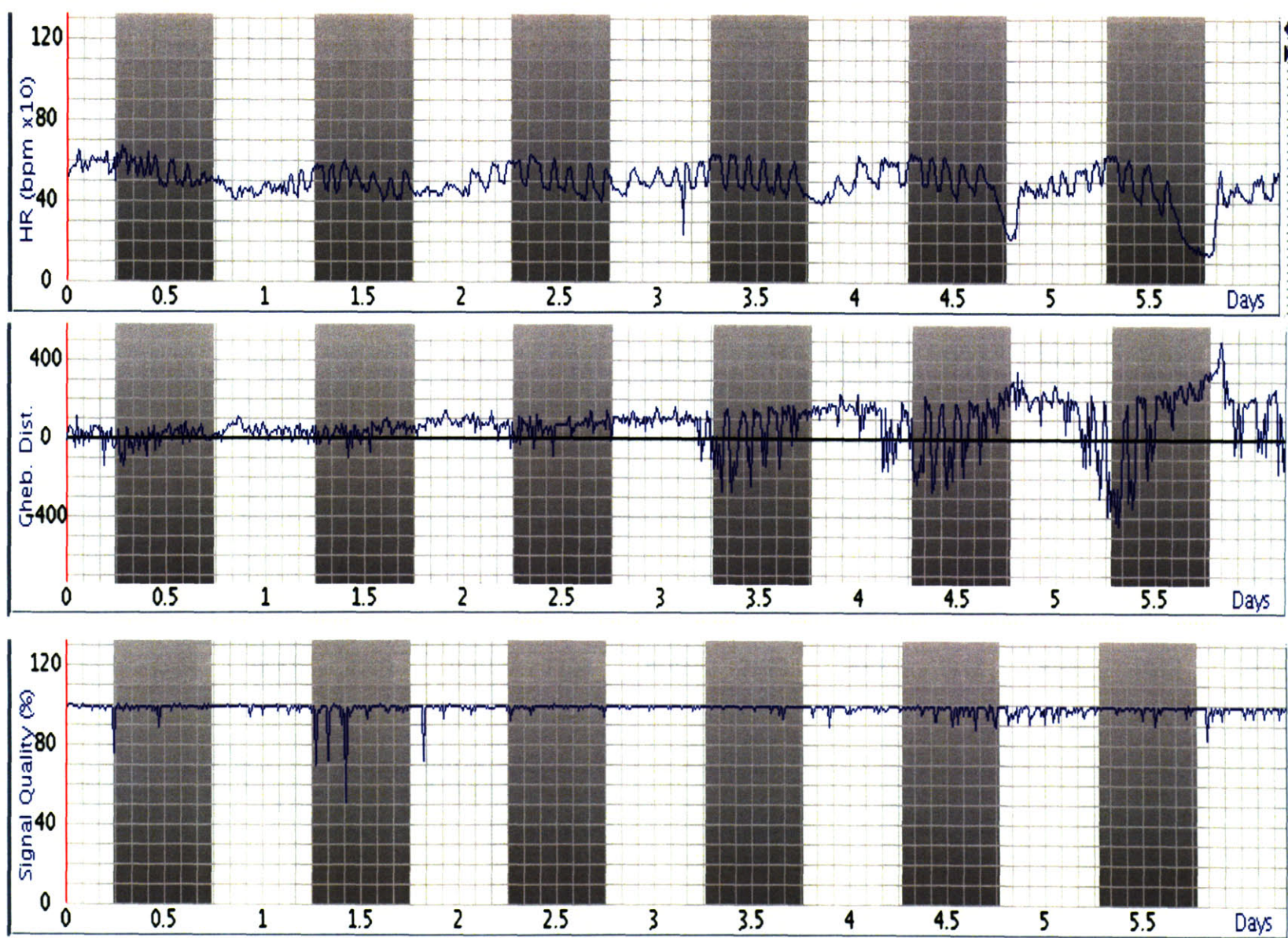


Figure B-16: heart rate, repolarization morphology and signal quality index for subject 0921122903 - 1 of 3



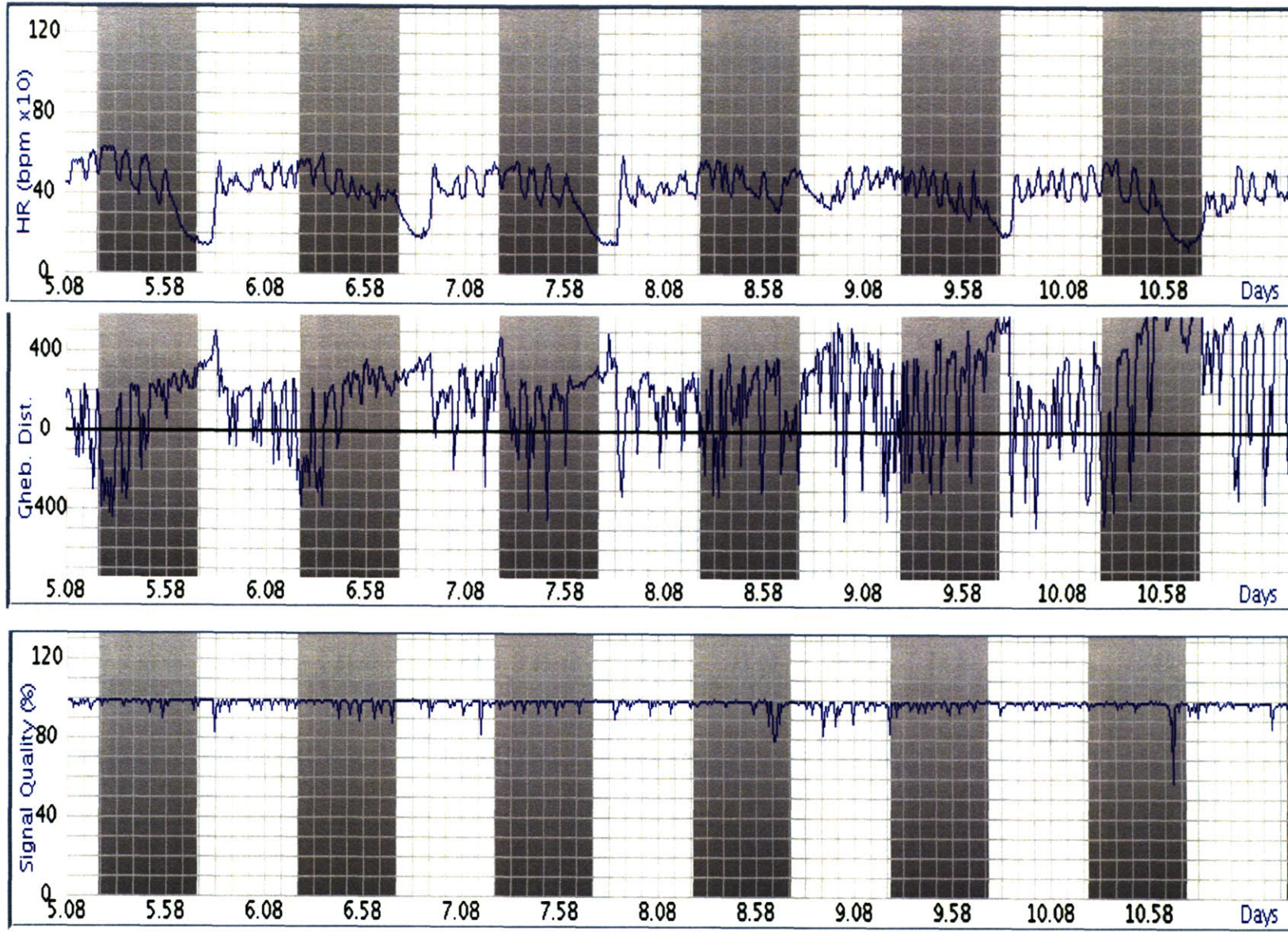


Figure B-17: heart rate, repolarization morphology and signal quality index for subject 0921122003 - 2 of 3



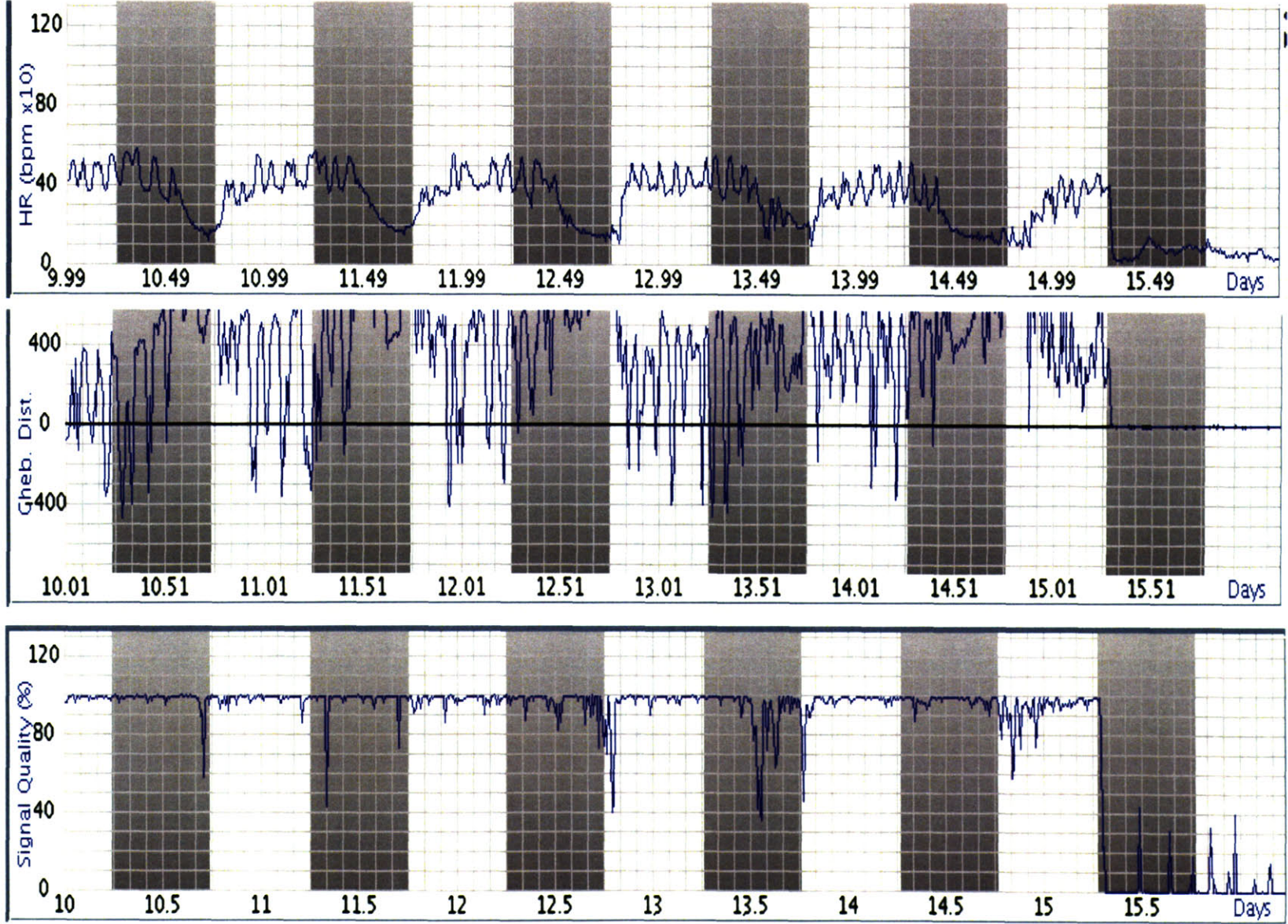


Figure B-18: heart rate, repolarization morphology and signal quality index for subject 0921122903 - 3 of 3  
192



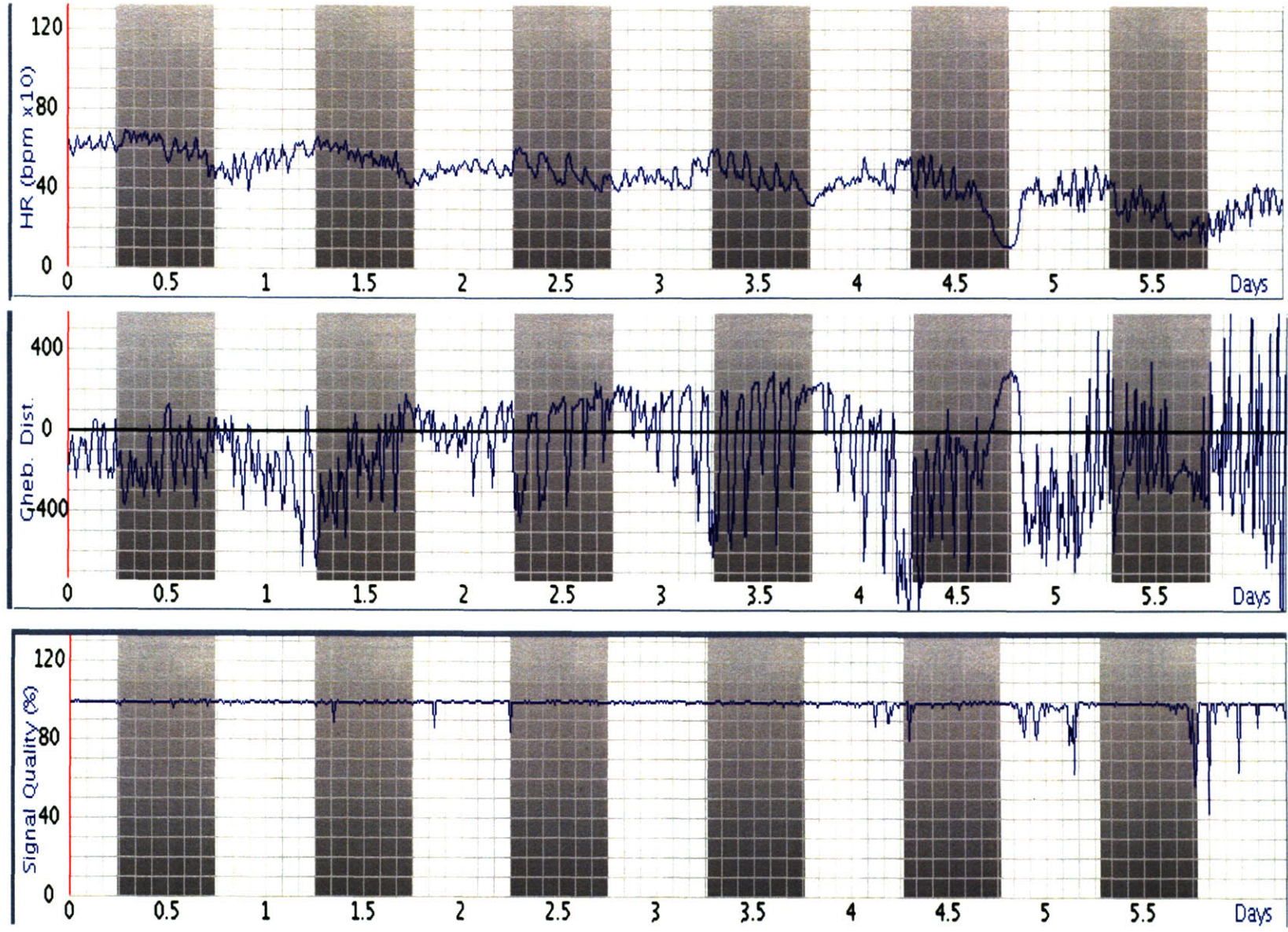


Figure B-19: heart rate, repolarization morphology and signal quality index for subject 0922122003 - 1 of 2



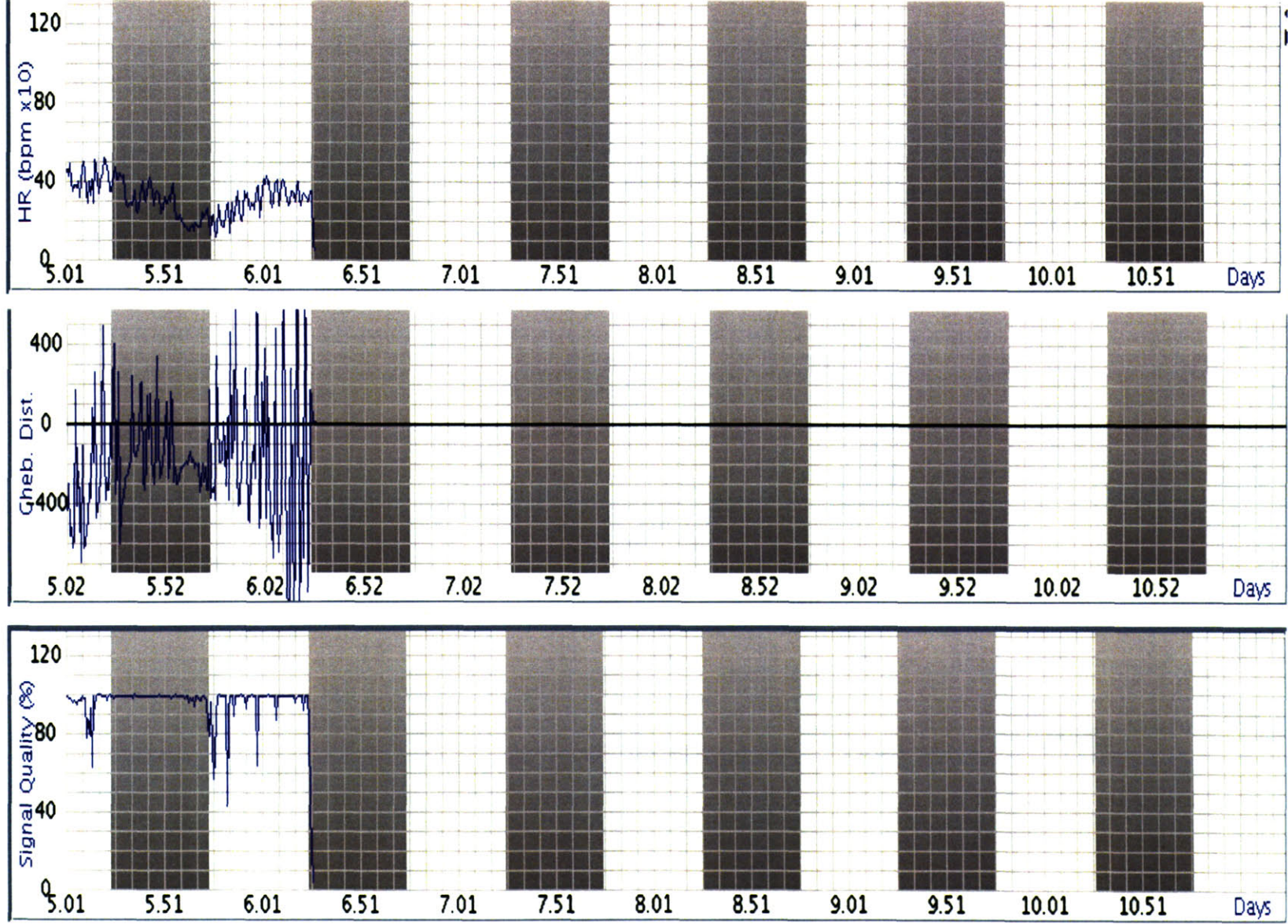


Figure B-20: heart rate, repolarization morphology and signal quality index for subject 0922122903 - 2 of 2  
194



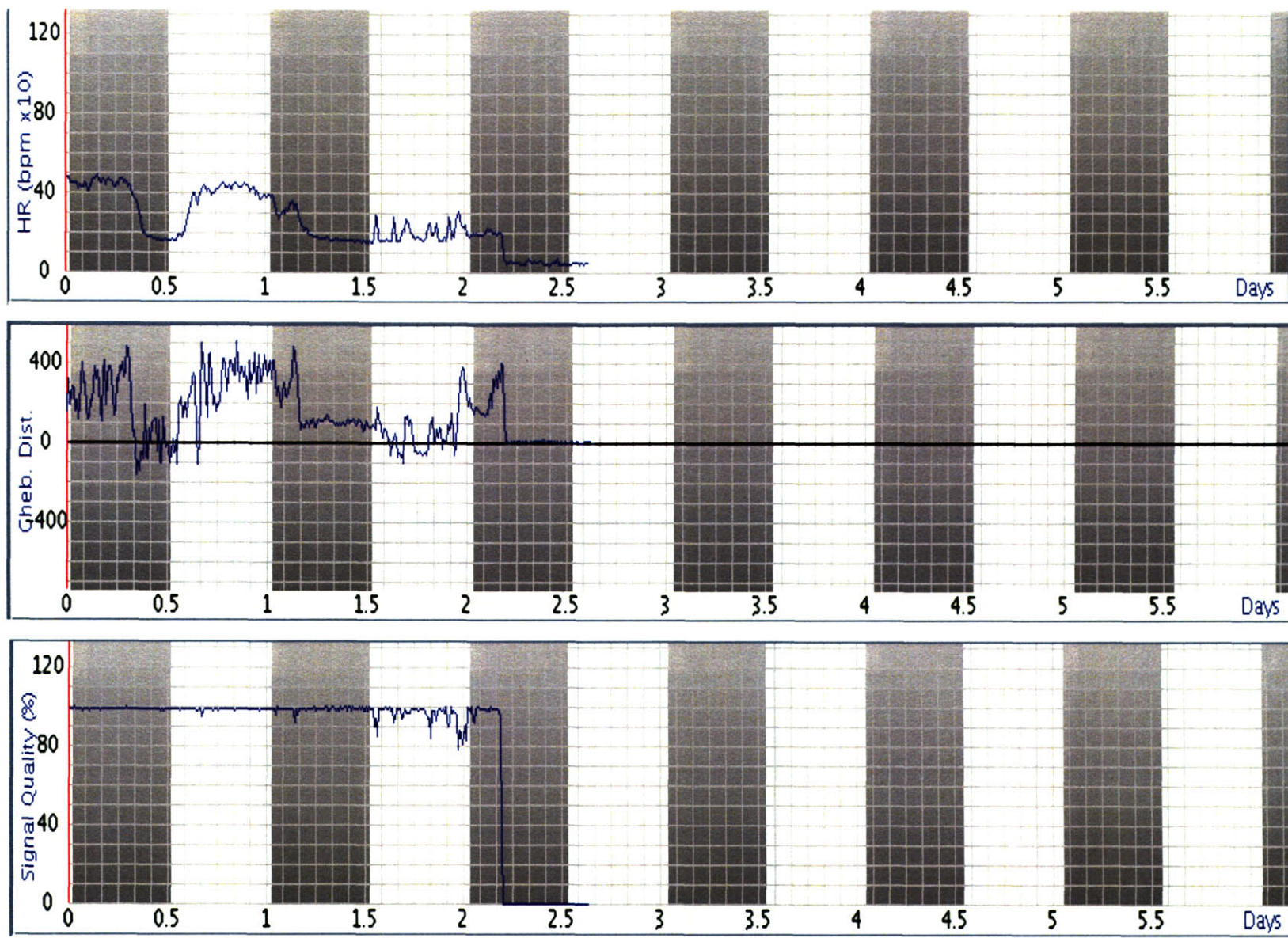


Figure B-21: heart rate, repolarization morphology and signal quality index for subject 1608011604



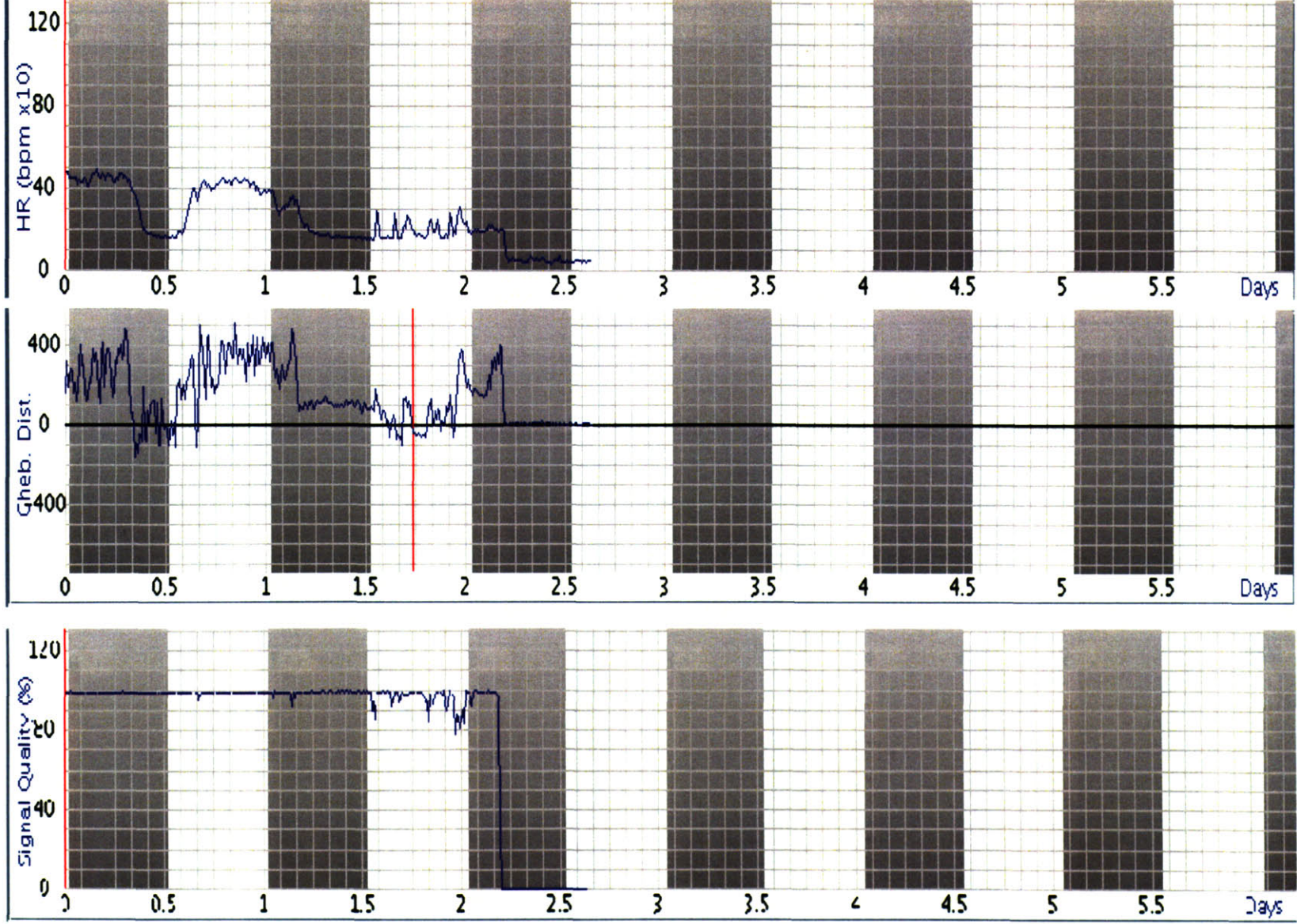


Figure B-22: heart rate, repolarization morphology and signal quality index for subject 1808011604  
196



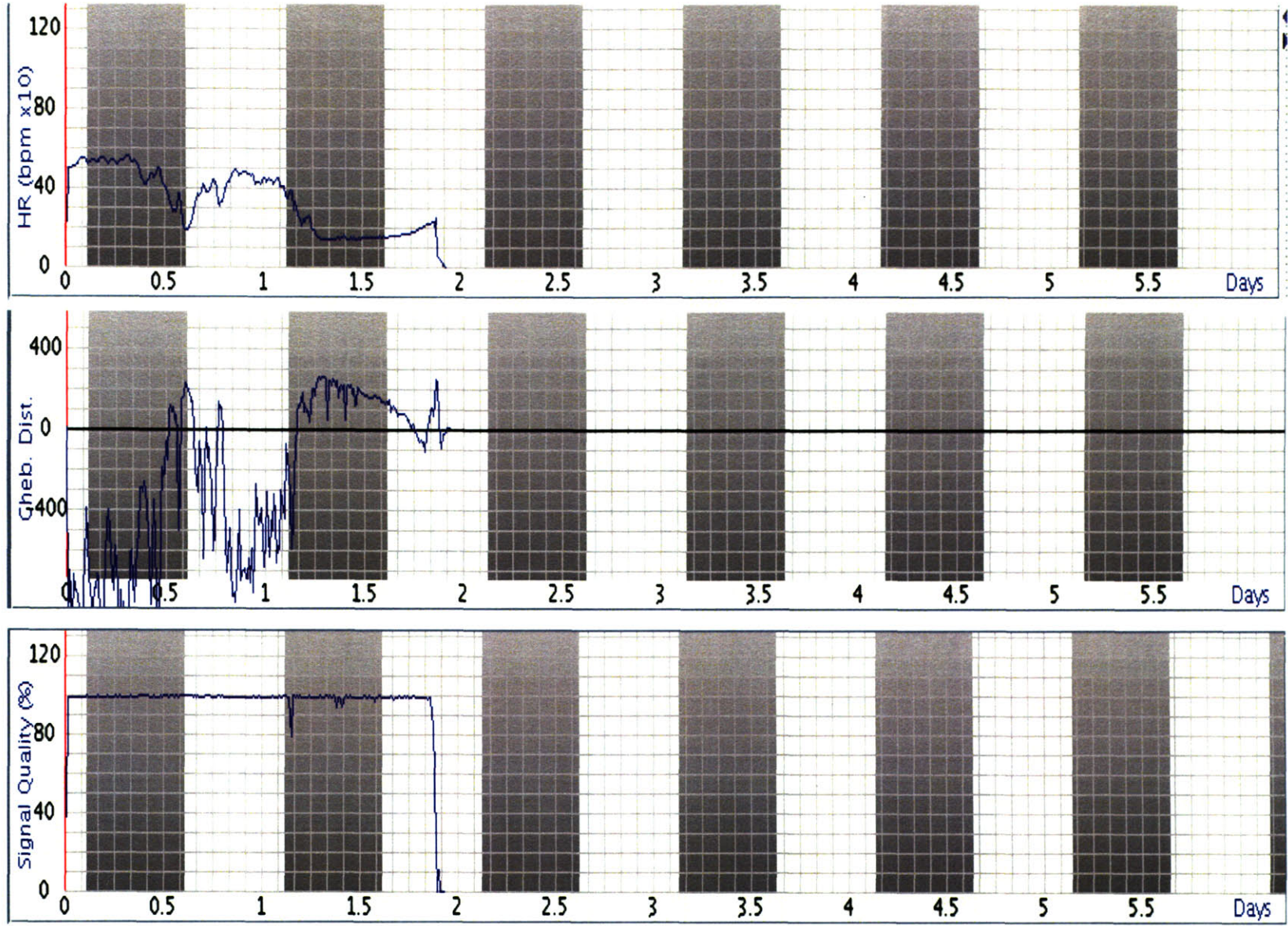


Figure B-23: heart rate, repolarization morphology and signal quality index for subject 2190020704



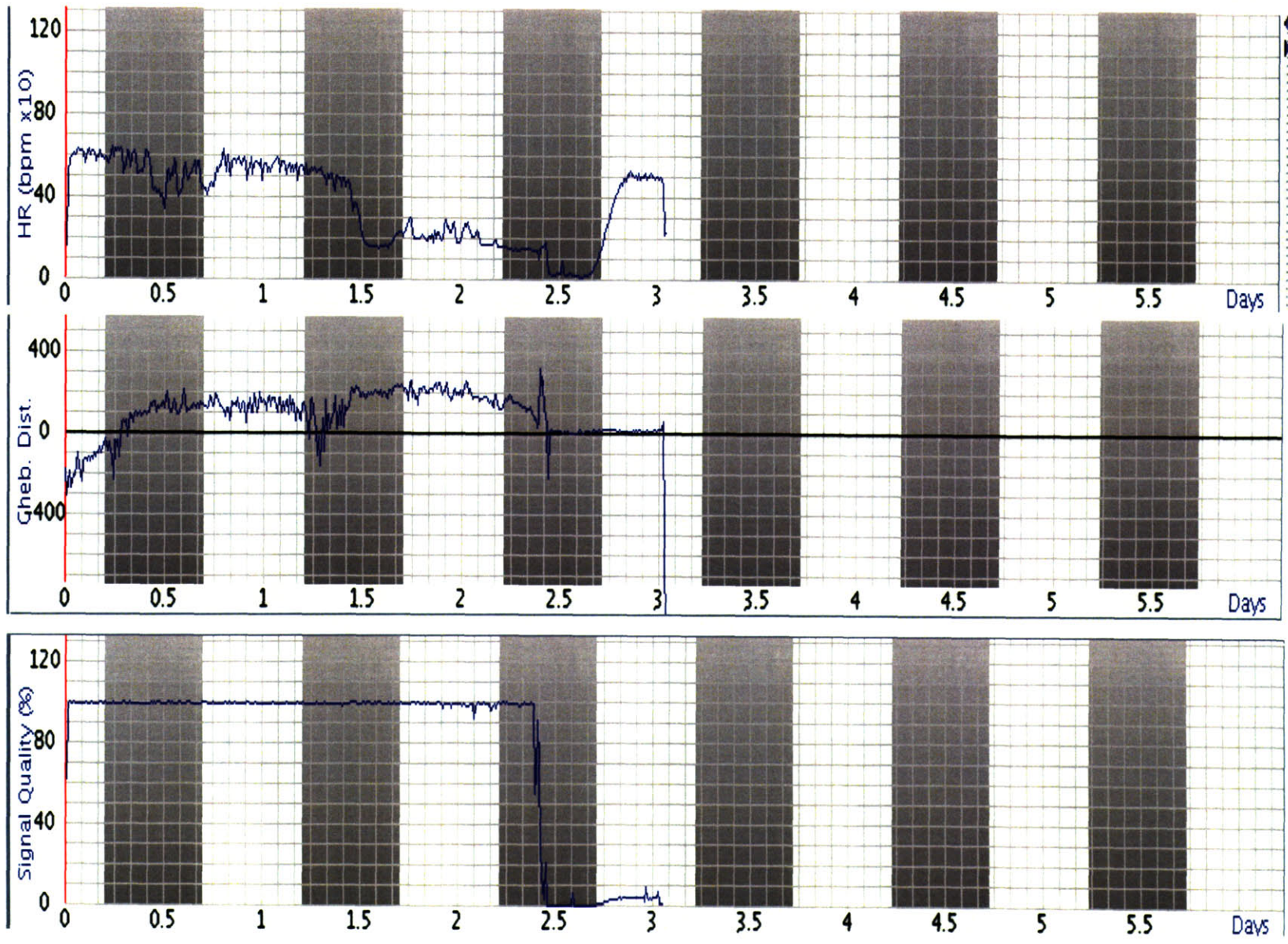


Figure B-24: heart rate, repolarization morphology and signal quality index for subject 2241020104  
198



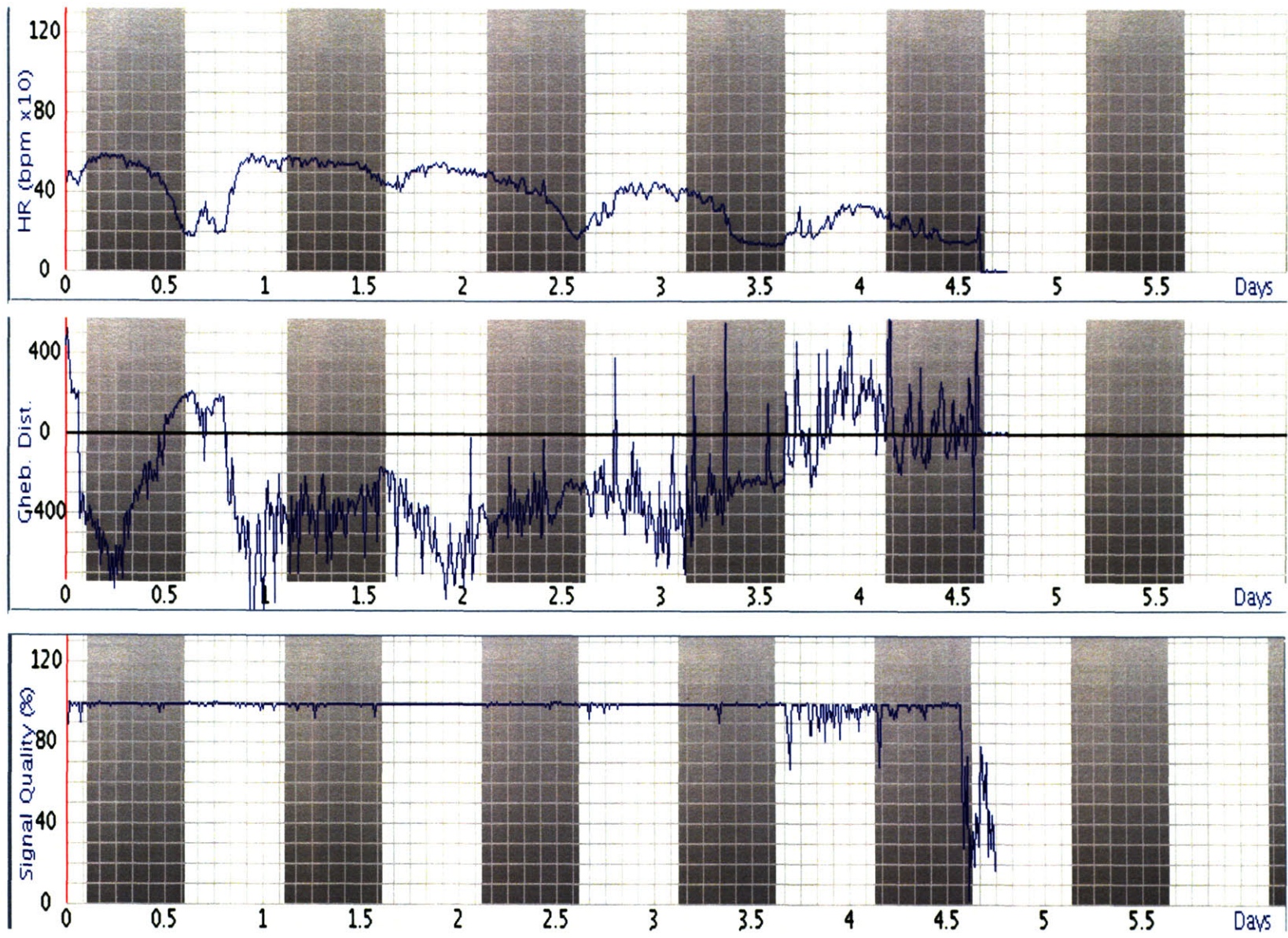


Figure B-25: heart rate, repolarization morphology and signal quality index for subject 2334020604  
199



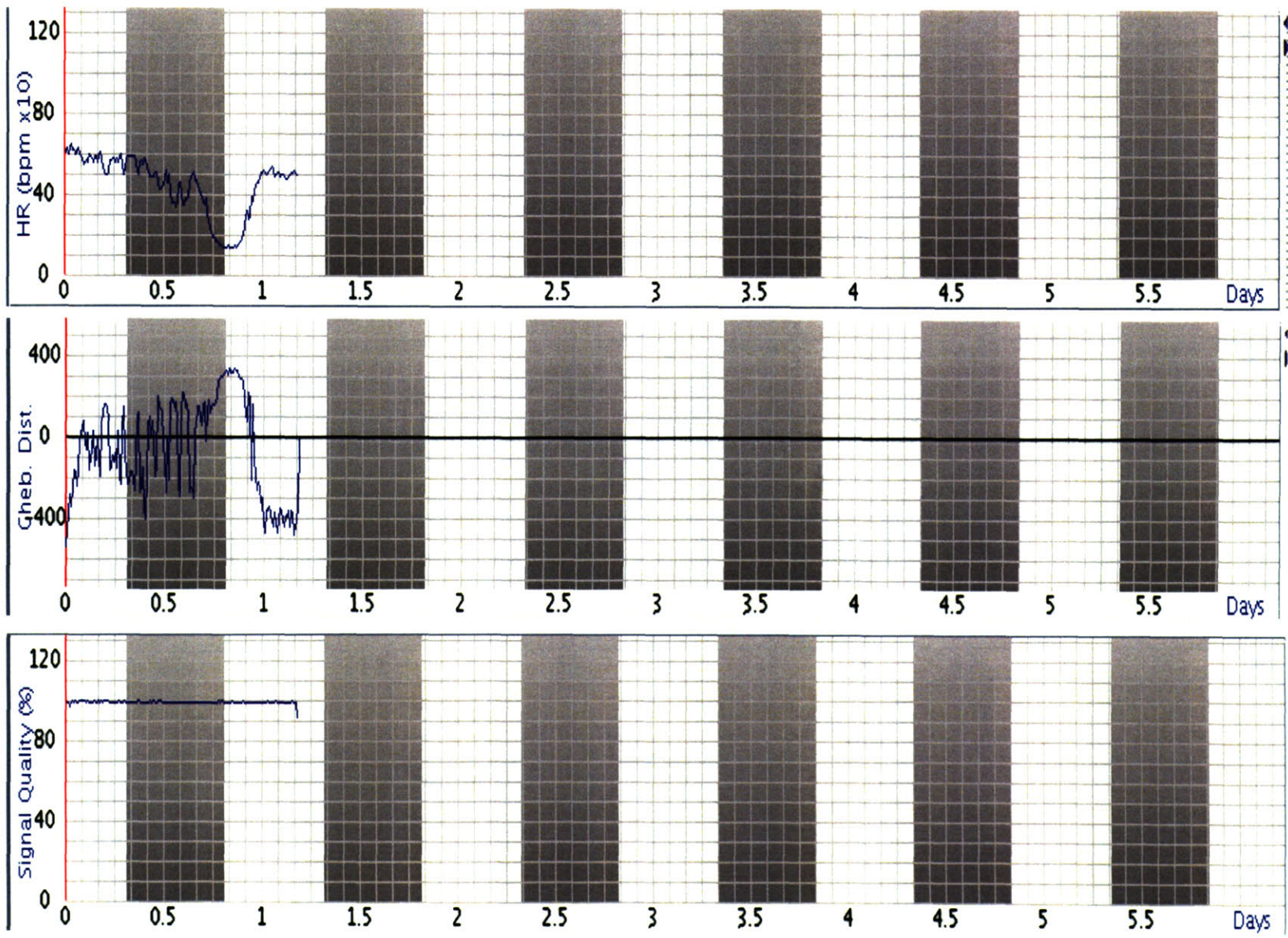


Figure B-26: heart rate, repolarization morphology and signal quality index for subject 2335020604



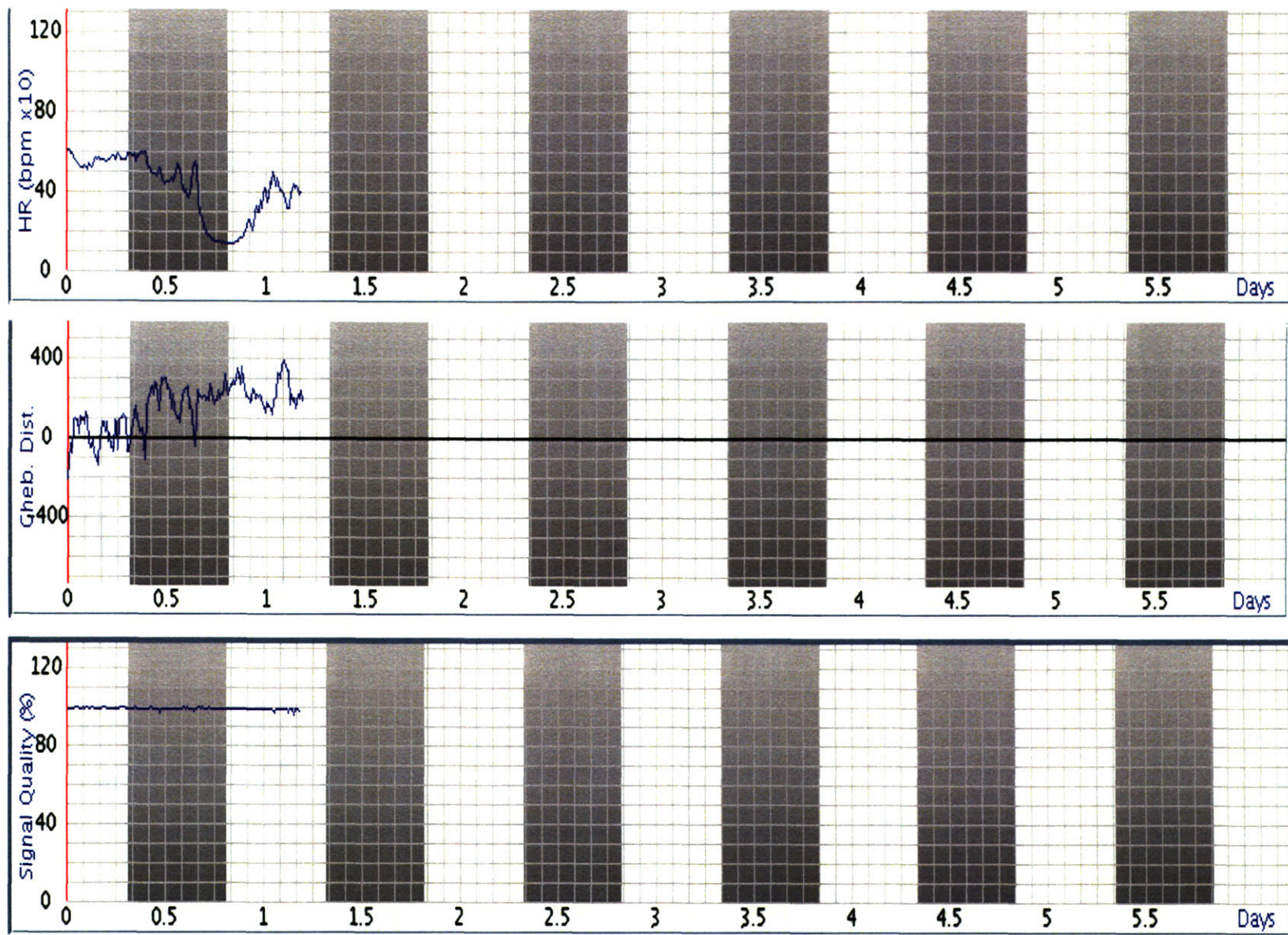


Figure B-27: heart rate, repolarization morphology and signal quality index for subject 2336020604  
201



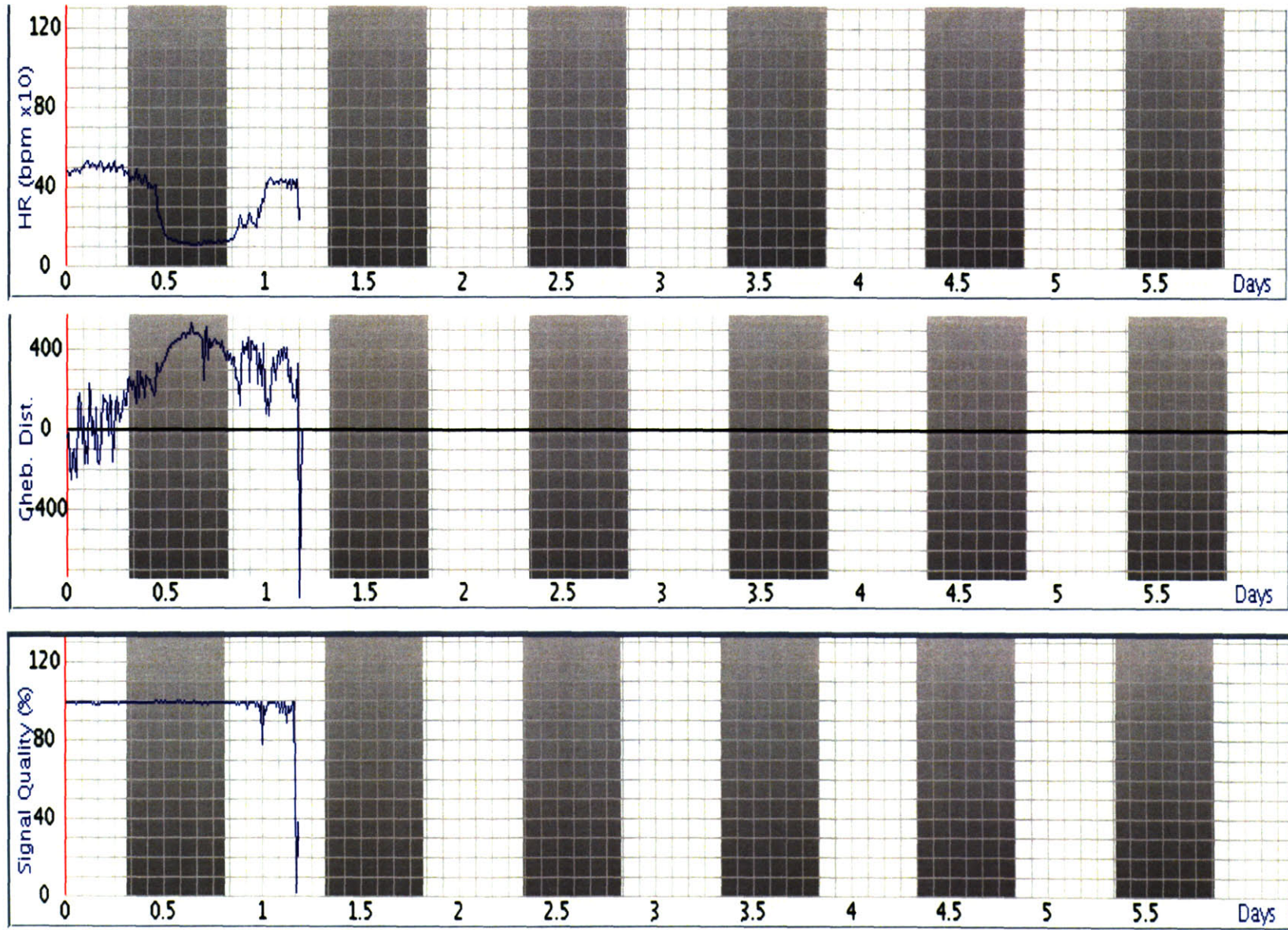


Figure B-28: heart rate, repolarization morphology and signal quality index for subject 2338020604  
202



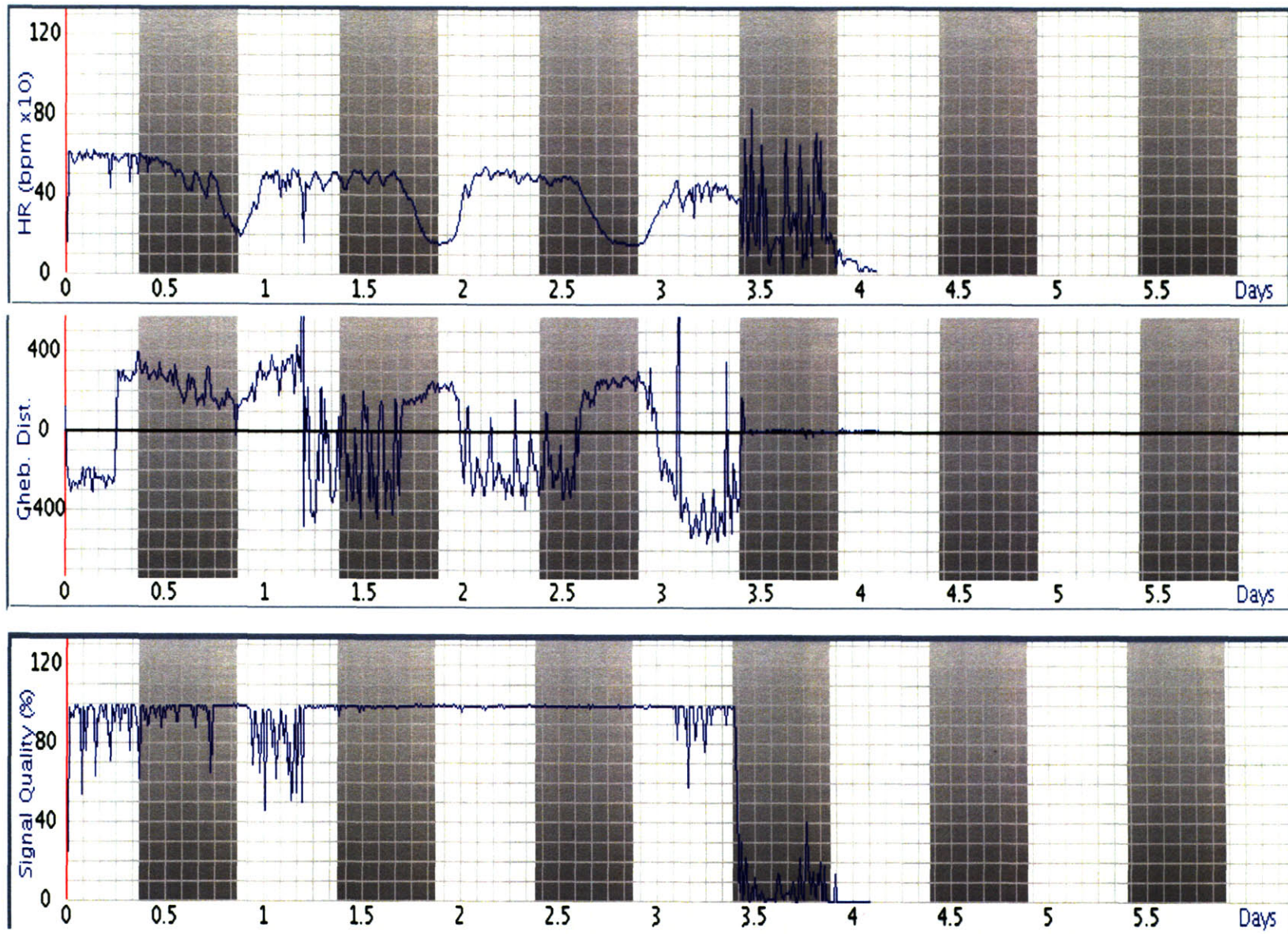


Figure B-29: heart rate, repolarization morphology and signal quality index for subject 2541020404  
203



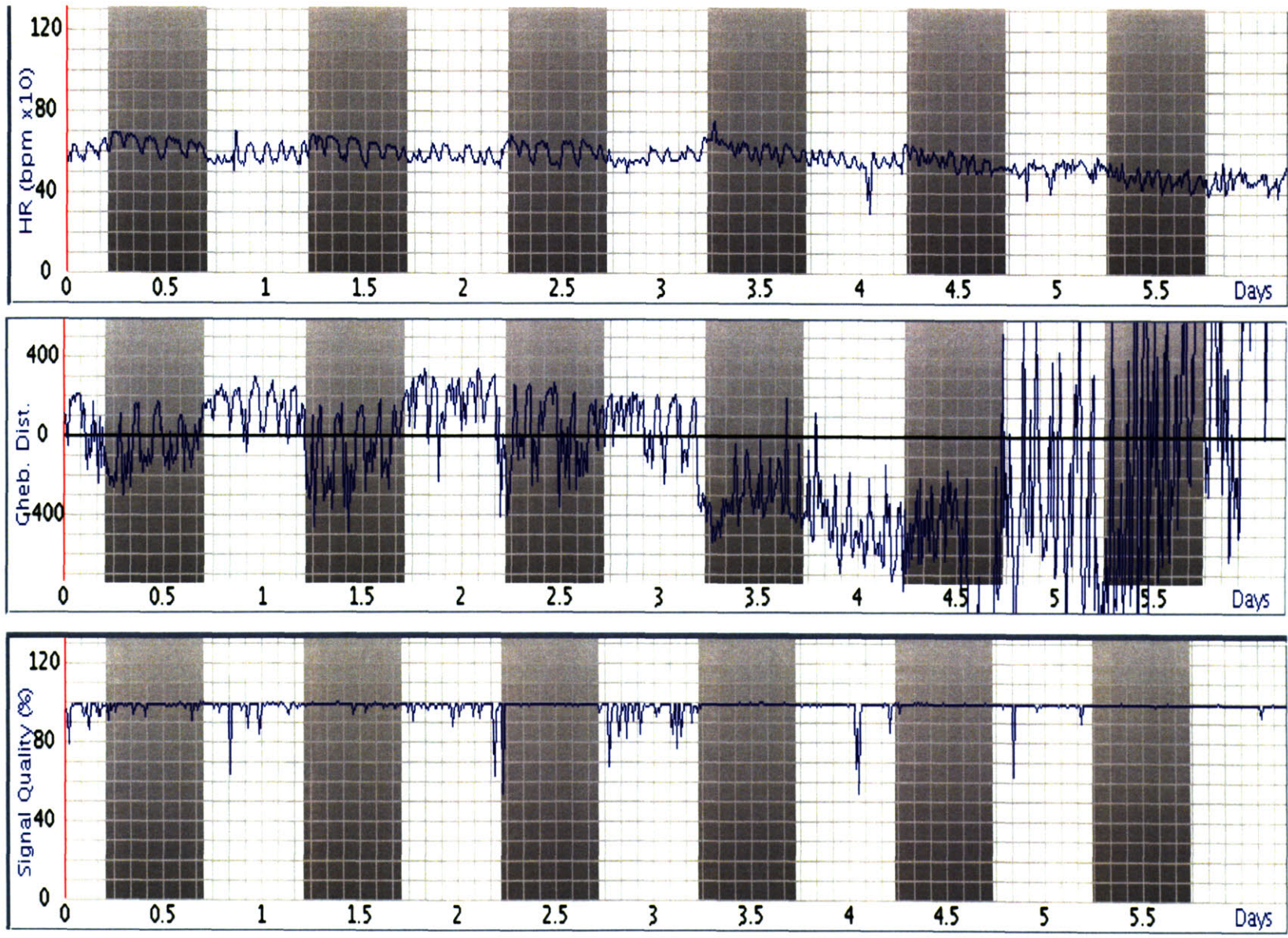


Figure B-30: heart rate, repolarization morphology and signal quality index for subject 2767022103 - 1 of 2  
204



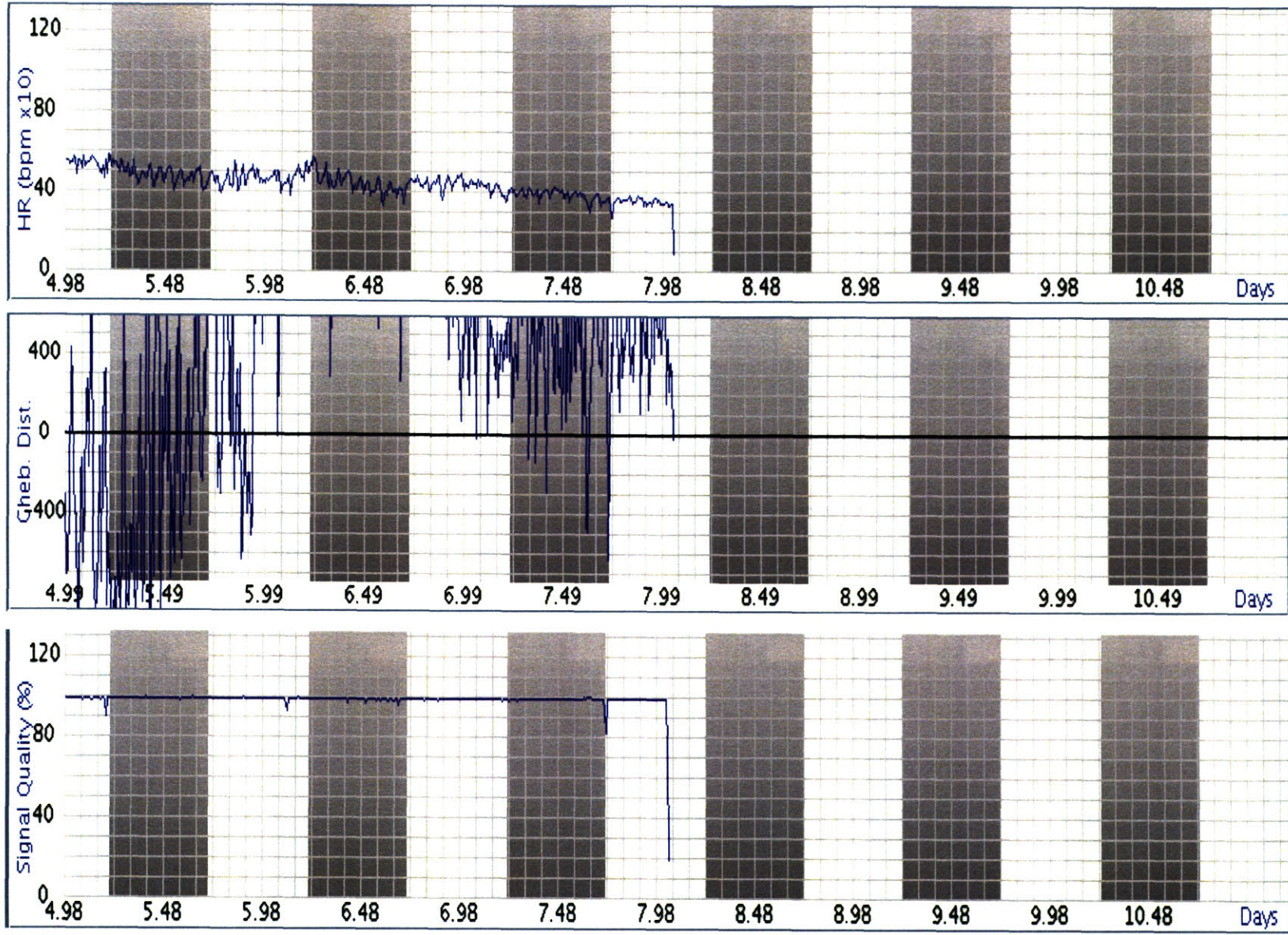


Figure B-31: heart rate, repolarization morphology and signal quality index for subject 2767022103 - 2 of 2  
205



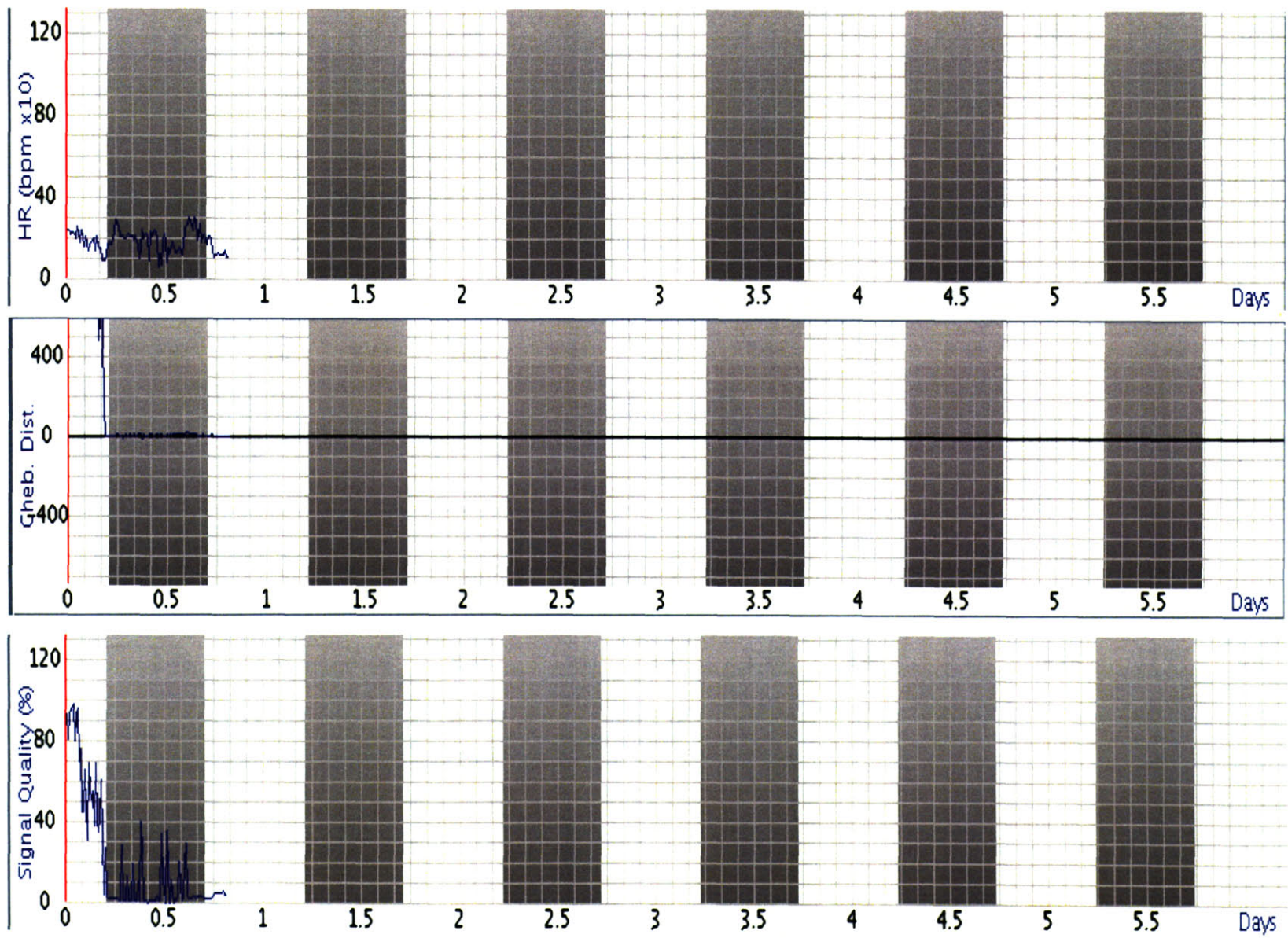


Figure B-32: heart rate, repolarization morphology and signal quality index for subject 2786022103  
206



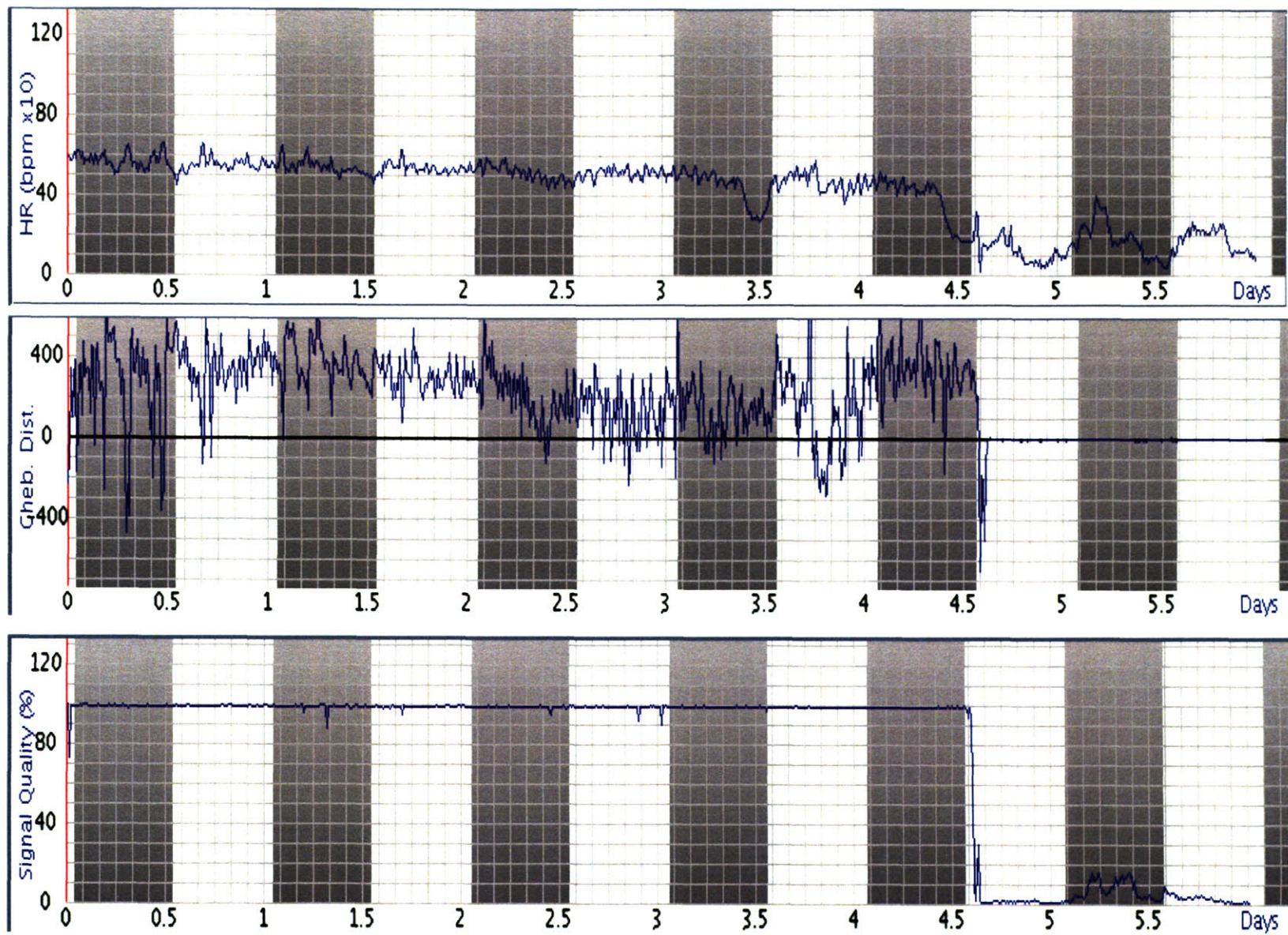


Figure B-33: heart rate, repolarization morphology and signal quality index for subject 3222031004



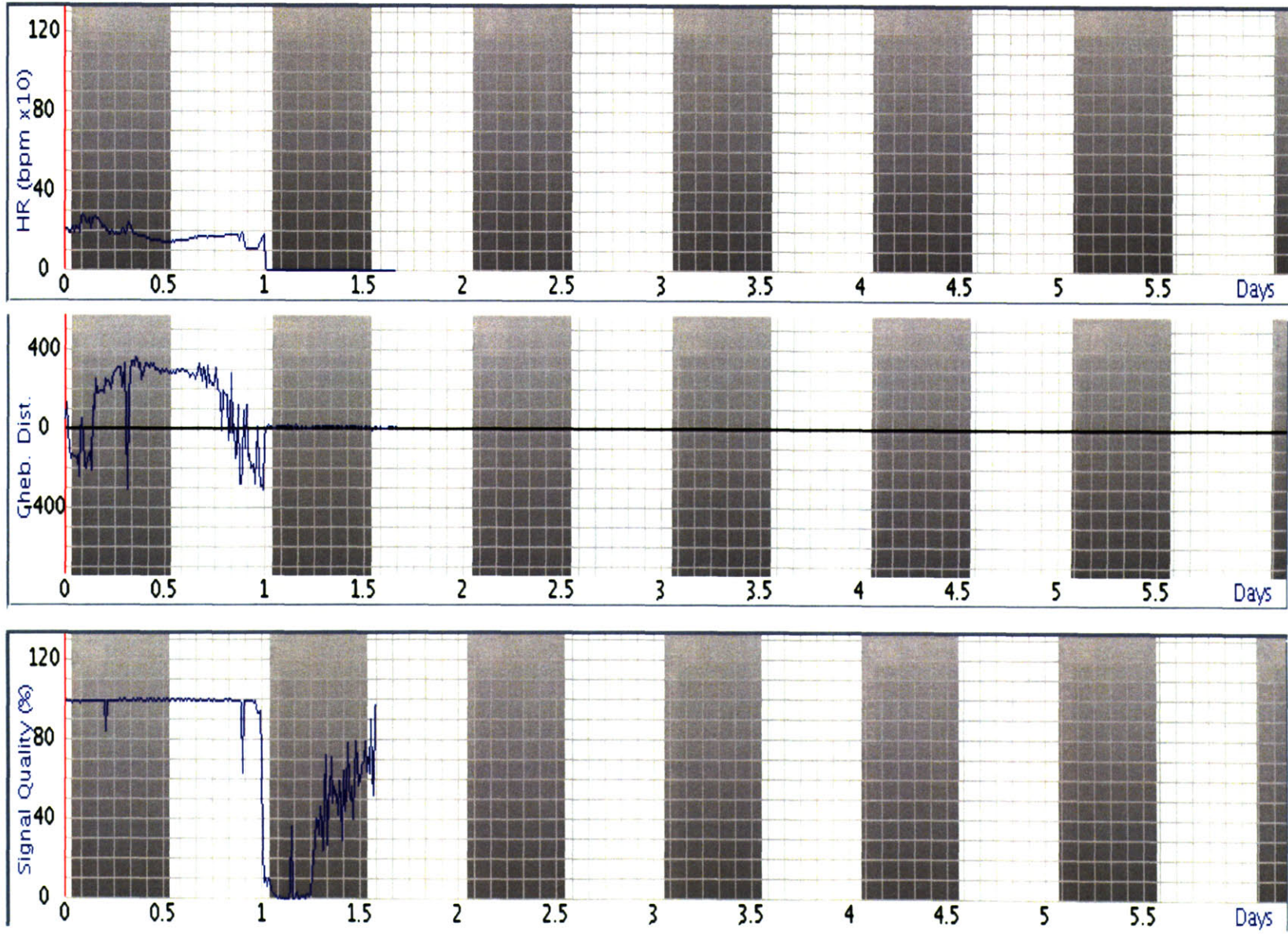


Figure B-34: heart rate, repolarization morphology and signal quality index for subject 3225031004  
208



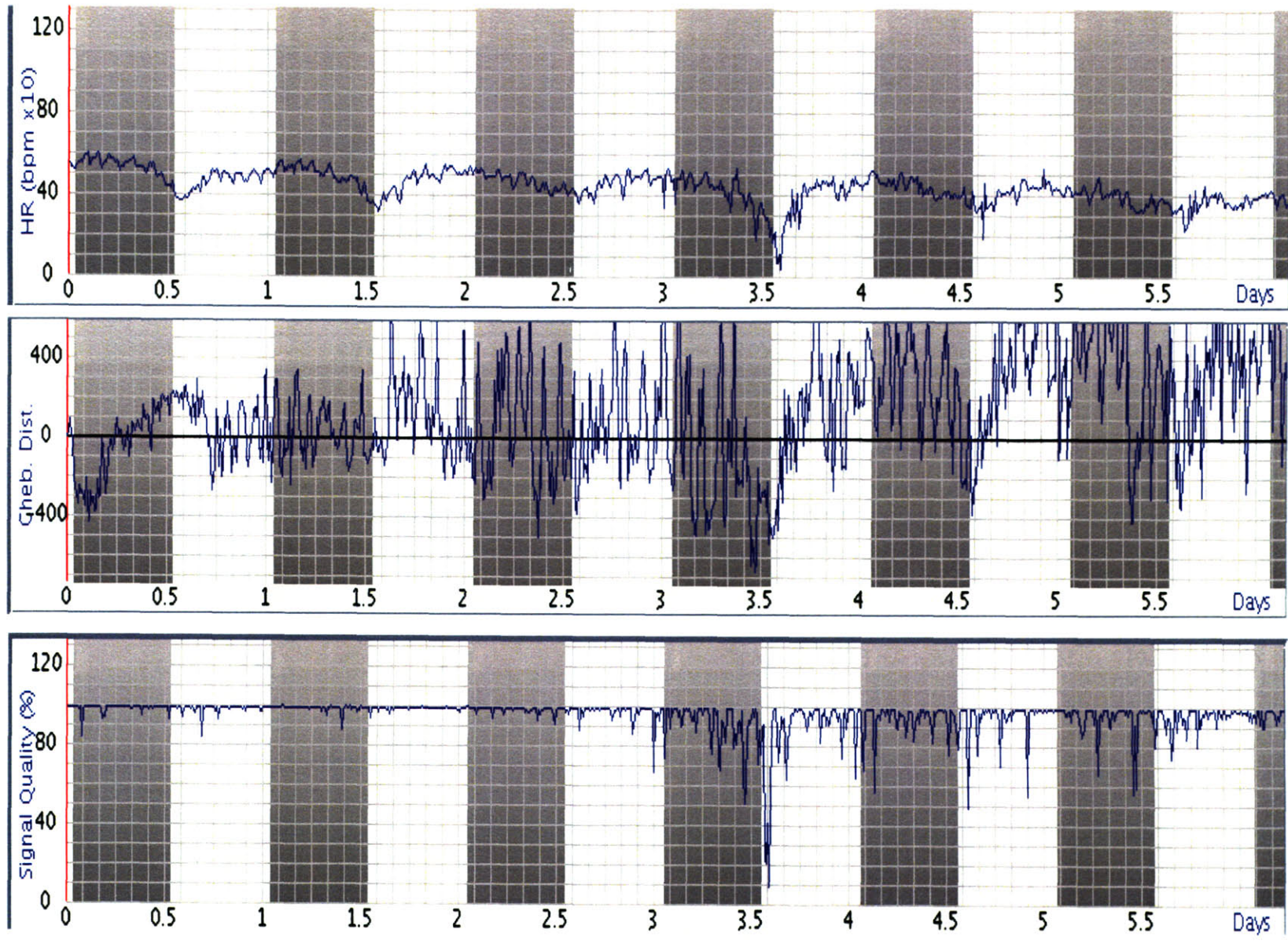


Figure B-35: heart rate, repolarization morphology and signal quality index for subject 3231030904 - 1 of 2  
209



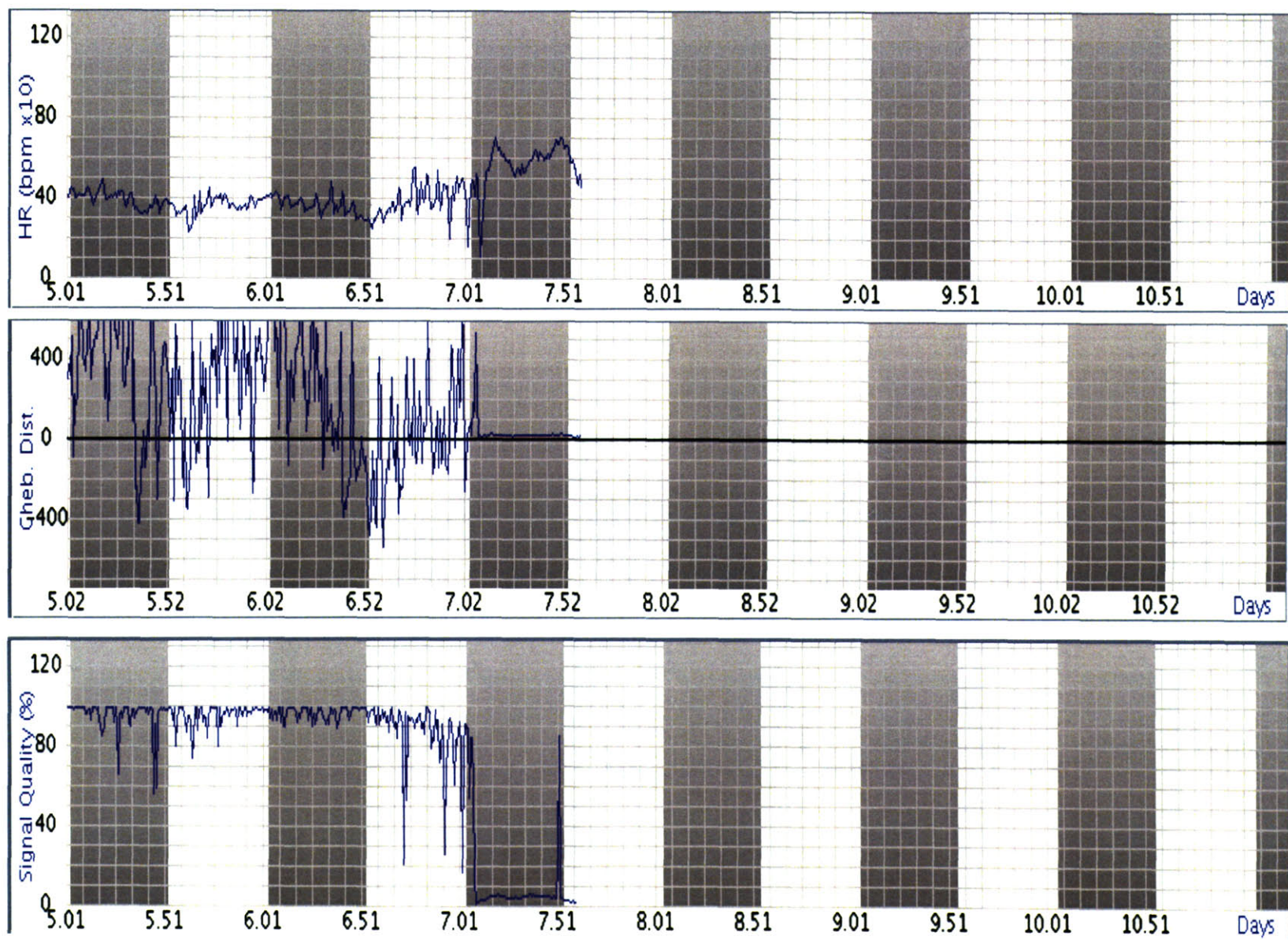


Figure B-36: heart rate, repolarization morphology and signal quality index for subject 3231030904 - 2 of 2  
210



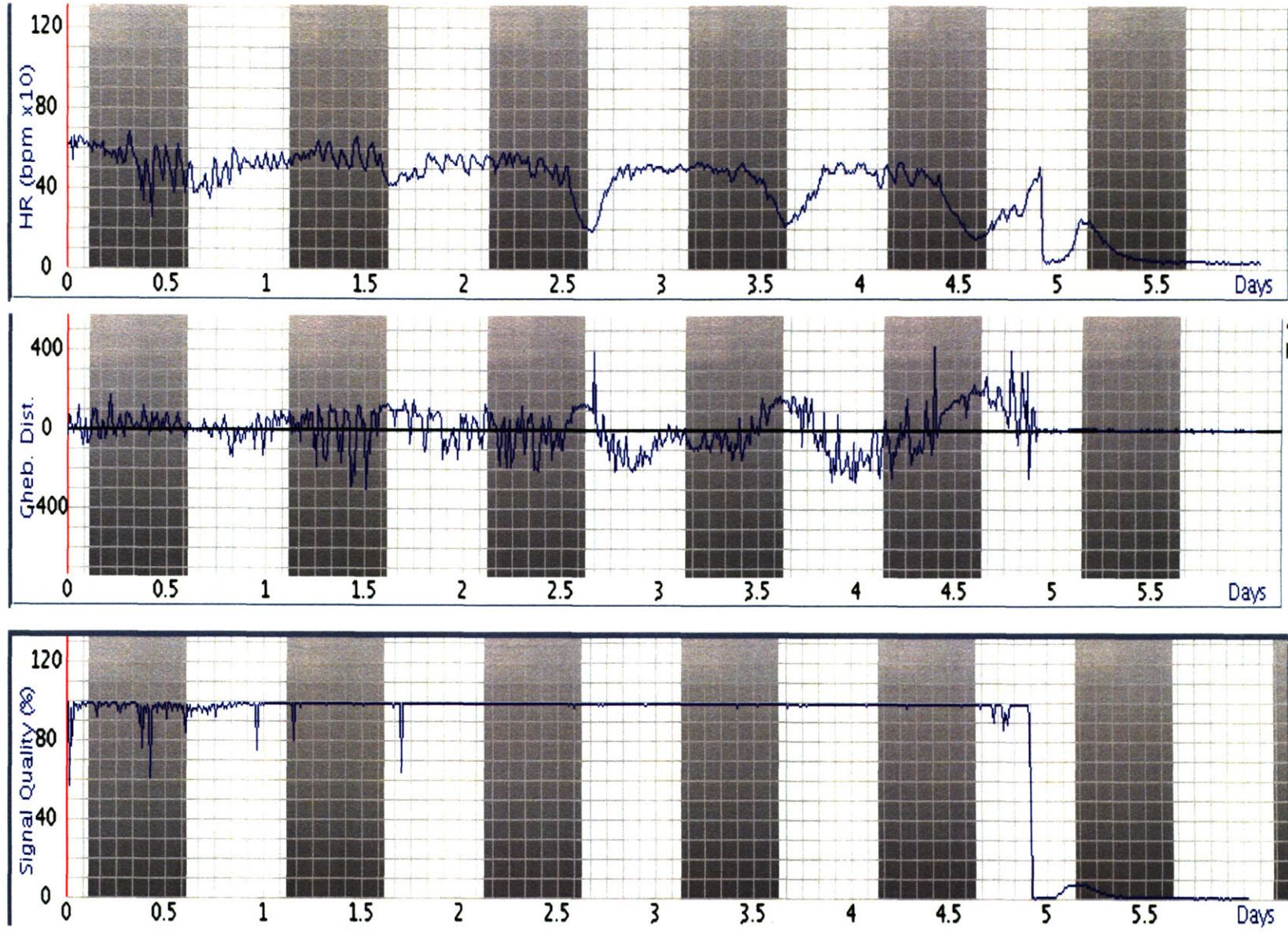


Figure B-37: heart rate, repolarization morphology and signal quality index for subject 4630040604



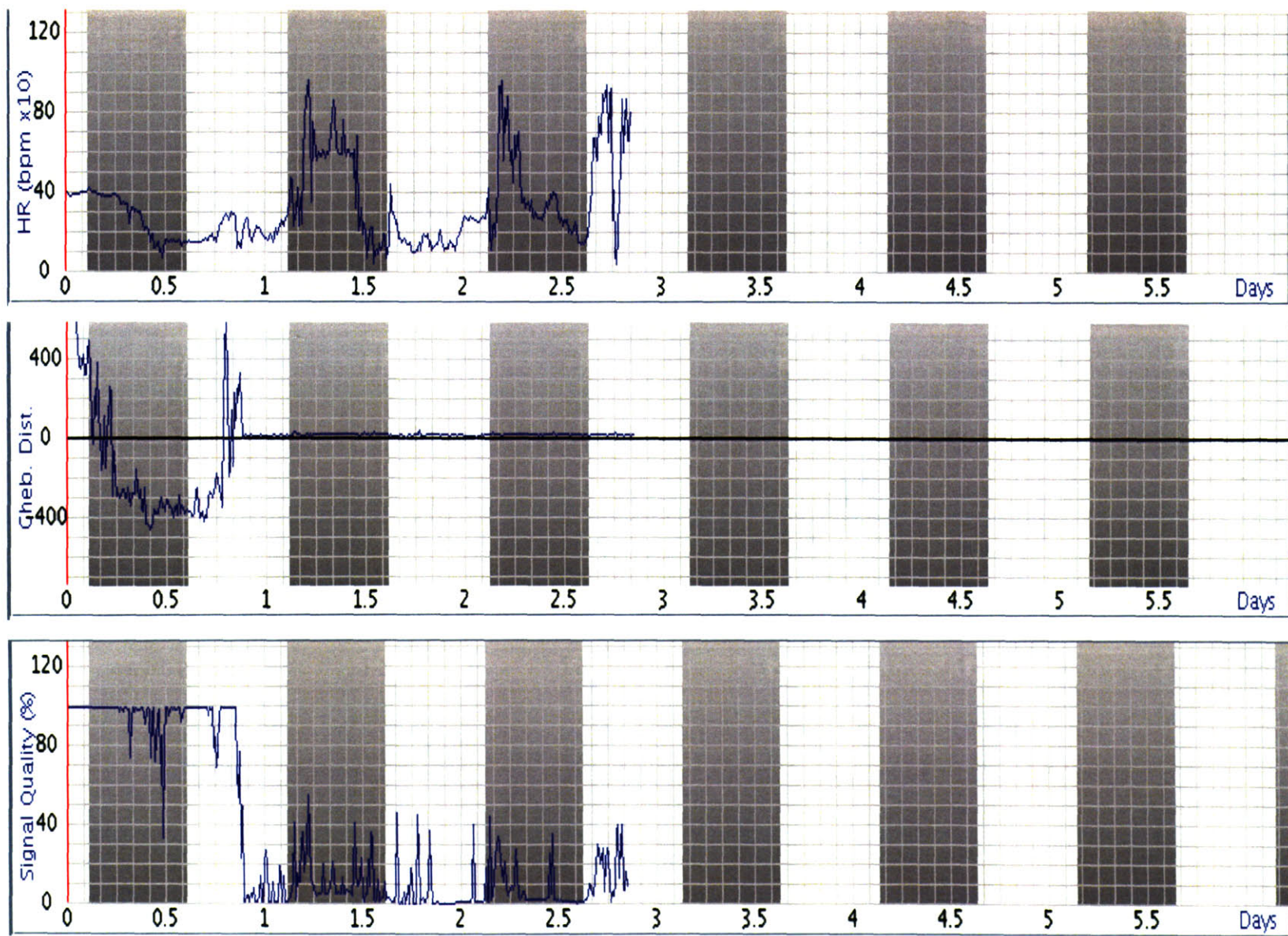


Figure B-38: heart rate, repolarization morphology and signal quality index for subject 4631040604  
212



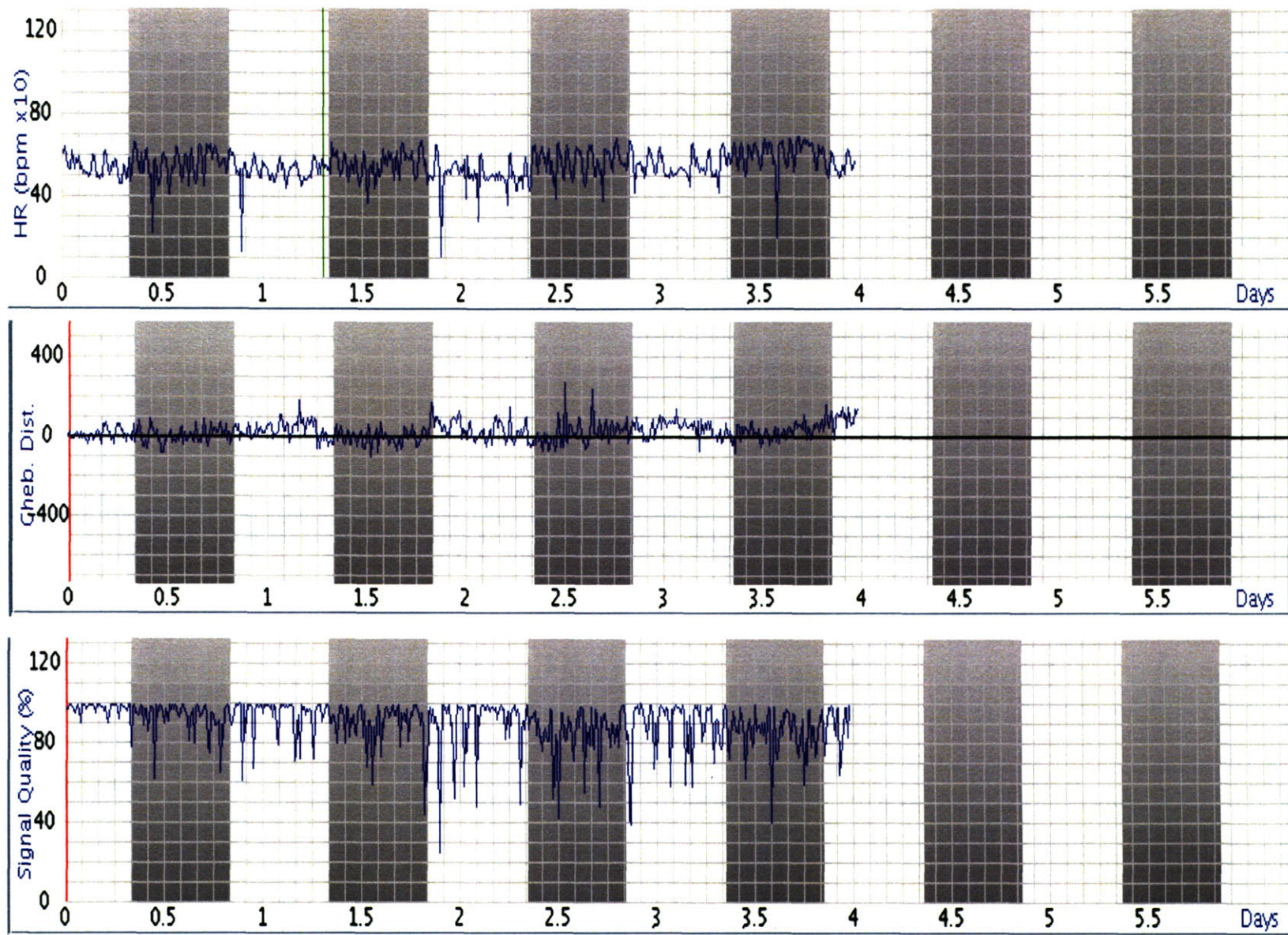


Figure B-39: heart rate, repolarization morphology and signal quality index for subject 5462040105  
213



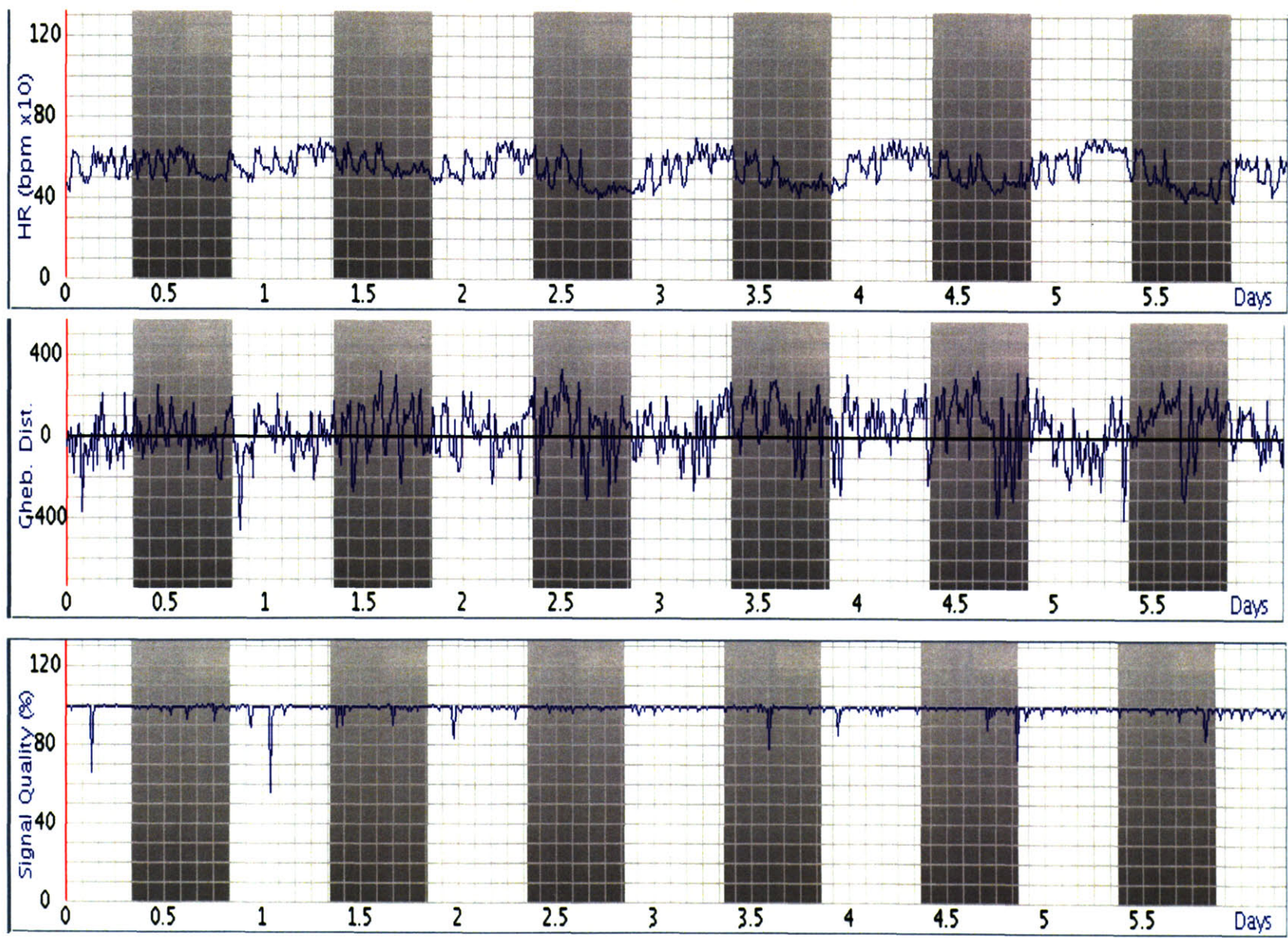


Figure B-40: heart rate, repolarization morphology and signal quality index for subject 5463040105 - 1 of 3  
214



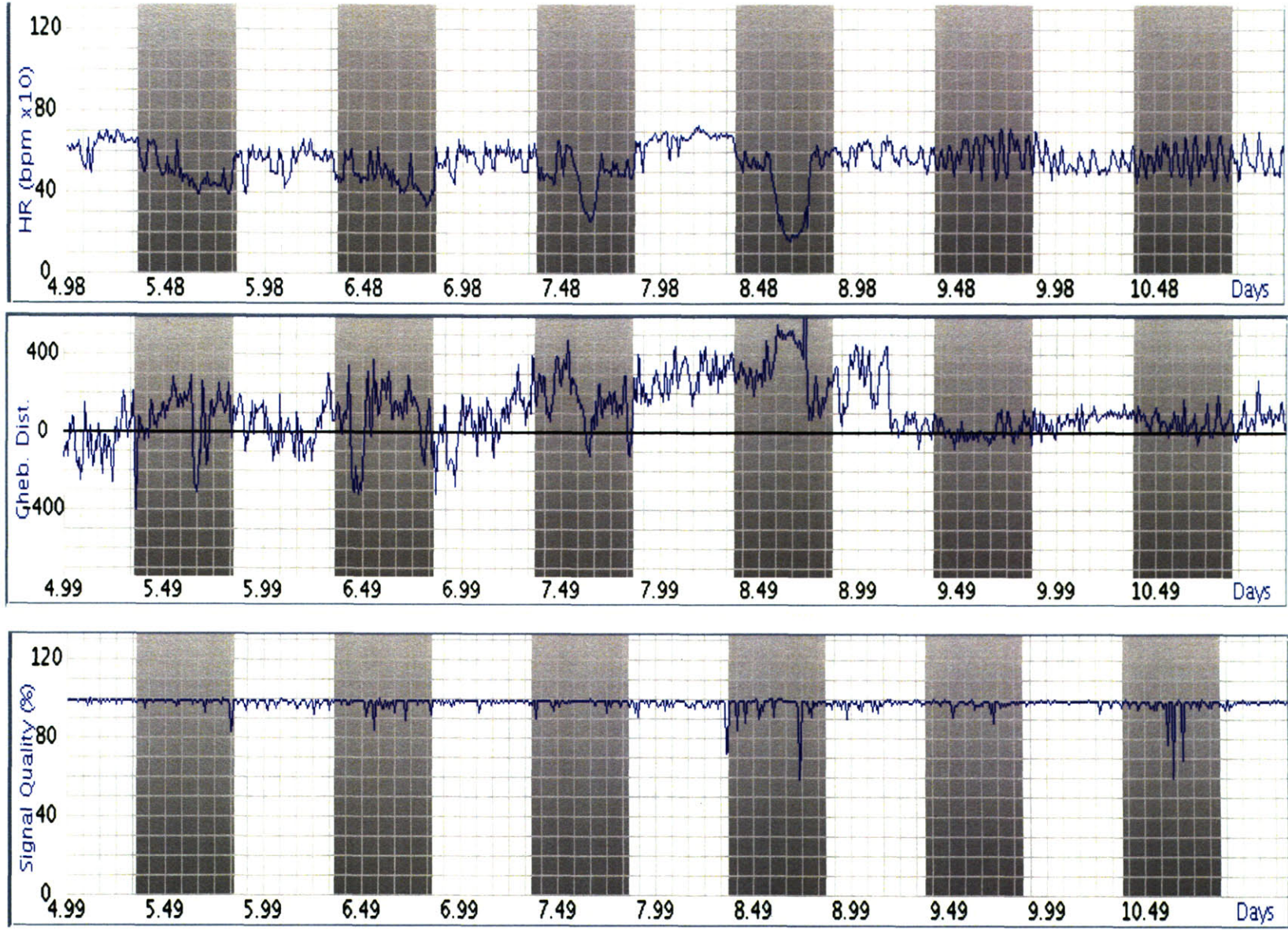


Figure B-41: heart rate, repolarization morphology and signal quality index for subject 5463040105 - 2 of 3  
215



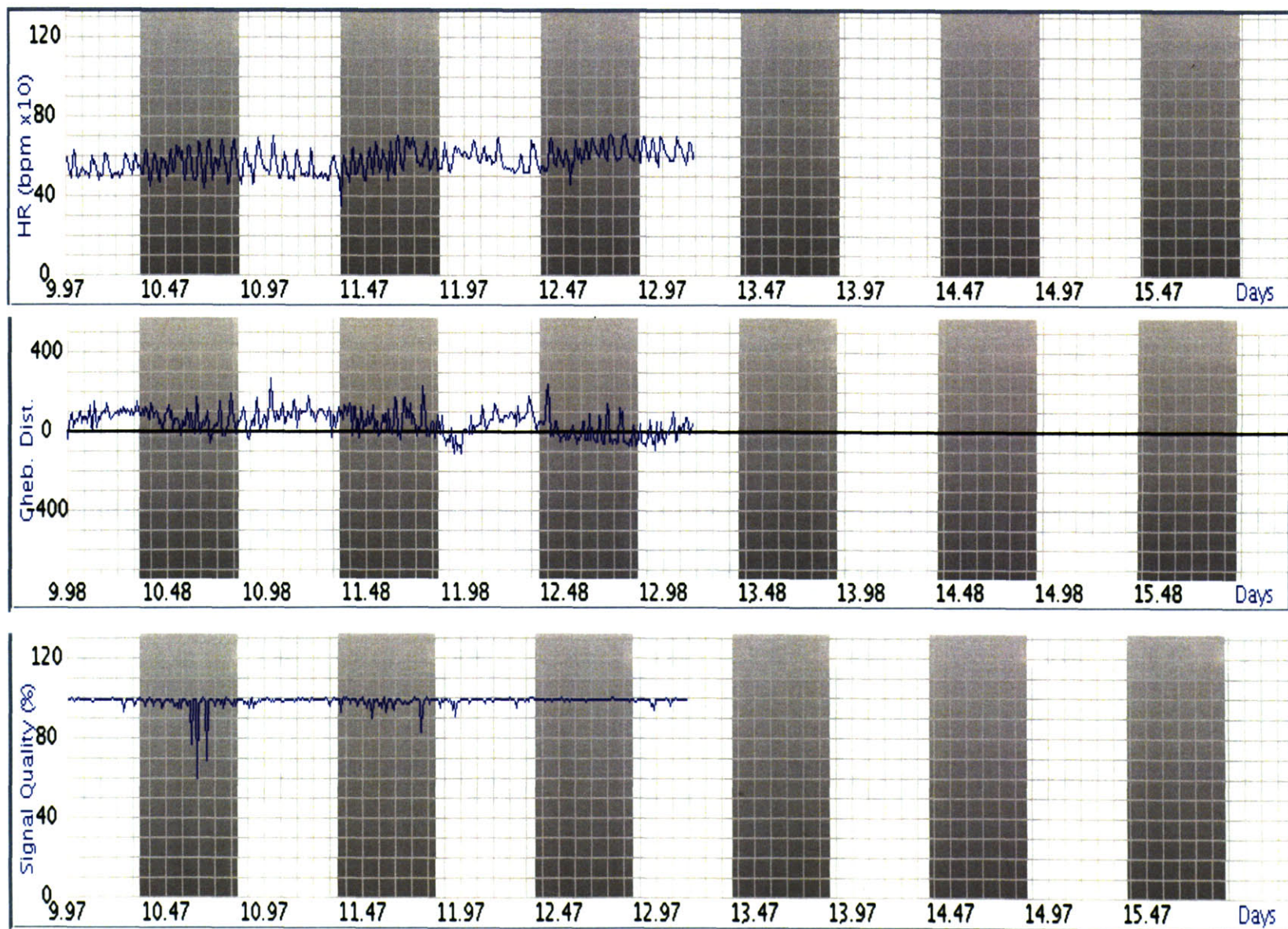


Figure B-42: heart rate, repolarization morphology and signal quality index for subject 5463040105 - 3 of 3  
216



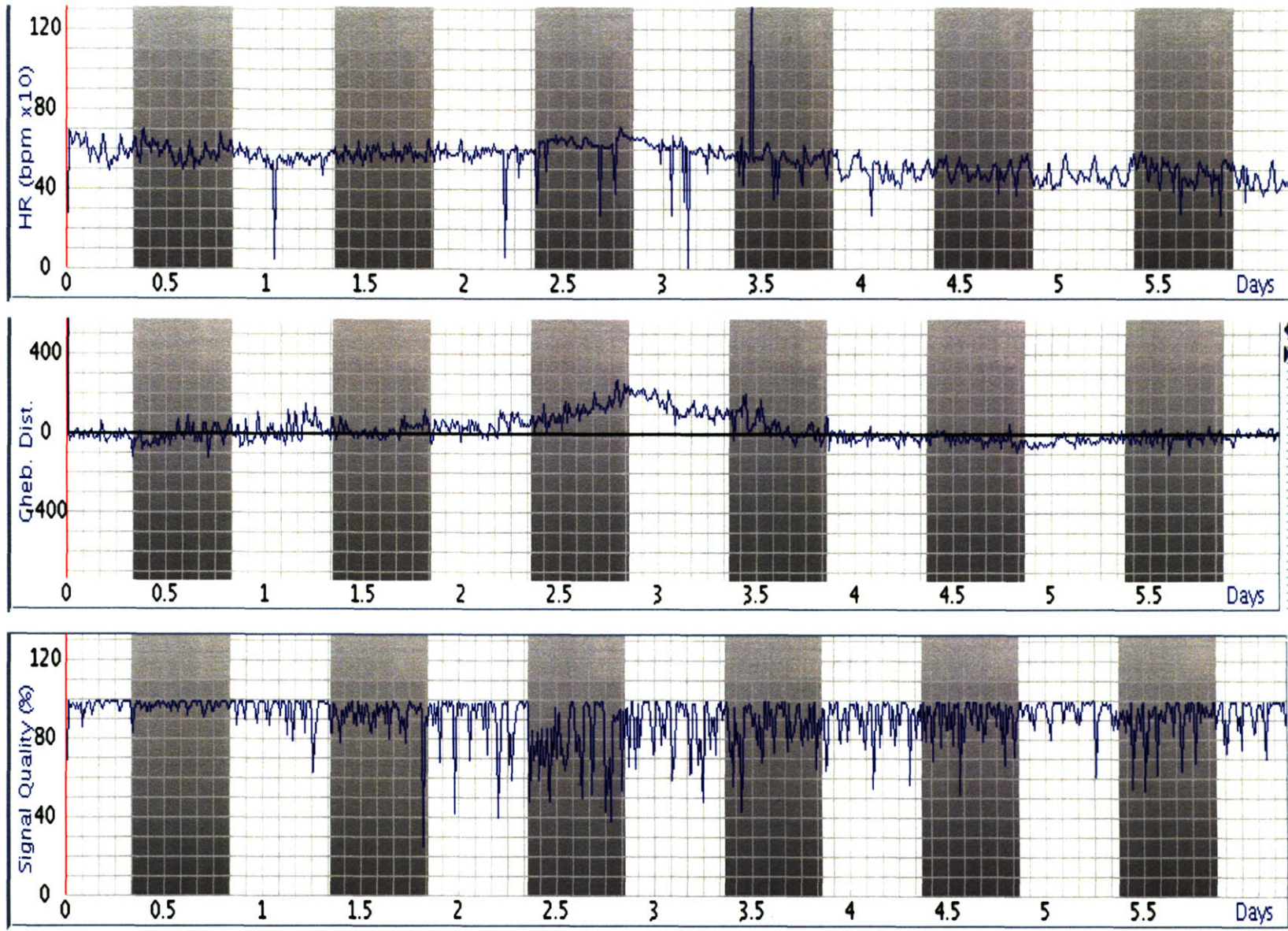


Figure B-43: heart rate, repolarization morphology and signal quality index for subject 6591081803 - 1 of 2



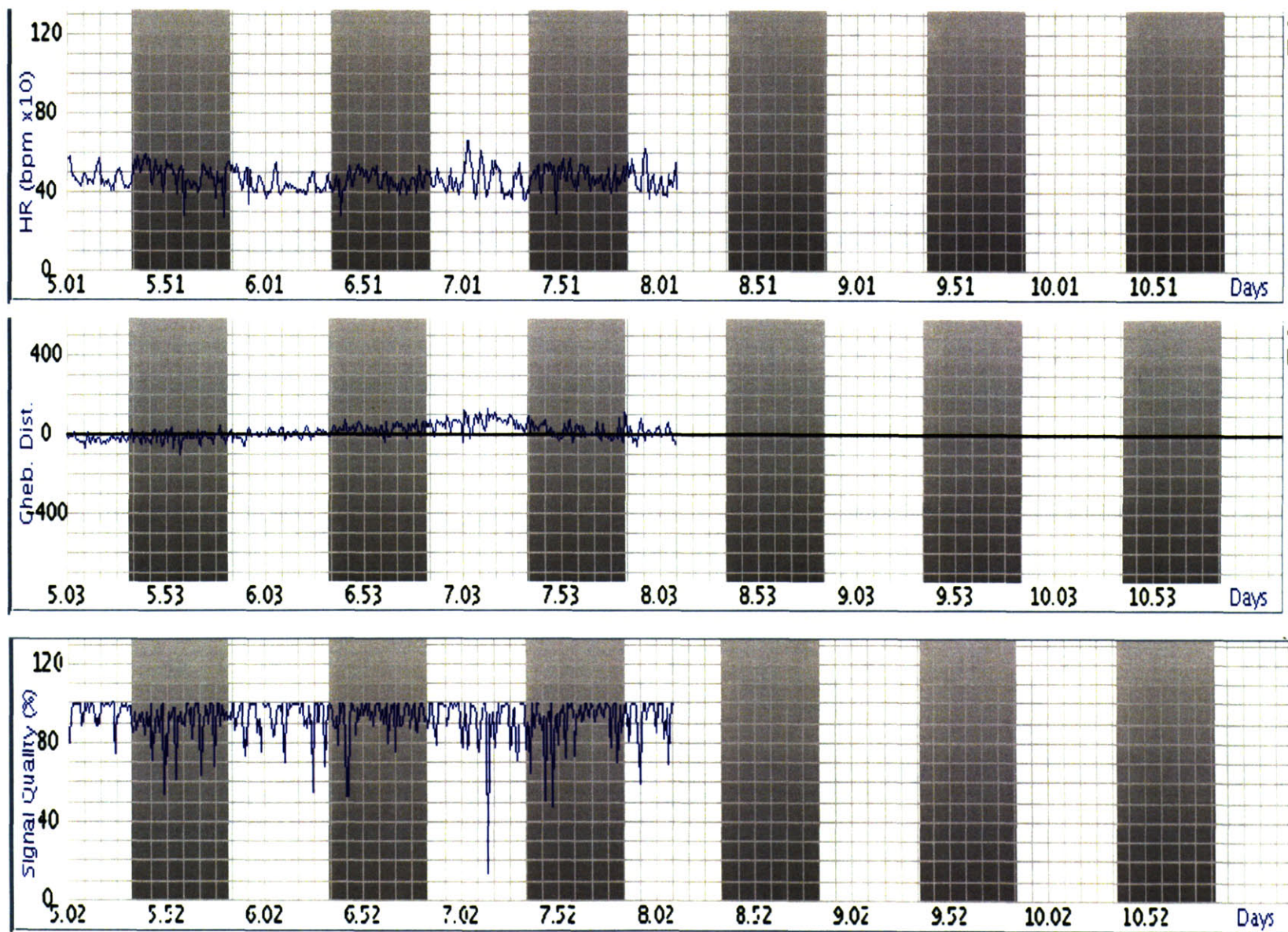


Figure B-44: heart rate, repolarization morphology and signal quality index for subject 6591081803 - 2 of 2  
218



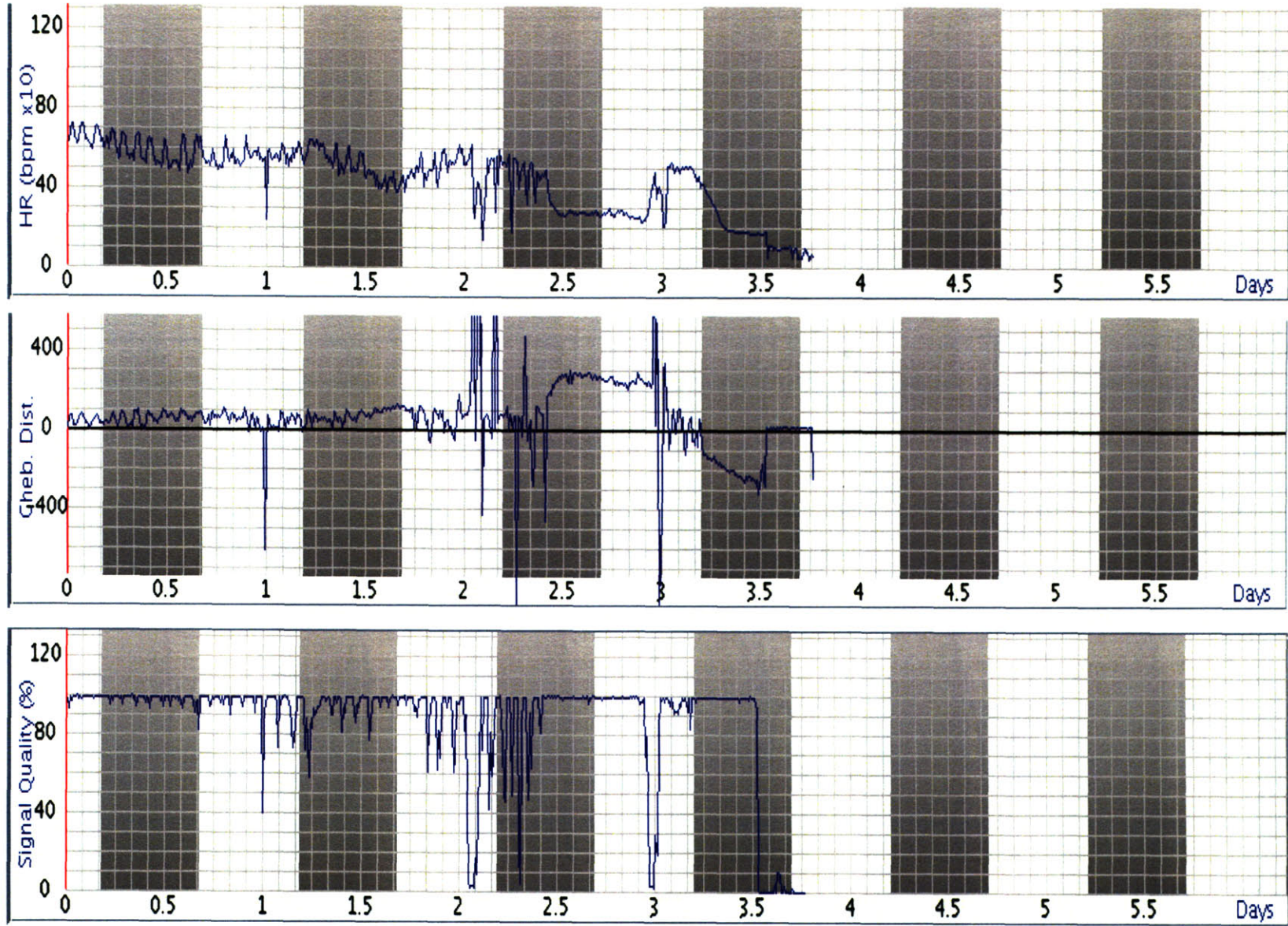


Figure B-45: heart rate, repolarization morphology and signal quality index for subject 6842083003  
219



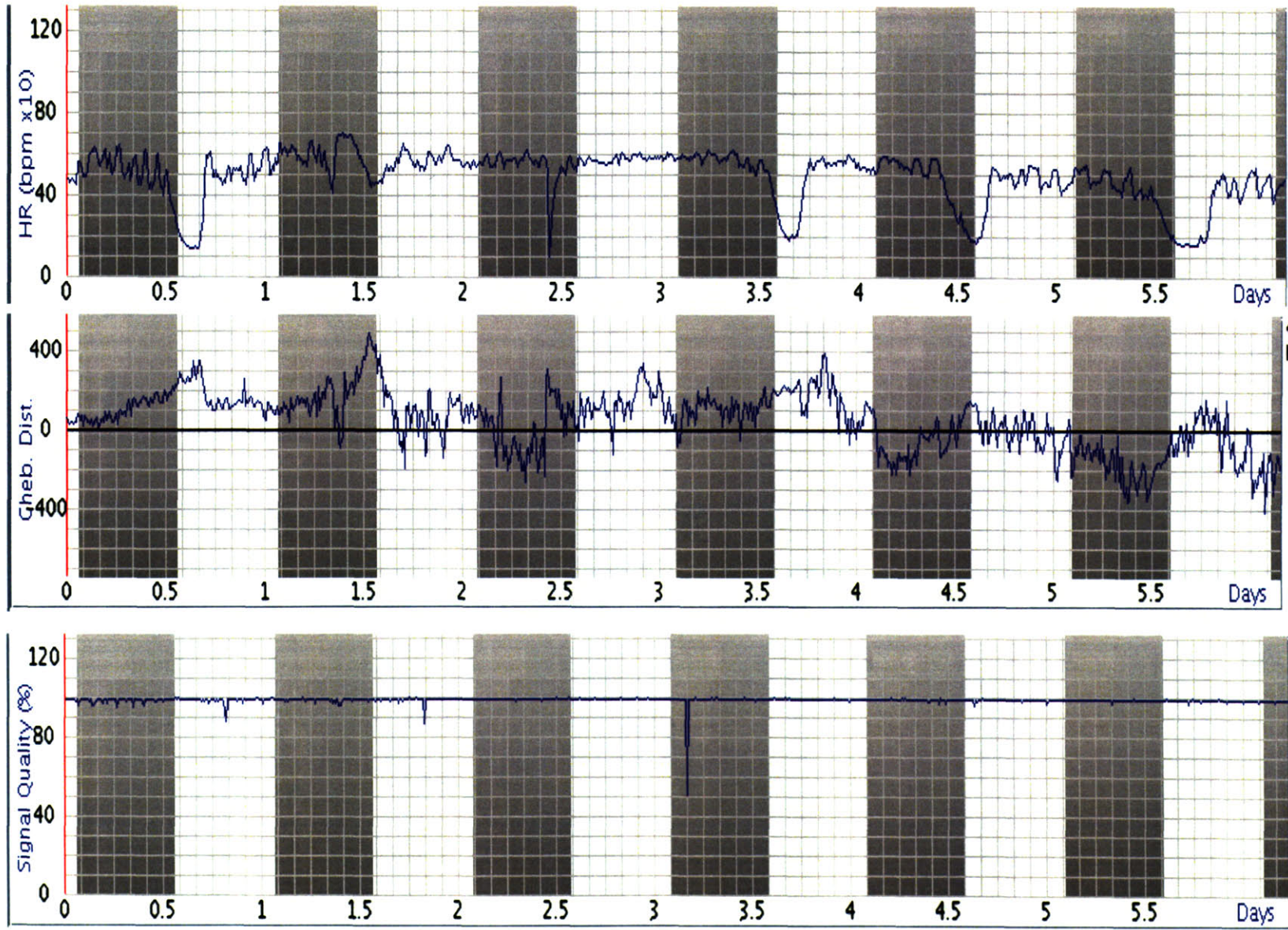


Figure B-46: heart rate, repolarization morphology and signal quality index for subject 6846090403 - 1 of 2  
220



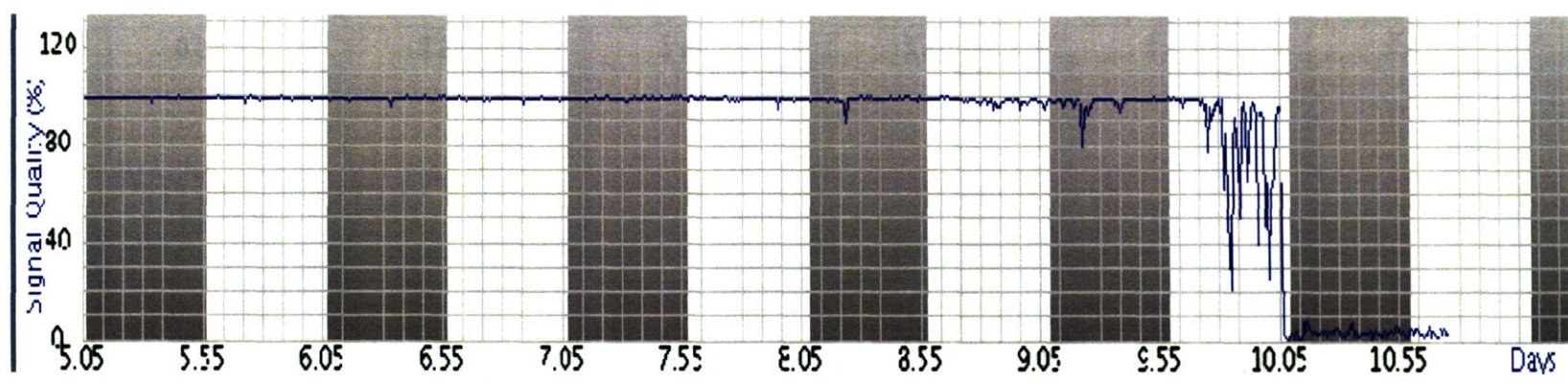
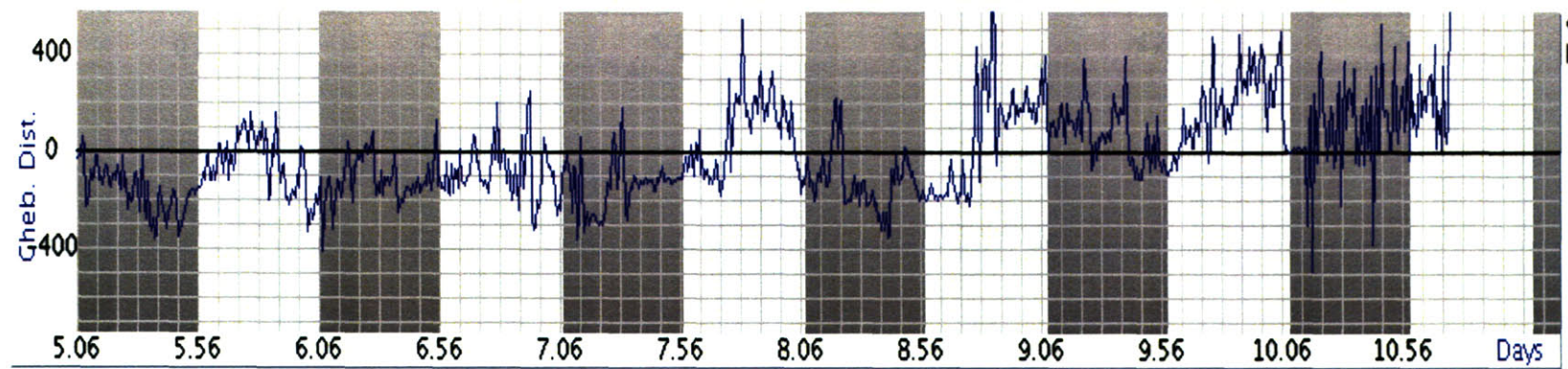
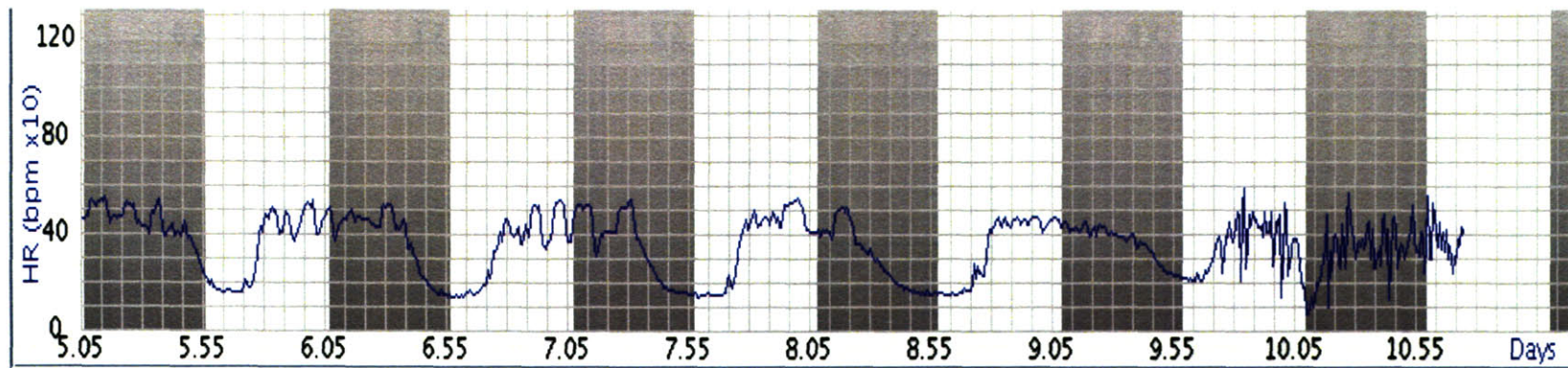


Figure B-47: heart rate, repolarization morphology and signal quality index for subject 6846090403 - 2 of 2  
221



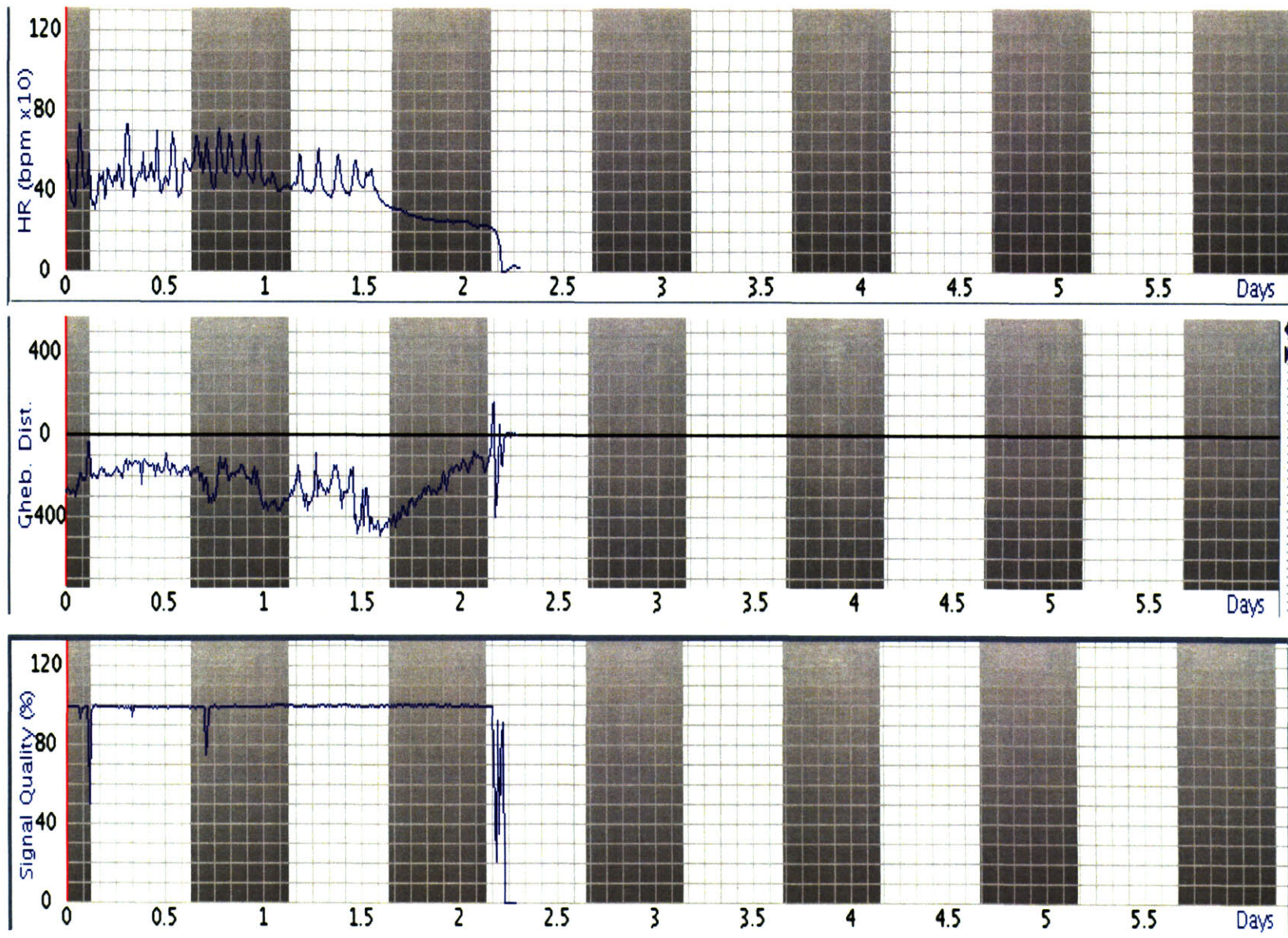


Figure B-48: heart rate, repolarization morphology and signal quality index for subject 7602091903  
222



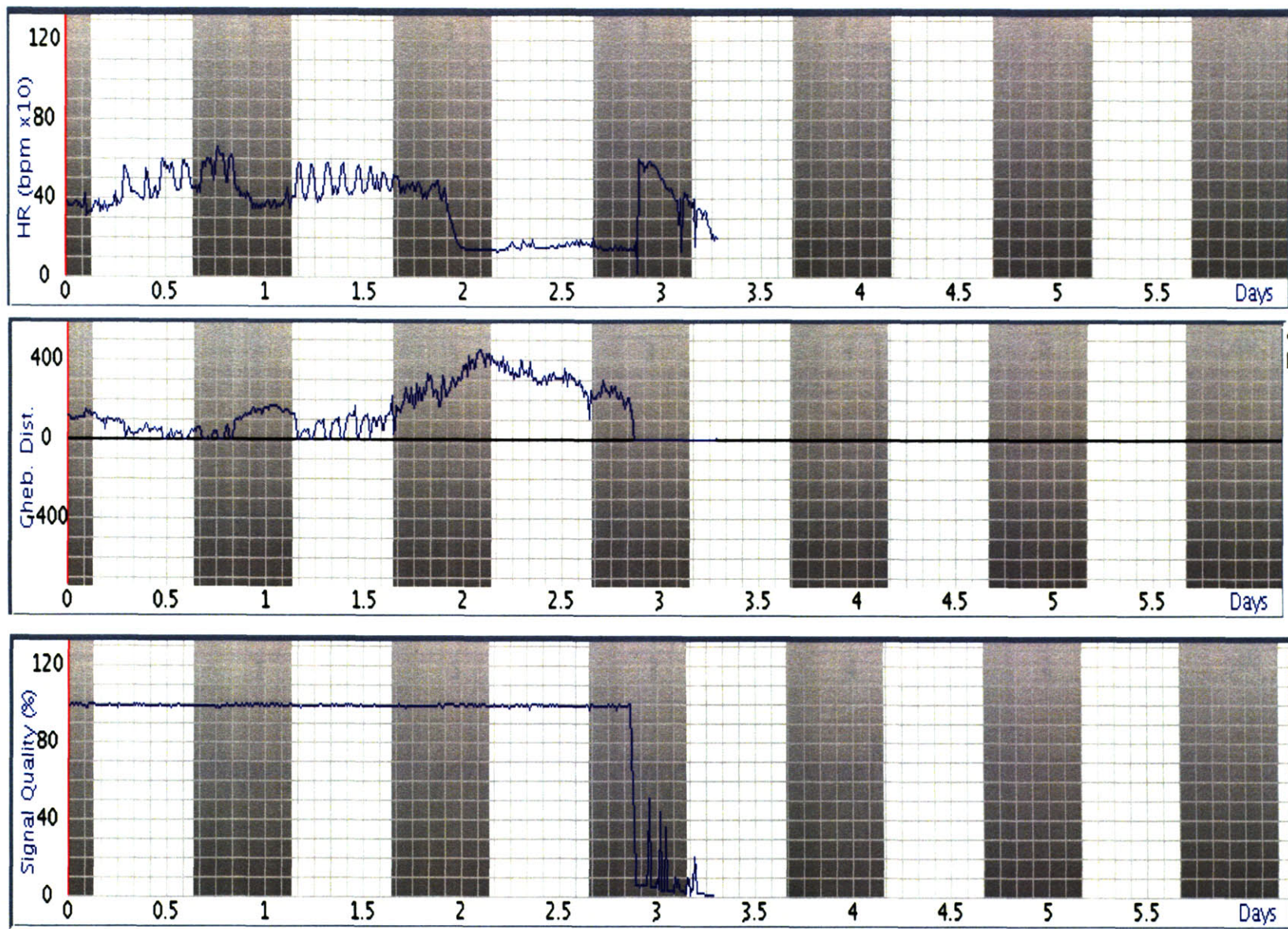


Figure B-49: heart rate, repolarization morphology and signal quality index for subject 8083100303  
223



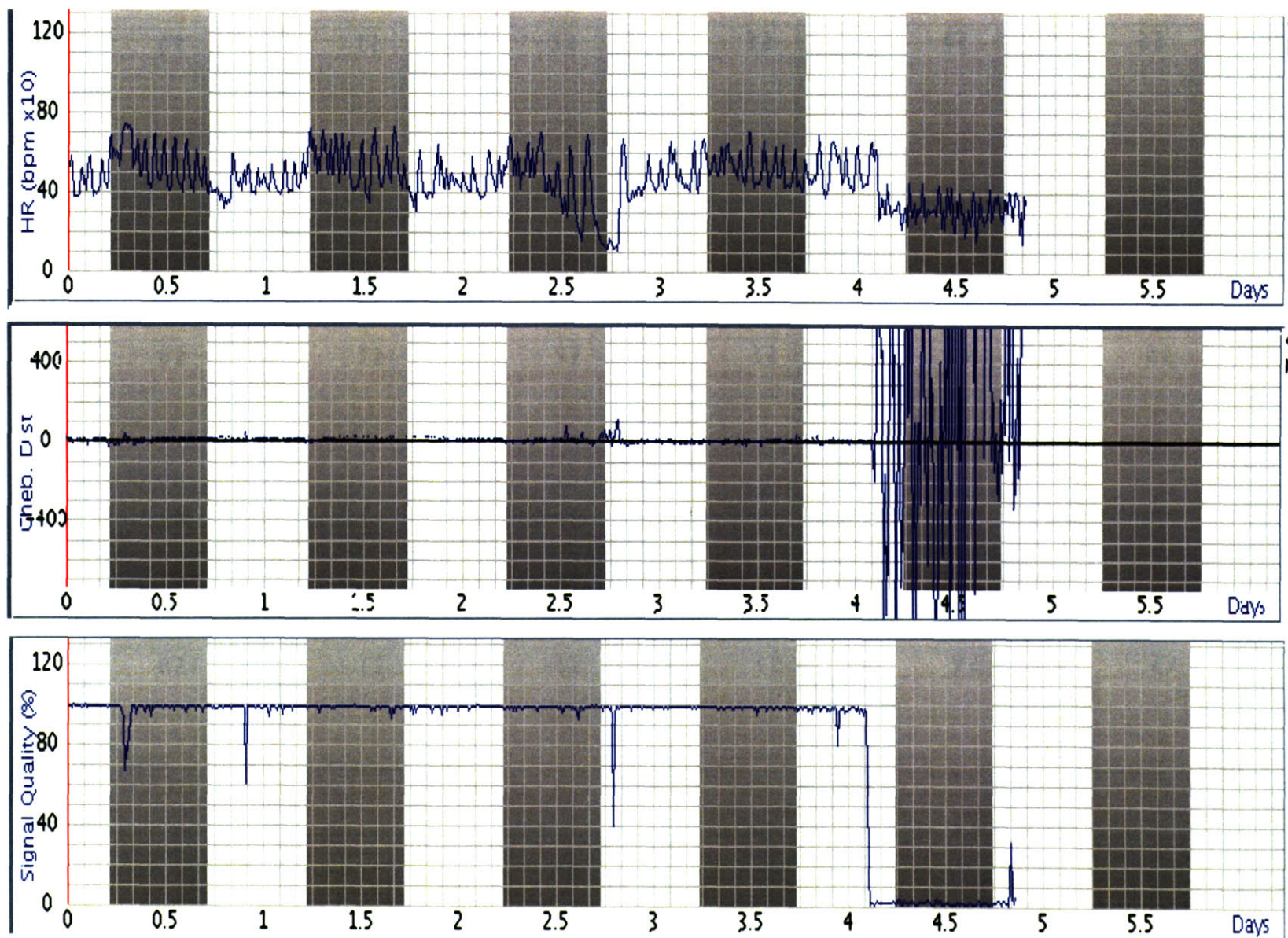


Figure B-50: heart rate, repolarization morphology and signal quality index for subject 8086100303  
224



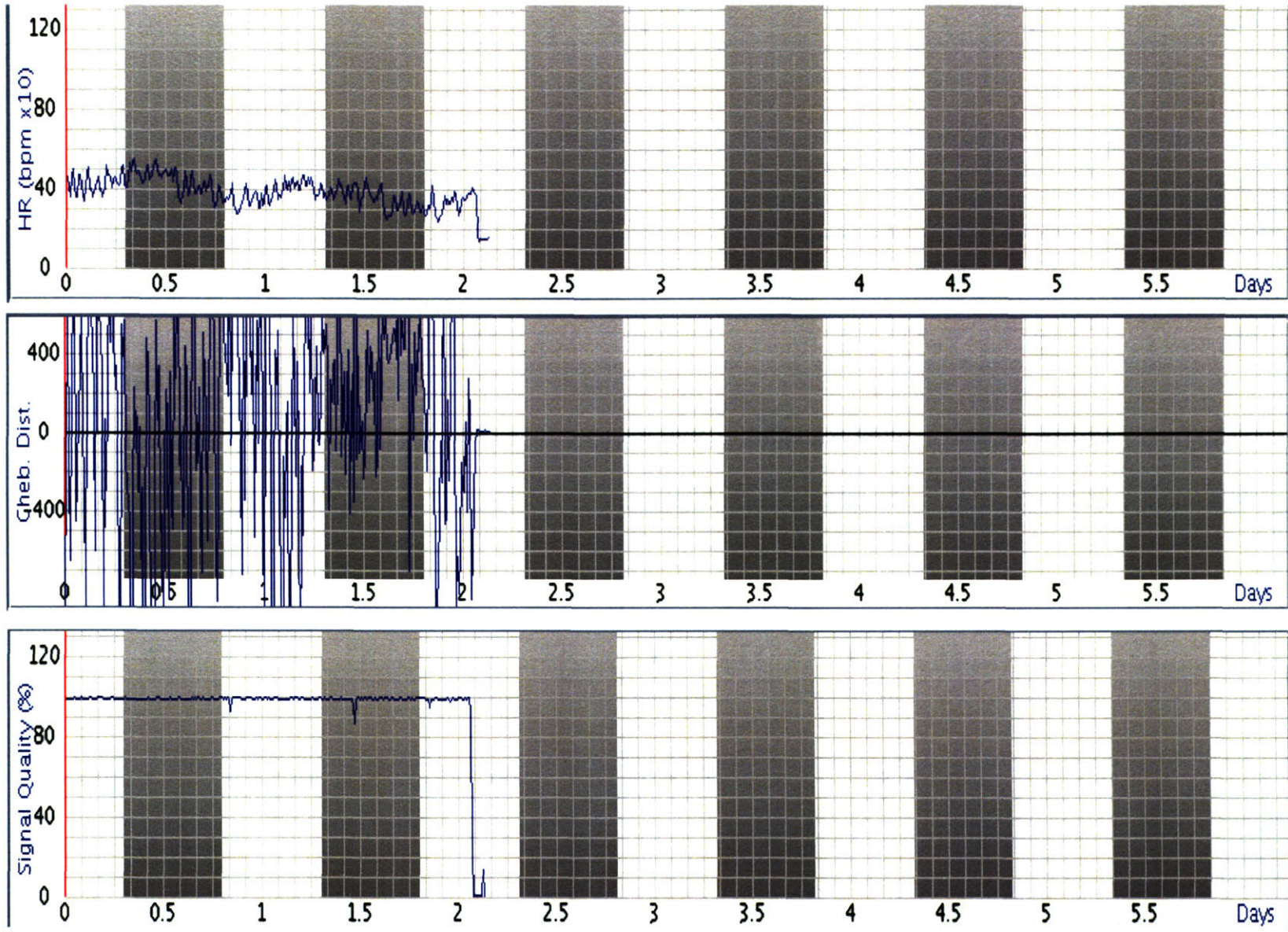


Figure B-51: heart rate, repolarization morphology and signal quality index for subject 9050040505  
225



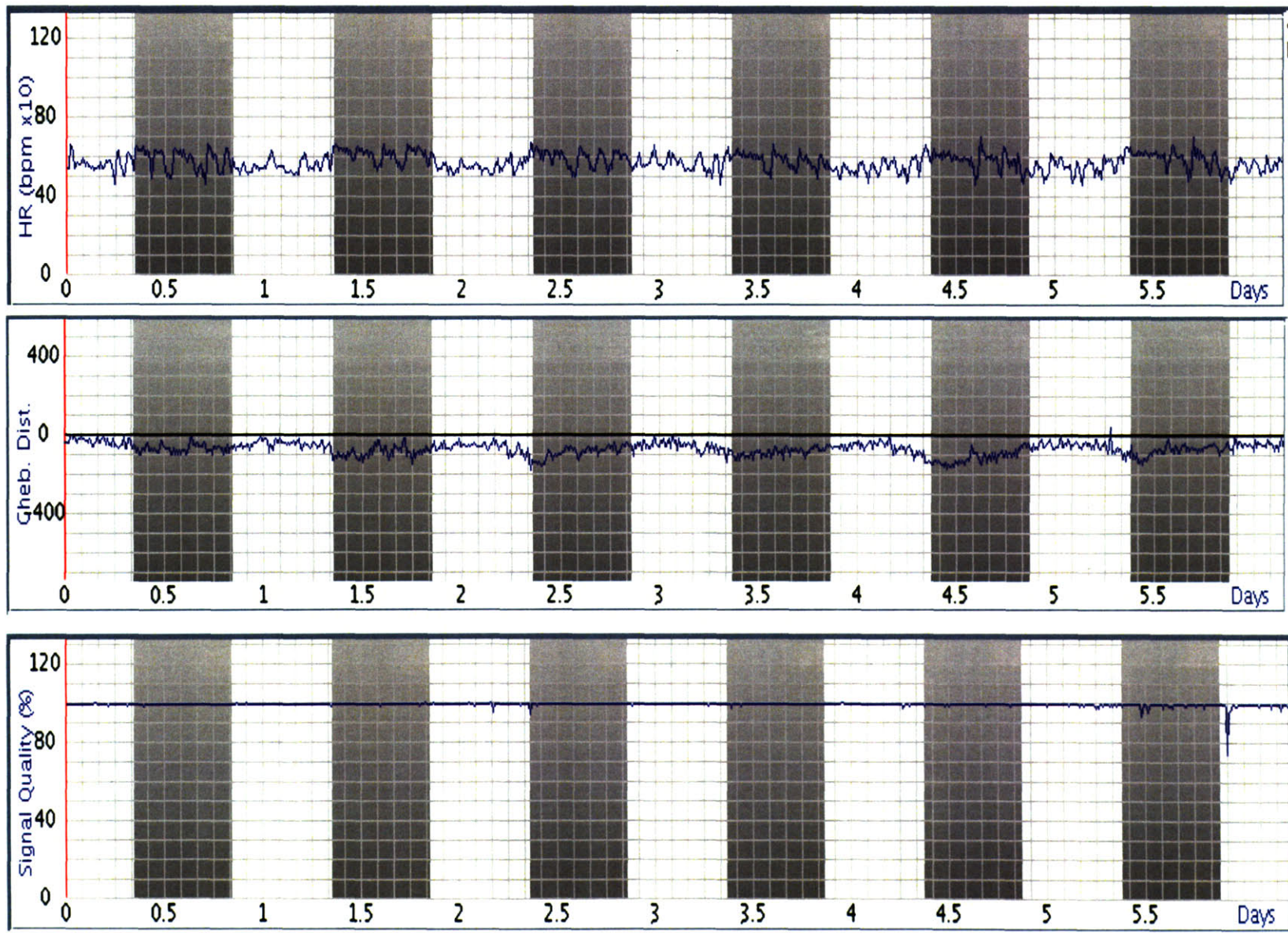


Figure B-52: heart rate, repolarization morphology and signal quality index for subject 9394222603 - 1 of 3  
226



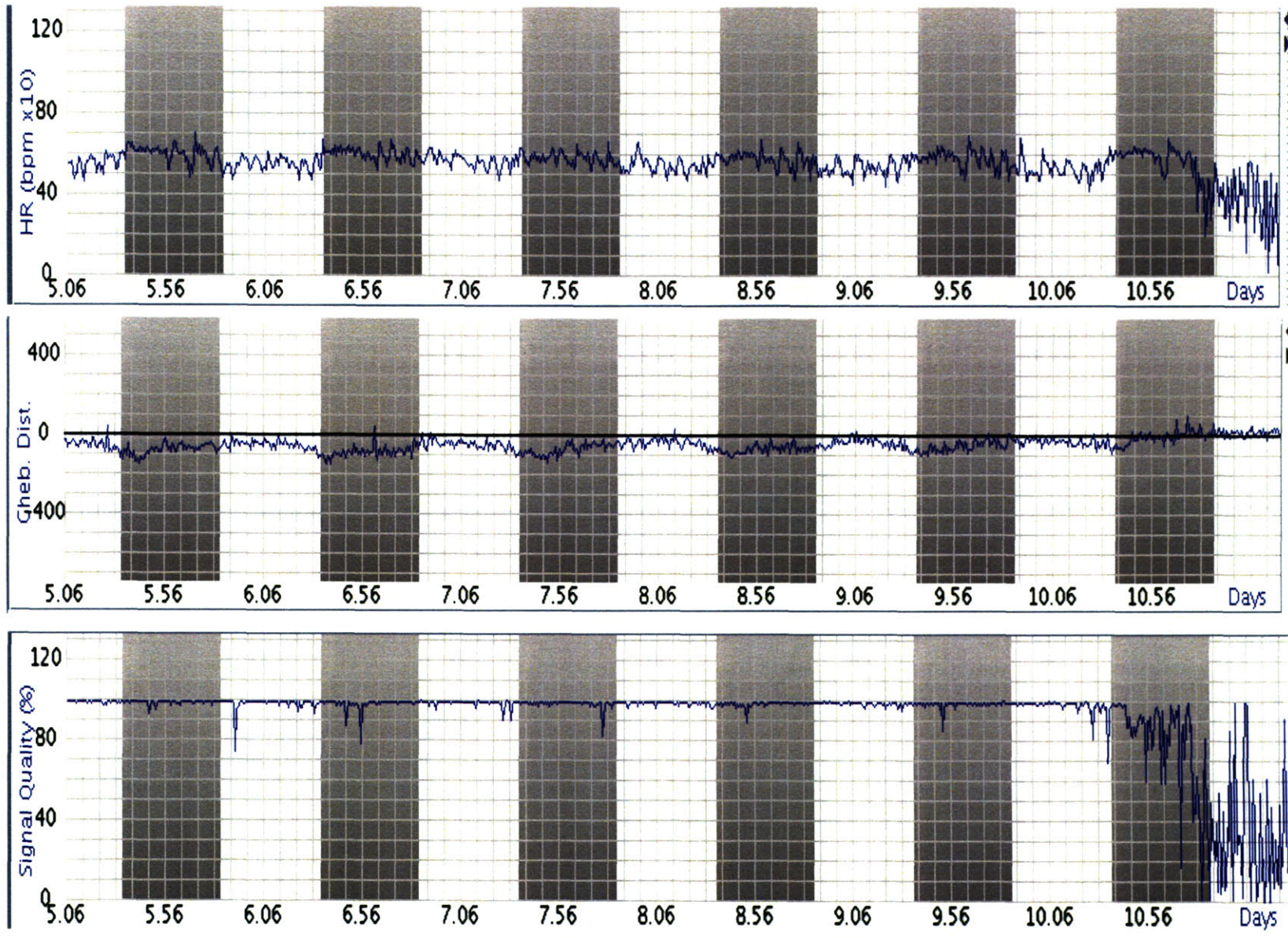


Figure B-53: heart rate, repolarization morphology and signal quality index for subject 939411603 - 2 of 3  
227



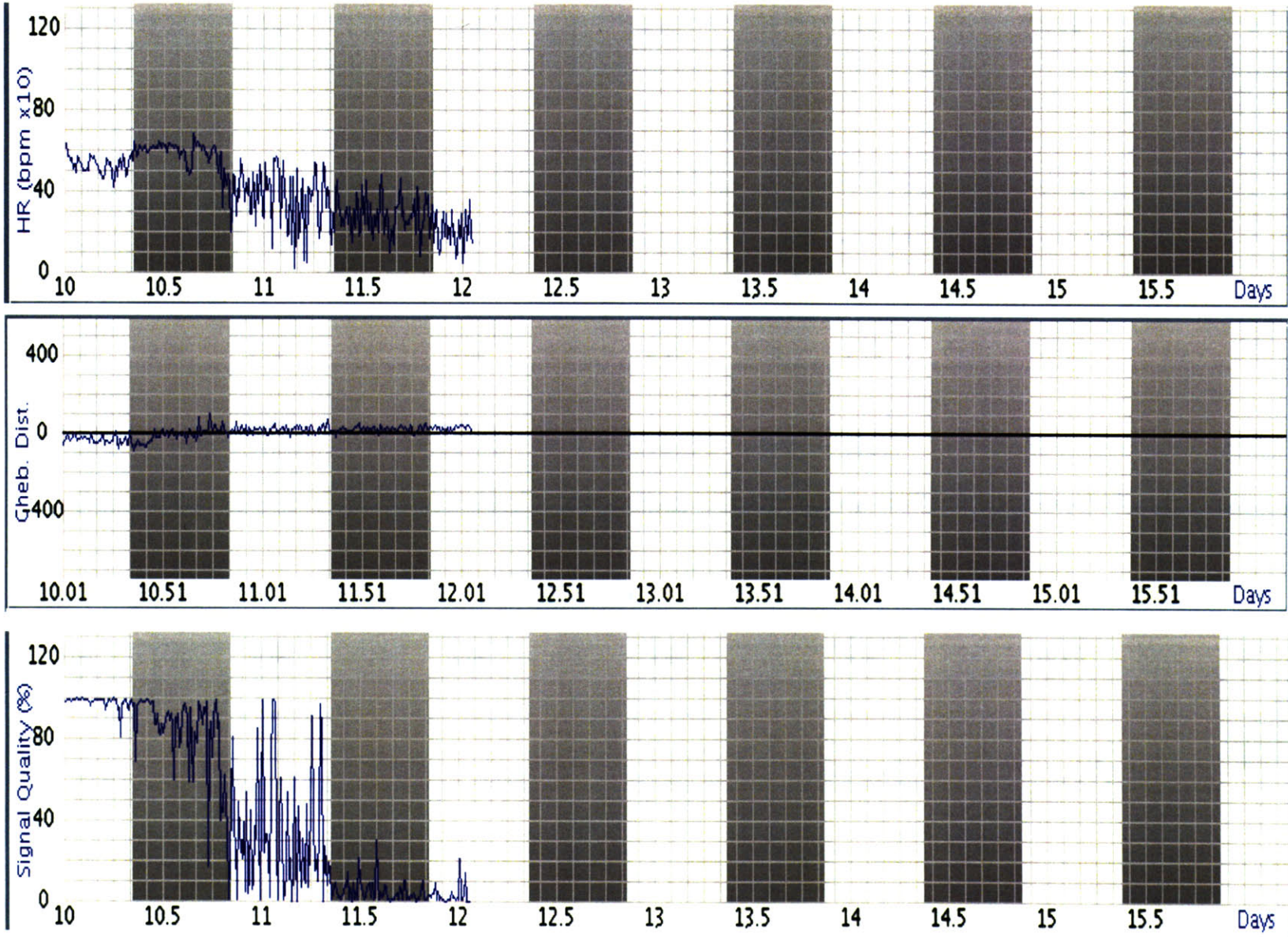


Figure B-54: heart rate, repolarization morphology and signal quality index for subject 939411603 - 3 of 3  
228



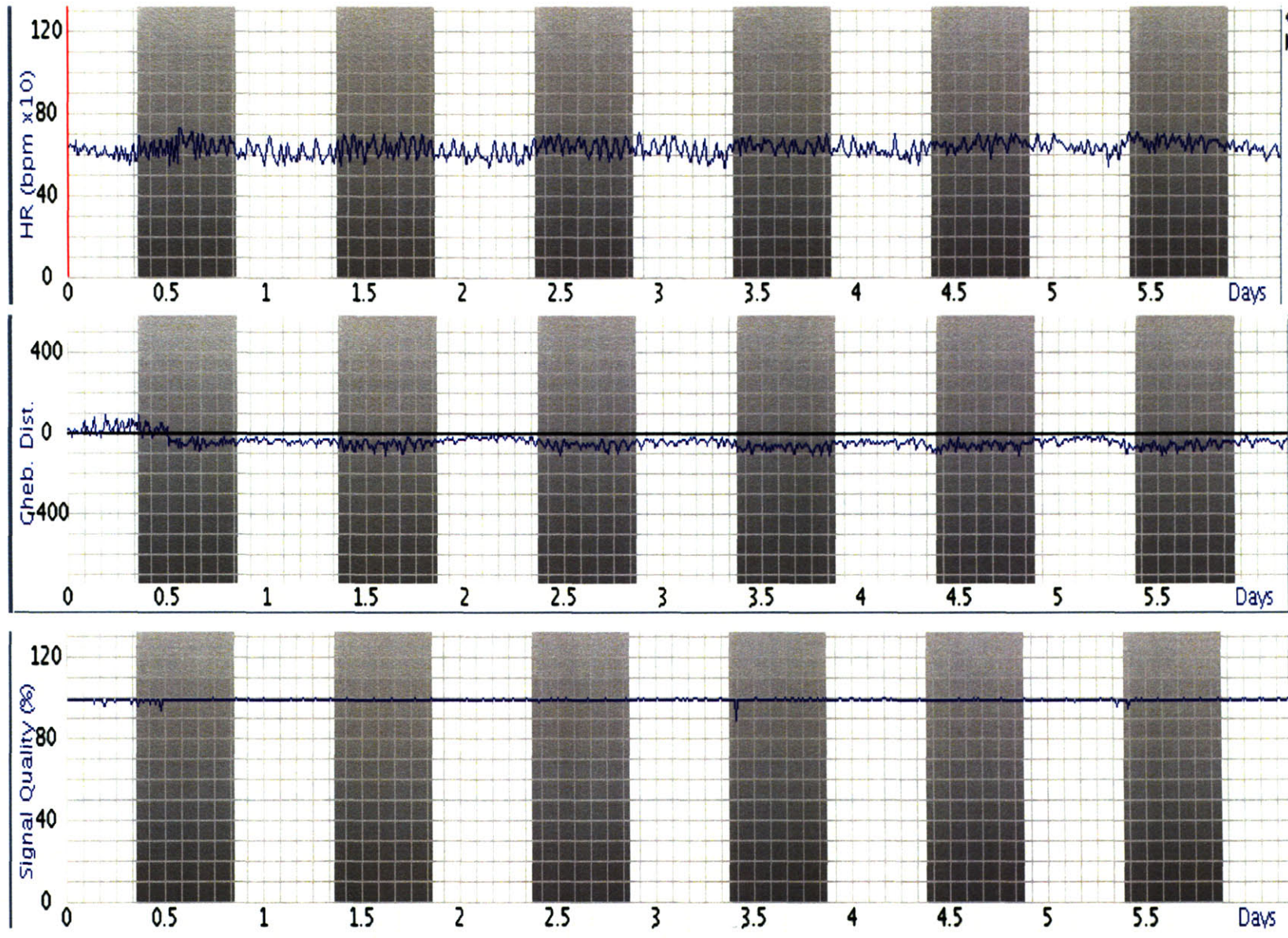


Figure B-55: heart rate, repolarization morphology and signal quality index for subject 9399222603 - 1 of 4  
229



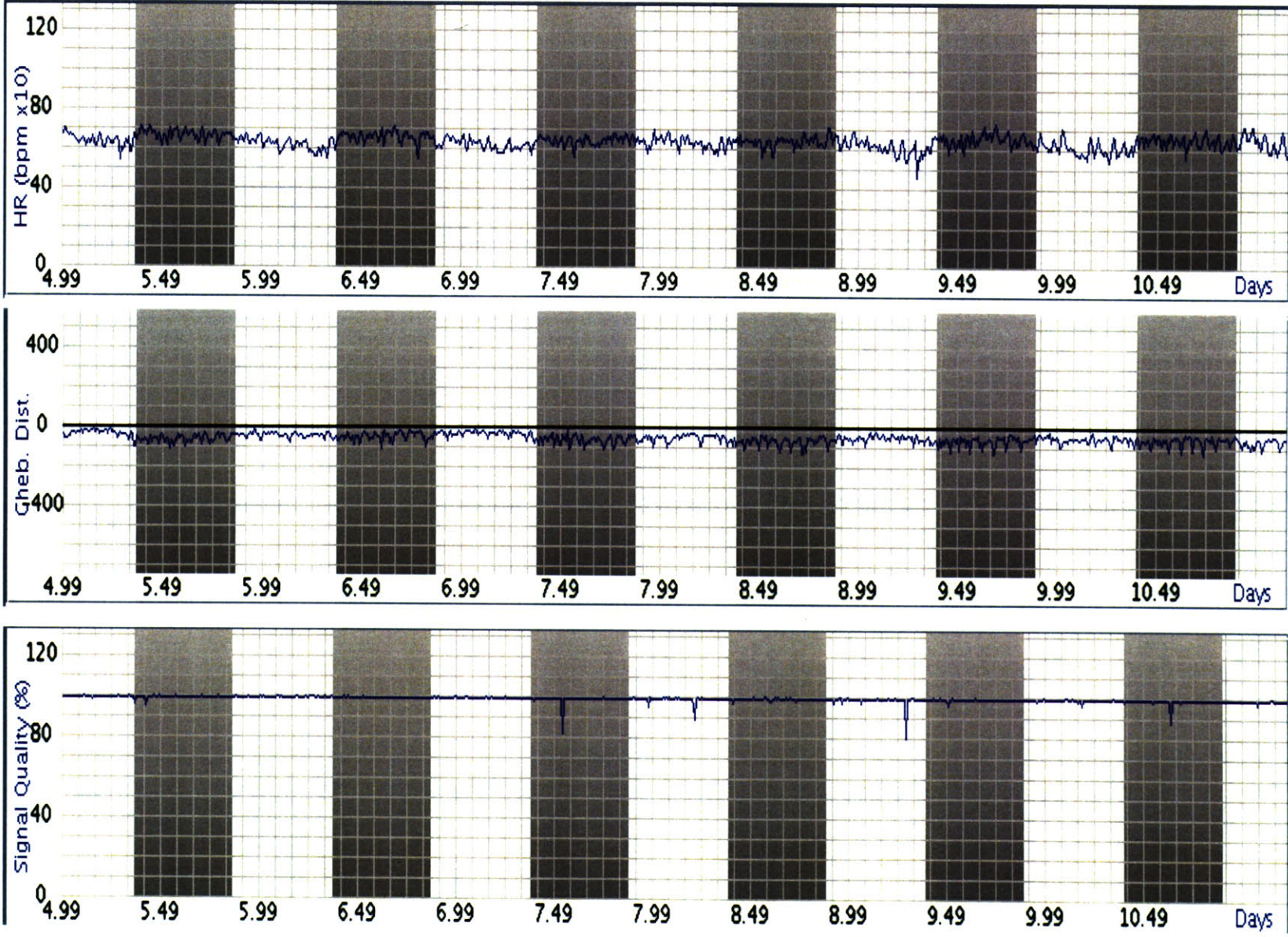


Figure B-56: heart rate, repolarization morphology and signal quality index for subject 9399111603 - 2 of 4  
230



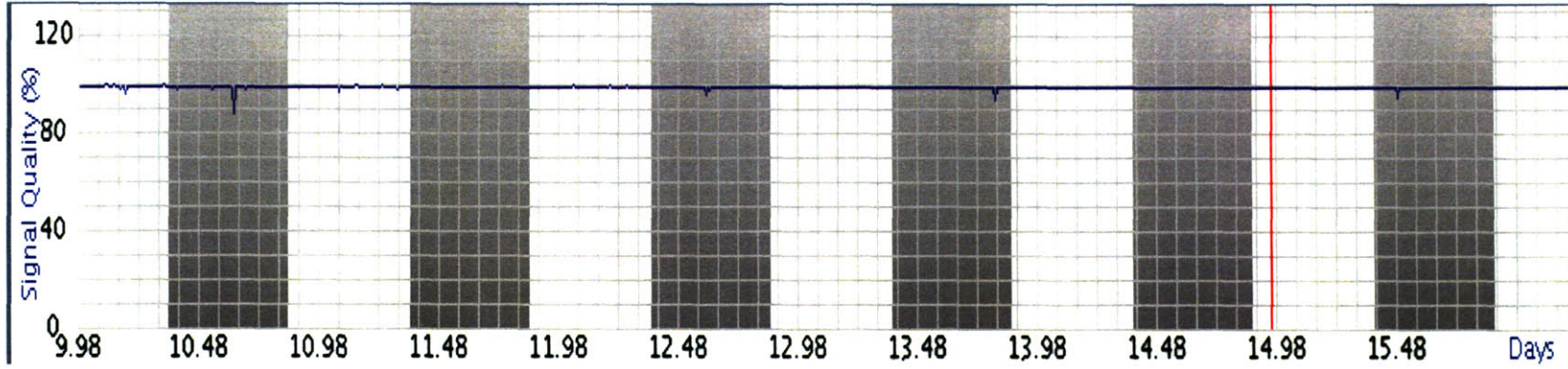
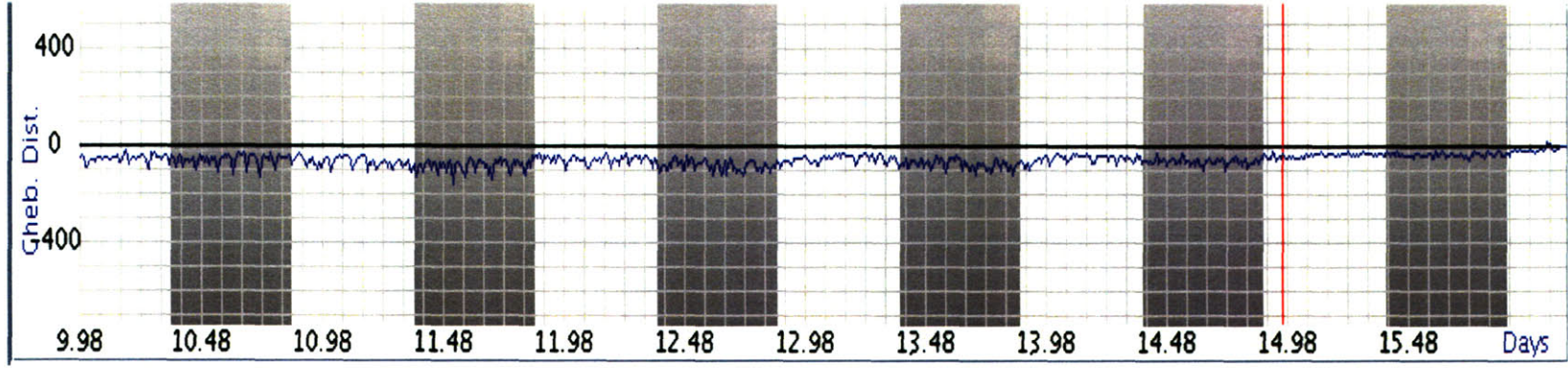
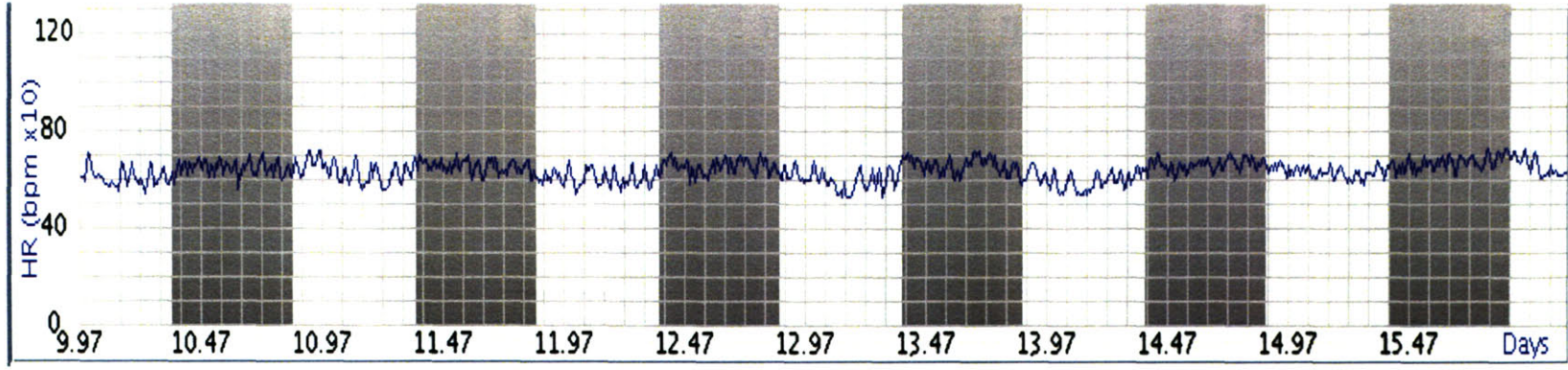


Figure B-57: heart rate, repolarization morphology and signal quality index for subject 9399111603 - 3 of 4  
231



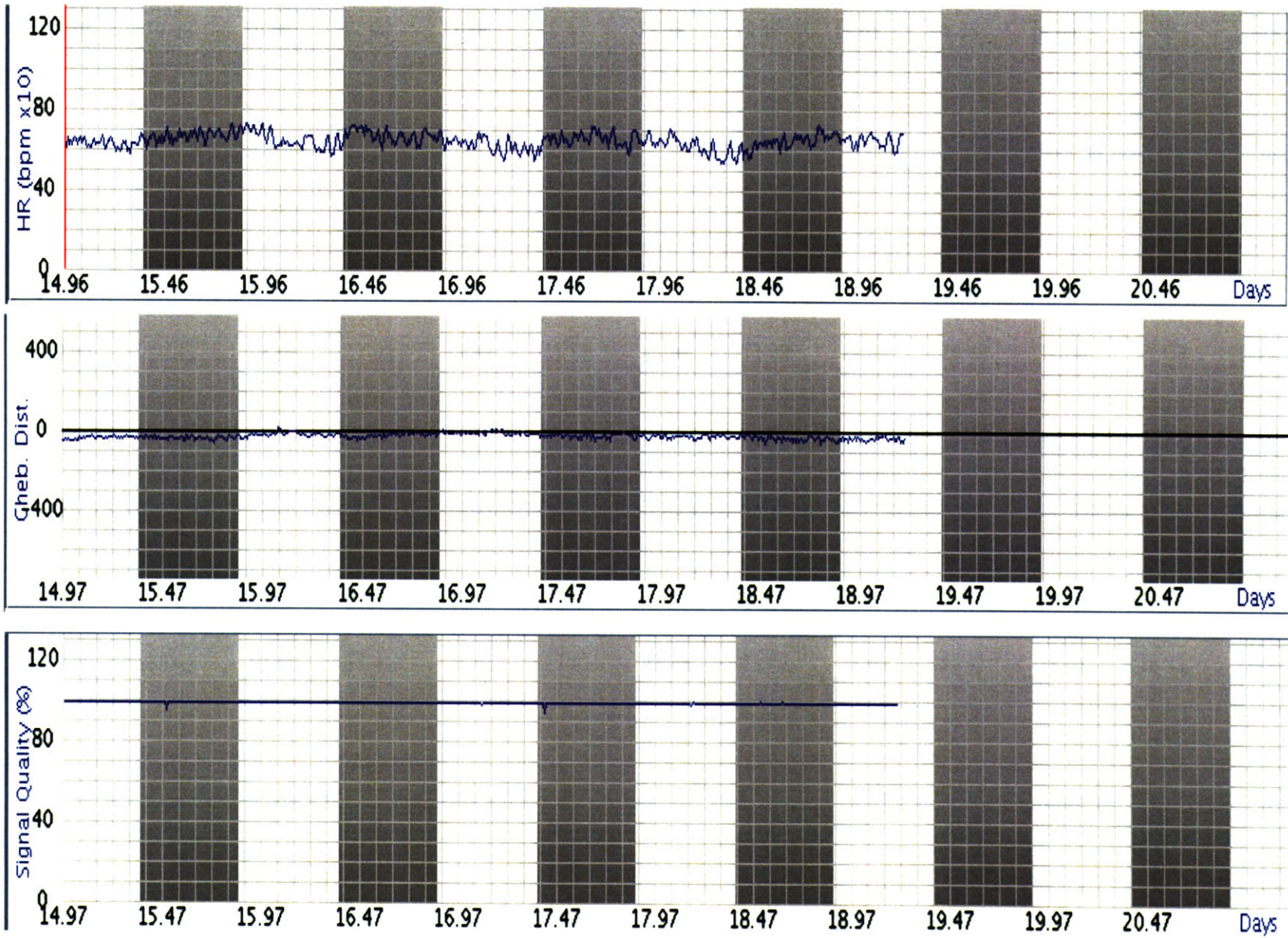


Figure B-58: heart rate, repolarization morphology and signal quality index for subject 9399111603 - 4 of 4  
232



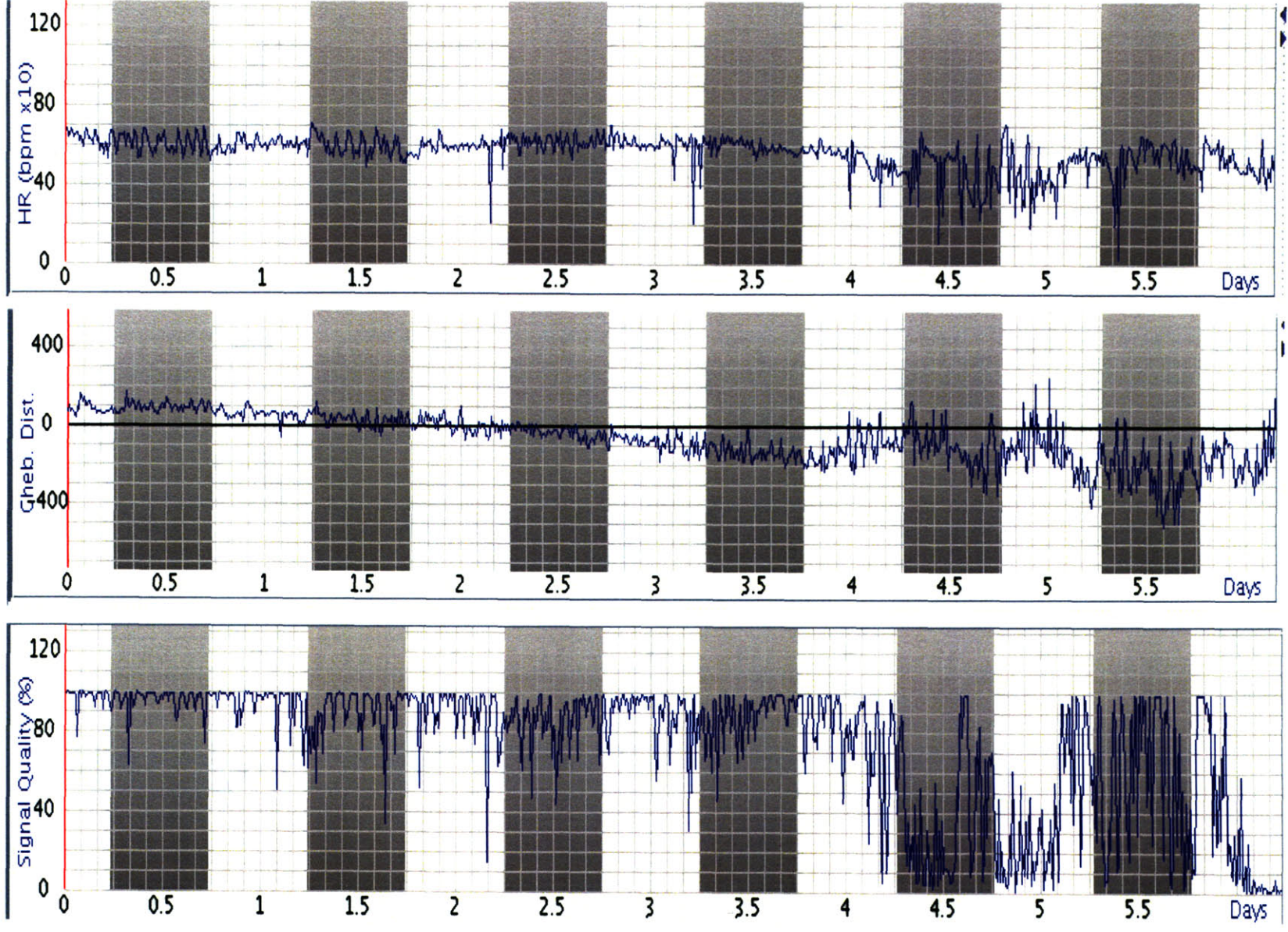


Figure B-59: heart rate, repolarization morphology and signal quality index for subject 9715112203 - 1 of 2  
233



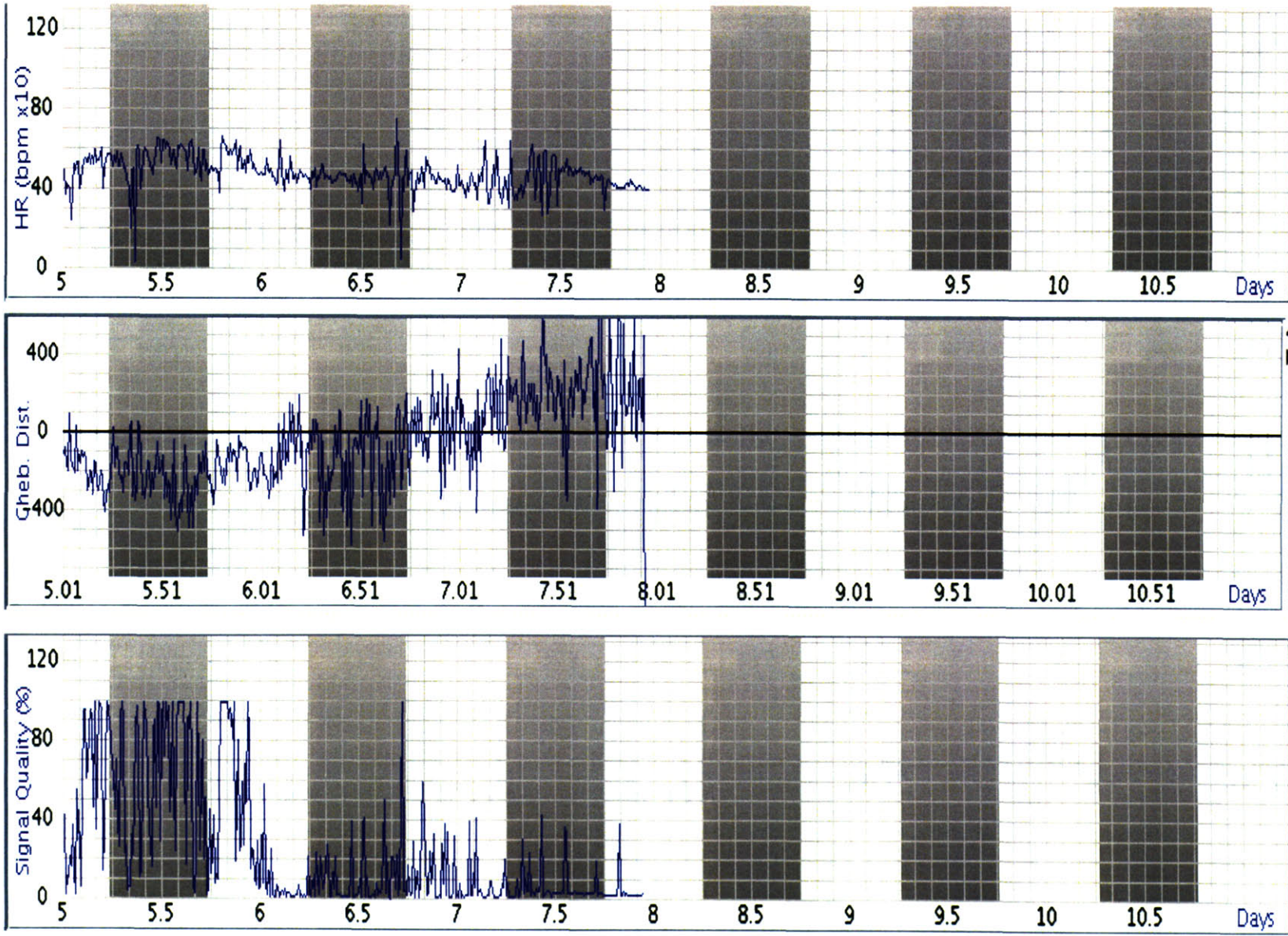


Figure B-60: heart rate, repolarization morphology and signal quality index for subject 9715112203 - 2 of 2  
234



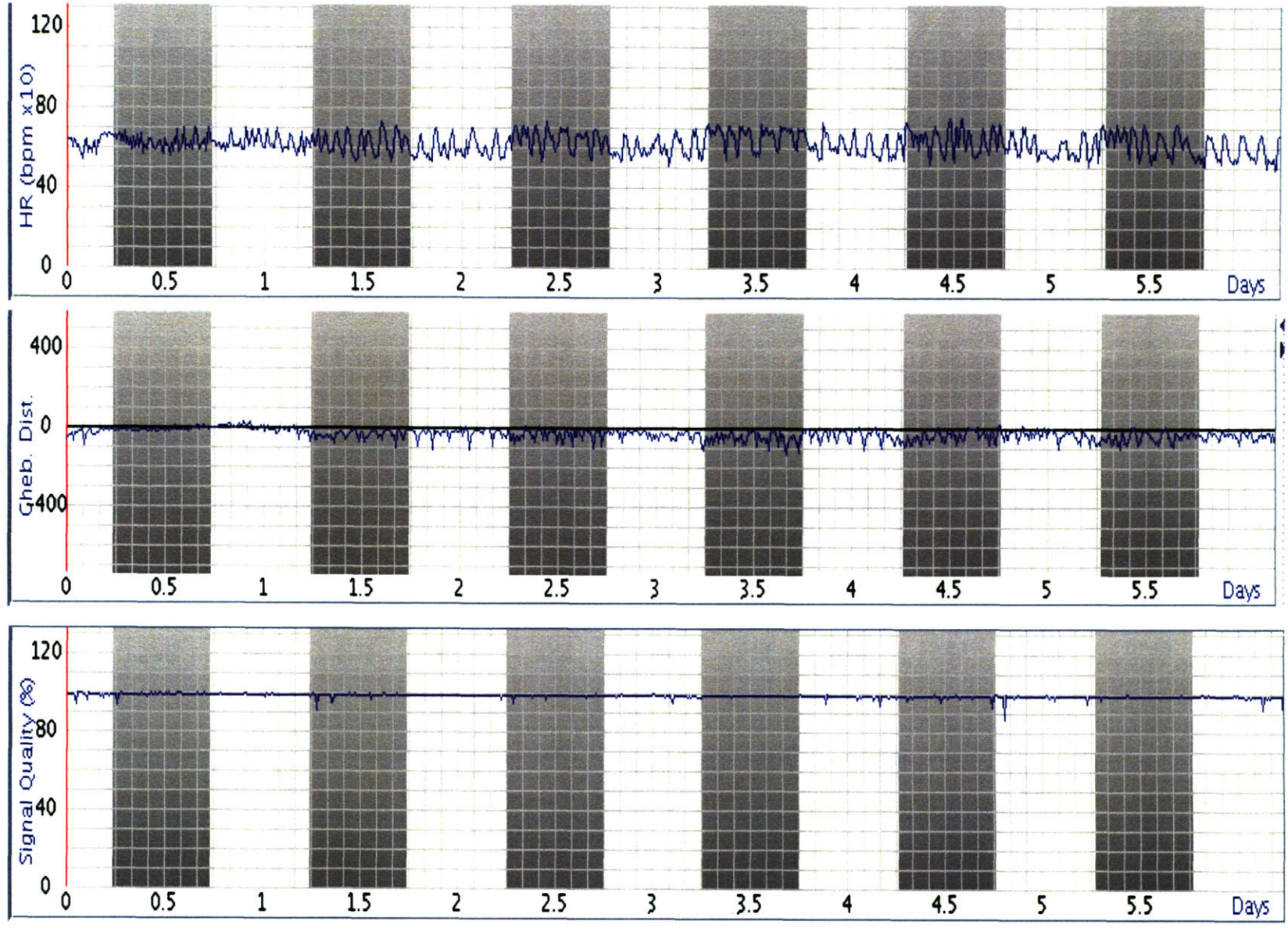


Figure B-61: heart rate, repolarization morphology and signal quality index for subject 9775112103 - 1 of 3  
235



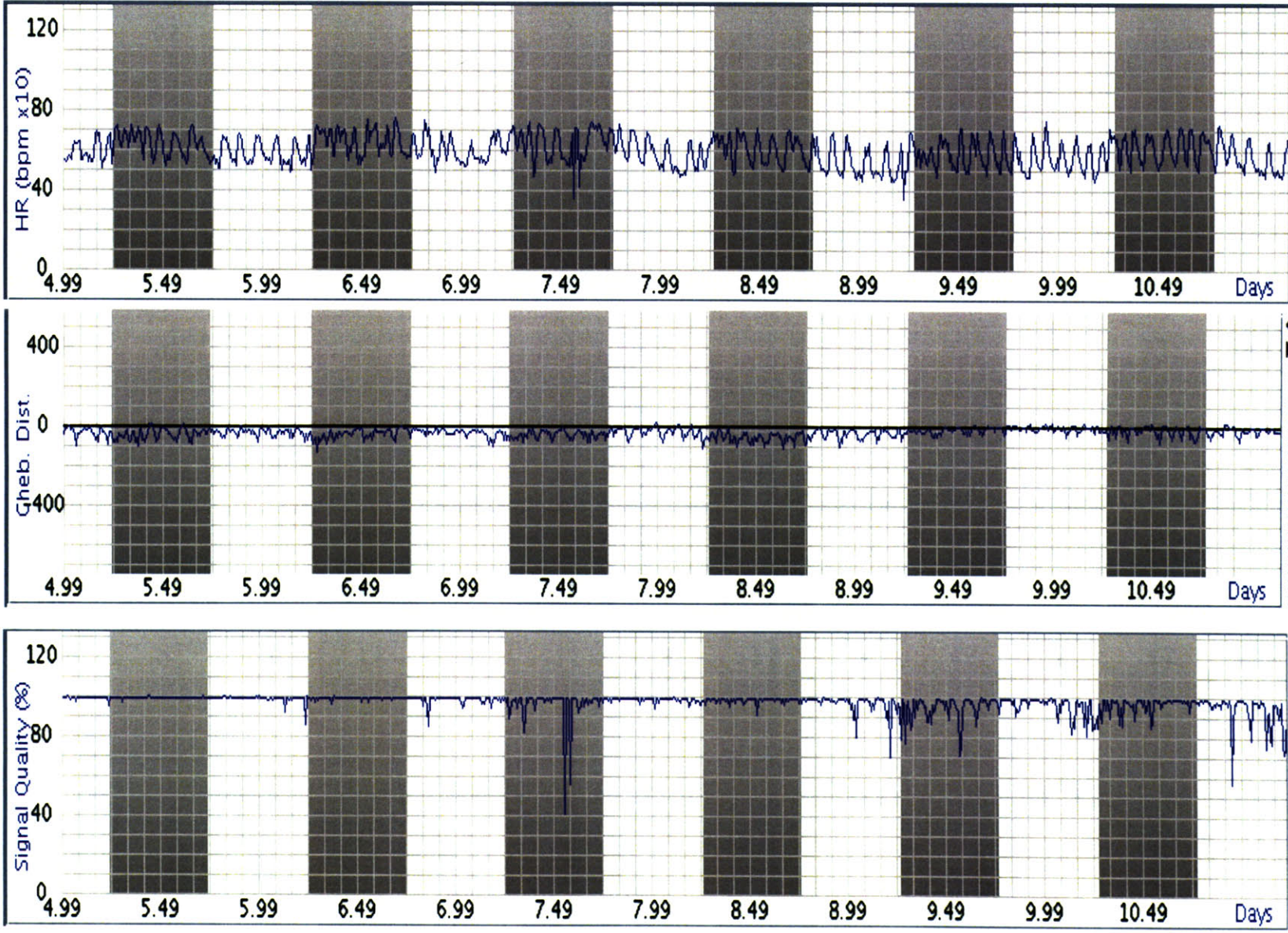


Figure B-62: heart rate, repolarization morphology and signal quality index for subject 9775112103 - 2 of 3  
236



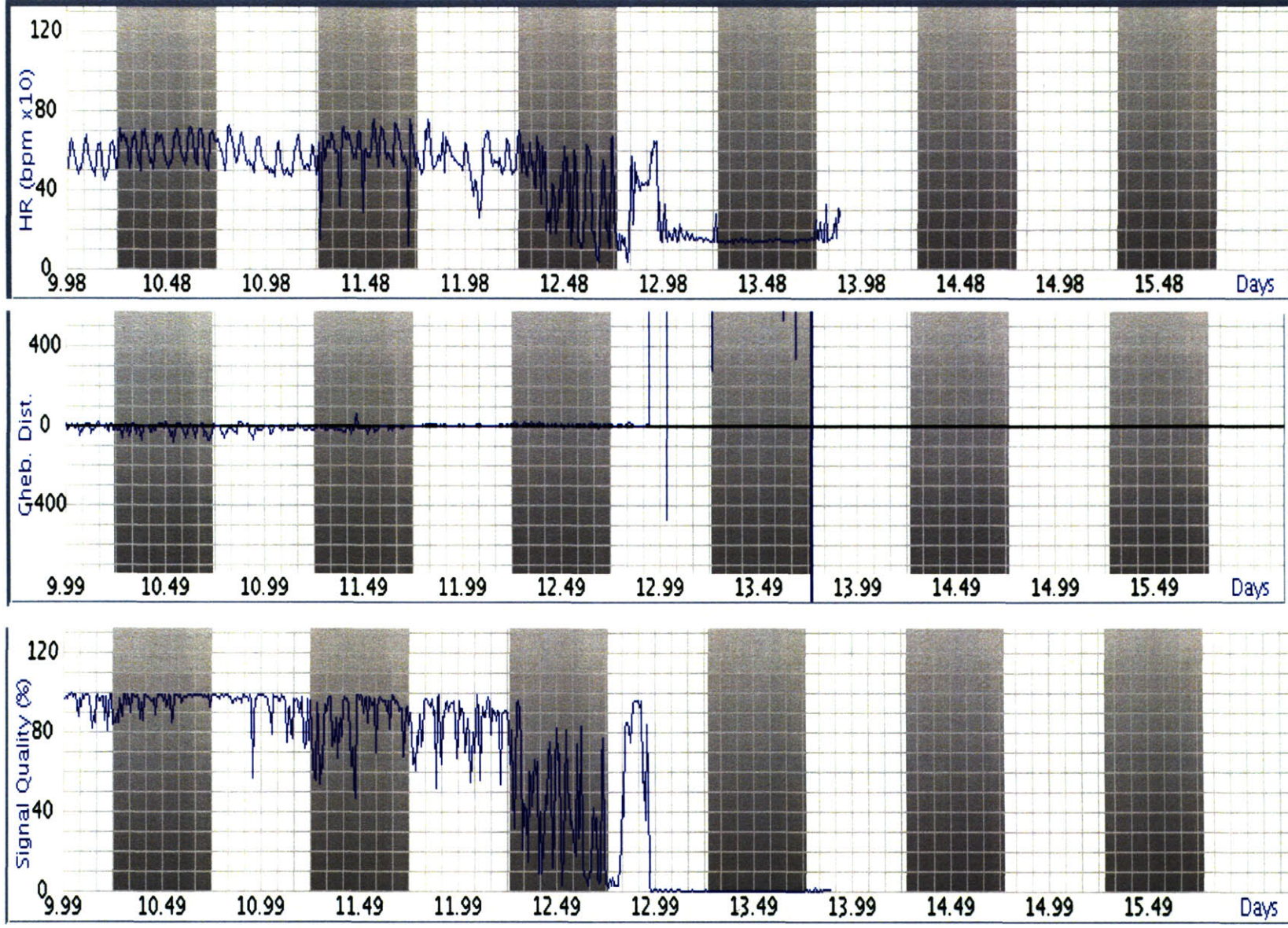


Figure B-63: heart rate, repolarization morphology and signal quality index for subject 9775112103 - 3 of 3  
237



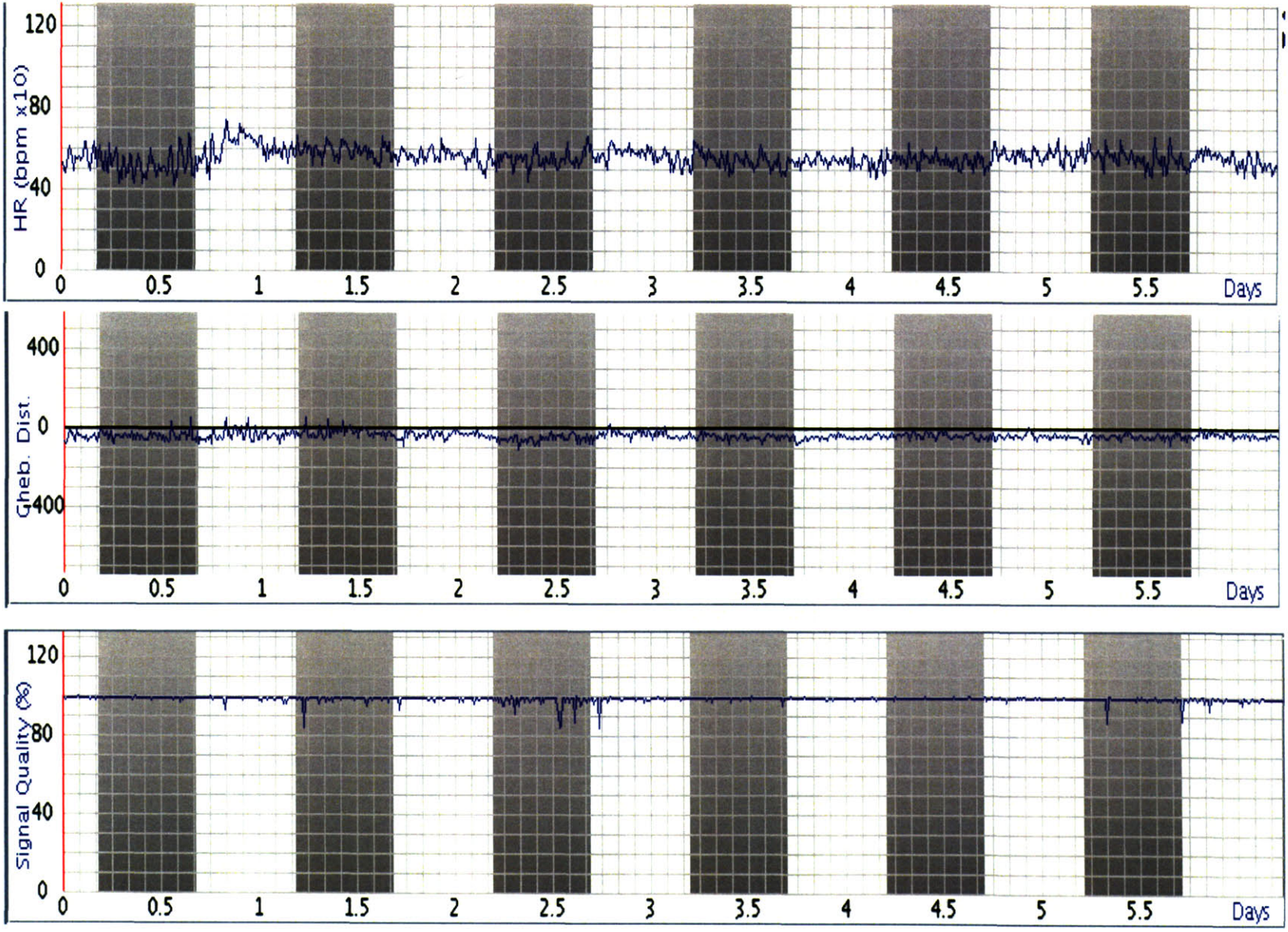


Figure B-64: heart rate, repolarization morphology and signal quality index for subject 9907120503 - 1 of 2  
238



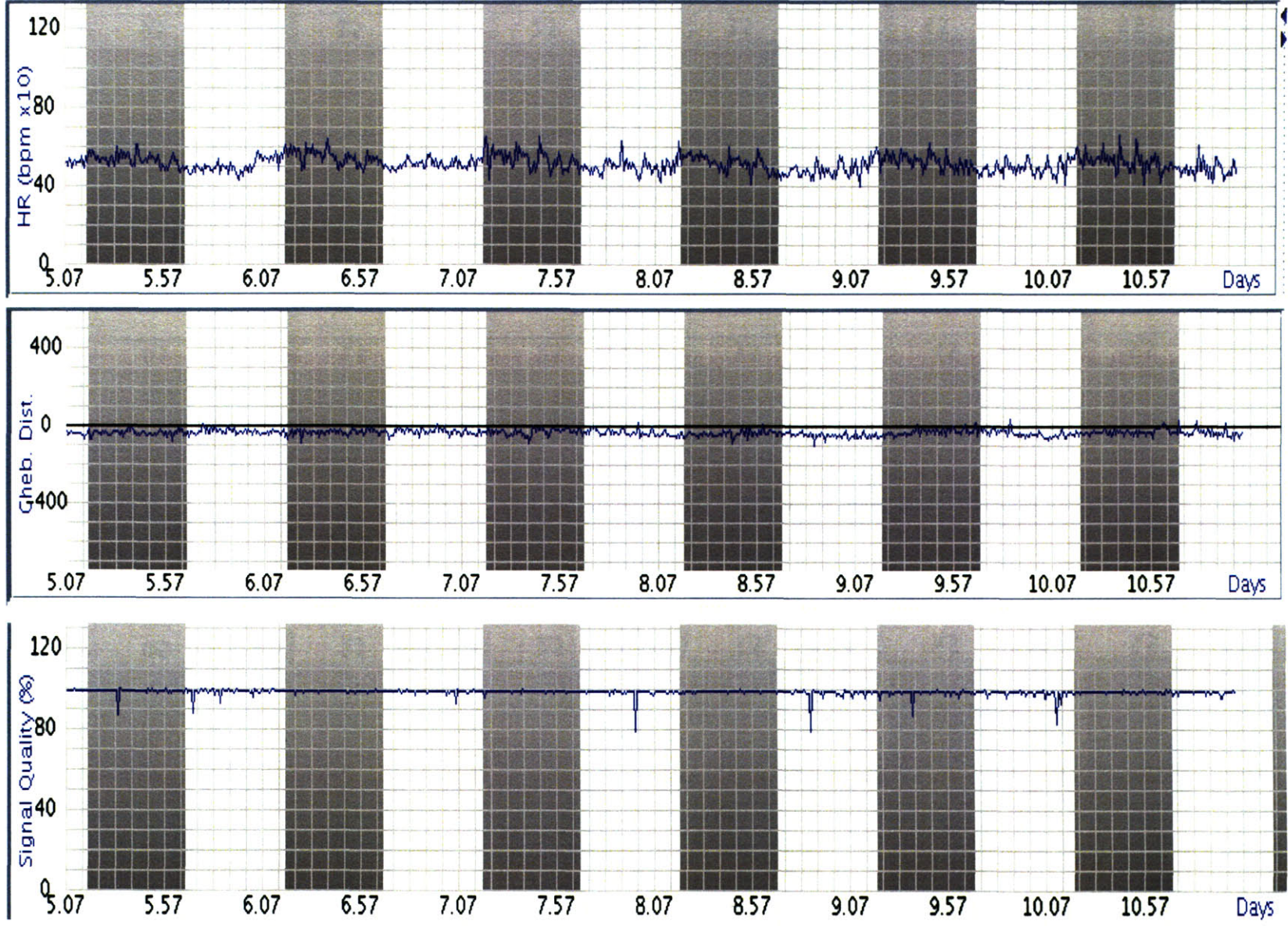


Figure B-65: heart rate, repolarization morphology and signal quality index for subject 9907120503 - 2 of 2  
239



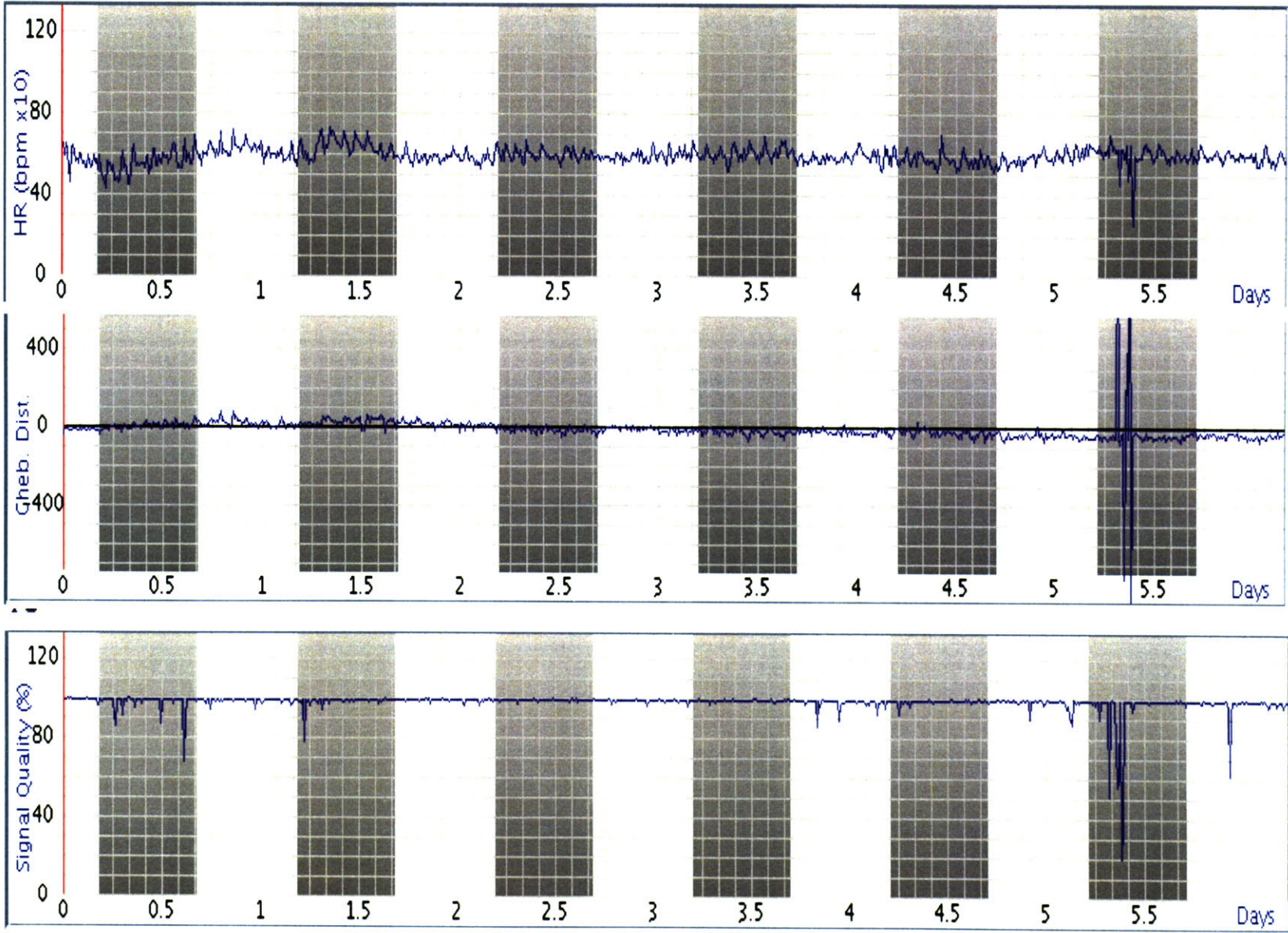


Figure B-66: heart rate, repolarization morphology and signal quality index for subject 9908120503 - 1 of 2  
240



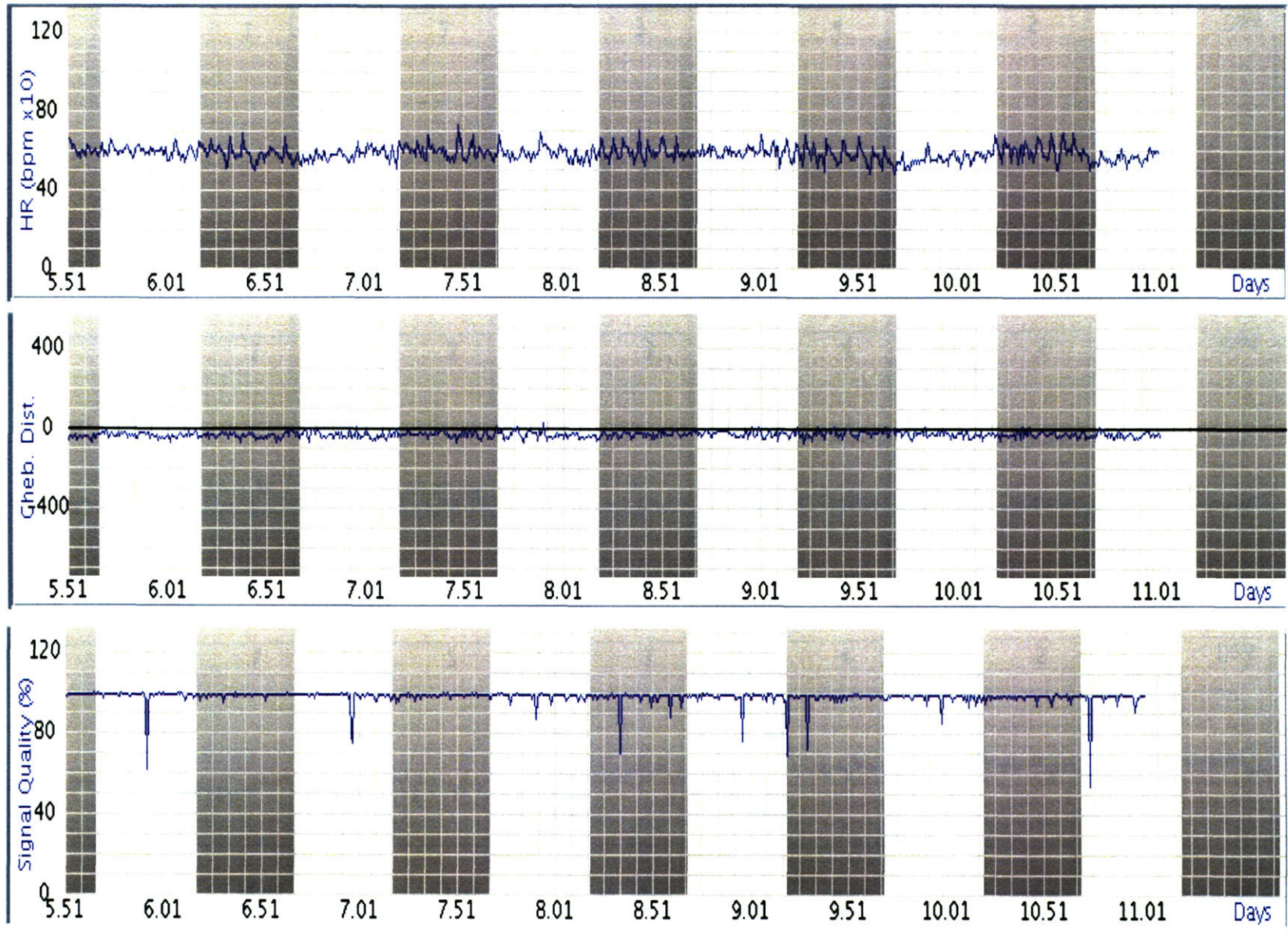


Figure B-67: heart rate, repolarization morphology and signal quality index for subject 9908120503 - 2 of 2  
241



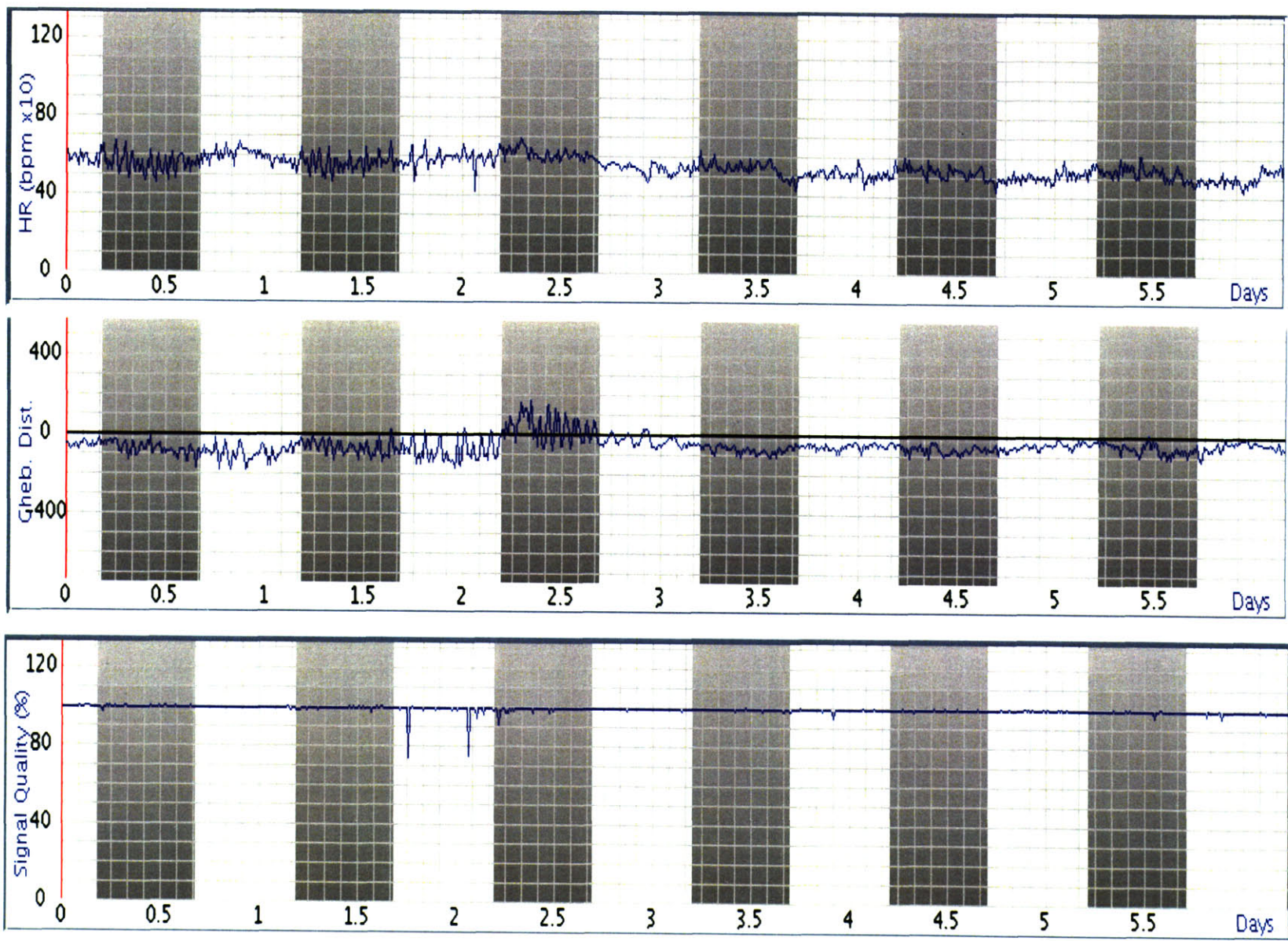


Figure B-68: heart rate, repolarization morphology and signal quality index for subject 9909120503 - 1 of 2



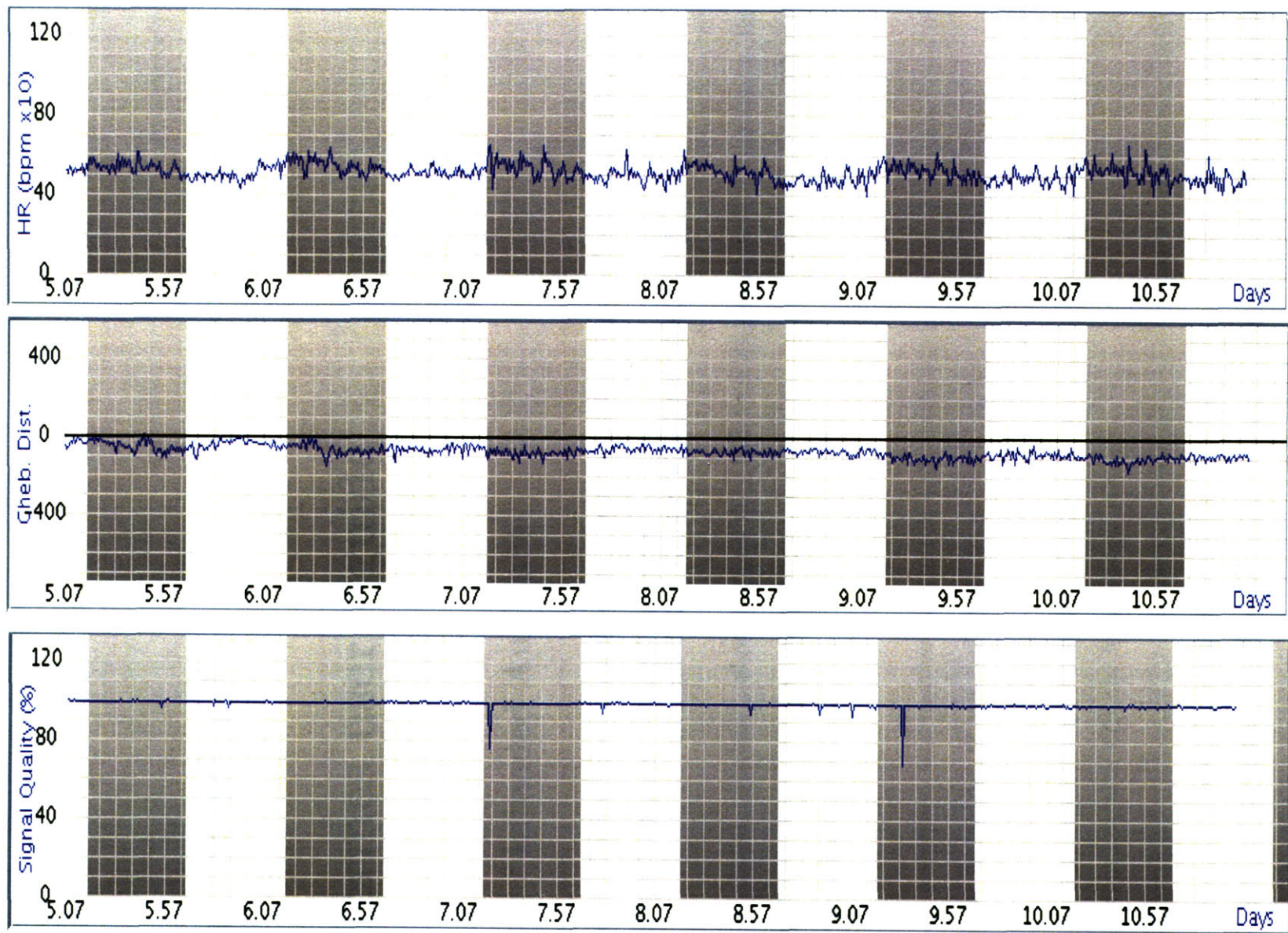


Figure B-69: heart rate, repolarization morphology and signal quality index for subject 9909120503 - 2 of 2  
243



THIS PAGE INTENTIONALLY LEFT BLANK

# Appendix C

## Hermes user's guide

### C.1 Intended Audience

Chapter 3 details the several software facets comprising Hermes. Users interacting with the software fit into one of several categories:

1. the lab technician, whose responsibility it is to start and stop data acquisition, input appropriate record information (genotype, date of birth, etc.), and monitor the health status of the animal periodically.
2. researchers who monitor data trends and waveforms to understand disease state, drug efficacy or toxicity, or any number of parameters applicable to their study design.
3. engineers writing new modules for Hermes or otherwise debugging or developing software that interacts with the foundational software.

This user guide is intended primarily for those in category 2 above, namely researchers who will use the online visualization tool in a research capacity. An up-to-date hardcopy user guide for lab technicians is available in the animal facilities near the data collection

servers. A software developer guide for engineers requiring detailed information on Hermes source code and architecture is quite lengthy and of little use in an appendix. For access to the hardcopy software developer guide, please contact George Moody of the Laboratory for Computational Physiology at [george@mit.edu](mailto:george@mit.edu).

## C.2 Getting started

In order to view the archived mouse data, a user needs a username and password. At the time of this writing, the data remains confidential and accessible only to authorized users. To request access to the murine database, please contact George Moody ([george@mit.edu](mailto:george@mit.edu)).

The equipment required for viewing the mouse database is an Internet-connected computer. No formalized tests have been conducted to determine minimum RAM or CPU speed, but the user experience will invariably depend in part on the speed of the computer and the Internet connection speed. The computer should have a web browser and the Java Virtual Machine (JVM) plugin installed. Most Windows machines are pre-configured with JVM, while Linux machines often require manual installation of the plugin. To download the JVM, visit <http://java.sun.com>.

## C.3 Viewing a Record

Upon visiting the appropriate URL, which will be provided along with account login details, the Hermes applet loads automatically. The applet may require several minutes to load. When the applet has loaded, a screen appears with a list allowing selection of a record. Upon selecting the preferred record, click on the *Load Record* button. When the record has loaded, click on one of the following tabs in the upper portion of the window: *Database*, *Heart Rate*, *Signal Quality Index*, *Repolarization Segment*, *Report*, or *Help*. These tabs are explained below.



### C.3.1 Database

To change the actively-loaded record at any time, select the *Database* tab to load a record by selecting it from the list then pressing the *Load Record* button. Be sure to click the *Load Record* button! Otherwise the previously-loaded record will remain active.

### C.3.2 Heart rate

A sample screenshot of the heart rate panel is shown in figure C-1.

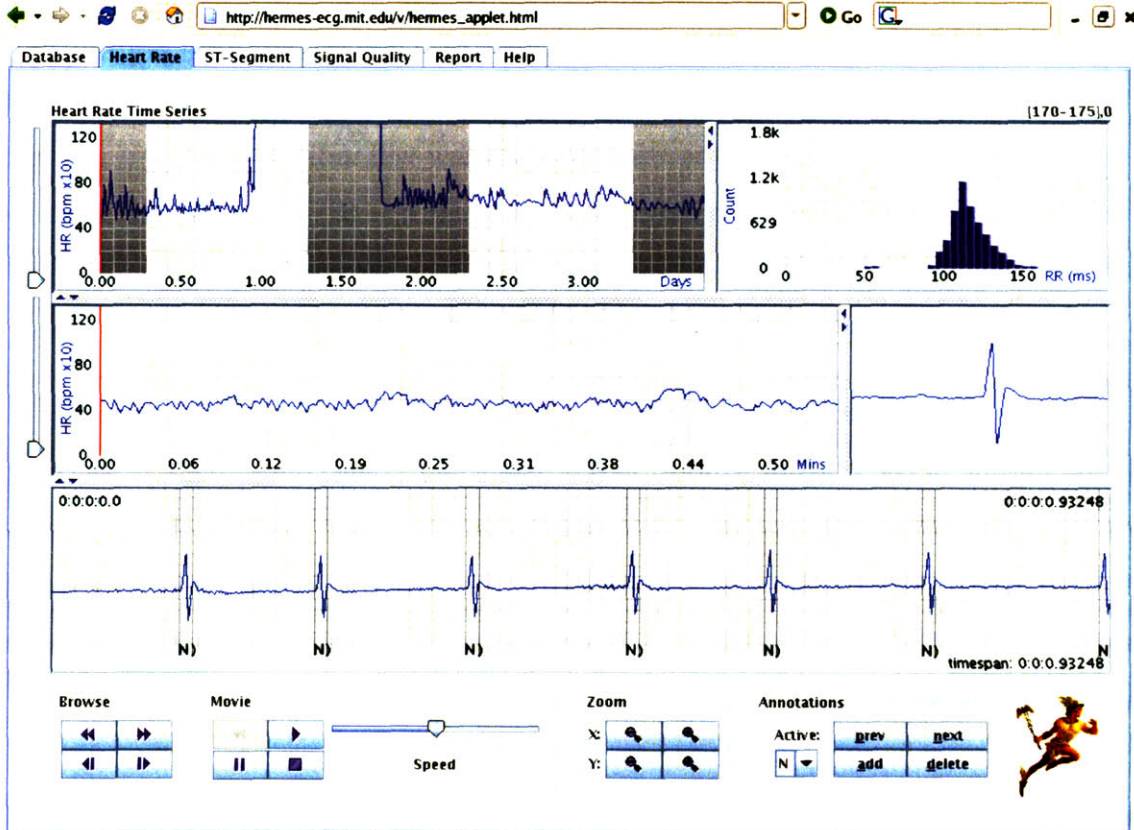


Figure C-1: A sample screenshot taken from the *Heart Rate* panel of a mouse in the murine database.

The heart rate panel consists of several windows. The upper-left window is a long-term heart rate plot, with light and dark cycles shaded; the upper right window shows a histogram of the currently-active 10-minute segment <sup>1</sup>. The middle-left window shows an instantaneous

<sup>1</sup>The currently active segment is denoted by a vertical red bar. Upon loading a record the first 10-minute

heart rate signal at a high resolution, where the instantaneous heart rate signal corresponds to the selected 10-minute segment in the upper-left long-term heart rate trend plot <sup>2</sup>. The middle-right window shows a single beat, which when browsing corresponds to the right-most annotated beat in the lower window (which holds a time slice of the waveform data).

## Browsing

Browse buttons located in the lower-left of the panel permit reverse and advance of waveform data by a full screenwidth (upper-left and upper-right buttons, respectively); the lower-left and lower-right buttons permit reverse and advance by a half screenwidth. Clicking a browse button will reload the lower panel with the appropriate waveform data, and timemarkers in the upper left and upper right of the waveform window will indicate the begin and end time of the data segment relative to an acquisition onset at  $t = 0$ . A label in the lower right of the waveform window indicates the time spanned by the shown data slice.

## Zooming

Near the middle of the bottom window is a box labelled *Zoom* containing four buttons. The upper buttons change the x-zoom (time scale) and the lower buttons change the y-zoom (waveform amplitude). Labels in the waveform window will change to reflect changes in timescale, but no visible side effects - besides signal amplitude adjustment - occur with clicks of the y-zoom buttons.

## Temporal navigation

The long-term and instantaneous heart rate trend plots are intended to provide a means by which the user can perform interactive data mining based on heart rate events of interest. Figure C-2 shows an example of a user clicking an instantaneous spike in heart rate (as shown by the vertical marker in the middle-left window) to isolate the corresponding time slice of

---

segment is active. Clicking on a point in the trend plot makes it the active segment

<sup>2</sup>As denoted by the vertical red bar

underlying waveform. Inspection of the waveform in the lower window reveals that the spike in heart rate results from a false positive annotation generated by the QRS detector.

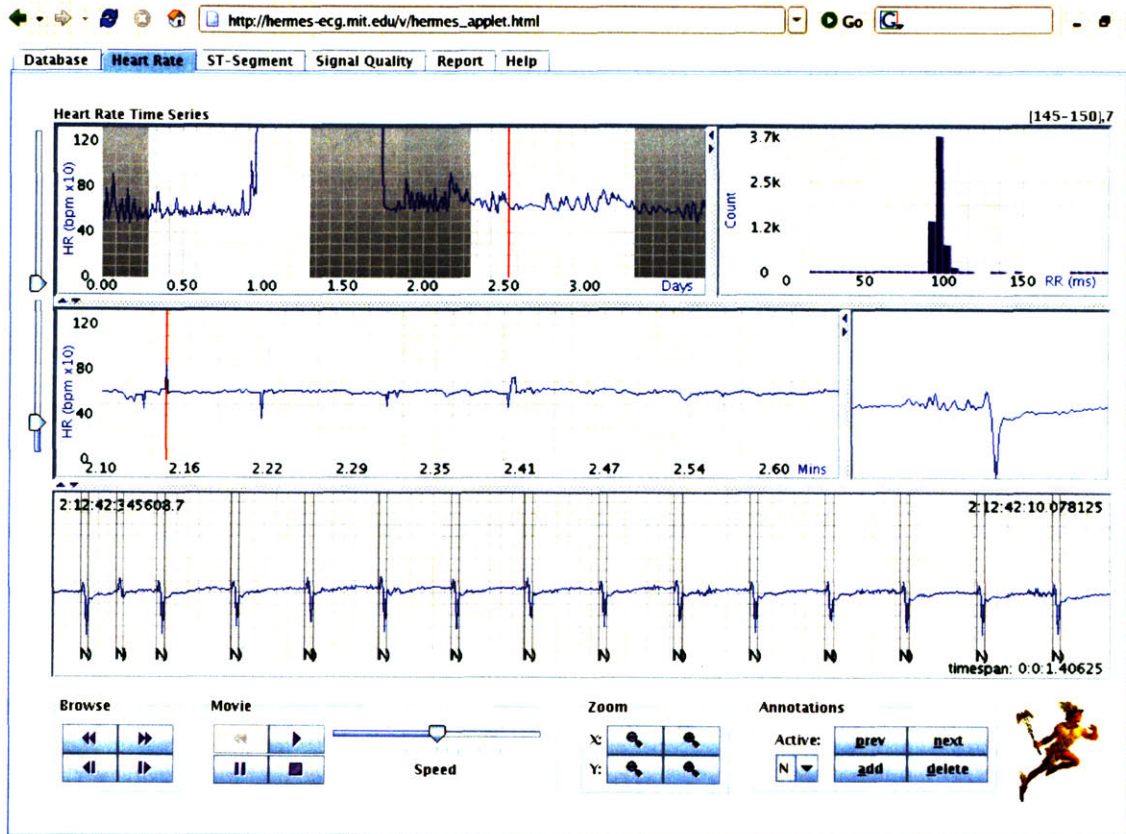


Figure C-2: A sample screenshot taken from the *Heart Rate* panel of a mouse in the murine database. In this example the user has selected a sharp instantaneous spike in heart rate in the middle plot (as shown by the vertical bar). The waveform annotation in the lower panel indicates that the QRS detector generated a false positive detection.

## Setting memory depth

As a user navigates through a record, (s)he may require assistance in remembering which points on a timeline (s)he has already visited. Upon right-clicking on the upper-left or middle-left window, the user will see a menu with a *Memory Depth* option. The user may select a memory depth from 1 to 5. With a memory depth greater than one, subsequent clicks on a trend plot will be denoted by a thicker vertical line; the thicker the line, the more recent the click. Figure C-3 shows an example in which the user has chosen a memory



depth of 5. The user is temporally navigating local heart rate minima from left to right, as evidenced by the thickening line from left to right.

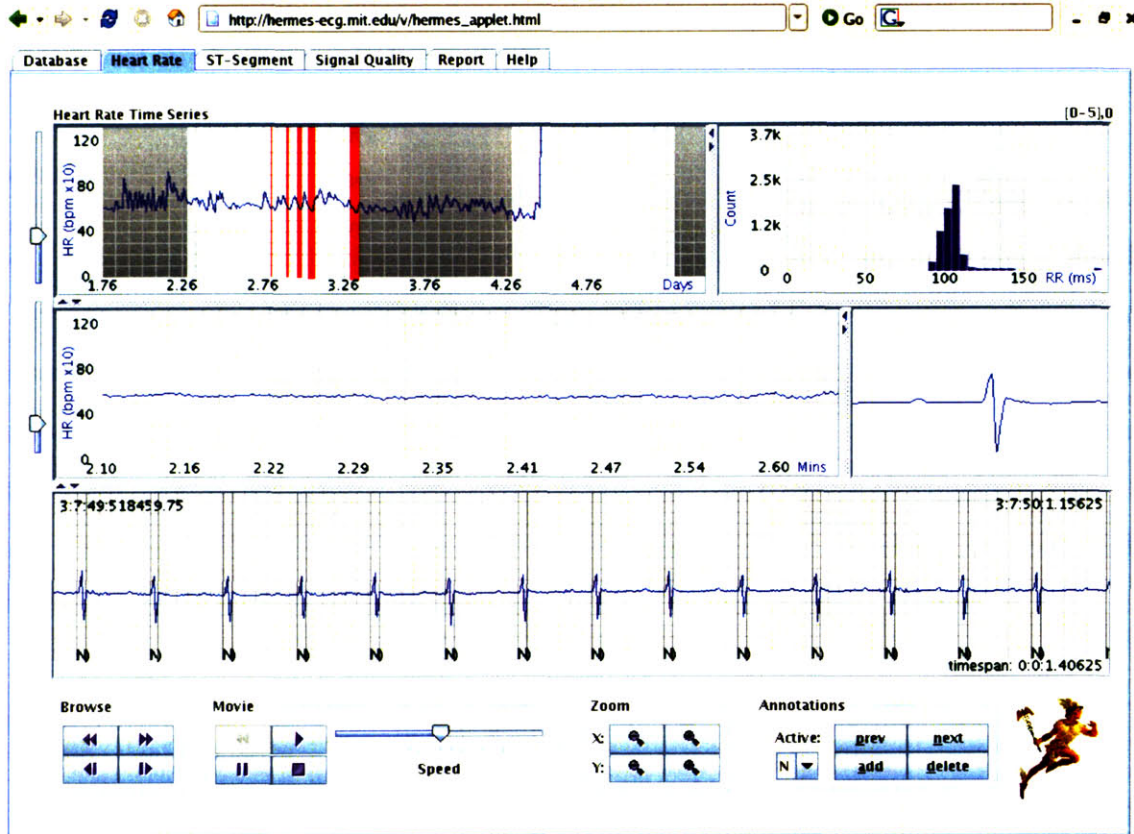


Figure C-3: In this example the user has selected a memory depth of 5 to recall previously visited points of interest in the long-term heart rate trend plot. The thickening bars from left to right indicate that the user is navigating from left to right.

The upper (long-term) and middle (instantaneous) heart rate windows have independent memories. Figure C-3 shows a user invoking the memory feature on a long-term heart rate trend plot. So may a user employ the memory feature on the middle heart rate window independently.

### Statistical navigation

Equally as important as trend information is that of statistical information. For example, to isolate probable ectopic beats one is far better served by the ability to select outliers in a

RR-interval histogram instead of scanning a heart rate time series for dips and spikes. The upper right panel shows a histogram of RR intervals for the selected 10-minute segment. By right-clicking within the histogram window and choosing *Set Scan Range*, the user will be permitted to choose which bins of the histogram (s)he would like to view. After selecting *Set Scan Range* the user should click on the first bin of interest, then move the mouse to the last bin of interest and click again. All bins in this range, which will be highlighted in red, will be included in the search. Red highlighting in the histogram panel indicates that statistical navigation criteria have been established. The user may then move to the previous and next annotations within a bin by clicking on the *Prev* and *Next* buttons, respectively, in the Annotations sub-panel. The currently-active bin will be highlighted in green. Clicking next (previous) after all beats within a bin have been viewed moves the currently active bin forward (backward). Clicking next (previous) beyond the last (first) bin will not produce any noticeable response.

### **Annotation navigation**

Instead of navigating a record by trend or statistical information, the user may wish to navigate by annotation. For example, one may wish to see all PVCs in a record. In order to do so, the user should select the appropriate annotation from the drop-down list in the *Active Annotation* list at the bottom-right of the heart rate panel. By then clicking the *Previous* or *Next* buttons, the user will advance to the previous or next annotation of the selected type, provided that such an annotation exists in the record.

### **Changing x-axis labels**

In the dKO genotype, the age of the animal is an important parameter. Though most subjects are implanted and monitoring is begun at roughly the same stage in life (30-35 days of age), the user may require a more precise understanding of the subject's age rather than the elapsed time of acquisition. By right-clicking in the long-term heart rate plot, and selecting *Subject Age* from the *X-axis Labels* drop-down menu, the user will change the

axis labels on the trend plot to reflect mouse age rather than elapsed acquisition time. By right-clicking and selecting *Elapsed Time* from the *X-axis Labels*, the user changes the x-axis labels back to elapsed time.

### Setting brady- or tachycardia thresholds

If the user wishes to see information about bradycardia and/or tachycardia in the summary report for a record, (s)he can choose the desired thresholds by right-clicking in the long-term or instantaneous heart rate window (upper-left and middle-left, respectively.) The user may choose *Set Brady Threshold* or *Set Tachy Threshold*, after which a magenta horizontal line will track mouse movement. The purpose of this horizontal line is to indicate the threshold that will result from clicking the mouse at that point. Upon selecting bradycardia and/or tachycardia thresholds, the selected rate threshold and beyond will be shaded in both the long-term and instantaneous heart rate windows.

### C.3.3 Signal quality index

The signal quality index (SQI) panel provides three windows. The upper window is a long-term trend plot of SQI as a function of time, while the middle window is an instantaneous time series of SQI comprising the active 10-minute segment selected in the top plot. The bottom window shows a time slice of the underlying waveform at the selected point in time. Figure SQIREF shows a sample SQI panel screenshot.

In a manner identical to temporal navigation using heart rate plots discussed in section C.3.2, the user may select areas of interest to view by simply clicking on the desired time point in the upper or middle window.

Annotation of data is intentionally not permitted in the SQI panel; annotation buttons are altogether absent. The purpose of preventing multiple panels from permitting annotation is an attempt at mitigating a user from unwittingly duplicating annotations in two or more panels.



### C.3.4 Repolarization segment

The repolarization segment tab provides long-term (top window) and higher-resolution (middle panel) point-and-click plots just as those available in the heart rate and SQI panels. The repolarization segment panel has additional user-adjustable settings. Right-clicking within the middle panel provides the user with choices for setting an elevation and depression threshold. This is the value above (for elevation) or below (for depression) which an alarm will be triggered, provided that the repolarization morphology metric remains above or below the threshold for more than 30 seconds. Additional settings, also selectable through the popup menu, permit the user to select signal quality and axis shift filter criteria. Stronger noise quality filters impose more strict criteria for alarms than weaker noise filter settings. A high setting requires that the signal quality index (SQI) remain above 90% for the entirety of the time that the threshold has been breached in order for the episode to be flagged as an alarm; a medium setting requires a 70% SQI and a weak setting requires a 50% SQI.

The axis shift filter similarly has three pre-defined settings. The strongest setting requires a substantial deviation in QRS morphology<sup>3</sup> to occur concurrently with a threshold breach in order for the breach to be flagged as an axis shift rather than an alarm. The weakest setting is more sensitive to changes in QRS morphology and will reduce the number of alarms, perhaps to the extent of introducing false negatives.

Both the axis shift filter and the signal quality filter may be turned off. Turning off the signal quality filter imposes no SQI constraints on alarms; any breach of threshold longer than 30 seconds, regardless of the signal quality, triggers an alarm. Turning off the axis shift filter is similar; all breaches, in spite of accompanying QRS morphology change, are flagged as alarms with no false alarm mitigation.

---

<sup>3</sup>As measured by the signed QRS integral relative to the isoelectric value - see chapter 6

## C.4 Annotating data

Annotation of data can take two forms: addition and deletion. In order to delete an annotation the user must click the *Delete* button in the Annotations sub-panel. By then moving the mouse over the annotation to be deleted (which will be highlighted in green when the mouse is in close proximity) and clicking the user will enact the deletion. In order to add an annotation the user must determine which annotation will be added by selecting from the drop-down menu in the Annotations sub-panel. By then clicking on the *Add* button in the Annotations sub-panel and subsequently clicking on the desired point in the waveform panel, the user will create a new annotation.

# Appendix D

## Hermes as a web portal to Physionet

### D.1 Physionet background

Physionet ([www.physionet.org](http://www.physionet.org)) is a public service of the Research Resource for Complex Physiologic Signals, funded by the National Center for Research Resources of the National Institutes of Health. Physionet is far more than a data repository; it is a dynamic entity for sharing open-source software and knowledge. In its close affiliation with the international annual Computers in Cardiology Conference, Computers in Cardiology has been the fountainhead of timely and interesting challenges, the responses to which have led to lively debate, new insight, and in at least one case, commercial opportunity. (The 2000 Computers in Cardiology Challenge from Physionet dealt with the question of detecting apnea from the electrocardiogram, which led to a novel technology for detecting cross-coherence in the mechanical manifestations of breathing with neuronally-controlled heart rate. The technology, called cardio-respiratory coupling, or CRC, has a pending patent and has earned the attention of several commercial entities.)

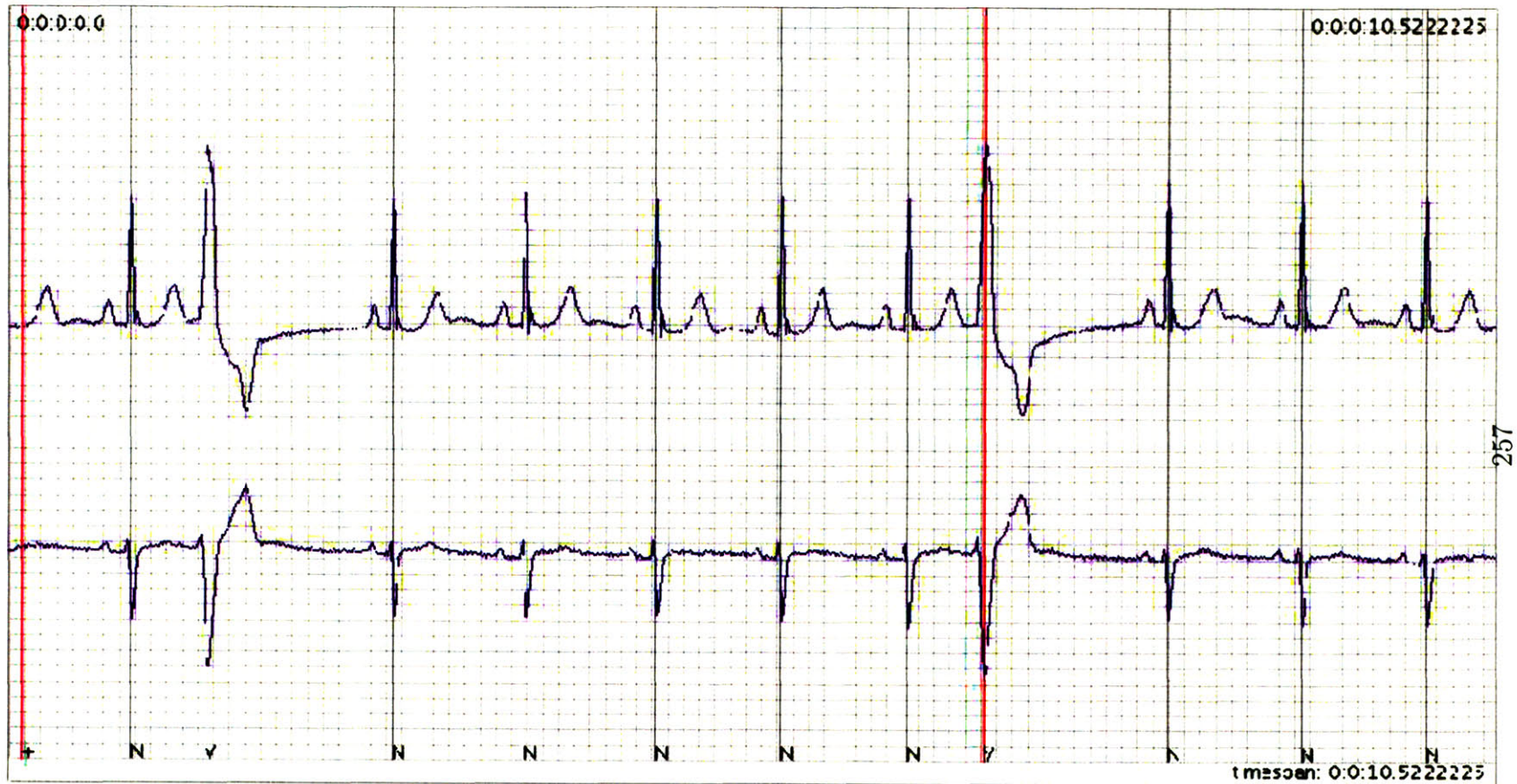


## D.2 The virtual lab

A founding tenet of Physionet was that of collaboration, and Hermes will play a role in a new Physionet *virtual lab* offering. The virtual lab will allow users from around the world to work together on software design, database collation and annotation. Hermes' contribution to the virtual lab will come in the form of providing a web portal to all Physionet databases, permitting authorized users to visualize and annotate the same data from disparate geographical locations as though all were sharing a file within office walls.

## D.3 Read-only visualization of gold-standard databases

In a context more tangible to all users, all gold-standard Physionet databases (eg MIT-BIH arrhythmia database) will be available for simple online viewing through a web browser. Because the gold-standard databases have already been meticulously annotated, they will be available for read-only access (in contrast with databases under construction in the virtual lab environment). Nonetheless the visualization tool provides a useful service to casual users by circumventing the need for users to download software and data to a local machine for visualization. Sample screenshots of Hermes on Physionet - viewing gold-standard databases - are shown below.



**Browse**

⏪	⏩
⏮	⏭

**Movie**

⏪	⏩	⏸
⏮	⏭	⏹

Speed

**Zoom**

X:	🔍	🔍
Y:	🔍	🔍

**Annotations**

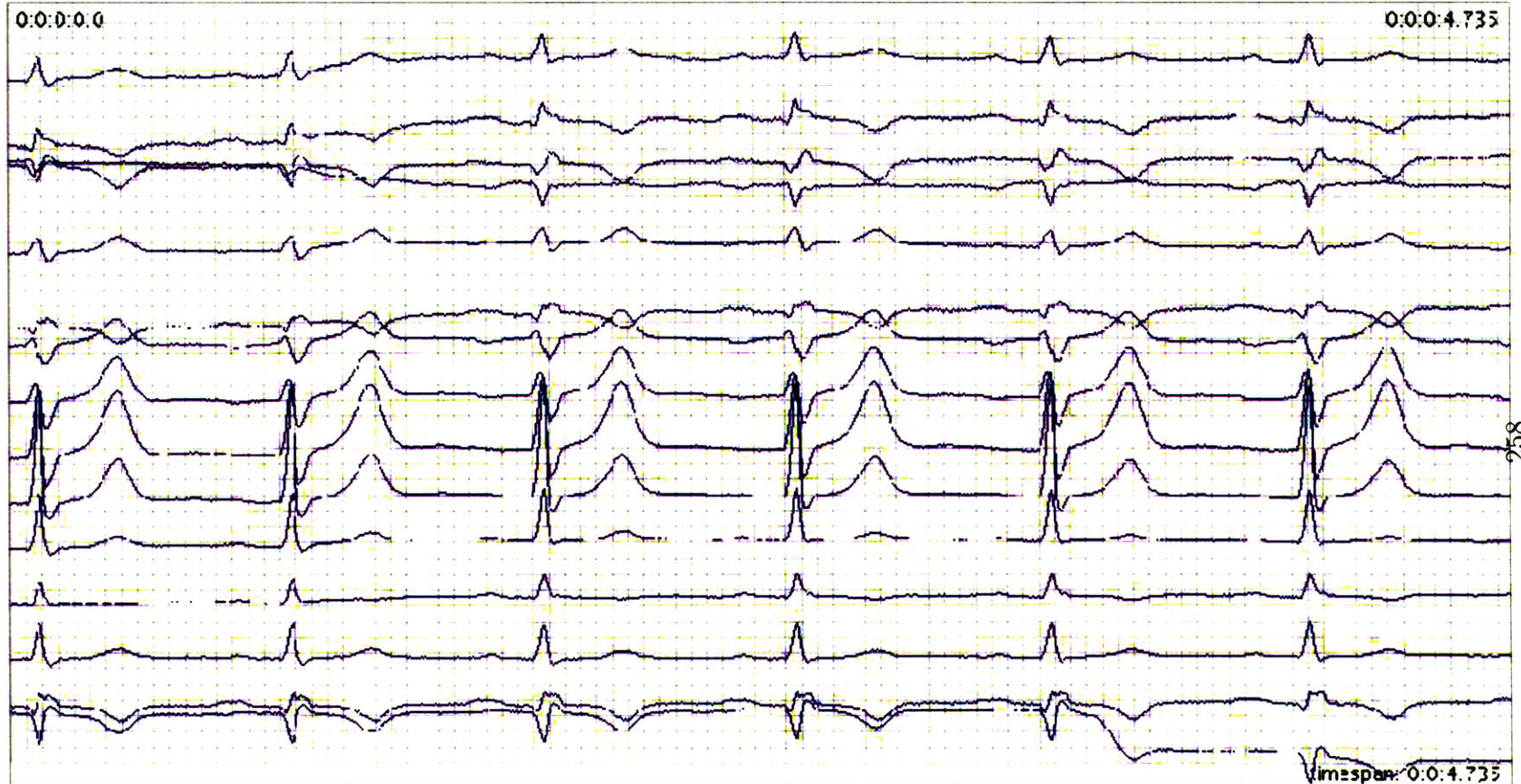
Active: N ▼

prev	next
add	delete



Figure D-1: A screenshot of Hermes viewing a 2-lead ECG record from the Physionet MIT-BIH arrhythmia database. This database has been annotated by a team of human experts; consequently it is a gold standard database.





Browse



Movie



Speed

Zoom



Annotations

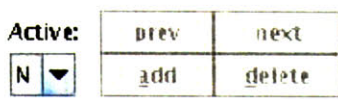


Figure D-2: A screenshot of Hermes viewing a 15-lead ECG record from the Physionet PTB arrhythmia database. This database has not been annotated.



# Appendix E

## Chebyshev Decomposition Examples

Chapter 2 describes the choice of repolarization segment begin and end points, while chapter 6 describes an algorithm for Chebyshev decomposition that performs calculations to describe shape features of the segment. This appendix shows sample waveforms with corresponding Chebyshev decomposition scatter plots.

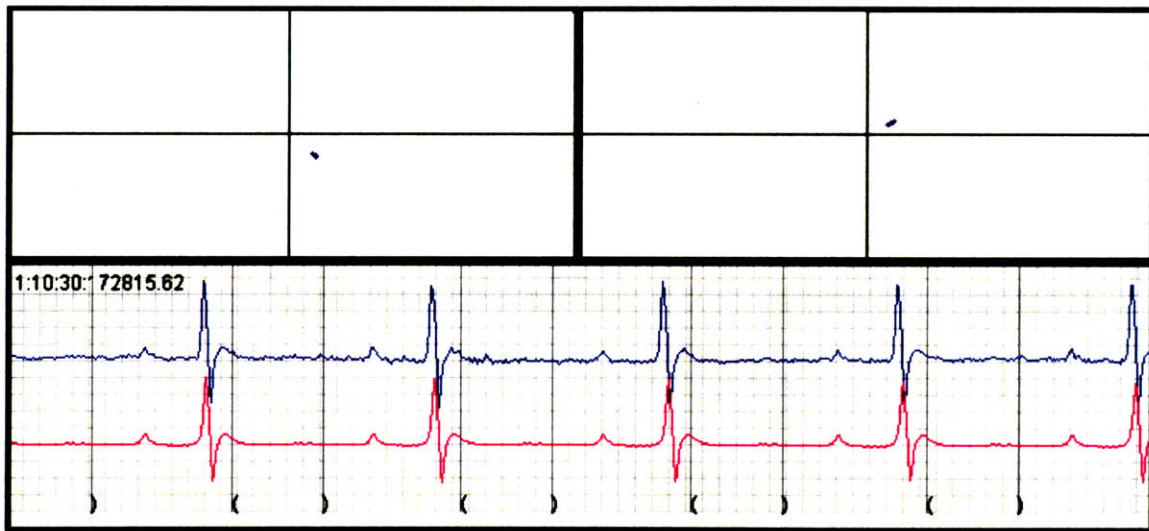


Figure E-1: Chebyshev decomposition example 1 of 23 - the top-left scatter plot shows approximately 100 consecutive data points (beats) of Chebyshev coefficient 1 (slope) vs. Chebyshev coefficient 0 (offset relative to isoelectric value); the top-right scatter plot shows Chebyshev coefficient 2 (curvature) vs. Chebyshev coefficient 0; the lower plot shows the underlying ECG waveform, where the top signal is the raw waveform and the bottom signal is a 64-beat trailing average beat.

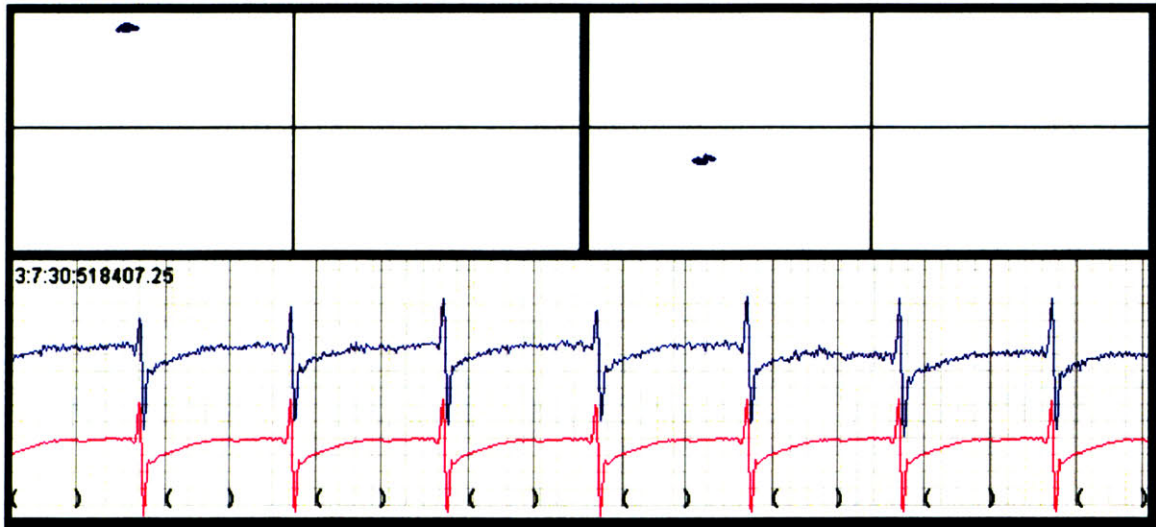


Figure E-2: Chebyshev decomposition example 2 of 23 - the top-left scatter plot shows approximately 100 consecutive data points (beats) of Chebyshev coefficient 1 (slope) vs. Chebyshev coefficient 0 (offset relative to isoelectric value); the top-right scatter plot shows Chebyshev coefficient 2 (curvature) vs. Chebyshev coefficient 0; the lower plot shows the underlying ECG waveform, where the top signal is the raw waveform and the bottom signal is a 64-beat trailing average beat.

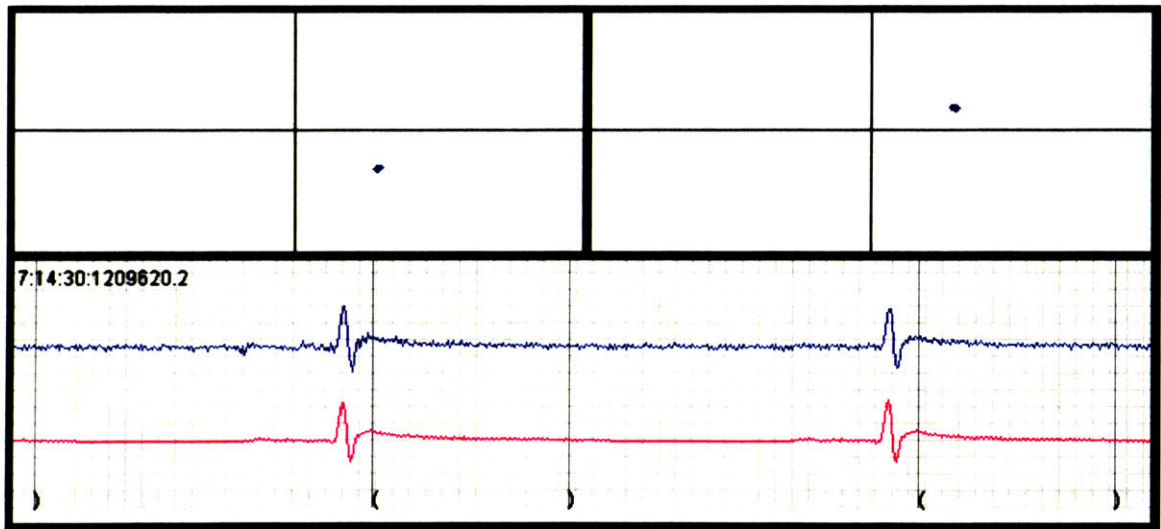


Figure E-3: Chebyshev decomposition example 3 of 23 - the top-left scatter plot shows approximately 100 consecutive data points (beats) of Chebyshev coefficient 1 (slope) vs. Chebyshev coefficient 0 (offset relative to isoelectric value); the top-right scatter plot shows Chebyshev coefficient 2 (curvature) vs. Chebyshev coefficient 0; the lower plot shows the underlying ECG waveform, where the top signal is the raw waveform and the bottom signal is a 64-beat trailing average beat.

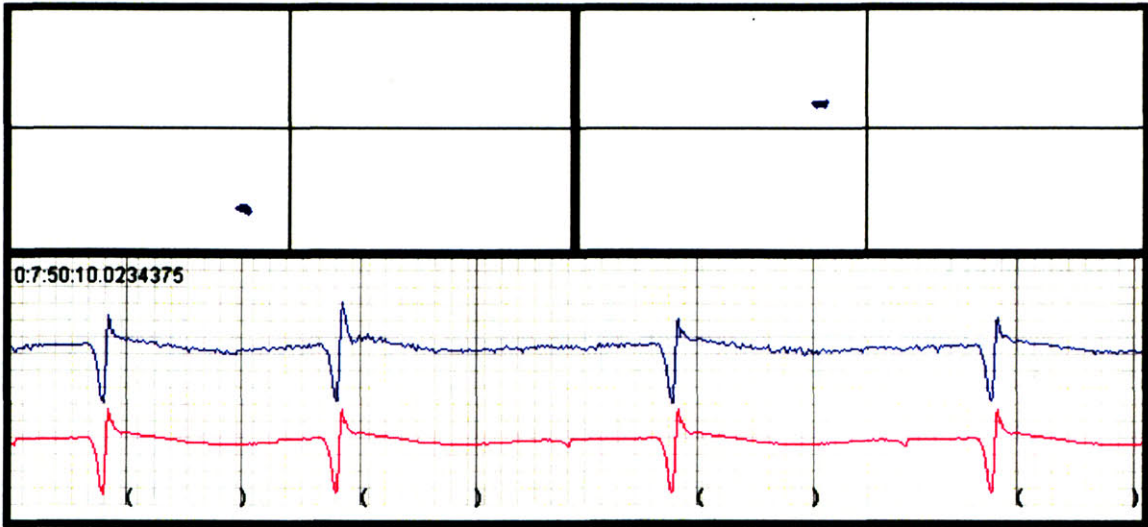


Figure E-4: Chebyshev decomposition example 4 of 23 - the top-left scatter plot shows approximately 100 consecutive data points (beats) of Chebyshev coefficient 1 (slope) vs. Chebyshev coefficient 0 (offset relative to isoelectric value); the top-right scatter plot shows Chebyshev coefficient 2 (curvature) vs. Chebyshev coefficient 0; the lower plot shows the underlying ECG waveform, where the top signal is the raw waveform and the bottom signal is a 64-beat trailing average beat.

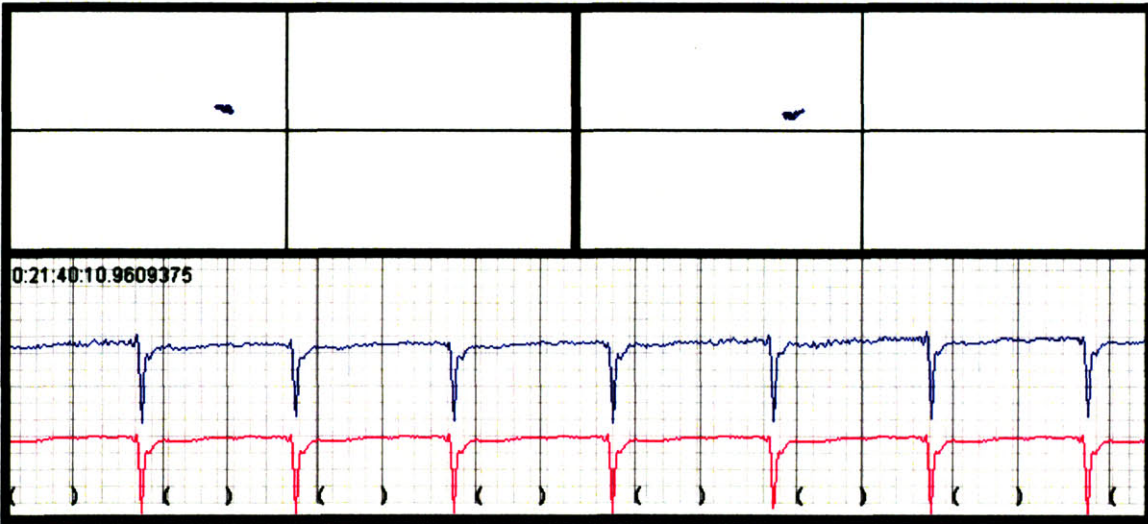


Figure E-5: Chebyshev decomposition example 5 of 23 - the top-left scatter plot shows approximately 100 consecutive data points (beats) of Chebyshev coefficient 1 (slope) vs. Chebyshev coefficient 0 (offset relative to isoelectric value); the top-right scatter plot shows Chebyshev coefficient 2 (curvature) vs. Chebyshev coefficient 0; the lower plot shows the underlying ECG waveform, where the top signal is the raw waveform and the bottom signal is a 64-beat trailing average beat.



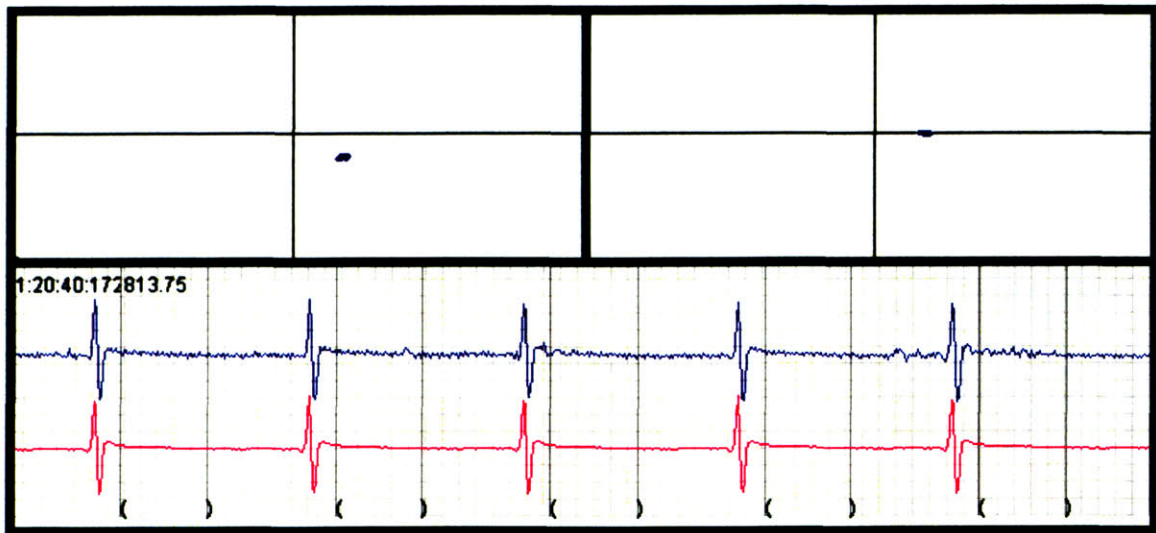


Figure E-6: Chebyshev decomposition example 6 of 23 - the top-left scatter plot shows approximately 100 consecutive data points (beats) of Chebyshev coefficient 1 (slope) vs. Chebyshev coefficient 0 (offset relative to isoelectric value); the top-right scatter plot shows Chebyshev coefficient 2 (curvature) vs. Chebyshev coefficient 0; the lower plot shows the underlying ECG waveform, where the top signal is the raw waveform and the bottom signal is a 64-beat trailing average beat.

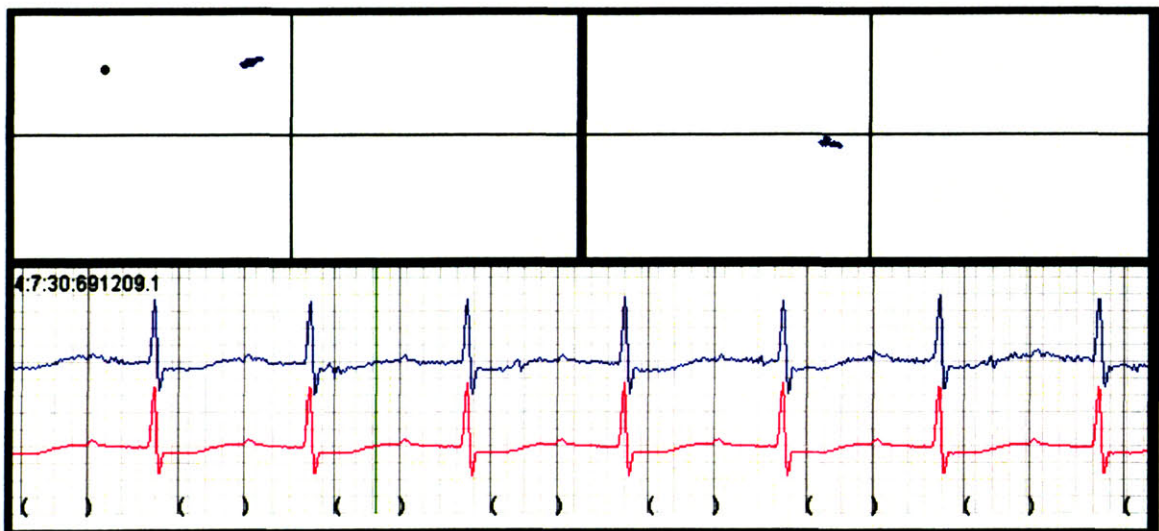


Figure E-7: Chebyshev decomposition example 7 of 23 - the top-left scatter plot shows approximately 100 consecutive data points (beats) of Chebyshev coefficient 1 (slope) vs. Chebyshev coefficient 0 (offset relative to isoelectric value); the top-right scatter plot shows Chebyshev coefficient 2 (curvature) vs. Chebyshev coefficient 0; the lower plot shows the underlying ECG waveform, where the top signal is the raw waveform and the bottom signal is a 64-beat trailing average beat.

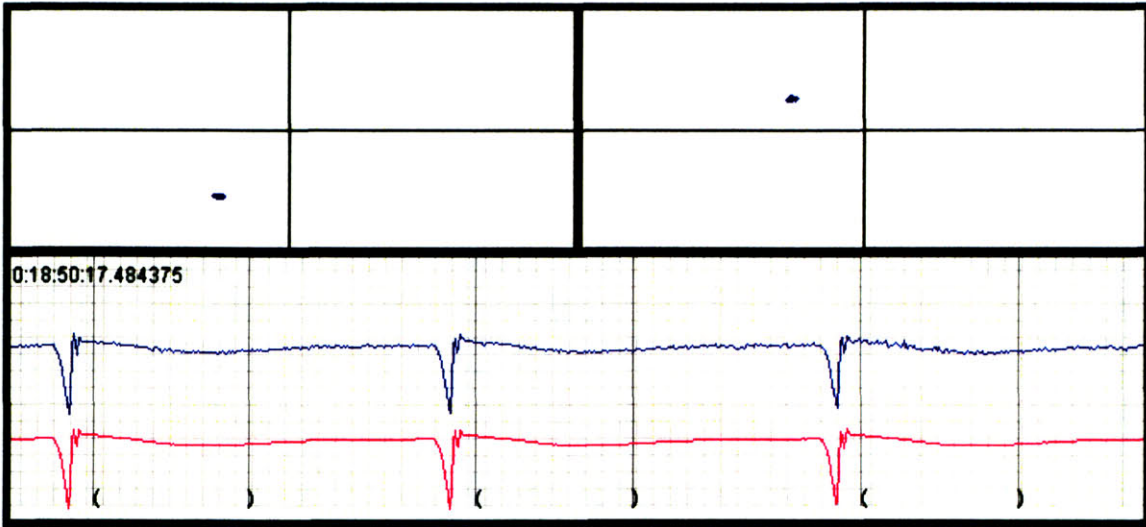


Figure E-8: Chebyshev decomposition example 8 of 23 - the top-left scatter plot shows approximately 100 consecutive data points (beats) of Chebyshev coefficient 1 (slope) vs. Chebyshev coefficient 0 (offset relative to isoelectric value); the top-right scatter plot shows Chebyshev coefficient 2 (curvature) vs. Chebyshev coefficient 0; the lower plot shows the underlying ECG waveform, where the top signal is the raw waveform and the bottom signal is a 64-beat trailing average beat.

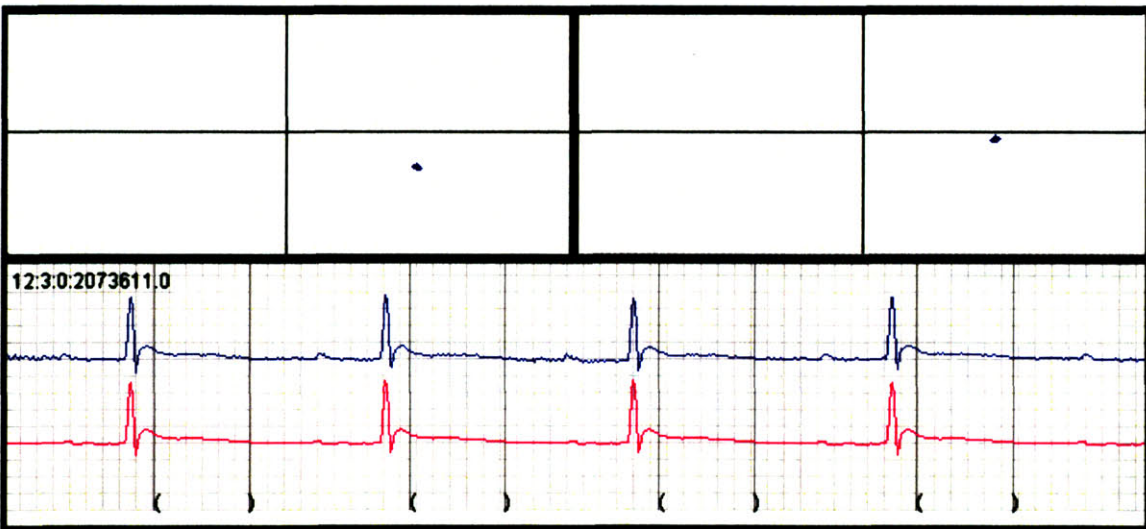


Figure E-9: Chebyshev decomposition example 9 of 23 - the top-left scatter plot shows approximately 100 consecutive data points (beats) of Chebyshev coefficient 1 (slope) vs. Chebyshev coefficient 0 (offset relative to isoelectric value); the top-right scatter plot shows Chebyshev coefficient 2 (curvature) vs. Chebyshev coefficient 0; the lower plot shows the underlying ECG waveform, where the top signal is the raw waveform and the bottom signal is a 64-beat trailing average beat.

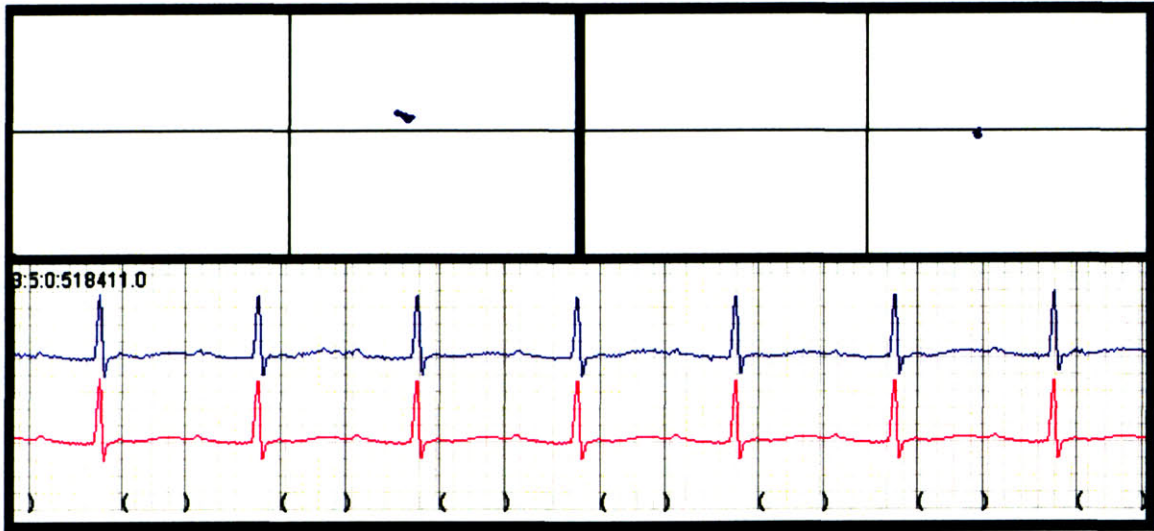


Figure E-10: Chebyshev decomposition example 10 of 23 - the top-left scatter plot shows approximately 100 consecutive data points (beats) of Chebyshev coefficient 1 (slope) vs. Chebyshev coefficient 0 (offset relative to isoelectric value); the top-right scatter plot shows Chebyshev coefficient 2 (curvature) vs. Chebyshev coefficient 0; the lower plot shows the underlying ECG waveform, where the top signal is the raw waveform and the bottom signal is a 64-beat trailing average beat.

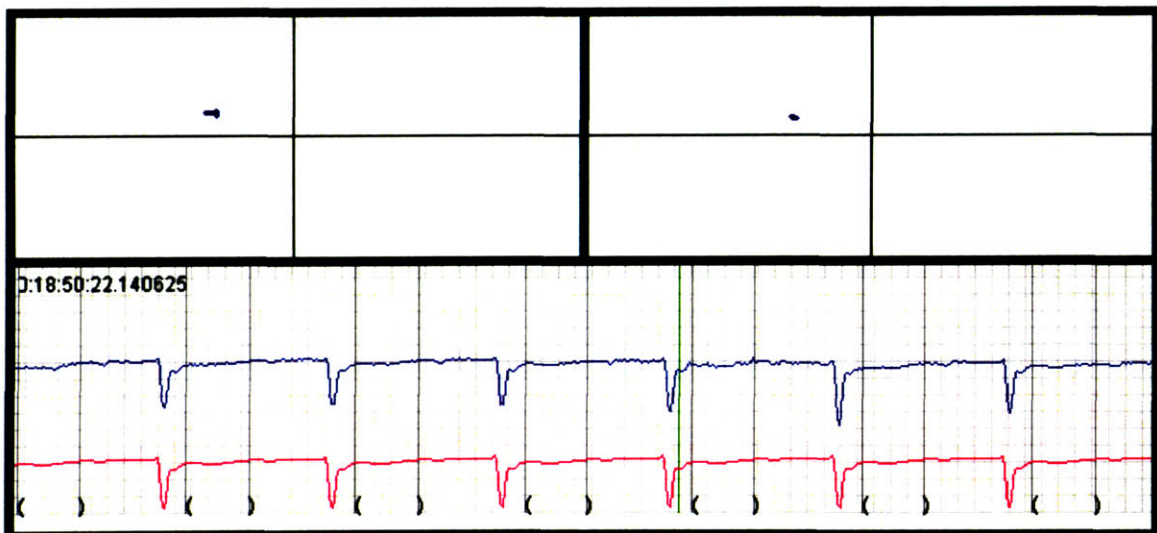


Figure E-11: Chebyshev decomposition example 11 of 23 - the top-left scatter plot shows approximately 100 consecutive data points (beats) of Chebyshev coefficient 1 (slope) vs. Chebyshev coefficient 0 (offset relative to isoelectric value); the top-right scatter plot shows Chebyshev coefficient 2 (curvature) vs. Chebyshev coefficient 0; the lower plot shows the underlying ECG waveform, where the top signal is the raw waveform and the bottom signal is a 64-beat trailing average beat.



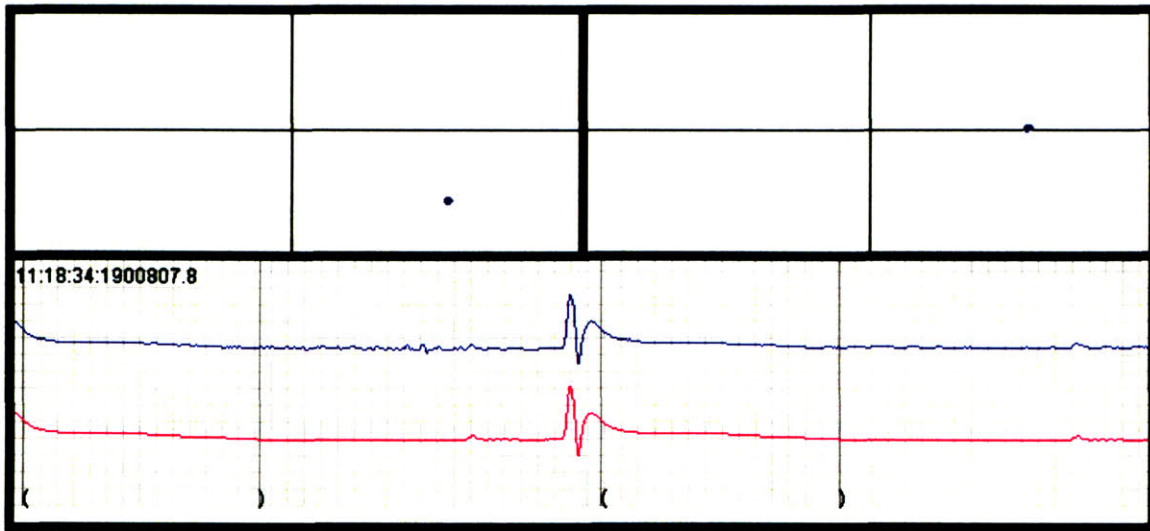


Figure E-12: Chebyshev decomposition example 12 of 23 - the top-left scatter plot shows approximately 100 consecutive data points (beats) of Chebyshev coefficient 1 (slope) vs. Chebyshev coefficient 0 (offset relative to isoelectric value); the top-right scatter plot shows Chebyshev coefficient 2 (curvature) vs. Chebyshev coefficient 0; the lower plot shows the underlying ECG waveform, where the top signal is the raw waveform and the bottom signal is a 64-beat trailing average beat.

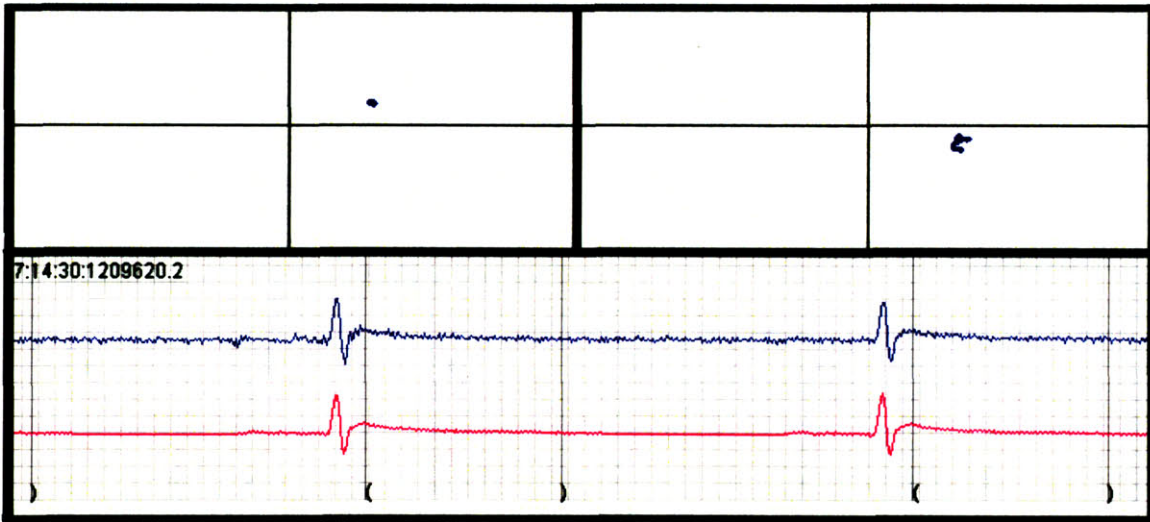


Figure E-13: Chebyshev decomposition example 13 of 23 - the top-left scatter plot shows approximately 100 consecutive data points (beats) of Chebyshev coefficient 1 (slope) vs. Chebyshev coefficient 0 (offset relative to isoelectric value); the top-right scatter plot shows Chebyshev coefficient 2 (curvature) vs. Chebyshev coefficient 0; the lower plot shows the underlying ECG waveform, where the top signal is the raw waveform and the bottom signal is a 64-beat trailing average beat.

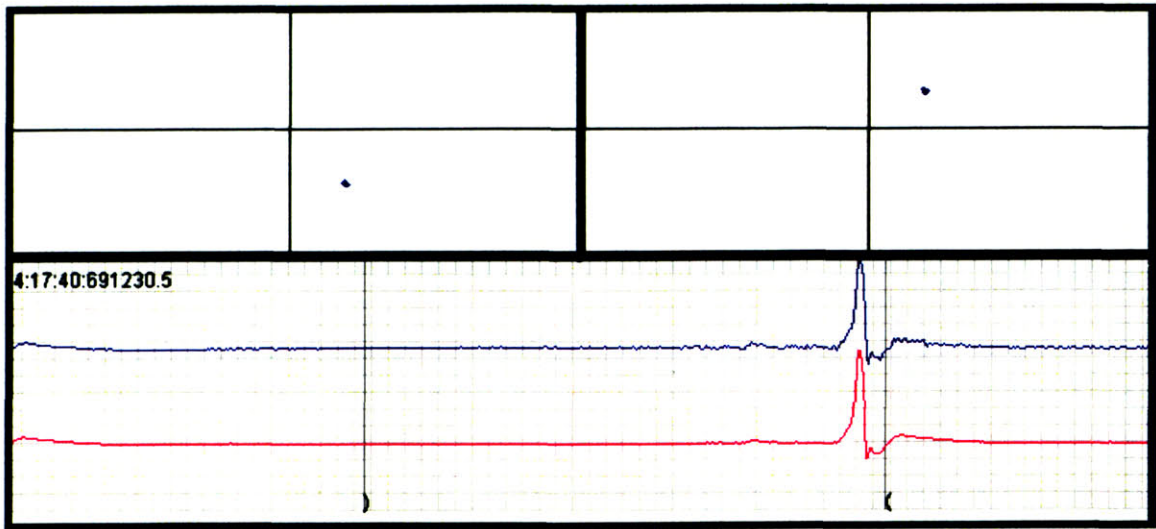


Figure E-14: Chebyshev decomposition example 14 of 23 - the top-left scatter plot shows approximately 100 consecutive data points (beats) of Chebyshev coefficient 1 (slope) vs. Chebyshev coefficient 0 (offset relative to isoelectric value); the top-right scatter plot shows Chebyshev coefficient 2 (curvature) vs. Chebyshev coefficient 0; the lower plot shows the underlying ECG waveform, where the top signal is the raw waveform and the bottom signal is a 64-beat trailing average beat.

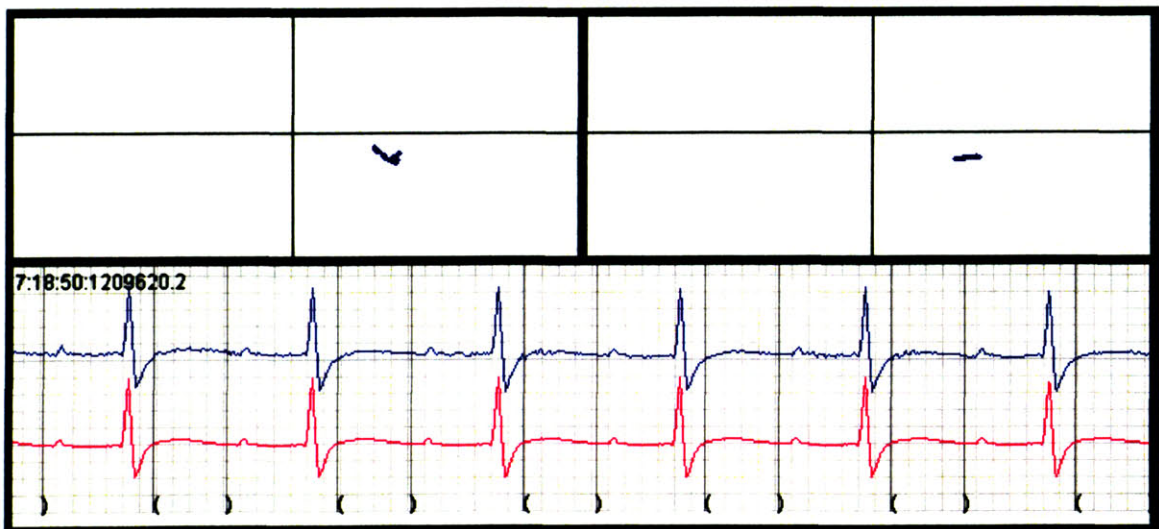


Figure E-15: Chebyshev decomposition example 15 of 23 - the top-left scatter plot shows approximately 100 consecutive data points (beats) of Chebyshev coefficient 1 (slope) vs. Chebyshev coefficient 0 (offset relative to isoelectric value); the top-right scatter plot shows Chebyshev coefficient 2 (curvature) vs. Chebyshev coefficient 0; the lower plot shows the underlying ECG waveform, where the top signal is the raw waveform and the bottom signal is a 64-beat trailing average beat.

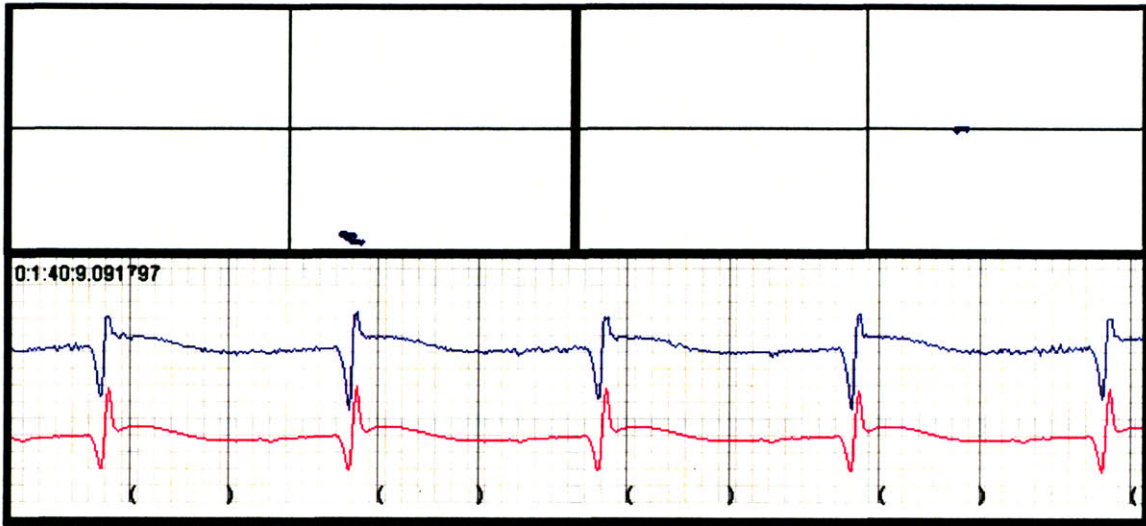


Figure E-16: Chebyshev decomposition example 16 of 23 - the top-left scatter plot shows approximately 100 consecutive data points (beats) of Chebyshev coefficient 1 (slope) vs. Chebyshev coefficient 0 (offset relative to isoelectric value); the top-right scatter plot shows Chebyshev coefficient 2 (curvature) vs. Chebyshev coefficient 0; the lower plot shows the underlying ECG waveform, where the top signal is the raw waveform and the bottom signal is a 64-beat trailing average beat.



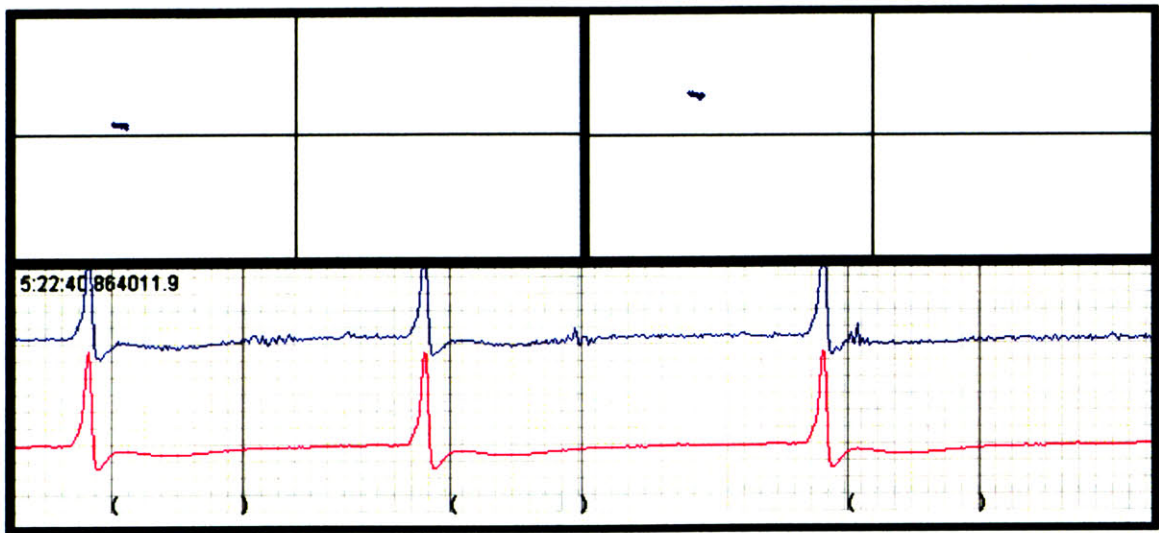


Figure E-17: Chebyshev decomposition example 17 of 23 - the top-left scatter plot shows approximately 100 consecutive data points (beats) of Chebyshev coefficient 1 (slope) vs. Chebyshev coefficient 0 (offset relative to isoelectric value); the top-right scatter plot shows Chebyshev coefficient 2 (curvature) vs. Chebyshev coefficient 0; the lower plot shows the underlying ECG waveform, where the top signal is the raw waveform and the bottom signal is a 64-beat trailing average beat.

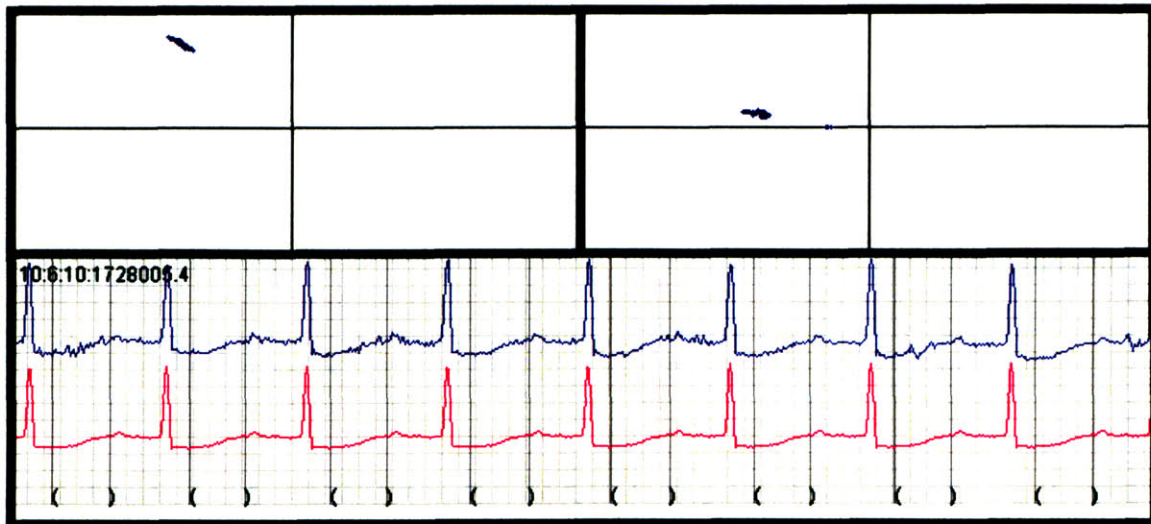


Figure E-18: Chebyshev decomposition example 18 of 23 - the top-left scatter plot shows approximately 100 consecutive data points (beats) of Chebyshev coefficient 1 (slope) vs. Chebyshev coefficient 0 (offset relative to isoelectric value); the top-right scatter plot shows Chebyshev coefficient 2 (curvature) vs. Chebyshev coefficient 0; the lower plot shows the underlying ECG waveform, where the top signal is the raw waveform and the bottom signal is a 64-beat trailing average beat.

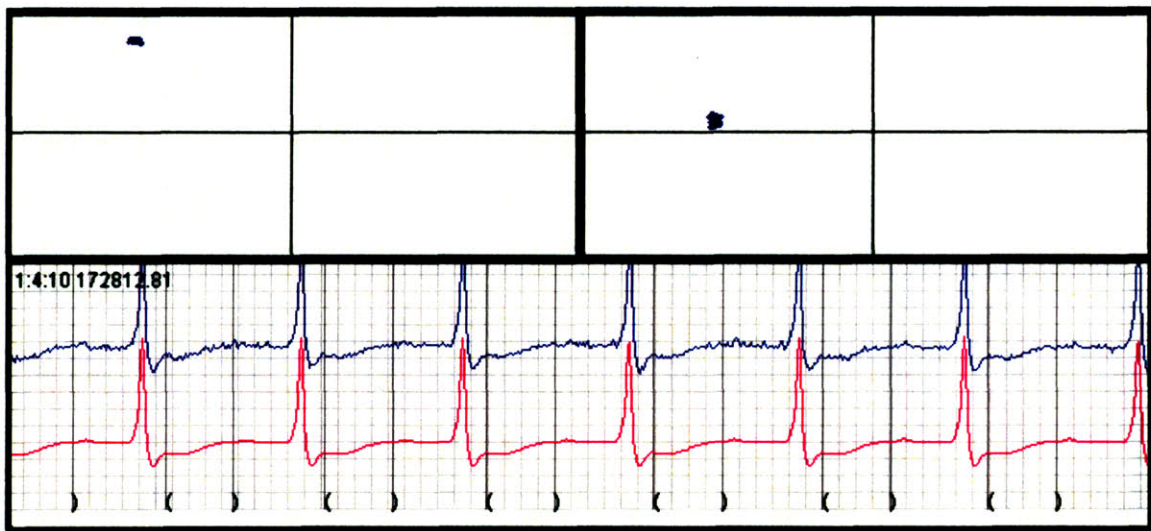


Figure E-19: Chebyshev decomposition example 19 of 23 - the top-left scatter plot shows approximately 100 consecutive data points (beats) of Chebyshev coefficient 1 (slope) vs. Chebyshev coefficient 0 (offset relative to isoelectric value); the top-right scatter plot shows Chebyshev coefficient 2 (curvature) vs. Chebyshev coefficient 0; the lower plot shows the underlying ECG waveform, where the top signal is the raw waveform and the bottom signal is a 64-beat trailing average beat.

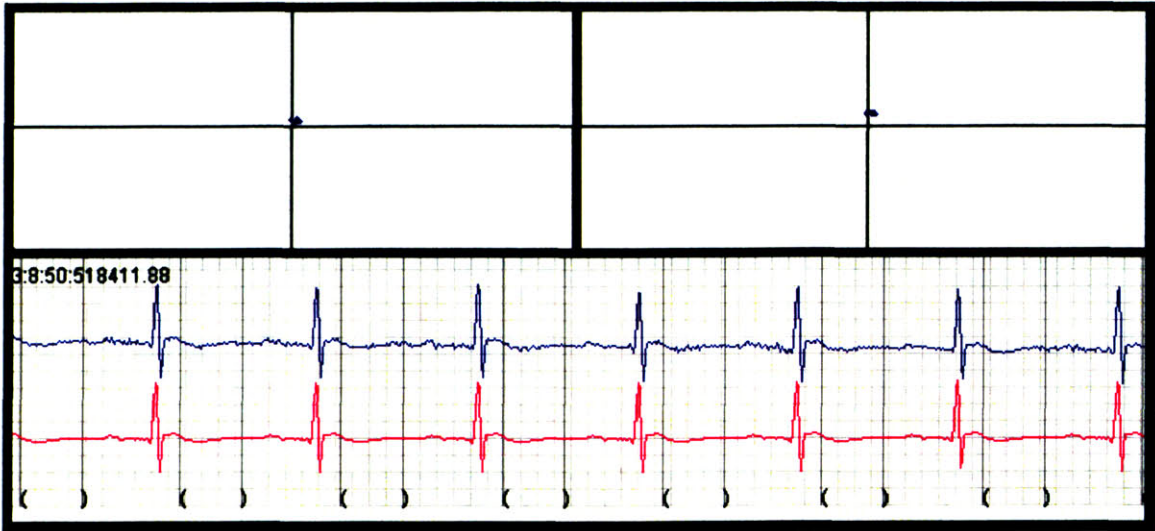


Figure E-20: Chebyshev decomposition example 20 of 23 - the top-left scatter plot shows approximately 100 consecutive data points (beats) of Chebyshev coefficient 1 (slope) vs. Chebyshev coefficient 0 (offset relative to isoelectric value); the top-right scatter plot shows Chebyshev coefficient 2 (curvature) vs. Chebyshev coefficient 0; the lower plot shows the underlying ECG waveform, where the top signal is the raw waveform and the bottom signal is a 64-beat trailing average beat.

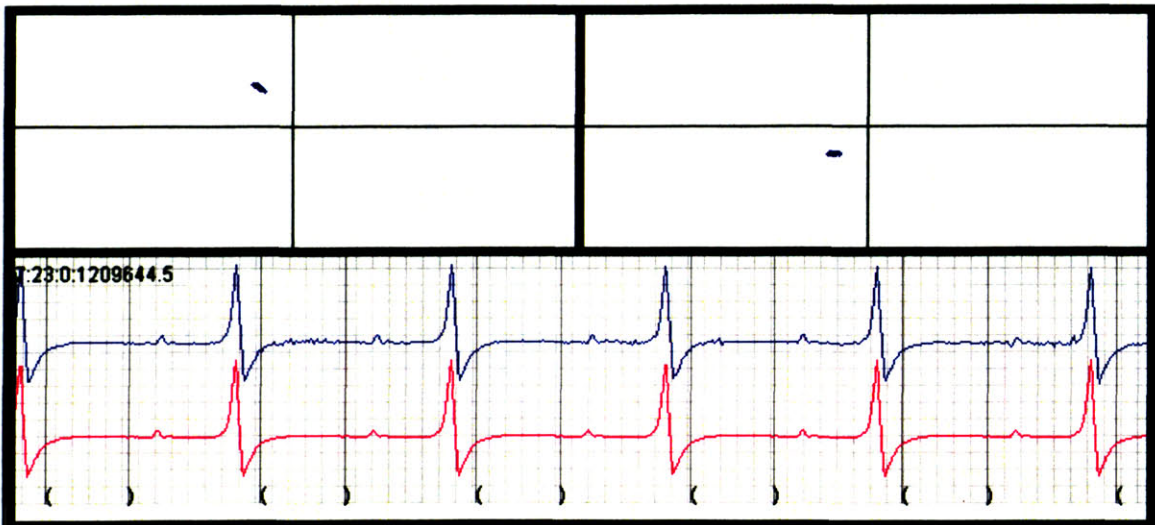


Figure E-21: Chebyshev decomposition example 21 of 23 - the top-left scatter plot shows approximately 100 consecutive data points (beats) of Chebyshev coefficient 1 (slope) vs. Chebyshev coefficient 0 (offset relative to isoelectric value); the top-right scatter plot shows Chebyshev coefficient 2 (curvature) vs. Chebyshev coefficient 0; the lower plot shows the underlying ECG waveform, where the top signal is the raw waveform and the bottom signal is a 64-beat trailing average beat.



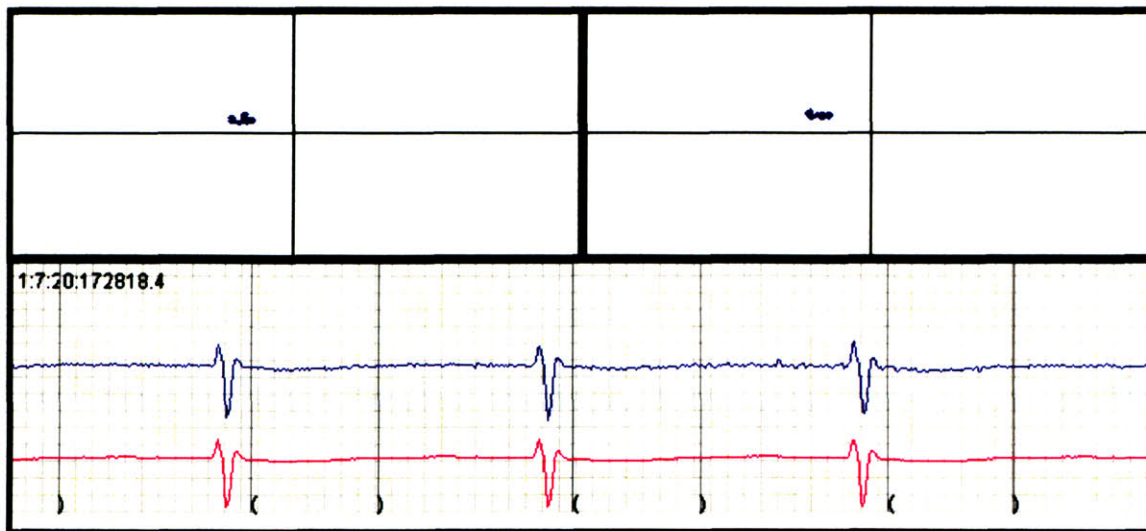


Figure E-22: Chebyshev decomposition example 22 of 23 - the top-left scatter plot shows approximately 100 consecutive data points (beats) of Chebyshev coefficient 1 (slope) vs. Chebyshev coefficient 0 (offset relative to isoelectric value); the top-right scatter plot shows Chebyshev coefficient 2 (curvature) vs. Chebyshev coefficient 0; the lower plot shows the underlying ECG waveform, where the top signal is the raw waveform and the bottom signal is a 64-beat trailing average beat.

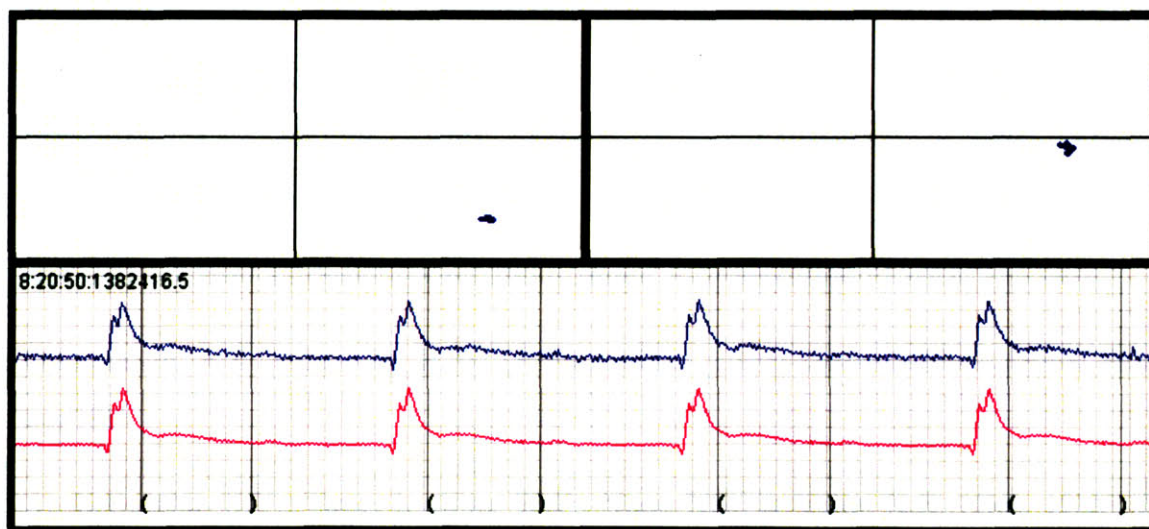


Figure E-23: Chebyshev decomposition example 23 of 23 - the top-left scatter plot shows approximately 100 consecutive data points (beats) of Chebyshev coefficient 1 (slope) vs. Chebyshev coefficient 0 (offset relative to isoelectric value); the top-right scatter plot shows Chebyshev coefficient 2 (curvature) vs. Chebyshev coefficient 0; the lower plot shows the underlying ECG waveform, where the top signal is the raw waveform and the bottom signal is a 64-beat trailing average beat.

THIS PAGE INTENTIONALLY LEFT BLANK

# Bibliography

- [1] *2002 Heart and Stroke Statistical Update* (2002) (American Heart Association, Dallas, TX)
- [2] Krieger, M. (Apr. 1998) *Proc. Natl. Acad. Sci. USA*, vol. 95 **4077**
- [3] Acton, S., Rigotti, A., Landschulz, K., Xu, S., Hobbs, H.H. & Krieger, M. (Jan. 26, 1996) *Science* **271**, 518-520
- [4] Press, William, Teukolsky, Saul, Vetterling, William, Flannery, Brian *Numerical Recipes in C, Second Edition* 113-116
- [5] Braun, A., Trigatti, B.L., Post, M.J., Sato, K., Simons, M., Edelberg, J.M., Rosenberg, R.D., Schrenzel, M., Krieger, M. (Feb. 2002) *American Heart Assoc. Circulation Research* **270**, 271-275
- [6] Dubin, D. (Cover Publishing Co., 2000) *Rapid Interpretation of EKG's* 97-202
- [7] Oppenheim, A.V. & Schafer, R.W. (Prentice-Hall, 1999) *Discrete-Time Signal Processing* 196
- [8] Ai, H.B., Cui, X.Y., Tang, L., Zhu, W.P., Ning, X.B. & Yang, X.X. (Oct. 1996) *Sheng Li Xue Bao: Studies on the Time Domain and Power Spectrum of High Frequency ECG in Normal Mice* **512**
- [9] Huhta, J.C. & Webster, J.G. (Mar. 1973) *IEEE Trans. Biomed. Eng.*, vol. BME-20 NO. 2 91-100



- [10] Feinberg, B.N. (Prentice-Hall, 1986) *Applied Clinical Engineering* 459-465
- [11] Kusumoto, F.M. (Fence Creek Publishing, 1999) *Cardiovascular Pathophysiology* 127-129
- [12] Haberman, R. (Prentice-Hall, 1998) *Elementary Applied Partial Differential Equations* 151-160
- [13] <http://www.physionet.org>
- [14] CDC Archives: <http://www.cdc.gov/mmwr/preview/mmwrhtml/0032336.htm>
- [15] *Nature Reviews: Drug Discovery*, Vol. 2 January 2003 38-49
- [16] Appleton G.O., Li, Y., Taffet, G.E., Hartley, C.J., Michael, L.H., Entman M.L., Roberts, R. & Khoury, D.S. *Determinants of cardiac electrophysiological properties in mice* J Interv Card Electrophysiol. 2004 Aug, 11(1):5-14
- [17] Jager, Franc, Moody, G.B. & Mark, R.G. *Detection of Transient ST Segment Episodes During Ambulatory ECG Monitoring* Computers and Biomedical Research 1998 31, 305-322
- [18] Dhananjay, V., Morley, G., Samie, F.H., & Jalife, J. *Reentry and Fibrillation in the Mouse Heart* American Heart Assoc. Circulation Research. 1999;85:174-181
- [19] Liu, G.L., Kovithavongs, K., Iden, J., Gulamhusein, R. & Kavanagh, K. *The mystery of the murine T-wave* Canadian Cardiovascular Congress Proceedings 2003
- [20] Dorn, R. & Jager, F. *Semia: semi-automatic interactive graphic editing tool to annotate ambulatory ECG records* Computer Methods and Programs in Biomedicine 2004;75,235-249
- [21] <http://www.efunda.com/math/Chebyshev/index.cfm>
- [22] Diehl et al.: *A good practice guide to the administration of substances and removal of blood, including routes and volumes* Journal of Applied Toxicology 21,15-23,2001

- [23] Jager, F. *Automated Detection of Transient Ischemic ST-Segment Changes During Ambulatory ECG Monitoring* PhD Dissertation, University of Ljubljana 1993
- [24] Moody, G.B. & Mark, R.G. *QRS Morphology Representation and Noise Estimation using the Karhunen-Loeve Transform* Computers in Cardiology 1989, 269-272
- [25] Jager, F. *Feature Extraction and Shape Representation of Ambulatory Electrocardiogram Using the Karhunen-Loeve Transform* Electrotechnical Review, Ljubljana, Slovenia 69(2): 83-89, 2002
- [26] Willerson, J.T. & Cohn, J.N. *Cardiovascular Medicine, 2nd Edition* Churchill Livingstone 2000
- [27] Agdhr and Strenstrom *Acta Paediatr* 1929; 33:493-588
- [28] Liu et al. : *In vivo temporal and spatial distribution of depolarization and repolarization and the illusive murine T wave* J Physiol 2003; 555.1: 267-279
- [29] Berul CI, Arnovitz MJ, Wang PJ & Mendelsohn ME *In vivo cardiac electrophysiology studies in the mouse* Circulation 1996; 94:2641-2648
- [30] Chu V, Otero JM, Lopez O, Morgan JP, Amende I & Hampton TG *Method for non-invasively recording electrocardiograms in conscious mice* BMC Physiol 2001 1: 6
- [31] Knollman BC, Katchman AN & Franz MR *Monophasic action potential recordings from intact mouse heart: validation, regional heterogeneity, and relation to refractoriness* J Cardiovasc Electrophysiol 2001 12: 1286-1294
- [32] London B *Cardiac arrhythmias: from (transgenic) mice to men* J Cardiovasc Electrophysiol 2001 12: 1089-1091
- [33] Tranquilo JV, Hlavacek J & Henriquez CS *An integrative model of mouse cardiac electrophysiology from cell to torso* European Cardiology Society Journal 2005; 7: S56-S70
- [34] Rosen, MR *The real thing* Circ Res 2000: 87; 6-7

- [35] Wang L, Swirp S & Duff H *Age-dependent response of the electrocardiogram to K<sup>+</sup> channel blockers in mice* Am J Cell Physiol 2000; 278: C73-C80
- [36] Danik S, Cabo C, Chiello C, Kang S Wil AL & Coromillas J *Correlation of repolarization of ventricular monophasic action potential with the ECG in the murine heart* Am J Physiol 2002; 283: H372-H381
- [37] Kirchhoff S, Nelles E, Hagedorff A, Kruger O, Traub O & Willecke K *Reduced cardiac conduction velocity and predisposition to arrhythmias in connexin40-deficient mice* Curr Biol 1998; 8: 299-302
- [38] Mohler PJ, Schott JJ, Gramolini AO, Dilly KW, Guatimosim S, DuBell WH, Song LS, Haurogne K, Kyndt F, Ali ME, Rogers TB, Lederer WJ, Escande D, Marec HL & Bennett V *Ankyrin-B Mutation causes type 4 long-QT cardiac arrhythmia and sudden cardiac death* Nature 2003; 421: 634-639
- [39] Hartley CJ, Taffet GE, Reddy AK, Entman ML, Michael LH *Noninvasive Cardiovascular Phenotyping in Mice* Institute for Laboratory Animal Research V43(3) 2002
- [40] Zipes, Douglas and Jalife, Jose *Cardiac Electrophysiology: From Cell to Bedside* WB Saunders Company, 1990
- [41] Saito T, Sato T, Miki T, Seino S and Nakaya H *Role of ATP-sensitive K<sup>+</sup> channels in electrophysiological alterations during myocardial ischemia: a study using Kir6.2-null mice* AJP - Heart 288:352-357, 2005